Author:
O'Keeffe, Caroline

Title:
The manufacture of hybrid micro-braids to improve composite through-thickness conductivity and achieve multifunctionality

THE MANUFACTURE OF HYBRID MICRO-BRAIDS TO IMPROVE COMPOSITE THROUGH-THICKNESS CONDUCTIVITY AND ACHIEVE MULTIFUNCTIONALITY

Caroline O'Keeffe

Department of Aerospace Engineering

University of Bristol

A dissertation submitted to the University of Bristol in accordance with the requirements for award of the degree of Doctor of Philosophy in the Faculty of Engineering

June 2022

Word Count 72484

Abstract

In the aerospace and automotive industries, demand for lightweight, fuel-efficient designs have resulted in an increase in carbon fibre reinforced plastic (CFRP) structures. However, concerns regarding difficult-to-detect damage in CFRP and the risk of in-service failure restricted further application. Current methods for damage inspection require costly downtime, and in-service sensors incur a weight penalty and potentially introduce defects. The development of multi-functional composites is key to improving material performance beyond the purely structural, and further reduce structural mass and volume.

The research aim was to manufacture and incorporate a reinforcing multi-material tufting thread and create a multifunctional composite by increasing mechanical performance and through-thickness conductivity (TTC). Two potential functionalities were investigated. The first, examined a fully integrated crack sensing capability by monitoring changes in through-thickness electrical resistance (TTER). The second, examined the susceptibility of a composite to inductive heating and investigated a new approach for composite thermoset curing and repairability.

The study described the braiding of a hybrid multi-material tufting thread comprising carbon fibre tows and metal wires. The braided thread enabled multi-material hybridisation that was fully integrated into the structure. Crack progression was successfully monitored by assessing changes in TTER. The presence of the hybrid thread also aided the induction cure of thermosets by increasing thermal uniformity and reducing hot spots during curing.

This research successfully demonstrated the manufacture of multi-material multi-functional reinforcement tufting threads. The hybrid thread provided an in-service fault detection method that addressed the parasitic nature of current probes without compromising on mechanical properties. It generated a sensing method that has been fully integrated within a composite structure with the potential to reduce servicing and inspection schedules. This study expanded material capability and has the potential to advance CFRP and composite use in industry.

Dedications

This work is dedicated to my family and friends.

To my amazing Nana, Uncle John, and Duncan.

Acknowledgements

My first thanks must go to my supervisors Professor Ivana K. Partridge, Dr. Giuliano Allegri, and Dr. Dmitry Ivanov.

The staff in the BCI labs deserve a special thanks. You are an incredible, invaluable group, and I could not have accomplished anything without you. Thank you to Dr. James Thatcher, Dr. Stephan Rea, Allison McIntosh-Smith, Ian Chorley, and Katie Smith for their assistance. Dominic Hardman, Mark Fitzgerald, Steve Harding, Richard Chaffey, and everyone else in the workshops who assisted me in developing my testing equipment and setup. Dr. Julie Etches and Dr. Yusuf Mahadik for programming and assisting me in synchronising the LabVIEW acquisition testing method.

I would like to thank the National Composites Centre (NCC) for use of their tufting equipment. A thanks to Pete Whitton and Harry Clegg, who tufted some of my samples.

A thanks to Gemma for the support and helping untangle my thoughts.

There are so many friends and colleagues who volunteered their time to me. I am very grateful to Harry, Rob, Jordan, and Peta. A big thank you to Steve, Arjun, Mike, and Beth for making time for a cup of tea and a chat.

Dr. Debra Carr for being an amazing friend, giving advice, direction and I cannot thank you enough.

Whilst doing this PhD I also undertook my ML assessment, and I would like to thank. Duncan, David, Jane, and Tipi for venturing out with me in all weathers.

Finally, to my husband Duncan. You kept me on track despite everything that 2020 had to throw at us. You proof-read, listened, and kept me focused. Thanks for being my compass and constant supporter. Looking forward to our next challenge and adventure. Thank you for all your love and support.

Author’s Declaration

I declare that the work in this dissertation was carried out in accordance with the requirements of the University's Regulations and Code of Practice for Research Degree Programmes and that it has not been submitted for any other academic award. Except where indicated by specific reference in the text, the work is the candidate's own work. Work done in collaboration with, or with the assistance of, others, is indicated as such. Any views expressed in the dissertation are those of the author.

Signed: ..... Date: .....

Contents

List of Figures

List of Tables

List of Abbreviations and Acronyms

2D	Two-Dimensional
3D	Three-Dimensional
AE	Acoustic Emission
AFP	Automated Fibre Placement
ASTM	American Society for Testing And Materials
BMI	Bis-Maleimide
BS	British Standard
CAI	Compression After Impact
CF	Carbon Fibre
CFRP	Carbon Fibre Reinforced Plastic
CNT	Carbon Nanotubes
CT	Computerized Tomography
CTBN	Carboxyl-Terminated Butadiene-Acrylonitrile Copolymers
CV	Coefficient of Variation
DCB	Double Cantilever Beam
DIC	Digital Image Correlation
DIN	Deutsches Institut Für Normung
DMM	Digital Multimeter
EC	Conformité Européene
EN	European Norms
ER	Electrical Resistance
FBG	Fibre Bragg Grating
FLIR	Forward-Looking Infrared
FOS	Fibres Optic Sensors
HMPE	High Modulus Polyethylene
HTS	High Tensile Steel

ILFT Interlaminar Fracture Toughness

IR Infrared

ISO International Standards Organisation

MF Multifunctionality

MFC Multifunctional Composites

MFM Multifunctional Materials

MFMS Multifunctional Material System

MFS Multifunctional Structures

MM Multimeter

NCF Non-Crimp Carbon Fibre Fabric

OOP Out-Of-Plan

PBO Polyphenylene Benzobisoxazole

PEEK Polyetheretherketone

PID Proportional Integral Derivative

PPS Polyphenylenesulphide

PTFE Polytetrafluoroethylene

PZT Piezoelectric Sensors

ROM Rule of Mixtures

SHM Structural Health Monitoring

TT Through-Thickness

TTC Through-Thickness Conductivity

TTER Through-Thickness Electrical Resistance

TTR Through-Thickness Reinforcement

UD Unidirectional

Glossary

There are a number of terms that could be used to describe the materials used in this thesis. For clarity, the following terms shall have the following meanings:

Wire: a long thin piece of metal that is used to fasten things or to carry electric current [1].

Tow An essentially twist-free assemblage of a large number of substantially parallel filaments [2].

Yarn A product of substantial length and relatively small cross-section consisting of fibres and/or filament(s) with or without twist [2].

Thread **1**. A textile yarn in general

2. The result of twisting together in one or more operations two or more single or folded yarns [2].

Braiding The process of interlacing three or more threads in such a way that they cross one another in diagonal formation. Flat, tubular, or solid construction may be formed in this way [2].

Braid, plait The product of braiding. Certain types of woven and knitted narrow fabric are described as braids [2].

For simplicity when the components of a braid are discussed whether during braid manufacture or as a part of a formed braid, they will be referred to in this study as a yarn. This is irrespective of whether they would normally be defined as tows, wires or threads individually.

List of Appendices

1 INTRODUCTION

1.1 General introduction

1.1.1 Background

In the aerospace and automotive industries, demand for lightweight, fuel-efficient designs has resulted in an increase in the use of carbon fibre reinforced plastic (CFRP) structures [3]. The Boeing 787 and Airbus A350 XWB airframes comprise of more than 50% carbon fibre, resulting in a 20% weight saving and a 12% improvement in fuel economy when compared to lighter equivalent aircraft types [4]. However, the traditional approach to structure development is to address the load-bearing function and other functional requirements separately, resulting in a suboptimal load-bearing structure with non-structural functions performed by add-on attachments resulting in added mass [5]. Multifunctionality (MF) is seen as a “key step” in delivering lightweight volume saving composite structural designs [6]. A multifunctional composite is made up of two or more materials that, in addition to their structural function, perform one or more additional functions [7]. The goal of MF is to reduce operational costs by optimising material and structural capabilities beyond the high specific stiffness and strength of CFRP.

Despite the high strength and stiffness to weight ratios of carbon fibre composites, the full potential of composite structures has not yet been realised. According to the IDTechEx Report, various challenges are impeding the development of fully commercial, multifunctional materials suitable for a wide

range of applications, one of which is the difficulty in producing composites with adequate conductivity and structural properties [6]. In composite aircraft structure, additional metal components are necessary to provide electrical functionality, for example lightning protection, electrostatic dissipation (ESD), grounding, and electromagnetic shielding (EMS) (Figure 1-1) [8]. Composites are susceptible to difficult-to-detect damage such as delamination. Delamination can considerably reduce the load-bearing capacity of a structure and increase the risk of in-service failure [9]. As a result, composites structures undergo extensive monitoring and costly downtime for inspection in order to ensure structural safety and integrity [10].

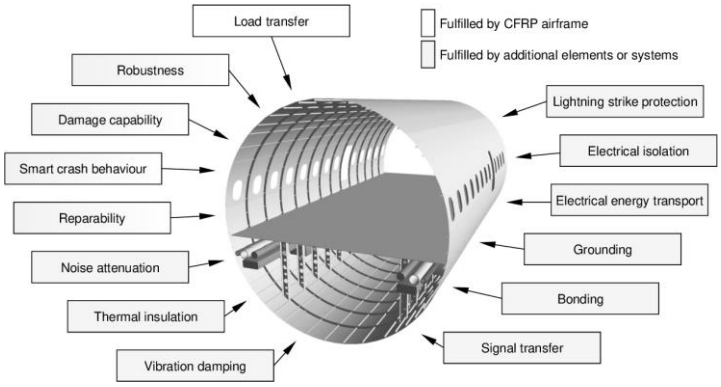

Figure 1-1 Task assignment of aircraft structures [8].

Acoustic emission, ultrasonic scanning, and X-radiography are examples of traditional non-destructive evaluation (NDE) techniques for detecting damage in composites [11]. While these techniques are adequate for application within a well-equipped laboratory and well-controlled environment, they are not appropriate for in-service monitoring and inspection [3]. The ideal solution is a delamination detection or structural health monitoring (SHM) system that can be used in-service [3, 12]. The aim of an SHM is to provide continuous, in-service evaluation of a structure's performance, generate real-time damage response, and provide an inspection method that can indicate when a structure needs maintenance or should be removed from service. The majority of SHM systems, for example fibre optics and fibre Braggs grating sensors, require the distribution of permanently installed sensors [13–15]. These sensors have a limited detection range within in their immediate vicinity and as a result, larger structures necessitate more sensors, and incur a mass penalty [16]. These sensors also have no structural benefit and can inadvertently cause stress concentrations within a structure resulting in sites of delamination initiation [17].

Current SHM technologies add mass to carbon fibre structures, undermining their cost-effectiveness, which is dependent on their lightweight and thus fuel-efficient qualities [18]. Airbus has specifically identified the requirement for a fully integrated sensor, that enables weight savings and less conservative structural designs [19, 20]. It also states that integration should be achieved at the manufacturing stage (Figure 1-2) [20].

Figure 1-2 In the Airbus Roadmap for SHM development, the Generation 1 CBM systems for "hot spot" monitoring (e.g., Delta Air Lines' wingbox fitting program) will be followed by Generation 2 applications, now in development, which enable less conservative, lighter weight designs [20].

1.1.2 Delamination resistance

Methods of improving delamination resistance include matrix toughening materials, 3D woven composites and through-thickness reinforcement (TTR) methods [21–23]. While improvements in delamination resistance can be achieved by modifying resin formulations for example by including liquid rubbers, core–shell particles, thermoplastics, rigid particles, and other additives, the resulting increase in resin viscosity makes optimising dispersion difficult [24–26]. 3D woven composites have had limited use commercially, because of

high production costs and manufacturing complexity, as well as limited processability [27]. Their poor shear and torsion qualities, due to the fact that yarns cannot be placed at angles other than 0 and 90 degrees, further restrict its use in the aerospace industry [21, 28, 29].

TTR methods such as Z-pinning, stitching, and tufting have all been investigated as methods to increase delamination resistance. Advantages of these TTR methods is that they introduce fibres or material in the thickness direction and can be included at strategic areas within a part [30–34]. However, they all come with disadvantages [35]. For example, Z-pinning is designed primarily for prepreg constructions with the inserted pins kept in place by the uncured matrix and are therefore unsuitable for liquid resin infusion [36]. Stitching utilises a double needle technique and like that of weaving requires access to both sides of a part [33]. This increases the extent of damage to the stitched preform, as the needles perforate the perform double that of tufting.

The advantage of tufting is that it is a continuous interconnected TTR method that uses a single needle, making it the simplest form of stitching [21, 37]. A number of studies have investigated tufting to increase delamination resistance and have identified thread robustness as a limitation in tufting efficiency and structure manufacture especially when using carbon fibre threads [23, 38, 39]. Thread damage during tufting was especially significant when carbon fibre tow was used. Its brittle nature often resulted in filamentation, splitting or shed fibres, and therefore is less reliable [23].

The majority of thread production is derived from the textile industry, and there is limited information available on thread optimization techniques for specialty composite applications. Conventional tufting threads were usually made by twisting yarns or fibres of materials for example carbon fibre, glass fibre or Dyneema®. Attempts to solve carbon fibre thread limitation have been investigated by overwrapping the carbon fibre with different materials, such as glass or Kevlar®, but this results in an additional component that does not provide any benefit to the final structure [23, 39, 40]. The over-wrapping of threads also introduces excessive profile changes or nip points along the thread which can result in snagging in the needle eye and subsequently thread breakage [23]. The process of turning and twisting yarn carries a risk of causing pre-damage and leads to the suboptimal placement of fibres in the composite,

as well as inadequate load-carrying ability, due to the twists it creates in the filaments. In other studies, metallic wire tufts were used to demonstrate lightning strike protective functionalities exploiting the conductive properties of the metal. Conductivity increases of 250 times for copper and 20 for stainless steel wire tufts are reported [41, 42]. Each of the above studies described investigated thread robustness or conductivity in isolation, with no consideration given to introducing a material that could enable further functionality. A method that could combine both thread robustness and conductivity could address the limitations expressed by prior reports discussed previously. One method that can combine materials is braiding. Compared to conventional co-twisted hybrid threads, braided structures contain intrinsically commingled yarns in repeating patterns. This ensures consistency in material placement and avoids uneven arrangement along the length of the thread.

1.1.3 Motivation

A number of restrictions for composite applications have been identified in the literature. On the material or structural side, poor conductivity, and susceptibility to delamination; on the operational side, the necessity for costly time-scheduled downtime for maintenance and inspection; and the need for parasitic mass for functionalities such as lightning strike protection and SHM. The robustness of tufting using carbon fibre thread is also a manufacturing challenge. Therefore, the present work will adopt a multimaterial approach in the manufacturing stage to simultaneously increase through-thickness conductivity in CFRP and maintain or improve structural performance. The concept is to take advantage of the electrical and load-bearing properties of metal and carbon fibre to investigate thread robustness, delamination resistance and through-thickness conductivity.

1.2 Research Question

Is it possible to demonstrate MF in carbon fibre composites by enhancing through-thickness conductivity by integrating a novel hybrid tufting thread?

1.2.1 Aims and Objectives

- This thesis aims to develop a hybrid tufting thread to achieve MF.
- To increase through-thickness conductivity without reducing structural capability
- To demonstrate MF in the form of an SHM system for crack detection by monitoring of electrical changes.

1.2.2 Novelty statement

This thesis describes the manufacture of a novel tufting thread that increases through-thickness conductivity of a composite. This will be done by braiding both metal and carbon fibre components, which has not been attempted before for a thread. The study will attempt to understand how to improve the robustness of tufting threads and how to hybridise these threads. In addition to the improved robustness, the combination of the metal and carbon fibre will inherently increase conductivity. The advantages of higher conductivity will be used to enable composite multifunctionality in the form of SHM.

1.3 Thesis structure

The literature review, in Chapter 2, provides a background on various disciplines amalgamated in undertaking this multifunctional research. A review on current MF research and terminology is provided with a discussion of considerations for composite industrial requirements. Specific attention is given to TTR methods and previous studies that investigated the application of TTR and braiding to enable MF in the context of SHM. This section details braid structure and braid manufacturing methods, along with current research developments into hybrid braids.

Chapters 3 and 4 describe the hybrid micro-braid manufacture, its structure, and properties. Chapter 3 specifically addresses the materials and yarns and the Herzog micro-braider specifications. The manufacturing challenges are identified and documented, highlighting the intricacies of multi-material braiding.

Chapter 4 details the creation of a braid manufacturing model. The LS-Dyna model was designed as a tool for braid manufacturing and initial braider–yarn assembly. The work in this chapter provides a method to assess dynamic braid

manufacture. It considers complex multiple and varying yarn interactions and could assist in achieving successful braiding.

Chapter 5 provides a comparison of the hybrid micro-braid to commercially available tufting threads. Included are details of test methods for SHM by measuring ER changes caused as a result of crack propagation during testing. Results of tenacity tests used to establish properties of the hybrid micro-braid and determine its suitability as a tufting thread are included. Properties such as robustness, tenacity, failure mechanisms, and defects of each thread are described and compared to provide a baseline comparison of the hybrid micro-braids' potential.

The aim of achieving MF in the form of SHM in composites is addressed in Chapters 6, and 7. Coupon level studies described in Chapter 6, were undertaken to establish the mechanical properties of both single tuft coupons and coupons containing an array of tufts. Chapter 7 describes a feasibility study to progress from simple coupon testing to more complex carbon fibre composite architectures. T-joint structural element demonstrator tests were conducted and highlighted the complexity of monitoring multiple crack progressions simultaneously. In addition, it addressed the effects of tuft pattern and electrode positioning in achieving a balance between mechanical properties and successful SHM.

Chapter 8 contains the conclusions and future work.

2 LITERATURE REVIEW

This thesis combines several disciplines, with a primary emphasis on multifunctionality (MF). This will be demonstrated by combining through-thickness reinforcement (TTR) and SHM through the use of hybrid braids. The review of the literature therefore looks at MF, TTR, structural health monitoring (SHM) and braiding. Braiding has been identified as a method to comingle and hybridise yarns and will be looked at in detail as it will be integral to the manufacture of the necessary novel multi-material braids. Other techniques relevant to yarn production, such as overwrapping and general comingling are also referenced in both the TTR and braiding sections where relevant. Because it is not the intention of this thesis to provide a material property investigation, a review of testing methods is not provided. The test methods used are solely to demonstrate MF capability and as a comparison method to non-functionalised specimens.

2.1 Multifunctional composites

2.1.1 Background and nomenclature

Composites are made up of a combination of two or more materials where each component provides a unique property to the final product [43, 44]. The aerospace, automotive and medical industries have been the predominant influencers for the rapid advancements in both material and structural designs. Materials research and development is focused on the desire for mass and volume reduction, optimal performance, and the subsequent cost savings.

Traditional methods for material and structural design address load-bearing and other functional requirements separately [5]. These methods result in a suboptimal load-bearing structure with parasitic-like functions, such as electrical wiring, resulting in an increased mass penalty. MF combines the capabilities of one or more sub-systems with that of the load-bearing structure, hence reducing the mass and volume of the total system [44, 45]. Desired additional capabilities include increased electrical capability, thermal properties and sensing (Figure 2-1 Various properties for a material to become multifunctional. Other properties, including processing requirements, can be added to the scheme [44].) [44]. The true benefits of MF can be realised when considered in initial design stages.

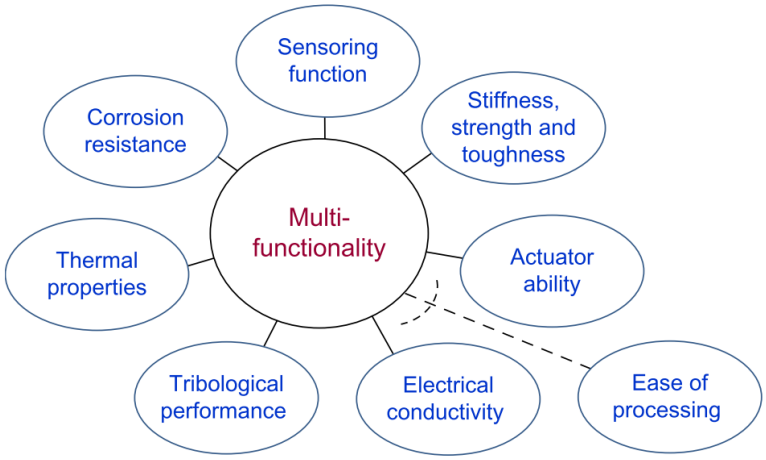

Figure 2-1 Various properties for a material to become multifunctional. Other properties, including processing requirements, can be added to the scheme [44].

Nature provides some of the most advanced multifunctional materials. For example, bones are natural organic/inorganic composites made of hydroxyapatite and collagen, that have various important functions such as supporting the body, muscle movement, and producing blood [7, 43, 46]. Researchers are attempting to mimic these advanced biological systems, to create optimal multifunctional composite/structures, and look towards nature for inspiration to seamlessly integrate material and structural considerations into the final structural component. Ideal MF will achieve synergistic, not parasitic property combinations.

There have been several recent reviews regarding the development of multifunctional materials [5, 7, 43, 45, 47, 48]. It is evident from the literature that ambiguity regarding terminology exists in the industry and many terms are

used interchangeably. This project will use the term Multifunctional Material System (MFMS) as proposed by Ferreira et al, to include combinations of composites, structures and materials which can within themselves be multifunctional [47]. A MFMS can be defined as a material which possesses a structural function together with at least one additional performance-linked function [7]. This additional function can be achieved via the addition of another material or combination of materials that generate a hybridised structure. Multifunctional material research draws on other disciplines such as biology, mathematics, physics, and design for development concepts so as to enable advances in overall capability.

The aim of an MFMS is the simultaneous performance of either multiple structural functions, combined non-structural and structural functions, or both. Irrespective of the taxonomy or the means by which it is achieved, the current objective of MFMS research globally is to enhance system capability, and autonomy, and to upscale this for commercial use. The emphasis for multifunctional composite design and application is on rapid customisation, and component cost reduction, light-weighting, and space saving. [6]. Interest in MF has increased dramatically. This interest can be demonstrated by the Web of Science core data report which shows an increase from 358 publications containing ‘Multifunctional composite” in the title in 2010 to 4283 publications in 2020 [49]. In the polymer matrix composite field, research areas striving to achieve MF have ranged from resin development to nanomaterials and hybridization [50]. A study of the literature shows that the properties of interest are those which mimic metals, such as thermal and electrical conductivity, fire retardancy, and smart materials [6, 45, 47, 51]. Within the aerospace industry there is a particular interest to achieve increased conductivity in a structure. Applications that would benefit from increased conductivity include sensing, self-healing, protection with respect to magnetic and electrical interferences, lightning strike protection, ballistic and crash response, integration of antennae or wiring, energy storage, and light emission [47, 52]. Other areas that would benefit from an increase in electrical conductivity, include electrostatic discharge, electromagnetic interference shielding or damage suppression [51–53]. Whilst the specific technique under development in this project has the potential to be applied to all these areas, the following section of the literature

review will concentrate predominately on SHM capability. In order to bound the scope of the research in the thesis SHM has been chosen to demonstrate a multinational capability. Therefore, SHM rather than the other functionalities identified above will be reviewed in the following sections.

2.1.2 Structural health monitoring

Structural Health Monitoring (SHM) describes methods of assessing the integrity of a structure using a permanent technique that provides an immediate or in-service response. It is also defined as a “process of implementing a damage identification strategy for aerospace, civil and mechanical engineering infrastructure” [54]. The capability for real-time damage assessment has developed into a critical issue in advanced materials such as composites [3]. As the time and effort invested in material and structural design have increased, a limiting factor in their application has come from safety concerns. This is due to the susceptibility of composites to suffer difficult to detect damage that could potentially lead to catastrophic failure [25].

Damage within a composite structure is complex and by consequence the progression mechanisms of failure in-service are more diverse in comparison to metals [55]. The main failure modes of composite materials are matrix micro-cracking, ply delamination and fibre breakage. The development of micro cracks generates stress concentrations between plies, resulting in interfacial stress and subsequently delamination. It is important to note that flaws or damage due to manufacturing processes can be present from the outset [56–58]. The complexity between parameters such as the matrix resin, the fibre types and length, sizing, and lay-up, all have an impact on the potential extent of this processing damage.

SHM therefore, relies on a comparison between an original state and any further subsequent states to determine the extent of damage and its effect on the overall lifespan of a structure. When in-service, processing damage has the capacity to evolve and grow, damage development usually results in a decrease in structure performance, tending towards total failure. The point of failure is reached when the amount of damage results in the structure or system being unacceptable to the user [54]. Industry utilises SHM to avoid instances of critical catastrophic failure that could result in life threatening situations [54].Traditional

non-destructive techniques include optical microscopy, ultrasonic scanning, acoustic emission (AE), infrared thermography, and X-ray radiography [59]. These techniques provide useful information when used in a laboratory or inspection facility, however, they are not suitable or appropriate for use in-service situations or non-ideal environments [3, 60]. Whilst they successfully detect areas of damage, they do not provide in-situ internal damage detection or warn of initial crack propagation. Current detection methods often require a structure to be put out-of-service and disassembled. In addition, they can be unsuitable for large structures and do not provide TT damage detection [61]. Other disadvantages include the requirement for specialist equipment, labour intensity and time-consuming testing methods, all resulting in a high-cost penalty.

Often a variety of SHM sensors are used in combination to provide a comprehensive assessment of damage detection during certification. For example, a combination of eddy-current foil sensors, AE and crack wires were used for full-scale fatigue testing of the Airbus A380. These sensors were installed throughout the fuselage and wings to provide detailed information on crack development, however, such an extensive amount of sensors is not appropriate for in-service assessment [20]. Crack wires are a type of electrical resistance sensor that trigger alarms when compromised by cracks or damage. They are a simple and mature technolgy currently in-service. Airbus utilises crack-wire lines to indicate if the tail of the aircraft contacts the ground during take-off [20]. The Boeing 787 utilises a tail strike sensor which can adjust the elevator position to reduce the potential for tail-to-ground contact [62]. The main disadvantages is that they are often bullky, are structurally parasitic and have a limited range of assessment [6, 20].

Many SHM systems rely on embedded sensors which may themselves introduce imperfection in a structure [25, 63]. This is due to material variations and adhesion issues at the interface, which all result in reducing performance and subsequently failure. The most common reported disadvantages of embedded sensors are lack of durability, limited range of detection, difficult to embed and parasitic mass [6]. Table 2-1 details some advantages and disadvantages of embedded sensors for SHM of composites. Ideally any method for SHM needs to avoid adversely affecting material properties or

excessively compromising weight savings, as well as being non-destructive. Whilst an effective SHM system will enable minimal labour contribution, maintenance, and out-of-service inspection costs, by comparison a truly MFMS will achieve this and also enhance overall material performance. For the true benefits of composites to be realised, it is essential that a method to detect, assess and monitor the generation of damage accumulation is developed to provide a means to determine the service life. Through incorporating a MFMS that enables SHM, the potential to expand composite structure designs and improve system performance can be realised [25].

Table 2-1 Types of embedded sensors for structural health monitoring, adapted from [6]

	Optical senser			**Piezoelectric sensors**		**Eddy current sensor**
Types	Interferometric sensors	Grating-based sensors (includes FBG)	Distributed sensors (includes OTDR)	Piezoelectric wafer active sensors (PWAS)	Piezoelectric fibres	
Advantages	Very high resolution and wide tolerance range	Easy to integrate for full life cycle, high sensitivity, good durability immune from EMI, highly multiplexed	Whole fibre acts as sensor giving excellent range.	Can be integrated into laminar or retrofitted, good range and sensitivity	Flexible, good mechanical properties, can act as actuator, sensitive and good range	Versatile installation, sensitive
Disadvantages	Single point detection, not very durable	High number sensors required for large range; higher scan rates increase complexity	Poor resolution and limited accuracy	Lower multiplexing capabilities, Low technology readiness levels	Lower multiplexing capabilities	Adversely affected by temperature, vibration, and EMI

2.1.2.1 Piezoelectric sensors (PZTs)

Piezoelectric sensor-actuators are the most common type of active sensing SHM [3]. Utilising a combination of actuators and transducers, an active sensor injects controlled diagnostic signals into a structure. Changes in the signal measurements indicate the presence of damage. Therefore, the assessment of data can be undertaken before and after a potential damage inducing event.

The technique has been proven to be more reliable for detecting both local defects and wider damage, although it requires more complex hardware and diagnostic systems for data interrogation. In addition, there have been cases of incorrect assessments due to variations in the environment [64]. The main limitation of PZT is that to be cost effective, only specific areas can be monitored and the positioning of the PZT must be based on historical damage assessments. This is only effective if a structure is used in a consistent way and has a failure pattern due to a predictable fatigue cycle or event. However, if unpredictable events such as a projectile or bird strike do occur, the limited positioning of sensors would not provide as accurate an assessment. Embedded sensors such as optic fibres and PZT have limited durability and are not repairable [60]. Interfaces between the embedded sensors have been shown to be a site of delamination although the literature suggests the effects on performance varies on situation.

2.1.2.2 Fibre optic sensors (FOS)

The use of optic fibres as sensors has had several years of investment and can be considered to be technologically mature within some operational situations [16, 65, 66]. Placement within pavements, bridges and buildings have all been researched along with in-flight structural assessments in aircraft [67, 68]. The small size of optic fibres makes them non-intrusive within a structure and have been shown not to deteriorate performance, although an extensive network is required for a comprehensive structural assessment [67]. The different methods for recording damage using FOS include interferometric sensors, Fibre Bragg grating (FBG), Raman scattering, and Rayleigh scattering. Often FOS are used to measure strain and temperature changes within a structure [16]. One study undertook a comparison of sensor placement, running parallel or perpendicular to the fibres, to determine their suitability for detection. Placement of optic fibres was shown to introduce a resin rich area known as a resin “eye” when placed perpendicular to the fibre, although it is also documented that this “eye” had little effect on the overall performance of the structure. Slippage of the fibre within the composite was also another historical concern, although limited, if care was not taken to ensure the optic fibre was placed in direct contact with the resin [16, 69]. The main limitation of FOS is in placement and embedding in composite structures, as the signal may be weakened and the OF may break

easily [70]. An extensive network of fibres is required to ensure complete measurement along with comprehensive understanding in order to predict where damage is likely to occur [67]. They are also susceptible to moisture, temperature and chemical exposure resulting in the need for them to be coated by polymeric film. This protective layer can reduce sensitivity in the ability to measure strain and also increases the diameter of the sensor. The resulting reinforced FOS is often ten times larger than the reinforcing composite material [70]. In the aerospace industry, despite the advantages and technical maturity of FOS there has been limited use outside of laboratory based or test specimens [68]. Airbus identified the absence of a mature, robust integration process as an industrial challenge [68].

2.1.2.3 Carbon fibres

The electrical conductivity potential of carbon fibres has been of interest in the industry for several years, however, it is yet to be fully exploited. The anisotropic nature of carbon fibre reinforced plastics (CFRP) presents difficulties when using electrical conductivity as a sensing method. Previous studies on the electrical conductivity of carbon fibres have focused on monitoring stiffness reduction and damage accumulation [71, 72]. Damage location detection has also been addressed. The effect of damage under different test modes on the ER of carbon fibre has previously been demonstrated [73, 74]. The studies indicate that fractures of both individual fibres and fibre bundles induce a decrease in the electrical conductivity of the sample, and that the amplitude of the resistance change is proportional to the number of broken fibres. The results monitored ER changes in-plane along longitudinal unidirectional CFRP laminates caused by monotonic and cyclic tensile loading. It demonstrated that ER can be utilised to monitor the specimen loading status even before fibre fracture occurs. However, once a fibre fracture occurs, ER rises in a stepwise fashion [73]. ER monitoring has also been used to detect damage in transverse UD laminates where electrical conductivity is dependent on the fibre-fibre contacts between plies [74]. In the transvers UD laminate, changes in ER were observed as a result of intraply matrix cracking and delamination and the disruption of the electrical network.

The anisotropic properties of carbon fibre are disadvantageous when utilising ER as a method of damage detection. The anisotropic properties result in the

electrical path being dominant in the in-plane direction. Therefore, the detection of delamination in composite laminates is more difficult due to the lack of conductivity in the TT direction [75]. However, a number of studies have successfully utilised carbon fibre as a structural sensor [53, 76]. The commonality in the ER technique of SHM is to monitor variations in the resistivity or conductivity along a structure to assess crack propagation and initiation [53, 74, 76]. The development of cracks or delamination in the material cause ruptures in the conductive paths, resulting in an increase in resistivity. The indication of resistance increase in a structure would provide an early warning to enable corrective maintenance to be undertaken before failure occurs. The effect of matrix cracking during delamination complicates the original conduction paths and often results in a decrease in resistance due to interply connections being made by broken fibres. This phenomenon has been noted by several studies [9, 74]. Several suggestions as to why the decrease in ER occurs including that the matrix cracking increases the likelihood that interply connection can take place. Another potential cause for ER decrease could be due to localised compression or intraply splitting resulting in an increase in contact between plies. Studies have demonstrated that for buckling, ER monitoring of a sample can indicate both initial failure of matrix cracking as well as critical delamination [74].

2.2 Through-thickness reinforcement of composites

2.2.1 Overview

A shortfall and common failure mode of polymer reinforced composite structures is delamination between individual plies [28, 33, 77, 78]. It is a failure mode that compromises the further expansion of composite use in a wider capacity in aerospace and industry. Focusing on the most common methods for through-thickness reinforcement (TTR), this section reports on current attempts to improve out-of-plane properties to avoid delamination. As stated previously, CFRP are made up of two main constituents: the matrix, and the fibre architecture. The matrix is the phase that binds the fibres and is often brittle in nature. The extensive use of composites is due to the high in-plane strength, stiffness, and low mass which in the out-of-plane direction is compromised depending on the properties of the resin matrix material, fibre lay-up and stress

loading. In the in-plane direction it has been reported that the tensile strength of CFRP composites ranges from 500 to 800 MPa. In contrast in the translaminar direction, it is only 20 to 30 MPa. The ability of a composite structure to resist delamination is dependent on both the 2D arrangement of fibres and the brittle nature of the matrix resin [79]. When subjected to out-of-plane forces or high energy impacts cracking ensues in the interlaminar region and matrix, resulting in delamination [28, 36, 80]. This delamination is exacerbated further by extreme TT static and fatigue loads, edge stresses, and environmental degradation [30, 81]. Damage can occur internally without obvious visual signs on the surface of the composite. This sub-surface damage and the lack of simplistic in-service damage assessment hinders the advancement of composite use, with concerns regarding the potential of catastrophic failure whilst in service [28].

There are two dominant methods currently the focus of research. Each method is concerned with restricting crack generation and propagation. The first is the development of high-performance toughened matrix materials, the other is the modification of the structure of the material or TTR. Material methods involve the production of resins which are resistant to crack propagation. Methods include, plasticising modifiers, use of co-polyamide interleaves, the addition of rubber particles such as carboxyl-terminated butadiene-acrylonitrile copolymers (CTBN), thermoplastic particles, nanotubes, chemical structure modification to reduce cross-linking and tailored matrix production [82–86]. This has resulted in the development of tough resins such as polyetheretherketone (PEEK) and polyphenylenesulphide (PPS) [36, 87–90]. The mechanisms proposed for explaining this enhanced toughness are triaxial dilation of rubber particles at the crack tip, particle elongation, cavitation and plastic flow of the epoxy [26, 91]. Reported improvements in fracture toughness for matrix modifiers range from 11% (PES) to 224% (CTBN) although increases in matrix fracture toughness does not always result in an increase in the interlaminar fracture toughness of composite laminates [26, 44, 89]. Moderate increases between 20-50% are most common depending on type and percentage volume of additive [84, 87, 92–94]. However, improvements to delamination resistance gained by using resin modifications is comparatively low, e.g., 0.6- 3 kJ/m^2 depending on modification, compared to TTR composites such as stitches (under 5–10

kJ/m^2), z-anchored fibres (up to 3.5 kJ/m^2) and z-pins (usually up to 15 kJ/m^2) [95]. Other disadvantages occur due to high viscosity and poor dispersion of additives. High viscosity makes this method undesirable for resin infusion, therefore, additive manufacturing is most commonly used in the prepreg industry.

TTR or 3D reinforcement achieves improved interlaminar strength by modifying the fibre architecture through the introduction of yarns in the TT direction and thereby providing transverse reinforcement [28, 33, 36, 77, 96]. This is not only cheaper than resin matrix methods but incurs a minimal manufacturing time penalty through an additional automated manufacturing step. TTR creates a “localised” 3D structure that connects plies through the thickness, or Z direction, providing mechanical resistance to delamination by bridging cracks should they develop [33, 80, 97]. Resistance to delamination minimises the extent of damage and crack propagation in the composite thereby preventing structural failure [28, 36]. In addition to TTR; research is also ongoing to utilise TTR as an alternative to mechanical fastenings and bonding [21, 36].

Current methods of TTR include stitching, tufting, 3D knitting, Z-Fibre TM or Z-pinning, and weaving [77, 98, 99]. The choice of reinforcement depends on the area to be reinforced and the final design criteria. The basic mechanism for delamination resistance is interlaminar crack bridging, however, this is dependent on the kind of TTR, laminate architecture, delamination mode, and the stress applied [100, 101]. The main uses of TTR in composite structures are to aid handling before liquid moulding, join composite structures, improve in-plane and TT strength, and improve impact tolerance and interlaminar toughness [28, 36]. Whilst improvements in the out-of-plane properties (e.g. 200 times increase in delamination resistance [102]) have been demonstrated, in-plane performance reductions have also been encountered and these could outweigh the benefits of introducing TTR into a material [103]. From the literature it is evident that parameters such as stitch type, yarn diameter, needle type, yarn tension, load direction, stitch density, spacing and pattern are all important considerations when applying stitching for TTR. Details on the effects of each type of TTR are discussed further in the following sections. To distinguish the difference between the 3D composites created by braiding, TTR will be referred to as a “localised 3D” process. 3D braiding forms a fundamental

3D structure in a single process, unlike TTR which involves the inclusion of an additional step for the insertion of yarn through a 2D structure [30].

2.2.2 Stitching

Stitching is a simple, cost effective TTR technique based on conventional sewing method and has been investigated as a delamination reduction technique in composite materials since the 1980s. It is one of the most effective TTR methods for damage resistance, with a reported 40% decrease in delamination area compared to an unstitched laminate [33, 77, 104, 105]. Several stitch variations are available to incorporate a high tensile strength yarn into a preform [21, 33, 98, 106]. Yarns with high stiffness and strength properties such of glass, Kevlar®, carbon and aramid are commonly used to improve structural performance [26, 107]. The benefits of Vectran™ have also been studied and is seen as an alternative to Kevlar® due to its higher stiffness and resistivity to moisture [26, 108]. The modified lock-stitch is one of the most commonly used stitches in structural composites and the automotive industry [31]. Other stich alternatives are chain stitching, and standard lock stitching (Figure 2-2) [109–111].

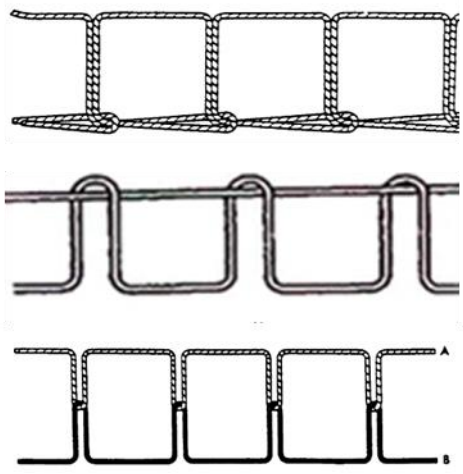

Figure 2-2 Typical stitch types used for through-thickness reinforcement; From the top Chain Stitch (ISO 101), Modified Lockstitch and Lockstitch (ISO 301) [109–111].

The main advantages of stitching are its versatility, cost-effectiveness, full automation and that it requires only slight modifications to current manufacturing equipment and procedures [112]. Stitching provides the capability to modify both preforms and prepregs although studies have shown fibre damage is more prevalent in preforms due to needle penetration. Choices

in stitch and yarn material type along with the potential to use more than one yarn type provide adaptability and flexibility in manufacturing [104]. A disadvantage of stitching is the requirement for access to both sides of the composite, however, the technology has rapidly developed [21, 36, 113]. One-sided stitching technology provides the capability for cost-effective automated manufacturing. It overcomes difficulties when processing large or thick structures as well as reducing localised defects [30]. ALTIN, ITA and KSL, and EADS have developed four blind stitch techniques: the chain stitch, multi-thread chain stitch, unchained open yarn loops, and blind chain stitch.

Thread diameter effects have also been reported, which determined that higher stitch density with smaller diameter thread is better than larger diameters at lower density [113]. The study suggests that the respective traction laws changed as the crack length increased and the load transferred on to the stiches. A higher density stitch pattern produced a more stable crack growth due to an increase in the number of stiches involved in crack bridging. Studies investigating compression after impact (CAI) strength show increases of up to 80% with a 40% decrease in impact delamination [104, 114]. Studies have shown that stitch failure types can vary even along the same row, with failure mechanisms ranging from breaking to thread pull-out [113, 115]. Conflicting information regarding the effect of stitch thread tension exists within the literature; indicating that tension optimisation is dependent on lay-up, thread material, application, and testing method. Studies have shown that stitching can increase shear strength and simultaneously cause a reduction in the in-plane mechanical performance [116, 117]. High thread tension can be beneficial for structural seams because it prevents yarn distortion and seam movement [98]. Conversely other studies have shown little difference between high tension and low tension with regards to CAI testing (323 MPa CV 9% and 303 MPa CV 6.2%), however, the study fails to quantify the low and high tension of the lock stitches used [116]. Stitch types and geometry significantly influence the tension parameters as well as fracture toughness thus affecting the drapability of the material making stitch type selection a critical factor in manufacturing process management [98].

Studies in the literature agree that stitched composites possess higher post-impact residual mechanical properties than their unstitched counterparts [79,

114]. Increases of up to 80% in CAI failure strain and 40% reductions in impact delamination have been reported [115, 118]. However, it has been reported that following impact stitched laminates had lower flexural strength (decreases between 2%-27%) and elastic moduli (decreases between 10%-22%) lower than un-stitched laminates [96]. The complexity of testing for variable load parameters is evident in the studies undertaken by Tan et al. (2012) where stitching effectiveness differed between low impact and high impact conditions. Further studies by this team determined that at lower loads the initial damage area in stitched composites was greater than in unstitched counterparts, however, propagation was reduced by the presence of the stitches [119]. Stitching has also been shown to provide a better CAI performance to cost ratio compared to tufting and Z-pinning [105].

Reductions between 2% and 45% in the in-plane properties are most commonly reported [103, 108, 113, 116, 118, 120–122]. Stitch density influences the degree by which in-plane tensile, compressive, and flexural strengths are reduced. Higher stitch density increases fibre damage due to needle penetration, fibre disruption, and the presence of knots within the laminates. Artefacts such as resin-rich regions, broken fibres, and yarn loops all negatively affect material properties. It has also been reported that the strengths of stitched composites were not affected appreciably by stitch density, however, laminates stitched in the parallel direction possessed higher strengths than those stitched in the normal direction [96]. The methods for testing delamination resistance of reinforced composites have been scrutinised by several studies because of conflicting results. [114, 123]. Methods at qualifying the effect of stitch density using the standard Double Cantilever Beam (DCB) test have proved limiting when applied to high stitch density due to specimen failure by compressive stresses as opposed to delamination. Care must therefore be made when interpreting and comparing results, due to testing variability in methods. Whilst this is a weakness in the use of DCB testing is still widely used to demonstrate TTR capability.

2.2.3 Z-pinning

Z-pinning involves the insertion of discontinuous thin rods (Z-pins or Z-Fibre®) into either prepregs or preforms (Figure 2-3). Materials such as pre-cured carbon fibre/bismaleimide matrix Z-pins, steel, titanium, glass, aluminium, boron and silicon carbide have all been used as z-pins [124]. There are several comprehensive reviews available in the literature providing extensive detail on the historical development of Z-pins, mechanical assessments and insertion methods [34, 105, 125, 126].

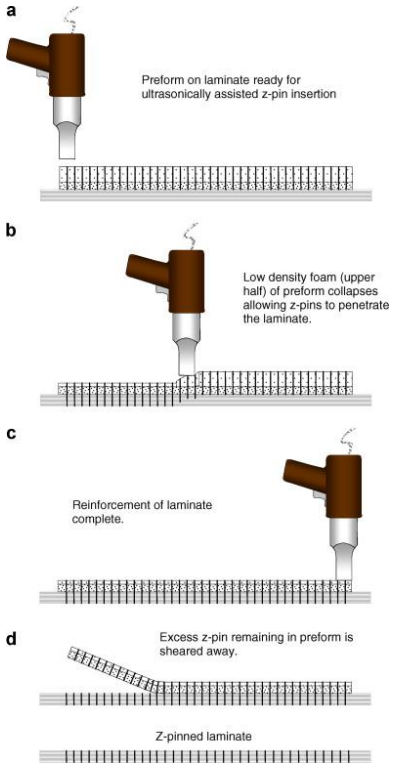

Figure 2-3 Schematic of the UAZ® process [125].

From a manufacturing perspective, Z-pinning has the advantage of requiring access to only one side of the laminate enabling the process to be undertaken directly on the mould [125]. Compared to stitching, Z-pining is a relatively expensive process, however, unlike stitching it does not create knots or loop artefacts within or on the surface of the composite, thus avoiding areas of stress concentrations which can reduce in-plane properties. Conversely, the anchoring effect present in stiches results in higher shear stress loads; up to 14 times greater than that of Z-pins. Stitches fail by pull out, whilst in contrast, Z-pins fail by tensile rupture prior to pull out [127]. Two methods have been applied to study the effects of Z-pins for composite reinforcement. These are the

examination of the effect of either a single Z-pin within a laminate coupon or a multiple Z-pin reinforced laminate. In-service use of Z-pins typically comprises of an array of Z-pins. It is evident from the literature that the use of multiple pins within a laminate introduces additional characteristics not present with a single pin. These include resin pockets merging, fibre waviness and Z-pin interaction and orientation, which all increase with higher Z-pin areal density and diameter [101].

Reproducibility and variability in pin alignment and orientation are concerns during processing [128]. Twisting and bending of the pins following cure have been observed in a number of studies. Z-pinned composites suffer from similar defects to stitching, such as resin rich pockets, damage to fibres due to pin penetration, fibre waviness and are often the cause of in-plane property reductions [26, 124]. Parameters such as pin-matrix bond strength, frictional contact between the pin and the laminates, and pin material properties influence the extent to which a pin will successfully “bridge” a crack preventing its propagation when in mode I loading [100, 129]. Z-pins do not prevent crack initiation, however, they do reportedly hinder subsequent propagation with the crack development progressing in an unstable manner through the Z-pinned area [77, 97, 127, 130]. Z-pin failures are caused by debonding between the Z-pins and the matrix, the internal splitting of the Z-pin leading to Z-pin pull-out, fibre fracture, resin deformation and resin crushing [26, 105].

2.2.4 Tufting

Tufting is a method of inserting a yarn through a fabric, textile or dry preform using a single needle. Tufting was commonly used in the manufacture of carpets and clothing but has now been adapted for the composite industry and has swiftly become the most efficient method for TTR [34]. Tufts are inserted using a hollow needle which retracts along the same insertion point. The yarn is held in place by friction between the yarn and preform or the yarn and a sacrificial foam support. This creates a double length of yarn with a loop on the back face of the preform as shown in Figure 2-4. This loop can be either trimmed before infusion or retained to form part of the structure which is embedded in the matrix resin. Alternatively, the tuft can be partially inserted within the preform resulting in an internal loop. The full penetration of the

preform by the tuft has, on occasion, been called ‘global-tufting’; whilst the partial tuft method is called ‘partial-tufting’ [33].

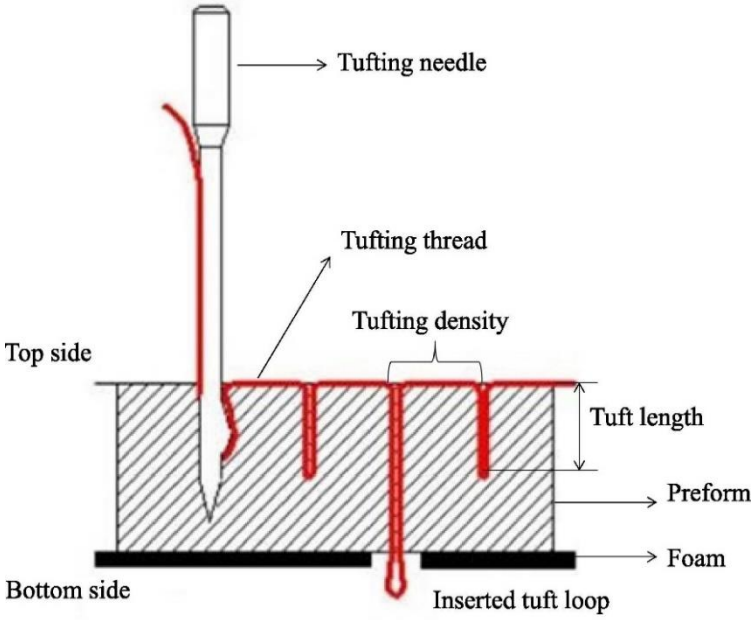

Figure 2-4 Schematic of tufting process [33].

Tufting has several advantages in comparison to stitching as a TTR method. Compared to a stitched yarn, tension in a tufted yarn is considerably reduced [131]. The lack of interlocked yarns avoids both stress concentration points and fibre crimping that are usually associated with crack initiation. Tufting is a one-sided technique that enables easier, more flexible and complex manufacturing possibilities [34, 132]. It is a fully automated process with a number of commercial machines available. Typical automated tufting units are comprised of a modular tufting base integrated with articulated robot arms.

Suppliers claim that robot accuracy can control placement of the tufts within +/- 0.05mm [133]. This provides consistency and reduces variability along a preform. Tufting offers wider choice for the end user compared to other techniques. The dexterity of the robotic arm provides a variety of tuft pattern arrangements and orientations, which can be tailored to requirements and enable bespoke optimisation. However, whilst tufting has this potential, a lack of comprehensive studies and large-scale application presents a considerable limitation for industrial use. An assessment of materials and laminate characterisation as well as a quantification of manufacturing parameters is greatly needed to enable predictability of overall structural performance

(Chehura *et al.*, 2014; Scott *et al.*, 2018). Most investigations on specific variables are limited to a handful or individual examinations and do not provide a comprehensive study to enable full optimisation of either the final product or a manufacturing protocol.

The present project examined the creation of a hybrid braided thread for tufting, therefore the following examination of previous studies on tufting thread parameters provides an insight on current successful tufting threads. Most commercially available tufting threads are carbon, aramids, and glass. As a result, most studies are concentrated on these available threads [38, 77, 135, 136]. A number of hybrid threads have been developed for other industries and highlight the advantages of optimised fabrics for different applications [137]. However, most of these hybrid threads are focused on providing a homogenisation of reinforcement and matrix combination or are for use in other industries and few have been formally investigated for tufting.

Thread properties have been shown to have a direct impact on delamination resistance potential, with properties of carbon fibre outperforming Kevlar® and glass [38, 138]. For example, one study examined fracture toughness of carbon fibre, Kevlar® and glass tufted specimens and reported an 895% (1851 J/m^2) increase for carbon tufted specimens, 798% increase (1670 J/m^2) for Kevlar® and 613% (1326 J/m^2) for glass [138]. The increase in fracture toughness was attributed to the tensile properties of the thread, with higher tensile modulus the higher fracture toughness. In this instance the tensile modulus of the carbon fibre, Kevlar® and glass thread were 210 GPa, 69 GPa, and 79 GPa respectively [138]. Other studies have similarly reported increases in fracture toughness between 3-10 times that of the untufted specimens [32, 38, 102, 133, 138–140].

Concern has been raised over diminished thread material properties due to thread imperfections and damage. The tufting thread must withstand friction, bending, kinking and wear during the processing stages. The brittle nature of the carbon filaments makes the carbon thread susceptible to local splitting under high curvature in the needle eye especially when used with highly packed preforms [38]. Kevlar®, and glass threads have been shown to be more robust and reliable from a manufacturing perspective than carbon fibre threads, though they do not provide the same increase in delamination resistance [133, 141].

Previous studies expressed particular concern over thread damage at insertion points and on the loops [38, 102, 133]. Damage to tufting thread was observed to be most extensive during the insertion step, as opposed to when the needle was retracted [141]. To overcome this, a two-step insertion process with an unthreaded ‘guide’ needle was proposed [141]. The method involved the ‘guide’ needle pre-punching holes in the preform followed by a threaded tufting needle. The first hole punch separated the preform fibres making a void for incoming thread. This reduced first friction between the threads and the preform, decreased the lateral contact and transverse compaction of the inserted thread on insertion. To enable the thread to be still held sufficiently within the preform the first needle was smaller than the tufting needle. While this procedure is quite simple, and the additional pre-punch lowers intrinsic thread damage, it adds another step to the production process and diminishes efficiency, which is otherwise a natural benefit of tufting. The addition of a needle increases the complexity of the programming step and, as a result, the production time.

Thread damage, tuft variability and the need for optimisation has been noted in several studies, but only a single piece of research examines the complexity of the needle insertion process exclusively [134]. This research used sensors bonded to a tufting needle to examine bending moments and strain experienced during the insertion process [134]. Of particular interest is its examination of the effect of different threads, most notably the effect of copper wire. It identified that the interactions of stiffer copper wire with the needle differed to that of Kevlar® and that more sudden changes in frictional forces were possible [134]. With the exception of thread stiffness, the research paper provides few recommendations to increase tufting optimisation. However, it provides a very beneficial insight to the forces experienced by the thread and needle.

Only one published research paper was found to formally address parameters for a successful tufting thread [36]. It emphasised that a relatively high twist level is a desired parameter, especially for carbon threads. The twisting compacts the threads, reducing the likelihood of filamentation when processed through the needle. Some novel threads comprising of overwrapped carbon tow have been examined for their suitability for tufting [23]. This overwrap reportedly protects the carbon tow from breakage. However, the introduction of additional material could present compatibility issues during infusion. Compatibility issues

are also a concern when integrating materials for thread development; varying properties in materials can cause asynchronous behaviour [23, 137].

One of the benefits of tufting is its ease of automation and manufacturability [33, 106]. The versatility provided by robot arms and the modular attachments of the current tufting machines provides the potential to tuft a wide variety of preform shapes and sizes. However, it is evident from the literature that variables that occur due to processing and manufacturing conditions require further assessment [36, 142]. Studies which have addressed manufacturing parameters have concentrated on the effects of tuft areal density, tuft size, loop length, tuft angle, presser compaction force, and needle penetration [34, 136, 143, 144]. A common difficulty experienced by a number of studies is the effect of needle size and shape on thread damage during insertion [34, 133, 141]. This is particularly important with respect to carbon fibre, where filaments are fragile and susceptible to local breakage and snagging in the needle eye [23, 141, 145]. Figure 2-5 shows a commonly available and an experimental tufting needle.

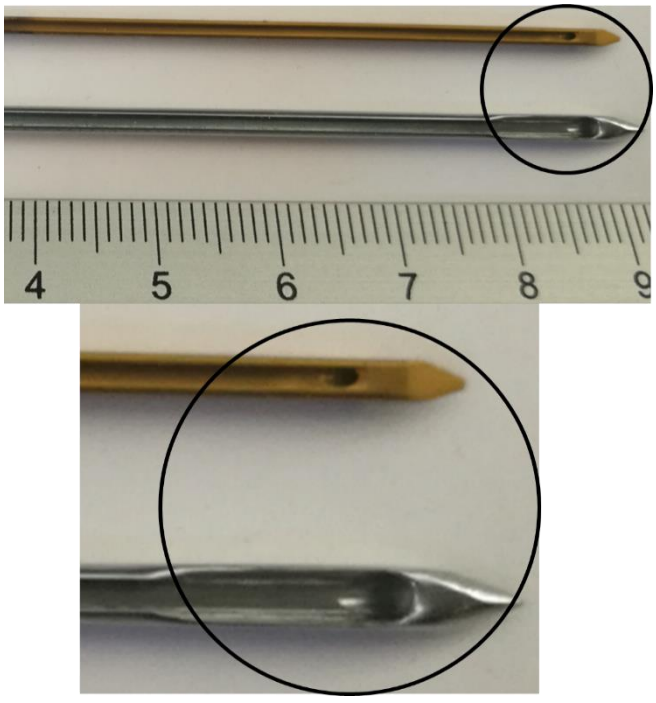

Figure 2-5 Tufting needles: [top] experimental needle and [bottom] commercially available. [Below] Magnified section of needle eyes highlighting the different shapes.

However, the general lack of bespoke needles causes significant problems for the tufting process. For example, thread diameters are restricted by needle eye diameter availability. It is unknown whether an improvement in reproducibility or

productivity would be achieved if more bespoke equipment were used. It has been suggested that reducing both length and thickness of the needle could reduce thread damage and ply crimping, but while previous studies have mentioned this, none have fully investigated [36, 133, 141]. Whilst these parameters and others have been proven to influence final structure properties, research is limited [146].

One previous study has shown that the type of supporting foam used can affect both efficiency and accuracy in the tufting process. Poor selection of this sacrificial support can cause pull-out of thread resulting in tuft free areas, irregular penetration depth, loop length variation and thread damage [36, 133, 144]. When choosing backing material, which at present is a trial and error exercise, consideration must be given to the elasticity, thickness, potential for debris release, and the thread type [36]. There is currently limited understanding of these variables and consequently material selection is often based on availability. A potential solution to avoid the need for backing material as suggested by one study, is to mount the preform on a solid support with sections cut out (Figure 2-6) [36]. Loop formation is accommodated in the free space underneath. However, the mounting support rigs or moulds would have to be custom made for each specific shape and tuft pattern.

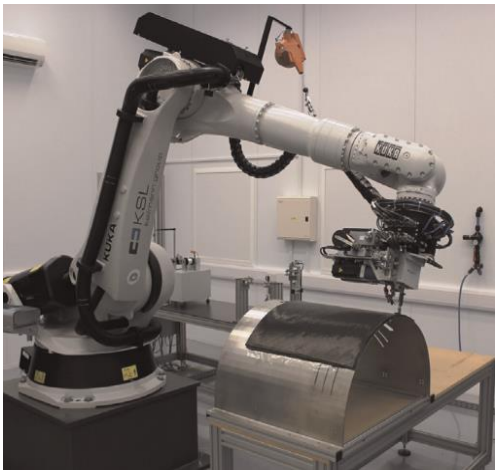

Figure 2-6 Robotic arm interfaced to KSL RS522 tufting head while tufting a simple single curvature preform on solid support backing [36].

Partially tufting the preform would overcome issues with backing material. The literature indicates that partial tufting reduces the possibility of resin pockets and avoids the creation of a resin rich layer on the underside of the laminate due to the external surface loops [38]. Another advantage of ‘partial tufting’ is the

presence of internal loops which appear to increase the capability of energy absorption due to complex resin-rich regions created within the composite [136]. However, partial tufting presents issues with manufacturing reproducibility; visual assessment of loop length is not possible and therefore it is not possible to know that the desired specifications of internal tuft lengths have been met. Therefore, internal imagery or methods to monitor the amount of thread inserted would have to be implemented [147].

The literature tends to concentrate on the final composite properties, with a limited number of studies dedicated to the use of tufts to stabilise an uninfused preform and the effect this has on manufacture [34, 148]. A single study [149], described the effect of tufts and tuft orientation of fabrics compared to untufted fabrics. It indicated that tufting decreases tensile properties by approximately 28% compared to untufted samples and highlighted the importance of the tuft orientations and its influence on fabric properties. The specimen tufted in the same direction as the tensile test (tufted 90°) had stronger strength than those tufted in the other orientations (tufted 0°, tufted 0/90°). Research has also shown that fabrics containing tufts aid in preform robustness, formability, handling and complex shape manufacture by resisting deformation, wrinkling and inter-ply slipping [78, 133, 146, 149, 150]. Conversely, tuft inclusion can also present disadvantages. Distortion and waviness generated by tuft insertion can lead to variations in fabric profiles affecting final product properties [34]. The presence of external loops can make handling a preform more difficult and care must be taken to avoid accidental pull-out [36]. Irregularities during infusion caused by tufting have also been documented; analysis of preform shape and size after infusion show discrepancies and variations of up to 18% in fibre volume. This has been caused by the compression of preform fibres in the vicinity of the tuft [135]. Introducing tufts into a preform or structure evidently increases the complexity of the failure mechanism. However, compared to an untufted laminate, crack propagation of a tufted laminate is considered to be stable and predictable [38]. Generally, crack propagation in a tufted composite can be categorised in two steps; first where the crack is restrained by tuft bridging; followed by a jump in crack length due to the failure of the tuft [133]. Failure mechanisms of the tufts include breakage, pull-out, bridging, and ploughing [38, 151]. Breakage of the tuft occurs usually at the crack interface.

Pull-out occurs when a tuft breaks within the tuft channel and pull-out of the broken thread fragments contribute to the energy dissipation through friction. Where a tuft debonds from the surrounding laminate, mixed loading causes the tuft to move or plough into the resin rich areas of the resin pocket. Maximum loading may be attained for significant shear displacement until the tuft reaches its maximum strength and eventually ruptures [151]. In mode I, tufting resists delamination by reducing crack opening displacement. In mode II it resists crack sliding ploughing displacement. Where loops are removed it has been shown that the tuft pull out behaviour is similar to that of Z-pins [32].

Previous studies have examined the effect on mechanical properties and failure mechanisms of the tufted composites of variables such as tuft length, density, and patterns [32, 108, 147]. What is evident from the literature is that manufacturing variables as well as tufting parameters determine the extent of mechanical behaviours of a composite laminate. Studies indicate that composite performance depends predominantly on the overall composite configuration and manufacturing parameters [143]. With respect to tufting, properties such as thread type and size, fabric type and lay-up, areal tuft density, and the speed of needle insertion have all been shown to have an influence and through further research can be tailored for specific use and optimisation [131, 140]. As studies in the literature all differ in some capacity, it is difficult to directly compare between them. However, overall, with respect to delamination, the incorporation of tufting is advantageous. Studies have indicated that introducing TTR by tufting increases both mode I and mode II delamination resistance [38, 116, 131, 133]. Like other forms of TTR, a compromise in the in-plane strength and stiffness is also observed due to artefacts such as resin pockets, localised fibre misalignment, fibre breakage and compaction (Figure 2-7) [34, 78, 102, 152].

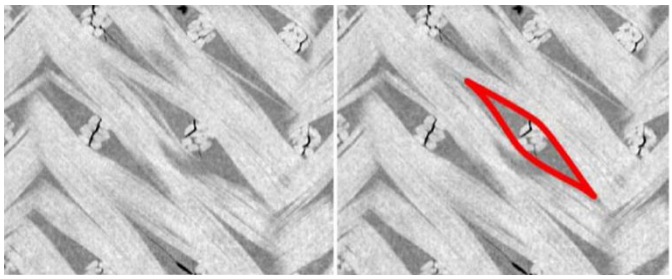

Figure 2-7 (Left) Planar section CT micrograph of a tufted laminate, (right) characteristic “eye” shaped resin-rich region formed around each tuft (no scale provided in original).

Thread damage such as thread rupture, splitting, crimping or stich line deviation during the insertion process can cause damage within the fabric resulting in substandard laminate properties. Increases of up to 16 times in mode I and three times in mode II in delamination resistance have been reported when compared to non-tufted composites [102, 140]. Decreases of in-plane properties have also been reported and attributed to damage to the ply fibres caused by needle insertion. Some reported between 15-40 % reductions [9, 116], with others reporting no variation in-plane properties [142, 153]. Whilst tufting does not reduce the likelihood of crack initiation it does reduce delamination development and the extent of damage.

Studies on the effect of tufted T-joints showed an increase of 10% in total energy absorbed during pull-off tests [154, 155]. Similarly compared to a non-tufted laminate, an increase of 30% in the CAI strength was recorded, with a slight decrease to 28% for an angled tuft [9, 38]. When testing CAI, it has been reported that the damaged area in tufted specimens is up to 4 times less than in non-tufted specimens [9]. Under quasi-static and fatigue pull-off loads, T-joints reinforced with tufts revealed changes in failure mode, with delamination between the skin and the stiffener stopping completely and the samples failing in bending. Reinforcement positioning was determined as an important factor in the damage tolerances of the tufted T-joints [9, 155]. Tufting at the fillet resulted in different failure modes for an untufted specimen and tufted specimen (Figure 2-8).

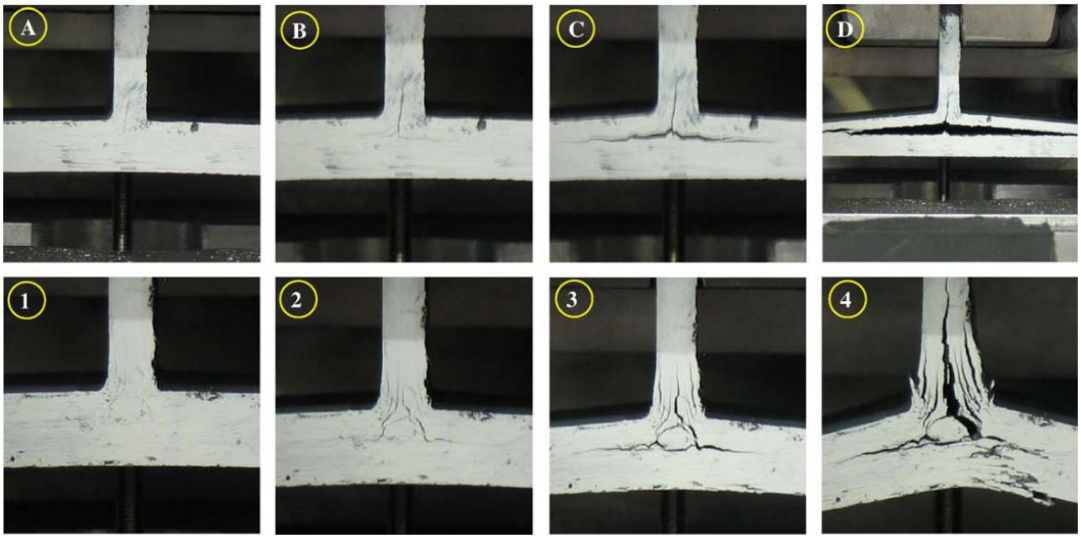

Figure 2-8 Comparison of the behaviour of samples manufactured using the RTM route with and without 3D (tufted) reinforcement [154].

Damage for untufted T-joints initiated at the weak fillet region (A), propagated into the web (B) followed by multiple delaminations (C) and the separation of the flange and the skin (D). In the tufted T-joints, cracks began near the noodle (1 and 2). The cracks propagated vertically in the web, resulting in multiple delaminations (3). The specimen failed in flexure after the delamination between the skin and the stiffener was halted (4). Despite the fact that the first failure occurred at a similar load, the overall load carrying capacity of tufted samples was increased by a factor of two [154]. Tufted samples had more failure artefacts than untufted samples due to the higher failure load [9].

2.2.5 Summary of TTR methods

Table 2-2 provides a summary of the advantages and disadvantages of the methods used to improve out-of-plane properties and increase delamination resistance. From a financial perspective, liquid resin infusion techniques are appealing because they are a less expensive alternative to prepreg manufacture especially for larger structures. Savings are made by reducing capital equipment costs and autoclave use. Cost reductions from $2 million to $500,000 have been reported despite the 25% increase in lay-up times and the associated labour costs [156]. Similarly, a laboratory cost model assessment approximated the economic implications of utilising tufting for a T-section. Tufted, untufted, and equivalent prepreg parts were compared and the tufted part was shown to be more cost effective than a standard aerospace prepreg. The untufted RTM part was substantially less expensive than both solutions, however, structural qualities were not considered [157]. The tufted T-section offered superior economy based on the through-life cost benefit of a lower mass solution, with a weighted cost per part estimated to be nearly 17% lower than the current prepreg solution [157]. The lifetime cost per part for a tufted component has been shown to be 14% lower than an untufted component and as much as 61% lower than the prepreg equivalent for an aeroplane rib pillar [158].

Table 2-2 Comparison of TTR methods

Methods	Advantages	Disadvantages
Resin modification E.g., Polyether, sulfone,silicone rubber, PEEK, CTBN,PES, Nano materials	Simple technique [26, 91] Extensively used in prepreg manufacture [89], 300% increases in ILFT reported [159] CAI improvements 20-55% No reduction in in-plane properties	Low ILFT under 2 KJ/m2 [24, 84, 85, 87, 89, 91, 94, 160] A moderate increase ILFT approx. 25% common [92][91] High viscosity resulting in difficulty processing [91], Can be difficult to automate (E.g. nanomaterials) Difficulties in distribution of particles, difficult to optimize (considerations include nano-filler loading, dispersion techniques, materials) [26] Increases in matrix fracture toughness does not always result in increase in the interlaminar fracture toughness of composite laminates [26, 89] Changes in glass transitions [89]
Stitching	ILFT 5–10 kJ/m2 [95] 40% reduction in impact damage area [104, 161] 80% increase in CAI 40% reduction in impact delamination [114, 118] Apparent Gic increase of 45 times compared to unstitched [123] Manufacturing process can be automated Consistent effects Yarn in the TT direction Localised reinforcement technique	2-45% in-plane property reduction [103, 118, 120, 121] Interlinking of two thread resulting in stress concentration, double needle technique Two-sided access to part needed The flexural properties of the stitched laminates are lower (between 15 and 30%) [162]
Tufting	ILFT 3-5 kJ/m2 [95] up to 200% increase in delamination resistance [102] 16 times compared to the un-tufted specimens, one needle, single-sided technique Thread held by friction 25-27% increase in CAI [38] 15% increase in shear, cyclic and compressive strengths [140] Manufacturing process can be automated Consistent effects Yarn in the TT direction Localised reinforcement technique	Handling difficulties before infusion Up to 20% reduction in tensile strength [38, 140] 5% reduction in stiffness [148, 154]
Z-pinning	10–15 kJ/m2 [95] 19–64% reduction in impact damage area [105, 125] 23%-60% increase in modulus [125] Not suitable for resin infusion methods	Pin alignment concerns Reduction in in-plane properties (>10%) 17% reduction in compression modulus Generally limited to prepreg [35] High Cost [95]

2.2.6 Through thickness structural health monitoring

This section examines the current studies dedicated to incorporating MF by using TTR techniques. As discussed previously, there are a number of studies dedicated to profiling the use of TTR to increase delamination resistance and the resulting enhanced mechanical properties. In addition, composite MF in the form of SHM has been subjected to several recent reviews detailing a wide range of methods such as nanotubes, piezoelectric ceramics, optical fibres, and Fibre Bragg grating (FGB) [93, 163–165]. Due to the broad range of topics that come under MF, most reviews provide a general overview with few providing in depth assessments of researched topics. The MF reviews assist in highlighting the importance, potential, benefits, and the general aim of incorporating MF. However, for researchers interested in specific topics such as introducing MF by TTR, a more focused review is likely to provide more clarity on the current state of the topic of interest. This review will specifically assess the current developments in TTR methods to enable delamination detection and composite degradation by monitoring the variation in ER.

Carbon fibre is predominantly electrically conductive in the in-plane direction, whilst the out-of-plane (OOP) conductivity is significantly lower and dependent on random fibre connections [73, 166]. The presence of the low conductive resin matrix also inhibits the formation of an electrical network, thus increasing the through-thickness electrical resistance (TTER). Due to this, composite laminate delamination studies commonly involve methods of increasing the through-thickness conductivity (TTC) to enable monitoring of any changes from a baseline value due to interlaminar cracking. Methods to increase TTC commonly involve incorporating a conductive material into a composite either by Z-pinning, stitching, or tufting. Delamination is assessed by monitoring an increase in ER caused by the disruption of the TT electrical pathways.

There have been a number of studies that examine the use of carbon fibre as a self-sensing composite due to is inherent conductive properties [73]. It has been demonstrated that fibre failure can be monitored by the change of electrical conductivity in plane. However, most approaches of this type do not yield enhancement of material performance, such as improved delamination resistance, or enable additional functionalities beyond the purely structural domain. The ability to monitor ER changes in these cases were essentially a

convenient but otherwise unintended property of the material. Likewise, these approaches do not work when the reinforcement is non-conductive in nature, as in the case of glass fibres.

Some studies have examined a purely theoretical assessment of the viability of employing a piezoelectric fibre to determine the bridging force and subsequently monitor delamination and crack propagation [167–169]. A limiting factor in the application and further expansion of this approach is the lack of experimental studies available to support these model based studies [170]. The first experimental study based on measuring TTER using Z-pins was undertaken by Zhang *et al* [171]. The authors characterised the ER of individual carbon/bis-maleimide resin (BMI) Z-pins when tested under tension using a four-wire multimeter (MM). This test complemented theoretical models and increased the potential of incorporating MF into composite materials by confirming the viability of using Z-pins as a sensing material to detect delamination. The research determined that changes in ER were due to the elastic elongation and deformation of the Z-pin and resulted in an overall increase in ER under tensile loading, as shown in Figure 2-9.The self-sensing capability of the Z-pins was consistent up to 0.8% elongation, after which random carbon fibre failure caused a significant scatter of ER values.

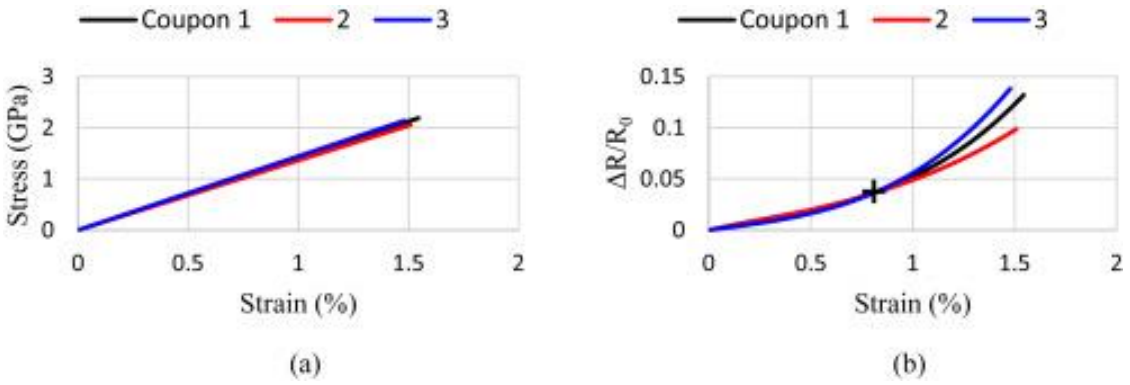

Figure 2-9 Tension results of three CFRP Z-pins, (a) stress and (b) fractional ER change [171].

This study also provided the first comprehensive examination of Z-pinned laminates under Mode I and Mode II testing and provided a direct comparison between conductive and non-conductive laminates in terms of delamination monitoring. Zhang *et al* provided details of the three-stage failure mechanism and ER profile of sensing Z-pins, illustrated in Figure 2-10 [171].

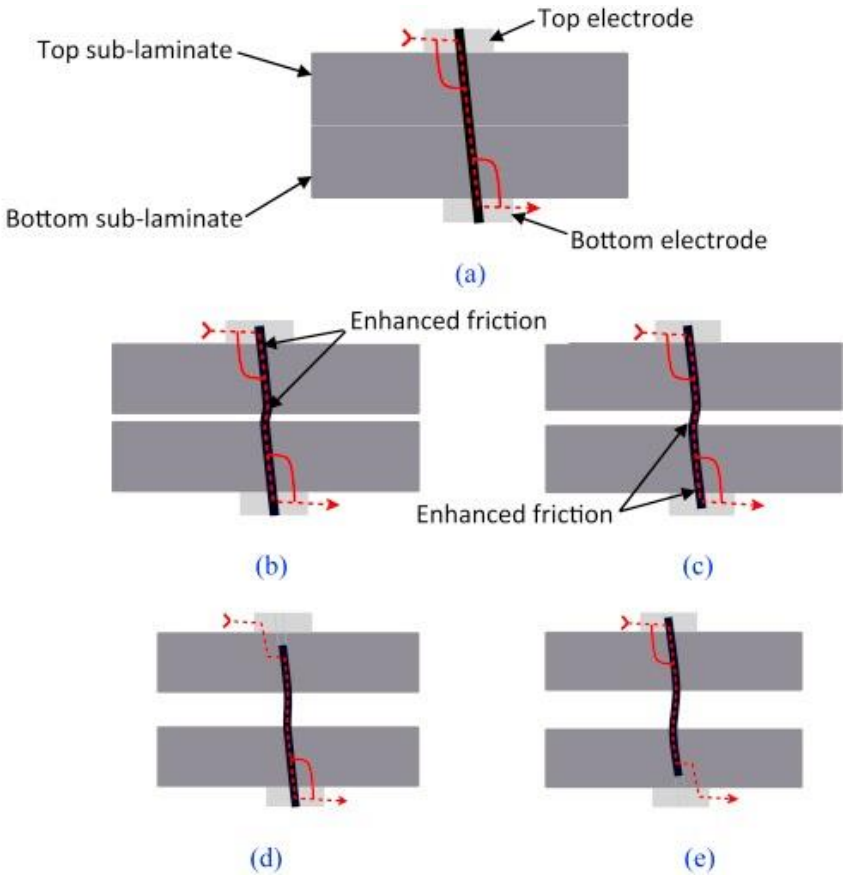

Figure 2-10 Pull-out snapshots of the Z-pin with sensing configuration, (a) stage I: pre-debonding from electrode; stage II: pull-out from (b) top electrode and (c) bottom electrode; stage III: pull-out from (d) top sub-laminate and (e) bottom sub-laminate; dashed and solid red lines indicate current paths [171].

These stages were confirmed by the observed load drops during testing and were different depending on whether or not a Z-pin was attached to an electrode. For the sensing Z-pin, the first stage was the result of the Z-pin/electrode debonding. The second stage was caused by the bridging force and the frictional connection between the Z-pin and the laminate, as well as the elongation of the Z-pin. Stage three consisted of the complete pull out of the Z-pin. For non-conductive glass laminates, it was initially speculated that the delamination of the Z-pin from the laminate should not be detectable via ER measurements. However, further investigations demonstrated that glass laminate coupons did provide an unexpected ER response during tests. An examination of the coupons determined that Z-pin filaments remained within Z-pin channels during pull-out and these filaments enabled a sufficient connection to provide finite ER values. Depending on the channel, the initial TTER values of the pin in the CFRP ranged between 17 Ω and 75 Ω, and between 35 Ω and 180 Ω in the GFRP. Overall, the magnitude of the actual TTER drop varies with

respect to the delamination arrival time, but the associated trend is consistent across all channels. A noisier ER profile was generated in these instances due to the scattered locations of the residual carbon fibres. Zhang *et al* further examined the practicality of Z-pin use as MF enablers in a subsequent study [172], which progressed from single Z-pinned coupons to assess the effect of multiple arrays of Z-pins in DCB coupons. Figure 2-11 presents the experimental set up of DCB samples.

Similar, to the previous study, an overall increase in ER was observed during testing. Both these works provide the most comprehensive account on Z-pin use for sensing and confirm the viability of employing Z-pins for achieving MF. The study showed that a 0.5 % areal density of Z-pins is sufficient to increase the apparent fracture toughness from 0.3 kJ/m^2 to 8 kJ/m^2 for CFRP and 0.2 kJ/m^2 to 10 kJ/m^2 for GFRP.

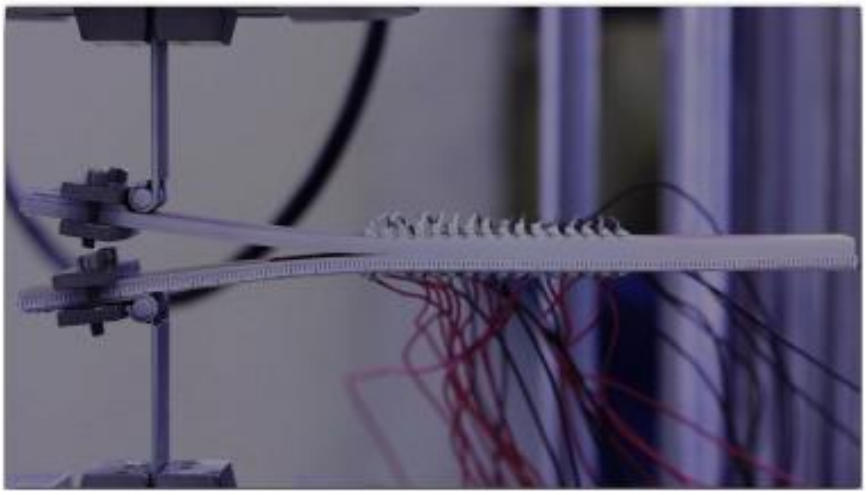

Figure 2-11 Snapshot of a DCB coupon under testing [172].

The main limitations of the aforementioned studies were the suboptimum configuration of the sensing Z-pins. The authors admit that the protruding Z-pins present a manufacturing disadvantage. In addition to this, the connection between the electrode and the protruding Z-pin caused an additional failure step not experienced by the mechanical Z-pins. This step involved the debonding of the Z-pin from the electrode after which the Z-pin then bridges the delamination in a similar manner to the electrically unconnected Z-pin. The method of connection of the electrodes also resulted in a weight penalty of approximately 10%, which would need to be addressed if the method were to be applied more extensively. The large number of sensing channels presents a further level of

complexity. An advantage of monitoring each individual channel as described in the studies is that a comprehensive interrogation of each individual row of Z-pins could be undertaken, and this provided detailed information on the delamination configuration. Whilst valuable, the work of Zhang *et al* does not consider aspects related to the on-line monitoring of damage and it does not address how the number of measuring electrodes can be optimised for specific applications.

Pegorin *et al.* also utilized Z-pins to enable MF but presented an alternative TTER measurement method. As shown in Figure 2-12, this method also used a four-wire method, but it consisted in measuring the ER of the full Z-pinned coupon, unlike the "Z-pin focused" method proposed by Zhang *et al* [173]. The research compared Z-pin material types and volume fractions and determined that the TTC of the unidirectional carbon-epoxy laminate coupons increased with both increasing Z-pin volume content and inherent material conductivity, following the rule of mixtures (ROM). The surface treatment of the coupons involved polishing, cleaning, and application of a conductive paste, before copper plates were adhered to opposite TT surfaces. A four-wire MM was then connected to the copper plates. To ensure a good connection between the copper plates and the unidirectional T700 carbon fibre-epoxy prepreg coupons, pressure was applied during testing using a servo-hydraulic machine [173].

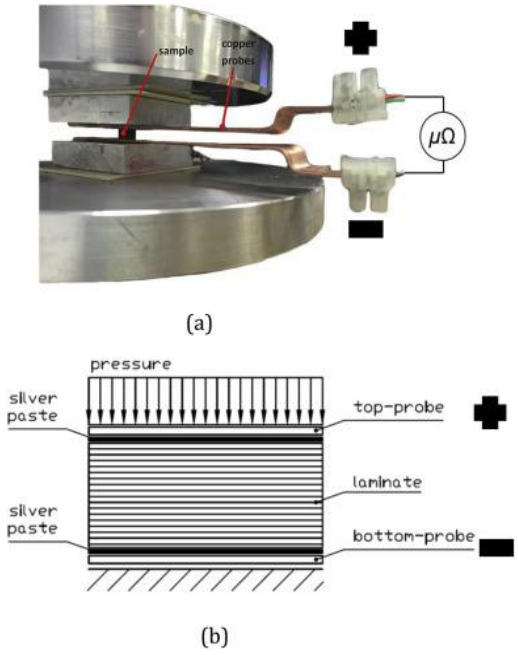

Figure 2-12 (a) Photograph and (b) schematic of the test used to measure the electrical conductivity of the unpinned and Z-pinned composites [173].

Pegorin's work provides an in-depth assessment of Z-pinning parameters, as well as assessing the potential application of different metals. Copper, titanium and stainless steel were all tested and the study indicates the potential for bespoke tailoring for specific requirements, although concern is expressed with regards to galvanic corrosion [173]. The suitability of using the ROM to predict the TTC for potential Z-pin composite combinations showed that the ROM predicted the trend of increasing conductivity but generally overestimated the value. This was attributed to Z-pin misalignment and in-plane fibre waviness. However, it is also possible that the connection method of the MM could affect this value. The benefits of using a four-wire MM are that it removes lead resistance and connection errors during measurement. Whilst a four-wire MM was used in this study, the MM connections were attached to the copper plates; consequently, the coupon ER is assessed under a two-wire resistance measurement and any ambiguity with contacts between the copper plate and the coupon is likely to have affected measurements.

Expanding on their previous work and that of Zhang *et al.,* Pegorin *et al* undertook DCB testing to determine the effect of Z-pin content and Z-pin material type on TTER changes [174]. The measurement of ER change due to crack growth was undertaken using a two-wire MM method shown in Figure 2-13 The readings were periodically measured by allowing incremental crack propagation to develop along the laminate, pausing the testing machine, and finally taking the measurement. The assessment of ER due to the crack growth was therefore undertaken in a stationary state and not during testing. This implies that visco-elastic relaxation of the coupon might have altered the output force readings.

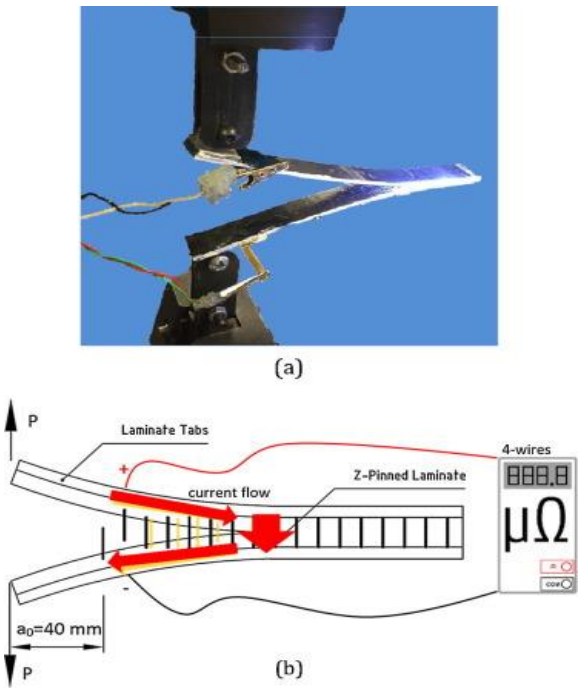

Figure 2-13 (a) Photograph and (b) schematic showing the electrical resistance measurement of a Z-pinned DCB specimen [174].

Although this testing method provides an initial assessment of structural performance, a truly synchronous monitoring of ER during crack progression would provide an interesting parallel study. Overall, the study determined that the percentage changes in TTER increased with increasing Z-pin volume content up to an optimum 2% (Figure 2-14). At 4% volume content, delamination progressed through multiple delaminations and not as a single crack. It was observed that the multiple cracks resulted in a reduction of TTER sensitivity.

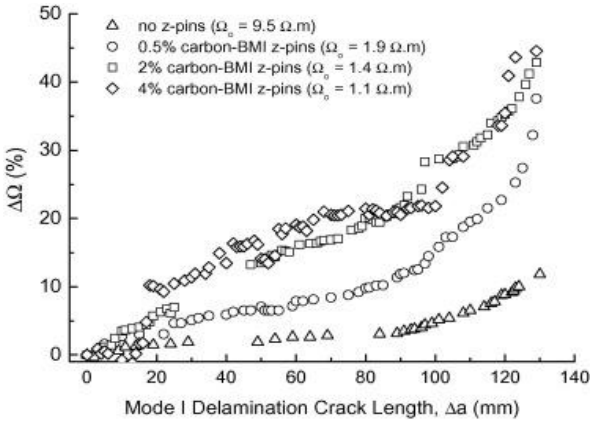

Figure 2-14 Effect of volume content of carbon-BMI z-pins on the percentage change to the electrical resistivity of the DCB coupons with increasing mode I delamination crack length [174].

In addition to this, as depicted in Figure 2-15, the study showed that carbon/BMI and copper Z-pins provided the greatest TTER changes compared to titanium and stainless steel [174]. This result was somewhat unexpected as it was assumed because titanium and stainless steel have higher intrinsic conductivities, this would cause a reduction of TTER at coupon level. Hence, it was speculated that larger variation of ER during delamination would occur; however, this was not the case.

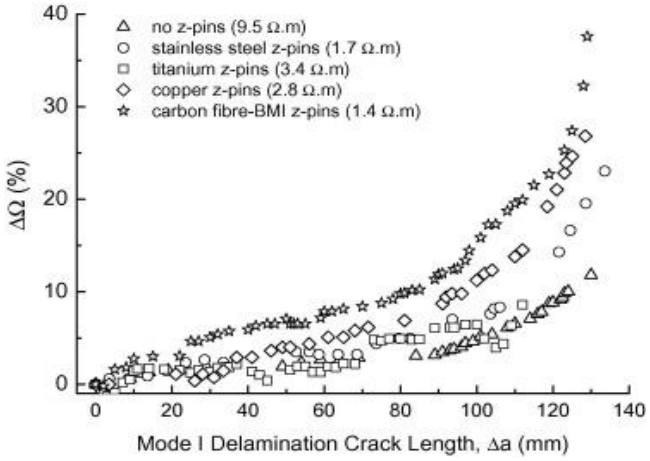

Figure 2-15 Effect of the of z-pin material on the percentage change to the electrical resistivity of the DCB coupons for increasing mode I delamination crack length [174].

The research suggested that the cause for this lack of ER change was the insulating effect caused by interfacial cracks around the Z-pin as a result of the difference in thermal expansion coefficients between the laminate and the TTR elements. These cracks reduce the connectivity between the Z-pins and the laminate and therefore reduce the overall conductivity of the entire coupon. It is also possible that the thermal expansion caused the copper and stainless-steel Z-pins to be drawn further into the laminate so that they are no longer flush with the top of the surface, preventing a good connection with the copper plate used for ER measurement. This mechanism clearly has the potential for limiting the Z-pins influence on TTC. Using a similar approach to the studies mentioned above, preliminary assessments were undertaken to establish the viability of tufting as a SHM technique. This study used ER changes in the Omega stiffened panels shown in Figure 2-16 [175].

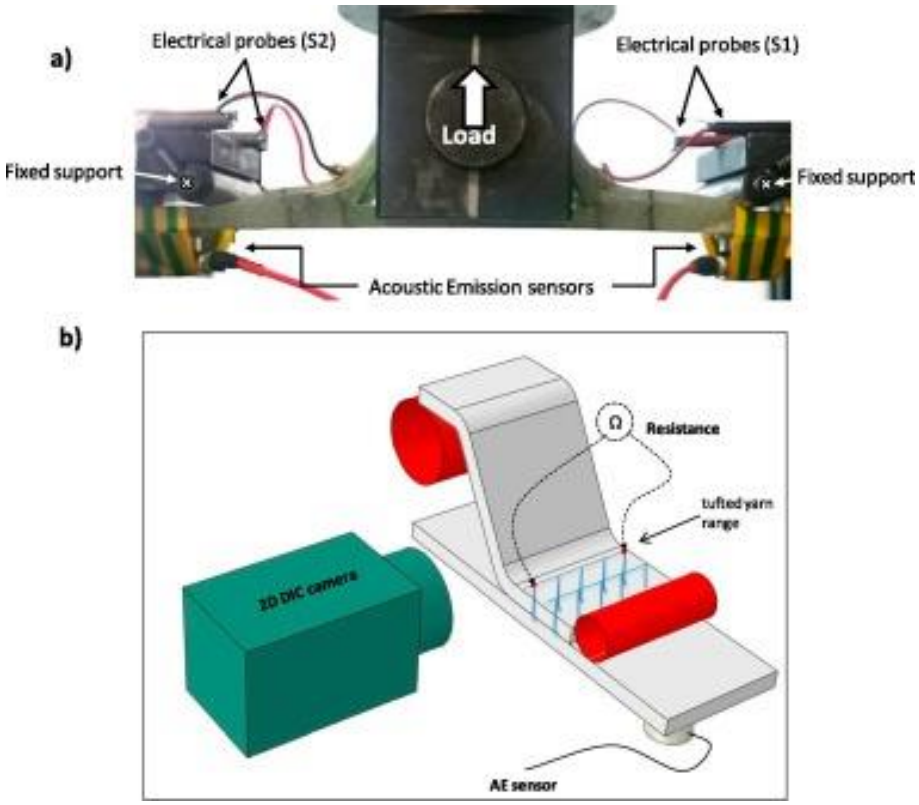

Figure 2-16 (a) Pull-off test setup showing the electrical probes and AE sensors, (b) schema of the multi-instrumentation utilized to characterize the samples under tests [175].

Tufting a carbon thread overwrapped with polyphenylene benzobisoxazole (PBO) into glass composites was used in the tests. The ER fluctuations of the carbon thread were monitored to see if damage had occurred. Martins *et al.* investigated the effects of impact testing, compression, and pull-off tests on these glass composite structures. Overall and similarly to previous tests using Z-pins, this study showed that the ER of the tufts increased with progressive damage. One test, utilising separate ER electrodes on either side of an omega stiffened panel showed that ER measurement could be used to detect the asymmetric delamination that occurred during pull-off, as shown in Figure 2-17 [9, 175]. Similar to the work carried out by Zhang *et al.,* who monitored Z-pin integrity, this study used a four-wire method to specifically monitor the tuft integrity and not that of the bulk structure.

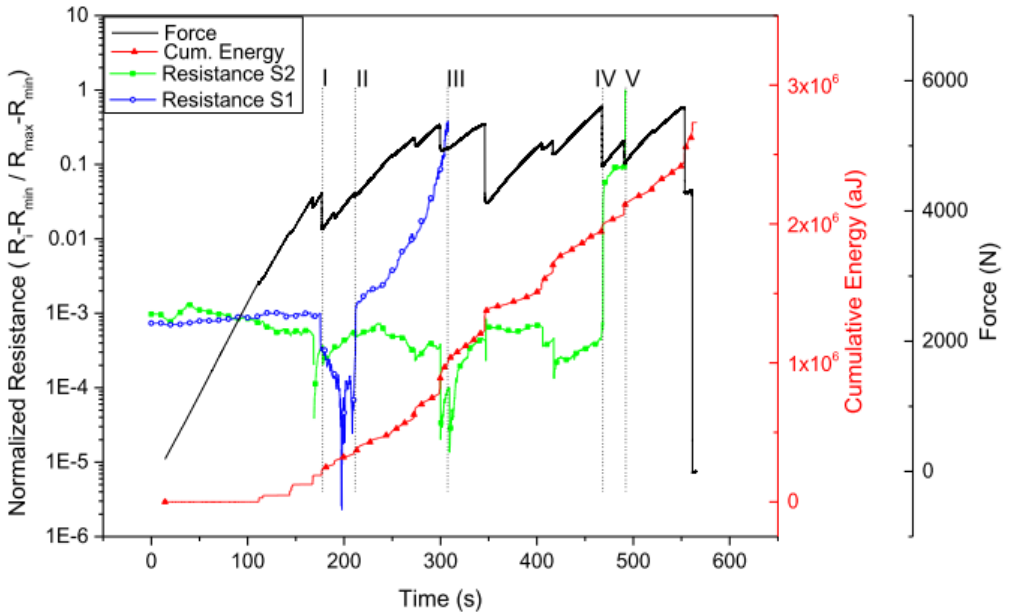

Figure 2-17 Typical behaviour of the load, electric resistance (S1, S2) and cumulative AE energy vs. time during a pull-off test [175].

Partially tufted coupons were prepared to prevent the possibility of external loops connecting on the underside of the coupons and creating an alternative electrical network. This study provided a unique insight into the localised delamination and ER profile along each specific tuft row. The primary cause of tuft failure, which resulted in an increase in ER, was found to be tuft rupture caused by delamination. The study did not state whether tuft pull-out occurred during the tests, despite the use of partial tufting in the specimen preparation. The study also described a decrease in ER during the test, which was also observed in the Z-pin tests, but with a much larger ER drop in this instance [175]. This decrease, despite the occurrence of delamination, was suggested to be due to unloading of the structure, relaxation of the thread causing a decrease in length and an increase in its cross-sectional area, as well as the degradation of the resin matrix, enabling an increase in electrical connectivity. This phenomenon of increasing conductivity despite structure degradation is negated once complete tuft rupture occurs, causing a significant increase in ER. It is also possible that thread degradation caused high levels of brooming of the carbon fibre, providing the opportunity for an increase in carbon fibre connection, increasing the density of the electric network through the structure and reducing the ER.

The viability of incorporating MF in sandwich structures using Z-pins and tufting was also investigated. Studies by Grigoriou *et al.* and Martins *et al.* each examined the viability of incorporating TTER monitoring in sandwich structures through the incorporation of Z-pins and tufting, respectively [152, 176]. Martins *et al* also examined the ER change during compression and impact testing of carbon fibre tufted sandwich structures [152]. The sandwich structures, depicted in Figure 2-18, comprised glass sheets with a polyurethane foam centre and were tufted with a carbon fibre/PBO overwrapped thread.

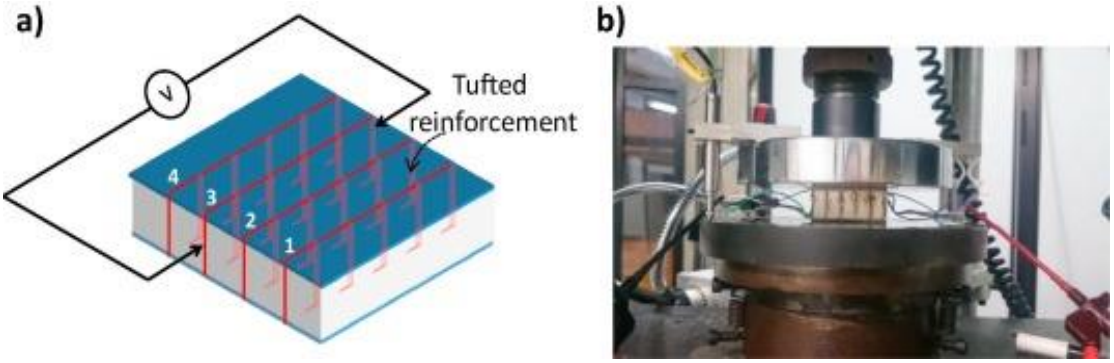

Figure 2-18 (a) Scheme of the two-wire electrical measurement in a single tuft thread, and (b) flatwise compressive test apparatus [152].

The tests were carried out using two wire electrical measurements and the electrodes were soldered directly to the tufts. Contemporaneous assessment of ER on a single tuft row was carried out during testing whilst the remaining tuft rows were examined incrementally, pausing the test. The characterisation involved two compression tests with incremental loading: one with monotonically increasing loading and the other with loading and unloading steps. Progressive damage due to impact was assessed by two subsequent drop-weight tests having energies of 5J and 10J, respectively. This work determined that the damage caused to the composite and the thread resulted in an overall increase in normalised ER, as shown in Figure 2-19. A decrease in ER during the initial stages was also observed and determined to be caused by fibre fragmentation, thread bending and resin cracking. This resulted in the carbon fibre fragments creating a larger electrical network. During the loading plateau, as expected, no change in ER was observed. The residual ER increase is caused by the fibre rupture and the breaking of the electrical connection [152].

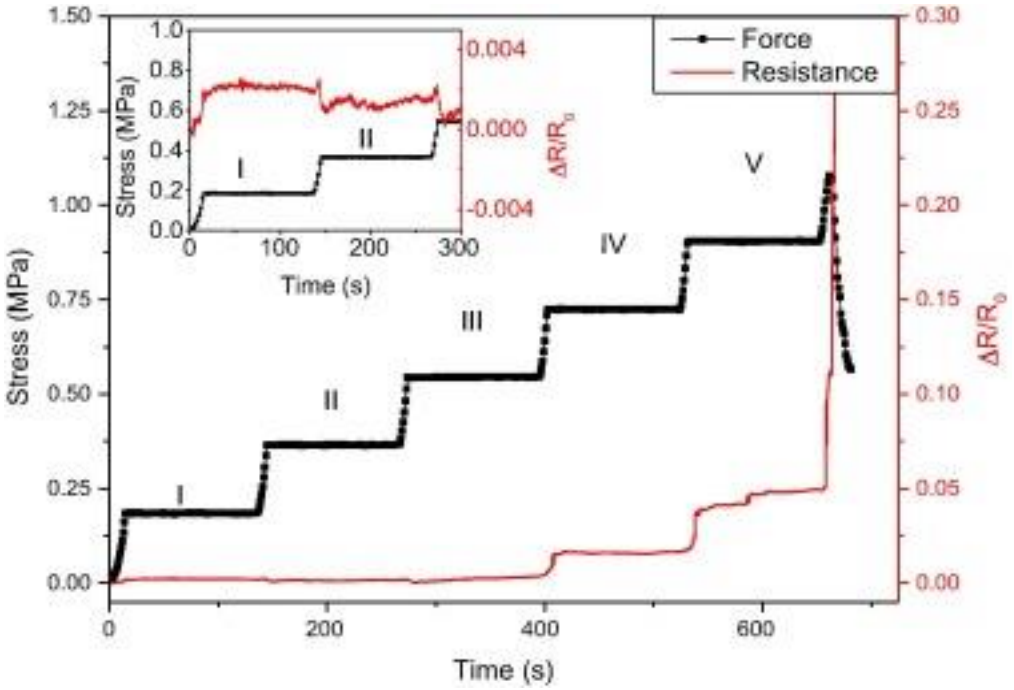

Figure 2-19 Typical response of the electrical resistance under the multi-step compressive test (the curve on the top highlights the slight drop of resistance) [152].

Impact testing showed similar results with ER decreases and increases influenced by the loading and unloading of the structure. Kalashnyk *et al.* examined the self-sensing capability of carbon fibres both dry and impregnated [177]. This piece of work provides a useful mechanical failure and ER profile of carbon fibre under tension. The results can be readily applied to subsequent studies utilising threads for tufting. The effects of broken fibres, filament connections, and void generation due to elongation are all referred to as causes of increased ER.

This study also mentions the protective advantage of overwrapping of the carbon fibre with polymer threads, indicating that this protects the carbon fibre thread during tufting. This, as suggested by the paper, prevented excessive filamentation of the thread after tuft rupture, which is likely to make the ER signal noisier due to the potential increase of random electrical connection points due to fibre breakage. However, no further examination or comparison to non-overwrapped thread was examined [152].

Grigoriou *et al.* compared the electrical and mechanical properties of different Z-pins and TTR volume content on sandwich structures comprising either polymer foam or balsa wood cores and carbon fibre skins. A direct comparison to

unpinned sandwiches was performed to determine the Z-pin influence on the sandwich composite. The results indicated that the Z-pins have little to no effect on the in plane properties of the sandwich parts, but increase the TTC by several orders of magnitude depending on the Z-pins' material properties [176].The work examined the effect of crushing and crack propagation, and like previous studies, it determined that the normalised ER increases in correlation with the extent of damage, as shown Figure 2-20.

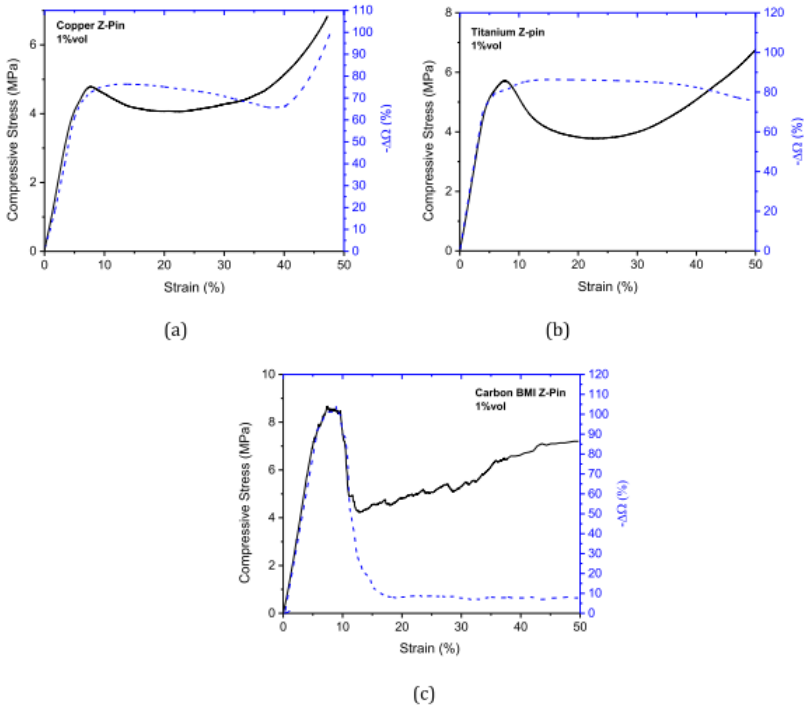

Figure 2-20 Effect of z-pin material on the change to the through-thickness electrical resistivity (dotted line) of the polymer foam core sandwich composites under flatwise compression loading. The compression stress-strain curve (solid line) is included. (a) Copper z-pins, (b) titanium z-pins, (c) carbon fibre z-pins [176].

It was observed during this test that failure mechanisms of the metal Z-pins and carbon Z-pins differed. The fracturing or rupturing of the carbon fibre Z-pins results in a more defined break in electrical network, causing a larger change in ER. The metal Z-pins tended to buckle rather than break, and whilst an increase in ER was observed, it was not of the same magnitude as for the carbon Z-pins. Grigoriou *et al.* also undertook DCB testing of Z-pinned coupons and determined that ER increased with an increasing crack length. Overall, the observed failure mechanisms were similar to those previously discussed.

2.2.7 Summary of TTR and SHM

The reviewed literature provides a comprehensive although preliminary assessment on the viability of using ER as a method for SHM of composite materials, using either Z-pins or tufts. Generally, studies have determined that ER increases are predominantly a result of the rupture of the TT electrical network, but there are also a number of different mechanisms, which depend on the TTR method. With respect to Z-pinned structures, failures are due to fibre breakage, Z-pin fibre detachment, Z-pin elongation or pull-out depending on the mode of testing, and Z-pin material. Studies observed that tufts, unlike Z-pins, did not display pull-out and have generally been observed to suddenly snap under testing. The studies also show that a decrease in ER can take place despite the occurrence of damage, due to the complex nature of the electrical network that is established due to fraying of carbon fibre filaments. Whilst is it not possible to determine the advantages and disadvantages between Z-pins and tufting for SHM due to the limited number of studies available, what is evident is that several configuration parameters should be considered in experimental investigation. Firstly, all the studies in the literature present different methods of measuring ER, namely either two-wire or four-wire configurations. Fundamentally, the four-wire method enables more accurate measurements due to the removal of contact ER. However, the use of a two-wire system is simpler, and it can be exploited in a comparative fashion to monitor extent of ER change, thus providing a suitable alternative. Connection methods are also significant: silver paste, soldering, clips, and compression have been employed, but no test establishes an optimum solution.

Another consideration is whether to test the composite as a whole or just the TTR material. Zhang *et al.* and Martins *et al.* assessed the structural integrity of the Z-pins and tuft thread respectively, before implementing their delamination sensing methods [9, 172]. Essentially, these tests were meant to first characterise the TTR materials and provide a correlation with laminate-level monitoring. The advantage of these methods is that they provided local area assessments of the structural integrity, as well as enabling characterisation of the modes of failure. However, attaching electrodes to each individual Z-pin or tuft row would lead to a weight penalty, as well as increasing the overall system complexity, which represents a major issue for industrial exploitation.

On the other hand, electroding individual TTR elements may be the only possibility for interlaminar crack detection if the laminate is non-conductive. Pegorin *et al.* and Grigoriou *et al.* exploited the in-plane conductivity of carbon fibre and established a method for bulk structural integrity assessment. This has the advantage of providing a simplistic whole structure monitoring system, although it does not provide local information on the delamination configuration. Indirect or direct connection to the TTR is another configuration aspect that has not been fully addressed in the previous studies. Where a direct electrical connection is made to the TTR elements, a variation to the failure mode was reported by Zhang *et al*, therefore it is possible that if an extensive assessment of individual Z-pins is undertaken in a similar manner; a change in overall failure mode of the specimen might occur [172].

Connection positioning on the laminate could also affect reliability of the integrity assessment. The studies undertaken by Zhang *et al,* Pegorin *et al* and Grigoriou *et al* are clearly monitoring the TTER through the direct connection of the electrodes on the top and bottom surfaces of the laminate. Zhang *et al* directly attached electrodes on the top and bottom ends of the Z-pins and this provided localised assessment of the Z-pins sensitive enough to detect the effect of TTR elongation and contraction due to the Poisson effect. Conversely, the tuft characterisation carried out by Martins *et al* is based on positioning all the electrodes on the same top surface. Despite the study's use of partial tufting to avoid electrical connections of the external loops, the inherent structure of tufts could have enabled an electrical network to be created along the top surface of the coupon. It is possible that when initially testing an undamaged coupon, the TTER is not being monitored and the electrical current would take the route of least resistance on the top surface of the coupon. It is also possible that rupture of the tufts did occur within the laminate during testing and delamination, but the surface electrical network did not break. This could also explain why the extent of ER decrease is so prominent at the initial stages of testing compared to other approaches.

2.3 Braiding

2.3.1 History, terminology, and classification

The basic geometry of a braid is provided in Figure 2-21 and depicts the braid angle, pick (S) and line (L) [178]. The braid angle, one of most important parameters, is determined by drawing a line along the longitudinal axis and another parallel to the braid yarn [179, 180]. Braid angles between 10 to 85 degrees are possible, with low braid angles increasing braid stiffness [181]. The repeats of the braid structure along the axis are called a stitch, pick or plait. Repeats perpendicular to the braid axis are known as lines [179, 181, 182].

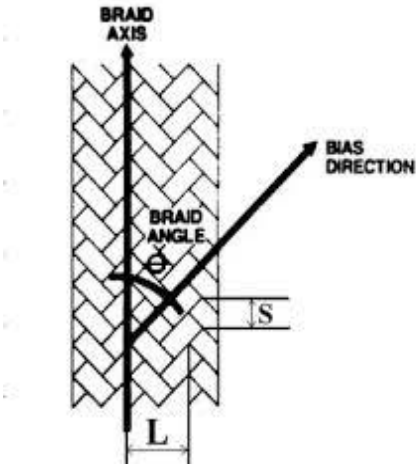

Figure 2-21 Schematic illustration of structural parameters of a braid [178].

The process, used in abundance in the textile and rope industries for centuries; has only relatively recently been employed in the fibre reinforced composite field. Despite this, the range of materials used has progressed rapidly from those of long natural fibres to those of mineral and synthetic origin. Dickinson's (1942) review details the use of flax, papyrus, grass, bamboo strips and hemp [183–185]. The development of polyester, aramid and high modulus polyethylene (HMPE) has provided more choice and speciality for specific industries [179]. Braided cylindrical tubes can be used to make rope, cord, hose reinforcement covering, braided rugs, composite tubes and coverings for electrical cables [182, 186]. They are essentially a freestanding structure and therefore suitable for use as a structural reinforcement in composites. Whilst evidence of the existence of braiding like that of knitting and weaving can be traced back to ancient civilisations, it is evident from the literature that little has

been done regarding nomenclature, categorisation and definitions. As early as 1953 Brunnschweiler expressed disappointment at “scanty information” and ambiguity related to definitions of braid and braiding and whilst he found no acceptable definition recorded, he contented himself in the use of the following definition:

“Cloth formed by the interlacing of one set of threads in such a manner that no two adjacent threads make complete turns about each other” [182, 187].

A standardised definition for braiding has been provided by the German Industrial Standard DIN 60000 as “two or three – dimensional fabrics with even thread density and closed fabric appearance whose braiding threads cross each other in diagonal direction to the selvedge”. The Journal of Textile Institute Proceedings defines braiding or plaiting as ‘’The process of interlacing three or more threads in such a way that they cross one another in diagonal formation. Flat tubular or solid constructions may be formed in this was way’’ [2]. But even this definition comes with additional notes on interpretations.

A simplistic definition of a braid is a structure produced by interlacing three or more strands [179, 185]. It differs from weaving and knotting by its unique oblique interlacement [183, 185]. Woven fabrics are formed by yarns interlacing at orthogonal or right angles whilst knitting is distinguished by the interlacement of looped yarns. The braid pattern and number of yarns determine the final braid geometry.

More current literature provides definitions which use a variant of the following: “a process of interlacing three or more strands of yarn in such a way that each strand passes over and under one another to produce an oblique interlacement” [178, 185, 188–190]. It is therefore evident that agreement on a simple general definition of a braid has proved difficult. What has been clear from the literature is that most authors agree that it is more advantageous to distinguish and classify braids according to broader classifications according to shape, structure, yarn intertwining, fibre orientations, the machine used to make the braid and the materials used [179, 185]. In addition to recent studies, the development of automated machines has enabled more distinct definitions [191]. The Handbook of Industrial Braiding, produced by Ko *et al*, is one of the most referenced texts in the literature. Produced to advance the development of

braiding and “bridge the communications gap”, it provides an entry point into the science and complexity of braid architecture and an invaluable grounding in terminology and definitions [178]. It is evident from the literature that most research and discussions have expanded from this initial text.

Braids can be classified into one-dimensional (1D) linear, two-dimensional (2D) and three-dimensional (3D) braids if based solely on the geometry of the interlacement and by using this definition a 3D braid can be either 1D or 2D [192, 193]. In this context a 1D braid would be a shoelace, cable, or rope whereas a 2D braid would be a tubular or thin flat piece of fabric. Alternatively, a linear braid could be termed 1D, a flat braid termed 2D and a tubular or solid braid 3D [179]. Again, the ambiguity of terminology is evident with options to classify braids according to a number of methods including by manufacturing method, micro or macro geometry, and meso unit cell [179, 194, 195].

3D braids are distinguished by the through thickness reinforcement within the structure. These can then be sub-divided into tubular, flat, and 3D solid [178, 179, 189]. As the division of braid type into 2D or 3D is more common in the literature the author will use this terminology [178, 179, 182, 189, 196–198]. Example models of 2D and 3D braid types are provided in Figure 2-22.

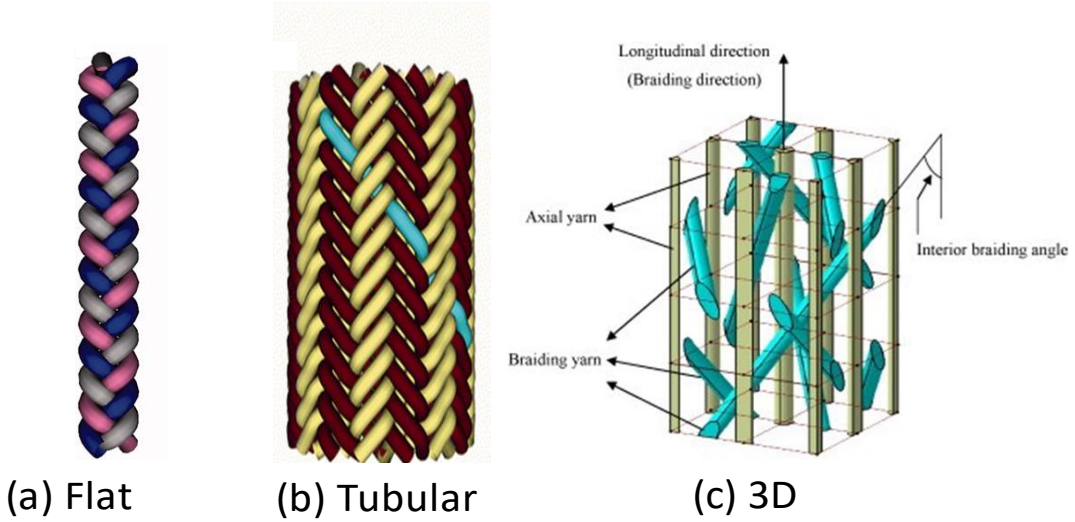

Figure 2-22 (a) Flat braid with 3 yarn pattern modified from [194], (b) tubular braid modified from [194] and (c) the fibre of 3D five-directional braided composites [295].

The type of braid produced is dependent on the machine and this thesis focuses on 2D tubular braiding owing to the type of braider used. Interlacement patterns describe the number of yarns which are passed over and under

subsequent yarns. The three most common are referred to as diamond, regular, and Hercules and will be discussed in more detail in Section 2.3.2 [199]. Figure 2-23 shows a simplistic classification of 2D and 3D braids.

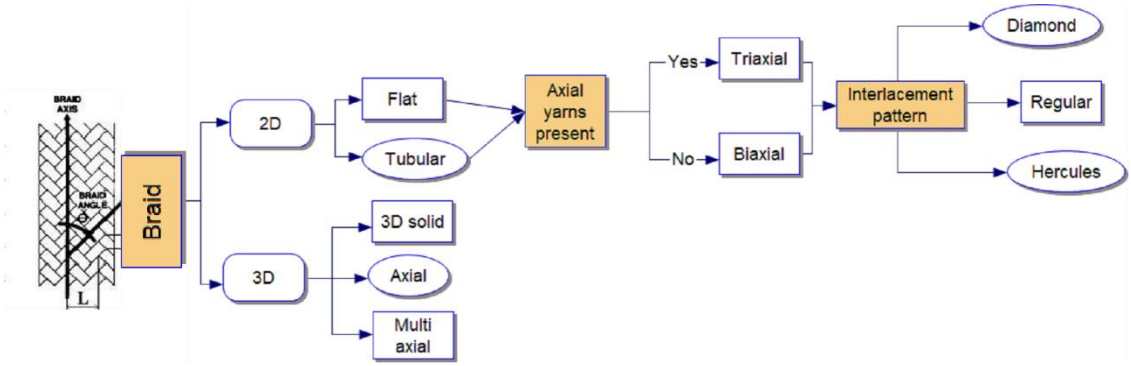

Figure 2-23 Braid classifications based on interlacement geometry.

2.3.2 Braiding machine development

The focus of this section of the literature review will be 2D tubular braiding and braid manufacture using a maypole braider as this what was available for the research in thesis. Figure 2-24 shows a vertical maypole braiding machine used in this project, indicating the main components. Early maypole machines were developed for the production of simple cords for garments and laces [182]. Despite the advancements in machine speeds and braid usages little has changed in the main principles of machine design [187]. The maypole braiding process involves the intertwining of the yarns in a helical pattern.

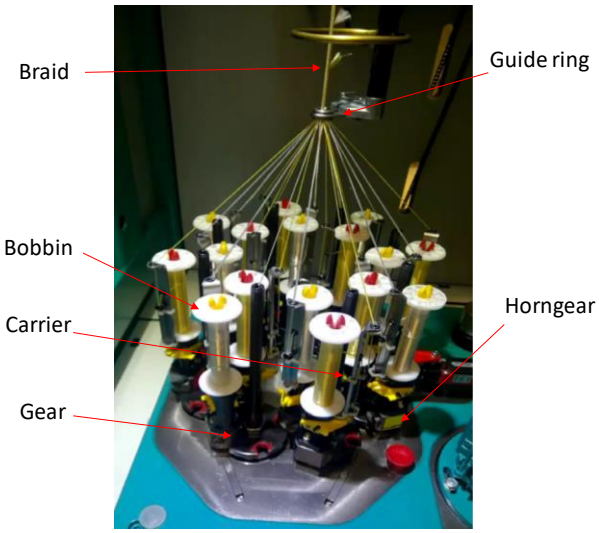

Figure 2-24 Herzog vertical braider.

The main components of a maypole braiding machine are the horn-gears, carriers, bobbins, take-up mandrel and the carrier track. In a maypole braiding machine, two sets of carriers travel along serpentine paths in either a clockwise or anticlockwise pattern. [200, 201]. The movement of the carriers along the path cause interlacement of the yarns in the centre (Figure 2-25). A take-up mechanism pulls the braid from the centre, the rate at which it pulls dictates several braid characteristics such as braid angle and fibre density [192]. A guide ring can be used during the braiding process to enable a more consistent convergence point for the braiding yarns. Maypole braiders are commonly used to produce braided rope. They also have the advantage of enabling a core to be over-braided to protect the inner material, a process like that of the outer sheath of an electrical cord protecting the inner wires.

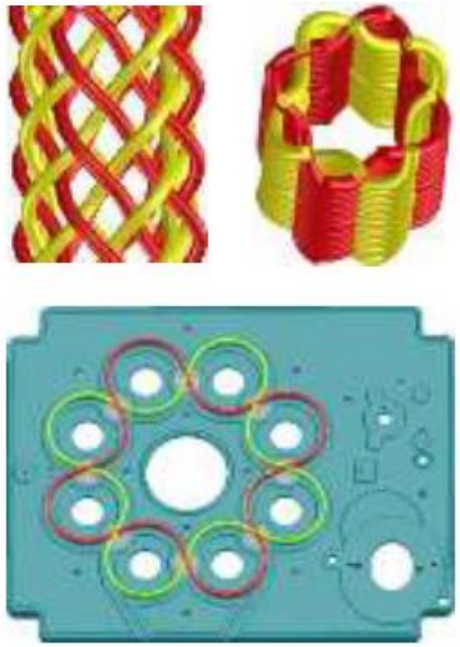

Figure 2-25 Carrier path of a maypole braider. Two opposing (red and yellow) tracks following and clockwise and anticlockwise direction. At full occupation produces a 2:2:1 braid [Herzog].

The main limitations of the maypole machine are its large size and therefore, space requirement in comparison to product size. The length of product produced is limited by the amount of yarn on the bobbins and initial machine set up is labour and time intensive. Maypole braiders can be used to make three different braid architectures classically called diamond, regular, and Hercules braids [186, 187, 202]. The patterns differ in the number of yarns passing over and under each other [203]. Figure 2-26 describes each of the three patterns.

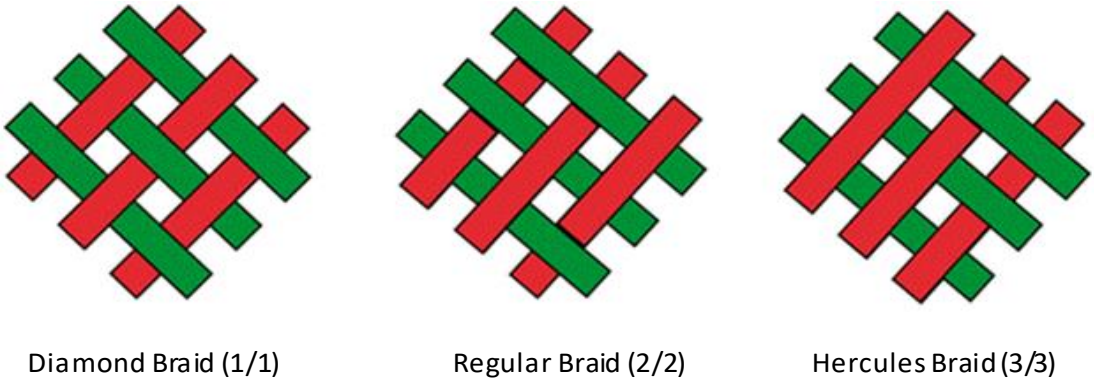

Figure 2-26 Basic biaxial braid patterns [296].

Braids with no yarns running parallel to the braid uptake are known as biaxial braids. Triaxial braids are produced by inserting yarns along the longitudinal direction and are used to improve the axial properties in a composite. The difference between triaxial and biaxial braid architectures is shown in Figure 2-27. Whilst the use of regular, diamond, and Hercules braids are readily recognised in the literature, it has been accepted that alternative notation systems, which consider the engineering aspects of the braid structure would be more beneficial.

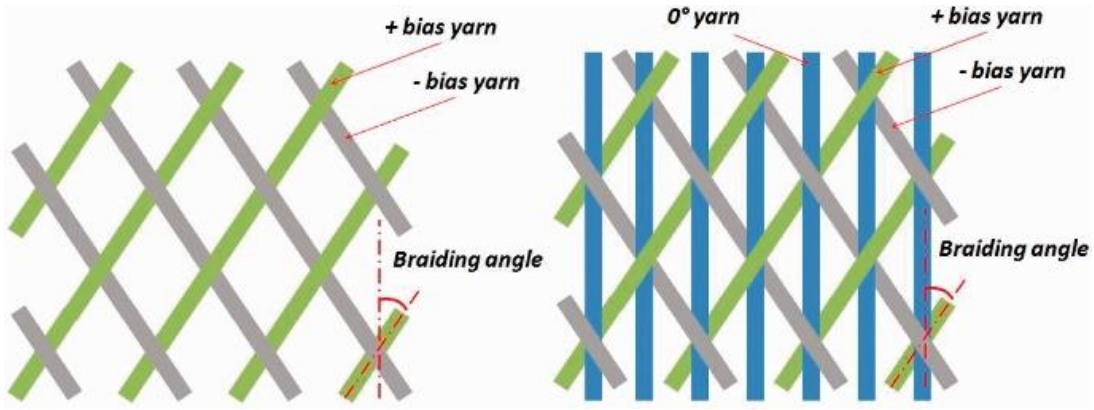

Figure 2-27 Biaxial and triaxial braids [297].

The system as detailed by Kyosev, (2015) provides a useful, unambiguous method of braid structure description. It combines the two most commonly used notations systems namely the “English” system and “German” system [192]. The English system uses the three common terms and also terms usually associated with weaving [178]. The “German” system describes the braid using two numbers, one which describes the intersection type and one which details

the number of yarns per group. It also details the floating length or interlacement type of a braid. Another method is to describe the number of yarns in which the braiding yarn moves around, using phrases such as “one over and one under” (1/1) or “one over and under two” (2/2), which describe diamond and regular braids respectively [192].

The system adopted by Kyosev will be used throughout this thesis as it has an advantage of assisting when mounting the carriers onto the braider. The system represents the “English” interlacement type “over one under one” as 1:1 and details the number of yarns within a group by using a dash followed by yarn number i.e., -1. Therefore, a regular braid which has one yarn passing over and under two yarns would be represented by 2:2-1. Figure 2-28 details the three most common patterns regular, diamond, and Hercules structure as represented by their common designation and by this notation system.

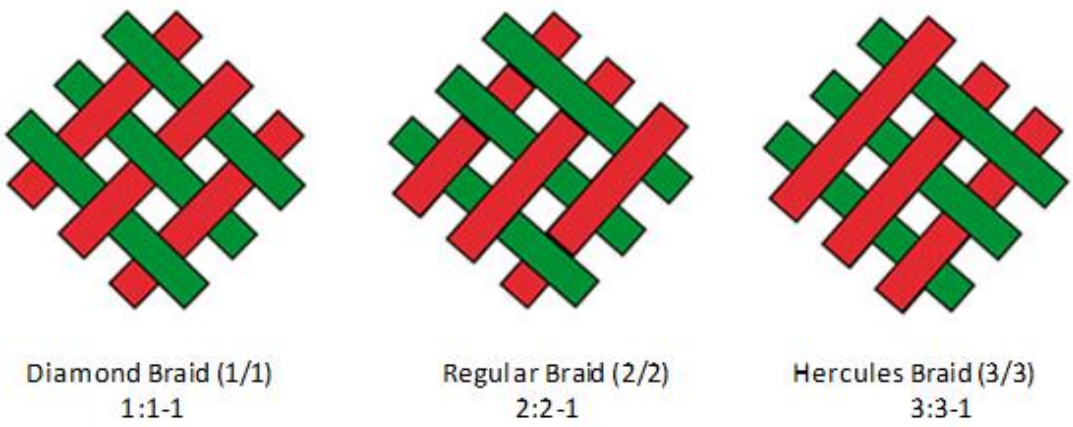

Figure 2-28 Basic braid patterns with English, German and Kyosev notations [296].

2.3.3 Hybrid braids

There are a limited number of research articles related to hybrid multifunctional braided materials available in the literature. Even fewer of them draw together the different elements of MF, the definition of which is provided in Section 2.1.1. The focus of this study is multi-material braids that provide MF i.e., a braid comprised of different yarn materials with each different material providing a different function or capability.

Within the literature, available articles can be broken down into three subject types:

- those which possess MF by the addition of nanomaterials adhered to a structurally braided material [193].
- those that contain a braid to improve mechanical or protective function within a larger hybrid composite structure.
- those comprised of multi-material braids with each individual material introducing a different functionality or capability.

The first category of articles are those which refer to multifunctional braids but are limited in scope to single material braided structures modified with CNTs or other chemical additives [107, 204]. The chemistry of the additives is of primary interest with the braided structure and material simply providing a secondary structural property. The second category of studies refers to over-braided cores, such as a fibreglass braided sheath containing a sensor [137, 205]. Whilst there are advantages to over-braided core sensors in providing electromagnetic shielding and structural protection, the core material is still a separate entity and not assimilated within the braid structure itself. It is therefore debatable whether it is a true hybrid braid as the braid structure is usually made up of a single material type [44].

There are a number of hybrid braid studies detailing braids containing both polymer fibres and reinforcement fibres or co-mingled yarns [137, 206, 207]. The focus of these studies was improving resin impregnation, void reduction, and assessment of manufacturing parameters, such as braid angle, on structural performance [107]. These mixed material yarns once braided can be considered hybrid braids, however, when consolidated the braided composites are no longer hybrid unless different reinforcement yarns were used. These multi-material braids have been classified as multifunctional in so far as they were designed to aid in the processability of a composite [44]. However, composite and final structural functionality is not improved therefore to classify them as such is misleading. Other hybrid braid studies have concentrated on tailoring components for increased mechanical performance, and focus on strength to weight ratio optimisation [208–211]. These studies examined various combinations of braided carbon fibre, glass, and Kevlar® yarns and studied the effect of braid angle, braid interweave patterns and the presence of axial yarns on mechanical performance and crash worthiness [209]. The study examined

carbon fibre and Kevlar® hybrid braids and found that an all-carbon fibre braid had the highest crush load (5.0 kN) and an all-Kevlar braid had the lowest (1.3 kN). The crush load decreased by approximately 8% when a set of carbon fibre braiding yarn was replaced with Kevlar yarn, and by approximately 46% when a set of carbon fibre axial yarns was replaced. The study concluded that of the braid investigated a braid comprising a set of braided Kevlar and carbon fibre in addition to a set of axial carbon fibre yarns would be most suitable for the application of crash-worthy structures because it has high crush energy absorption comparable to the all-carbon braid but with significantly better post crush integrity [209]. The study emphasised the significance of braid structure and material placement, as well as the tailorability of braid properties on mechanical properties. One study incorporated carbon fibre tows in the axial direction to enable electrical resistance (ER) monitoring of the braided composite (Figure 2-29 Photographs of (a) electrodes prepared on fabric before curing, and (b) moulds with grooves for wire to stretch during solidification [76].) [76]. It combined both the structural and insulating properties of the Kevlar® yarns to enable the monitoring of four individual carbon tows using a four probe multi-meter (Figure 2-30).

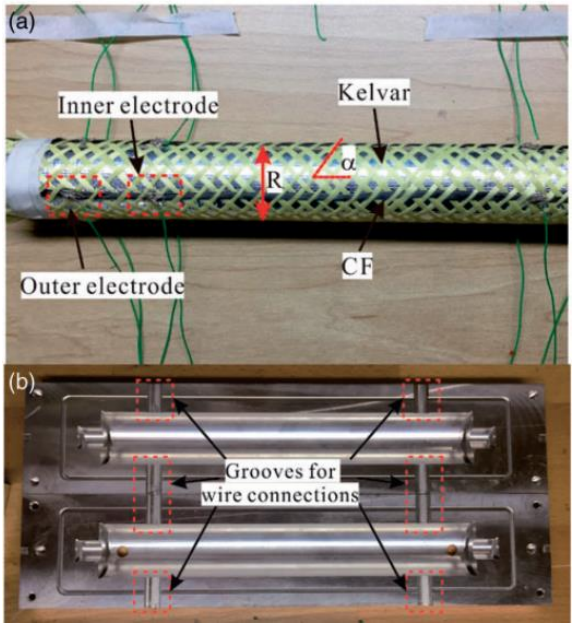

Figure 2-29 Photographs of (a) electrodes prepared on fabric before curing, and (b) moulds with grooves for wire to stretch during solidification [76].

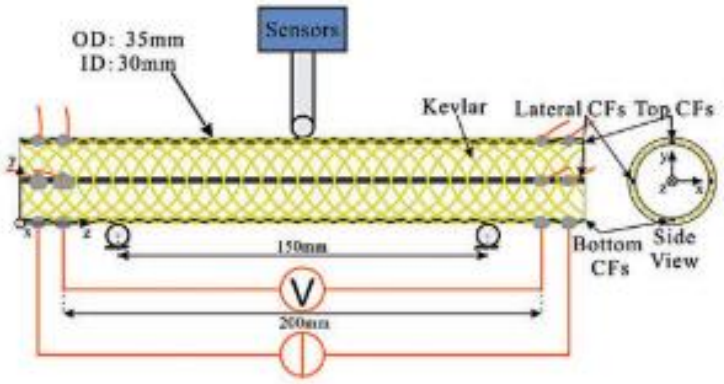

Figure 2-30 Structure of the FPRC tube and electrical resistance method concept during three-point flexural test [76].

Each carbon fibre yarn had four electrodes made of silver paste, and copper wires were consolidated into the conductive paste to form a stable connection. Each carbon fibre positioned as an axial yarn was electrically isolated by the Kevlar yarns, and each was used as an individual sensor to monitor the braid specimen in a flexural test.

A four-wire testing method with a constant 10 mA was implemented to measure changes in ER along the length of the carbon fibre yarns. The resistance value was measured by monitoring the measured voltage using Ohm's law. Depending on the placement of the carbon fibres relative to the crosshead different ER responses were recorded. ER decreased with increasing compression and increased with flexure for the carbon fibres at 0° and 90°, though the amplitude at 0° was greater with a maximum CV of -1.67% compared to -0.14%. The 180° carbon fibre mirrored the 90°. Under the same test, the resistance of CF at 45° decreased as the bending deflection increased. The behaviour of CF at 135° is the most complicated, as the resistance increased slightly and then decreased as displacement increases.

The sole purpose of carbon fibre inclusion was to exploit its conductive properties for use as a sensor to monitor deformation. This study demonstrated the structural self-sensing capability through ER changes within a nonconductive structure, described the influence of yarn positioning within the braid relative to the deformation and addressed practical concerns such as electrode attachments [76]. However, a fundamental point of this method is to measure the individual carbon fibre axial yarns, with the most important

requirement being that the bias yarns be isolated. It is a similar limitation previously described in using sensing z-pins, where each sensing part requires individual sensing wires [172]. It also does not address a method to assess ER in a conductive carbon fibre part where the conducive network will be more complex.

Other studies described in the literature manufactured and examined hybrid multi-material braids that contained a metal yarn braided into the structure [212–215]. These studies are the only ones that incorporate a metal component into a composite structure by braiding. The first created a braid comprising a Nylon 6,6 and Kevlar® core over-braided with a 2:2 pattern braid of three strands of nylon yarns, four yarns of Kevlar®, and a single copper wire (Figure 2-31) [213]. This study also exploited the advantages of using co-mingled yarns by incorporating thermoplastic resin yarns into the braid manufacture. This hybrid micro-braid was then woven and formed into hybrid fabric.

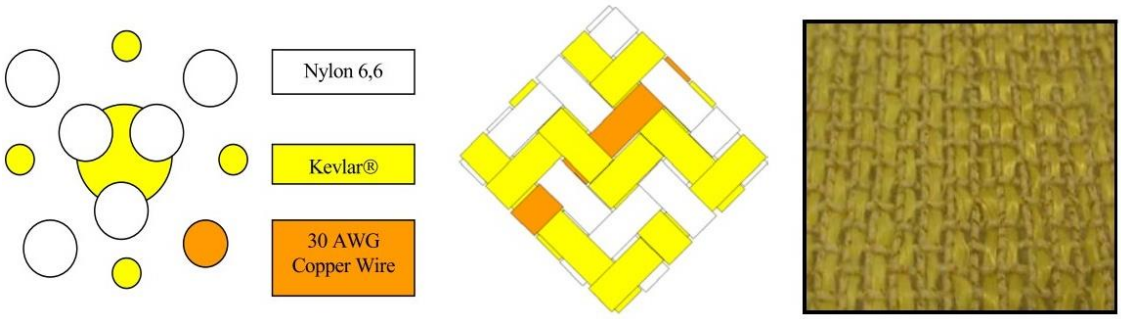

Figure 2-31 (Left) Schematic of cross-section of tubular braid architecture, consisting of Kevlar® , nylon, and copper wire, (middle) schematic of outer braided architecture with 2 up 2 down braid (2:2:1) pattern and (right) photograph of braids bi-directionally woven into fabric with additional Kevlar® fibres. Coils with opposite sense are woven adjacent to one another [213].

Similarly, another study replaced two reinforcement fibres with metallic stainless-steel yarns to produce a multifunctional braid for use as a supercapacitor (Figure 2-32). It should be noted that in both of these studies, the metal components within the braid and structure formed a spiral coil with the reinforcement yarns preventing any overlapping of the metal yarns. Manufacturing in this method offers the potential for tailoring of chirality [212]. Chirality is when an object has two forms which are mirror images and cannot be superimposed. The studies demonstrate the large number of parameters which need to be considered when manufacturing a braided hybrid component

but also the ease with which variations can be achieved and the potential for optimisation. They each demonstrated the flexibility provided by braiding manufacture with parameters such as braid size, yarn positioning, core diameter and braid angle influencing final composite functionality. The studies demonstrated the electromagnetic properties, resistive heating, sensing, and supercapacitor capabilities of hybrid multi-material micro-braids, respectively.

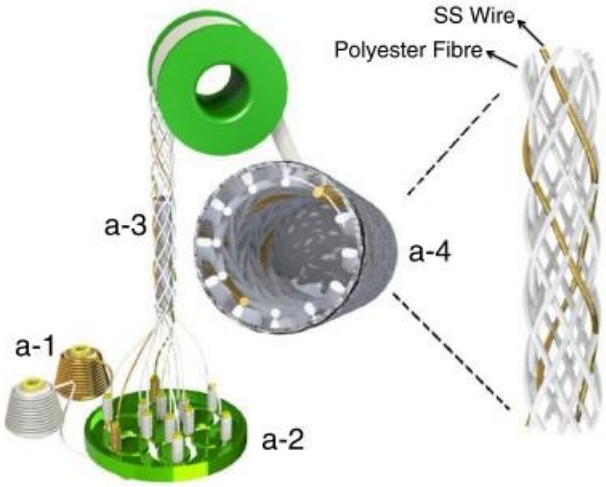

Figure 2-32 Schematic diagram to illustrate the 3D braiding process (a-1) polyester fibre and stainless steel wire bobbins, (a-2) braiding head, (a-3) as-prepared braid structure, (a-4) braided supercapacitor[215].

However, none of the studies examined the effect of these braids on the mechanical performance of composite structures. The addition of the multifunctional aspect of the hybrid material was assessed but no comparison to a standard material was provided. A direct assessment would have addressed any reduction in structural capability and provided a more comprehensive overview of the technology.

In addition, the hybrid braids containing the metal wire often resulted in an unbalanced braided structure [213]. This unbalance, caused by the different yarn sizes, can cause the collapse of yarns along the braid length component resulting in localized distortions and an uneven braid surface. Another consideration not addressed in these studies is the potential asymmetric failure pattern due to the different materials. Figure 2-33 shows the hybrid braid with a single copper wire. The unevenness of the braid surface can be seen along the right-hand side of the central braid. The extent of this waviness was minimised in this particular study by the incorporation of a core that supported the external

braid. However, the effect of this distortion on processability has not been addressed.

Figure 2-33 Kevlar® braided with copper wire [213].

2.4 Micro-braids

There are few studies in the literature that examine the manufacture and assessment of thread hybridisation through micro-braiding. In the composite field, most studies have been predominantly undertaken on large scale braided fabrics or over-braided mandrels that are not necessarily applicable to micro-braid dimensions or applications [185, 190]. The most comprehensive studies are those undertaken in the medical field where multifilament microbraids are widely used as sutures, as they offer higher tensile strengths, better handling properties and material combination flexibility [200, 201, 216, 217]. The advantages of braided sutures include damage and impact resistance, design tailorability, high strength and flexibility, structural durability, and cost effectiveness over their non-braided counterparts [181, 201, 218, 219]. The medical industry has extensively advanced suture performance using hybridised micro-braids, where the tensile properties indicate a key parameter for successful suture construction [216, 220]. Studies of micro-braided sutures demonstrate that the performance is determined by the collaborative effect of the different materials. Selection of the materials is considered based on final requirements and the integration of beneficial features such as absorption, and healing capability of different fibre systems along with a balance of mechanical properties [201].

The suture studies also advise that when designing structures, the symmetrical distribution of yarns in the braid must be considered. This is because the different mechanical properties of each yarn material can result in higher tension of some of the yarns during manufacture causing a spiral effect or undulating [201]. This spiralling effect can be seen as twisting and bunching of material asymmetrically along the braid.

Only recently has the composite industry began to investigate the benefits of micro-braiding. Del Rosso *et al* utilised micro-braiding to create micro-braided Fibre-Reinforced Polymers (mBFRPs) to increase impact resistance and energy absorption capabilities to create more damage tolerant structures. The studies reported 55.7% higher tensile strength and 96.2% higher toughness and improvements in the ballistic limits, up to 19.5% for certain types of mBFRP compared to their unidirectional (UD) and woven counterparts. Others have over-braided fragile components to increase handleability, robustness and durability [221, 222]. The interlaced structure of braiding has also been exploited to improve resin impregnation and for braid-trusion [218, 223, 224].

2.5 Summary

This literature review has identified that MF in CFRP is still in its early stages, and that implementing it on a large scale will necessitate a multidisciplinary investigation. Industry requires a method that increases electrical conductivity in CFRP for the purpose of enabling additional capabilities, such as lightning strike protection, EMI shielding, electrostatic coating, and complete circuitry. The method to achieve MF must be intrinsically introduced at the manufacturing stage, and that any increase in mass should be mitigated by the additional functionality. Industry also desires that future SHM methods are incorporated into a structure at the manufacturing stage.

The studies reviewed demonstrated that tufting can be used to increase composite TTC and delamination resistance depending on the materials used as a tufting thread, however, a number of issues were left unresolved. The thread materials used so far in studies have been limited to off-the-shelf options, with little or no attention given to developing customisation. Increasing the robustness using over-wrapping has been shown to be advantageous. However, the resultant parasitic mass of unwanted material is not desirable and

snagging in the needle due to the undulated thread profile has also been reported. Whilst previous studies have used metal wires to create hybrid braids, the construction, profile, hybridization manufacturing, and braid structure were not considered. Figure 2-33 provides an example of a poorly constructed hybrid braid that has an undulating kinked profile. This effect needs to be avoided for thread construction as the thread profile must pass through the needle eye unhindered. The studies into hybrid sutures provide the inspiration for manufacturing a tailored hybrid tufting thread to resolve these issues. From a braid manufacturing perspective, the balanced profile of the braided materials is required. The materials are chosen based on the final requirements and the incorporation of beneficial features i.e., metal to protect the carbon fibre during tufting and also introduce electrical conductivity, and carbon fibre for mechanical performance. The hypothesis is that this would produce a smooth braid profile that would ensure consistent and reproduceable tufting and create a composite with enhanced through-thickness conductivity.

The literature demonstrates that measuring ER changes as a result of damage can be utilised as a SHM method. However, when using ER as a method of damage detection, the anisotropic properties of carbon fibre are disadvantageous. These properties mean that the electrical path is dominant in the in-plane direction. As a result of the lack of conductivity in the TT direction, detecting delamination in composite laminates is more difficult.

This study will address the issues of thread robustness and composite conductivity identified in the literature review. It will take a multifunctional approach to investigating manufacturing methods for increasing thread robustness by using micro-braiding to create a hybrid thread. By incorporating the metal wire components in a balanced manner, they will offer protection to carbon fibre and prevent filamentation. Carbon fibre tow and metal wires will be used as precursors for this multi-material braid. This will take advantage of both the mechanical and electrical properties of the metal wire for synergistic multifunctional effect. Metal wires have previously been successfully used as tufting materials but incorporating them into a braided structure also allows for material property customization similar to that seen in the medical suture industry.

Tufting this hybrid metal-carbon fibre thread will not only increase robustness but also fundamentally increase CFRP electrical conductivity. It will also increase delamination resistance. These beneficial attributes are expected to compensate for the additional mass incurred from the introduction of the tufting material to the composite. The increase in through-thickness conductivity as a result of the metal in the hybrid thread could enable more extensive SHM assessment beyond that currently possible in just the in-plane direction. The viability of this hypothesis will be tested in this thesis, which aims to demonstrate MF by combining TTR with SHM by monitoring changes in ER

An analysis of the ER SHM testing methods used in other studies has informed the methodology that will be used in this research. ER will be monitored using a four-wire measuring technique as this will mitigate any lead resistance and connection errors during measurement. Electrode connection methods will incorporate methods used in the literature and use surface polishing, silver paint, copper attachment, and compression during construction to ensure stable connection. The research in the thesis will also investigate if it is possible to create a whole structure SHM by strategic placement of the electrodes. This it to reduce the number of electrodes, and therefore mass, required to enable SHM.

To ensure the issues identified in the literature review are satisfactorily addressed, focus will be maintained throughout this study on the following second order research questions:

Can micro-braiding be used to manufacture a metal-carbon fibre hybrid tufting thread?

What braid parameters have an impact on the manufacturability of a metal-carbon fibre braid?

Does the addition of the wire yarns improve the tuftability of the tufting thread?

Can MF in the form of SHM be demonstrated using a system to monitor changes in ER caused by crack propagation?

What effect does the placement of electrodes have on the ability to detect crack propagation?

What are the implications for up-scaling the SHM technique?

3 MATERIALS, BRAIDER LIMITATIONS AND BRAID MANUFACTURE

3.1 Overview

The manufacturing parameters and limitations of micro-braiders are discussed in this chapter. The chapter also describes the process of making micro-braid specimens, the materials used, micro-braid mechanical testing, and the suitability of using a braid as a tufting thread. Details on yarn and wire types, preforms, braid variants, and tufting patterns, as well as micro-braider setting constraints and tufting parameters, are included in this evaluation. S directed by the suture literature was decided that an even number of metal wires to carbon fibre tows would be investigated to reduce the number of braid configurations. This resulted in a balanced braid with the metal wires distributed evenly along the length of the braid. It also produced a braid surface that ran smoothly through the needle eye while ensuring a uniform and consistent braid angle.

3.2 Materials

The initial research described in this chapter details braider limitations and variations. These investigations sought to identify potential metal wire to carbon fibre tow combinations, as well as the overall braid geometry that would be used throughout this research. Titanium wire was used for an initial braider limitation

study. As a result of this investigation, it was determined that further use of titanium wire was unfeasible due to the cost involved in acquiring 0.1 mm wire in sufficient lengths. Therefore, for subsequent testing, braids comprising copper or copper nickel wires were used.

3.2.1 Yarns, threads, and wires

The carbon fibre component of the braids produced in this research consisted of Toray® T300 1k untwisted carbon fibre tow. Titanium, copper nickel, and copper wires were originally selected for this study due to their electrical conductivity properties and ease of supply. All metallic wires were 0.1 mm in diameter, which was the smallest diameter that could be feasibly sourced and that could be successfully wound onto bobbins. In addition to materials for braid manufacture, two commercially available 2k carbon fibre and 4k carbon fibre threads were used to provide a comparison to the hybrid carbon fibre-metal braids. These carbon fibre threads, manufactured by Schappe Techniques®, consisted of two and four threads of twisted carbon fibre tow, respectively. Further properties of the carbon fibre tow, threads, and wires are provided in Table 3-1.

Table 3-1 Braiding material details

Material	Carbon fibre tow	Titanium	Copper	Nickle chrome	Carbon fibre yarn	Carbon fibre yarn	Glass
Manufacturer [-]	Toray®	Block	Block	Scientific wire company	Schappe Techniques®	Schappe Techniques®	Saint Gobain Vetrotex
Type [-]	T300	-	CUL 100	NC0100	Tenax® Carbon HTA40	Tenax® Carbon HTA40	EC9 68 x 3 S260
Filament count [k]	1000	1	1	1	2 x 1000	4 x 1000	3 x 411
Linear density [g/km, tex]	67	-	-	-	140 (2 x 67)	268 (4 x 67)	204
Fibre/wire density [g/cm^3]	1.8	4.5	8.9	8.4	1.8	1.8	2.6
Diameter [mm]	-	0.1	0.1	0.1	-	-	-
Cross sectional area [mm^2]	0.04	0.007	0.007	0.007	0.08	0.16	0.08
Resistivity [Ω.m]	17 x 10^{-6}	43 x 10^{-8}	1.68 x 10^{-8}	100 - 150 x10^{-8}	106 x 10^{-3}	106 x 10^{-3}	
Thermal Conductivity [W/mK]	10	17	40	11	10	10	
Strain at Failure [%]	1.5	10	19	11	1.7	1.7	2.1
Tensile Modulus [GPa]	230	114	120	110	240	240	73

3.3 Braider limitations

3.3.1 Instrumentation details

A Herzog model 1/16 80 circular braider was used to manufacture the hybrid micro-braids. The braider consists of a maypole mechanism which can accommodate a maximum of 16 carriers (Figure 3-1). This micro-braider allows for a limited number of variables to be altered, such as number of yarns, pattern, yarn setup, and lay length. Each variable has a direct influence on the final braid structure and mechanical properties as previously discussed in the literature review Section 2.3.1.

Figure 3-1 Herzog 1/16 80 circular braider.

3.3.2 Carrier capacity – number of yarns in a braid

At full capacity, 16 carriers were used for braid manufacture and produced a 2:2:1 interlacement patterned braid. When using eight yarns or operating at half capacity, a 1:1:1 pattern was produced. In addition to operating at full and half-capacity, six, four and two yarn combinations were also trialled. However, on investigation these braids were deemed unsuitable due to twisting, non-braided sections, and undulation along the length of produced braid. Braid development was therefore restricted to either full or half capacity occupation in order to ensure a consistent uniform braid. It was quickly determined that 16 yarns produced a braid with a diameter too large to fit through the tufting needle eye and, so this configuration was discounted. The braider was operated at half-capacity for the remainder of the study, producing an eight yarned braid. As a result, only a 1:1:1 or diamond braid was produced.

3.3.3 Carrier configuration, pattern development and yarn orientation

An unexpected variable, which will be referred to as yarn orientation, depended on the placement of different yarn types in the micro-braider. It is a parameter that is usually only of concern when colour pattern is of interest, as it determines the visual patterns seen on the exposed side of the braid. It only affects the appearance of the pattern and not the interlacing composition or braid angle. A braided thread could contain the same number and type of yarns but look visually different depending on how the yarns are positioned in the braider. Figure 3-2 demonstrates the effect; when contrasting coloured yarns of glass thread (white) and carbon fibre tow (black) were used, different stripes are produced. Vertical stripes were produced when one colour or type of yarn was used for all carriers in one direction and a different one in the other direction.

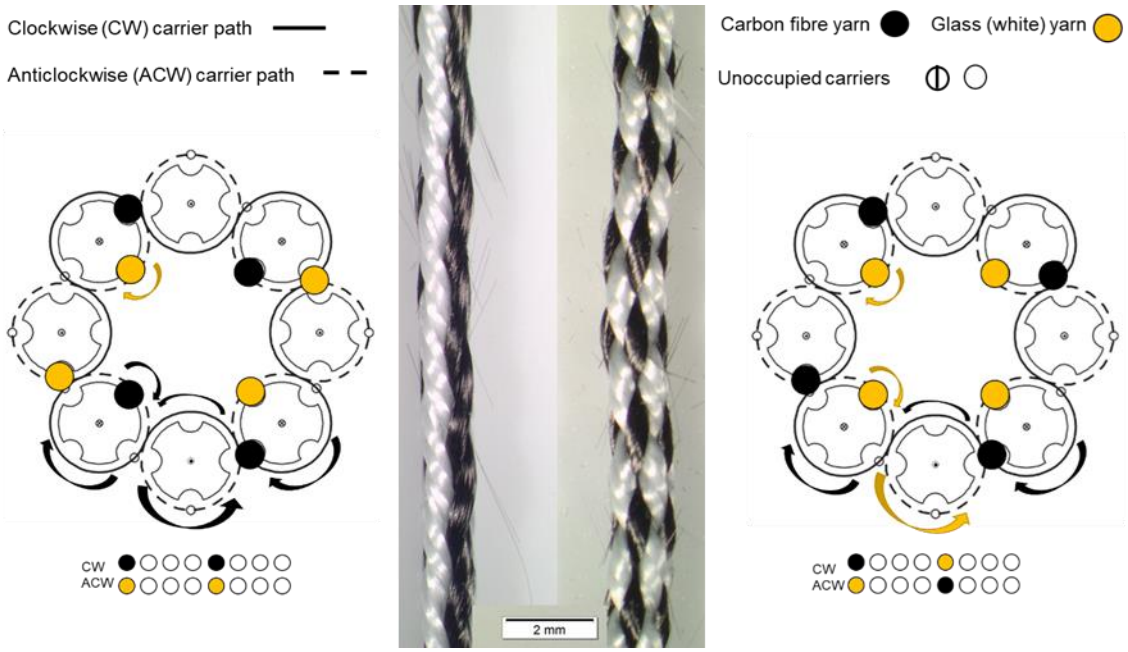

Figure 3-2 Glass–carbon fibre hybrid braids with corresponding carrier arrangements. Half occupation on a maypole braider. Carrier arrangements adapted from [298].

By alternating between yarn types in both carrier directions, a horizontal design was produced. The braiding interlacement pattern of 1:1:1 was identical for both. This variable would not normally need further consideration, however, when different materials were employed, the different material properties and how they interact during braiding and when interlaced was important.

When an assessment of whether both patterns could be produced using wire and carbon fibre tow was conducted, it was found that the horizontal pattern was not possible. It was established that if the metallic wires were placed sequentially between the carbon fibre yarns, the metallic wires sheared and broke the carbon fibre tow before any significant length of braid could be produced. This did not occur when the braider was set to all metallic wires on one set of carriers and all carbon fibre on the other. Therefore, this limited the hybrid braid production to a vertical striped pattern as shown in Figure 3-3

3.3.4 Effect of lay length on production

The lay length is the distance required for one strand to complete a full revolution around the axis of the braid. During braiding, the velocity of the carriers and the uptake velocity determine the braid structure and its final appearance. The carrier velocity of the braider used in this study was fixed. The uptake velocity was the only adjustable setting and was determined by setting

the desired lay length on the digital display. Changing the lay length changed the rate of braid uptake of the braider mandrel. The ratio of the braiding velocity and the uptake velocity determined the braid geometry, including braid angle. The braid angle is the angle of interlacement between two strands relative to the direction of braid production. A higher rate of take-up decreased the braid angle and generated a stiffer braid, whilst a lower uptake rate increased the braid angle and created a more flexible braid. Larger braid angles result in higher values for maximum strain and yield strain, whereas, lower angles possess greater radial loop strength [181]. A larger radial loop strength was considered a desirable property regarding thread robustness when yarn breakage during tufting occurred as the thread bent around the needle end and the needle perched into the preform.

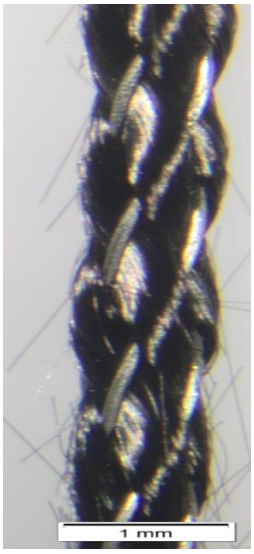

Figure 3-3 Titanium–carbon fibre hybrid braid.

The most efficient braider setting for manufacture was when the braiding velocity was consistent with take-up velocity and the braiding point remained stationary. When the take-up velocity was higher than the braiding velocity, this resulted in braids with loose interlacements and high flexibility which caused greater filamentation of the carbon fibre tow. Where the take-up velocity was lower than the braiding velocity, this resulted in the braiding point moving down towards the carriers causing colliding, knotting and breakage of yarns.

Another parameter affected by lay length was the pick count. The pick count is the repeat of the braid unit cell along the braid axis as discussed in Section 2.1.1. The lay length is inversely proportional to the pick count; therefore,

decreasing the lay length results in a higher pick count. In this study it was hypothesised that by possessing a high pick count and large braid angle, and by consequence a more compact braid; the wire component in the braid would provide protection to the carbon fibre tow during tufting, preventing excessive filamentation. The Herzog micro-braider permitted a variation of lay length settings, which were set on the digital display. An assessment to determine the most feasible lay length for a hybrid micro-braid suitable for tufting was undertaken. The produced braid needed to fit within a tufting needle with an eye diameter of 1.0 mm. The lay lengths of interest were 2 mm, 4 mm, 6 mm, 8 mm, and 12 mm. Tubular braids of carbon fibre 1k tow and titanium wire were produced using a 1:1:1 or diamond braid pattern.

The braider was operated at half capacity producing braids with a 1:1:1 braid structure. The hybrid braids produced contained four Toray® T300 1k 67 tex untwisted carbon fibre tows and four titanium wires. The carrier setting was arranged such that all the carriers in one direction contained carbon fibre tow, with the titanium wires in the opposite direction.

Whilst braid interlacement pattern also affects mechanical properties, investigation of the 2:2:1 pattern was not undertaken. This was due to the size restriction of the tufting needle. For a 2:2:1 patterned braid to be produced this braider would need to be operated at full capacity producing a 16 yarned braid. It was already determined that a maximum of eight yarns could be accommodated through the tufting needle therefore, at half capacity only a braid interlacement structure of 1:1:1 was produced.

As stated above, the lay lengths chosen for investigation were 2 mm, 4 mm, 8 mm, and 12 mm resulting in mandrel take-up speeds of 3.0 m/h, 7.1 m/h, 14.7 m/h, and 21.7 m/h respectively. Table 3-2 provides details on the braider production parameters. Fluctuations in the uptake speed were observed during production and displayed on the digital screen of the braider. An assessment of the speed and lay length variations was undertaken by recording the machines output for 60 seconds and averaging the last 30 values.

Table 3-2 Micro-braiding machine variables

Lay length setting [mm]	**12**	**8**	**4**	**2**
Mean recorded lay length [mm]	12.0	7.9	3.8	1.9
SD	0.6	0.3	0.2	0.1
CV [%]	5	4	5	7
Mean rate of uptake [m/h]	21.7	14.7	7.1	3.0
SD	0.9	0.7	0.2	0.6
CV [%]	4	5	3	19
Pick per Inch [ppi]	16.9	25.4	50.8	101.6
Mean horn gear speed [rpm]	120.1			
SD	4.9			
CV [%]	4			

The pick count value given in Table 3-2 was the output value provided by the instrument, however, the variation in uptake speed would indicate that some variability in pick count was likely to occur along the length of the braid. The braider did not have the capacity to provide a record of this change. Whilst it was not possible to record the change of pick per inch during manufacture, a pick count was determined through a visual assessment of images taken under a microscope and using ImageJ software. Figure 3-4 shows titanium - carbon fibre hybrid braids of lay lengths 4 mm, 8 mm and 12 mm produced during this research.

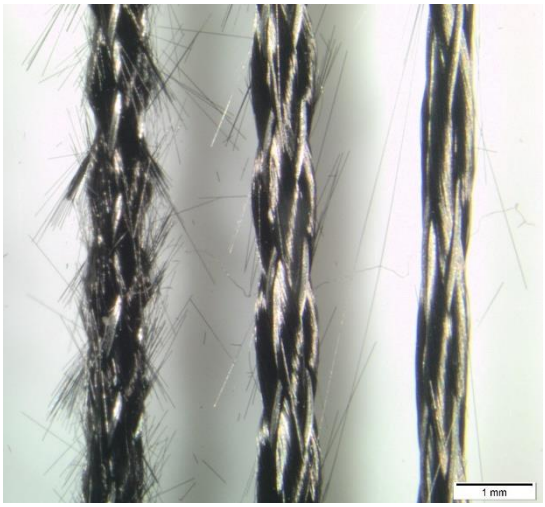

Figure 3-4 Typical titanium hybrid braids, (left to right) lay lengths 4 mm, 8 mm, and 12 mm.

All the braids produced exhibited filamentisation of the carbon fibre tow, which increased with decreasing lay length. Whilst it was possible to set the braider to

lay lengths below 8 mm, it was found not to be practical or safe to continue production. During manufacture of braids of 2 mm, 4 mm, and 6 mm lay lengths, the braiding point moved down towards the carriers resulting in yarn breakage and potential damage to the mechanism. Although small amounts of braid with a lay length of 2 mm were produced, they were insufficient to be used to determine linear density. Similarly, only 200 mm of a braid with a lay length of 4 mm was produced. For completeness, details are provided for the 4 mm lay length braid although, these measurements were taken from a small sample and cannot be considered statistically significant. In some instances, some twisting was evident in the braids although it was difficult to determine if this twist was introduced during braiding or due to miss handling when removed from the braider. The braid interlacement pattern in all three produced braids was 1:1:1. The titanium wire cross-sectional area did not alter along the braids, however, the carbon fibre yarns spread out and flattened to occupy spaces between the interlacement points. Filamentation and crushing was most evident in the 4 mm lay length braid as shown in Figure 3-5.

Figure 3-5 Titanium–carbon fibre hybrid micro-braid – 4 mm lay length.

Splaying of the carbon fibre was more evident in 8 mm lay length braid (Figure 3-6) compared to the 12 mm lay length braid (Figure 3-7) but it possessed fewer crushed and crimped fibres than the 4 mm lay length braid. The splaying of the carbon fibre tows resulted in greater differences in braid diameter along the interlacement points for the 8 mm lay length braid. As expected, as lay length increased, the braiding angle decreased along with the linear density and pick count.

All the braids produced were tubular braids, despite having the appearance of a flat braid caused by the splaying of the carbon fibre tow and the movement of the wires. All the braids were essentially closed braids, that is the yarns next to each other touch, although in the braid with a 12 mm lay length some gaps were evident between the wire and the carbon fibre tows.

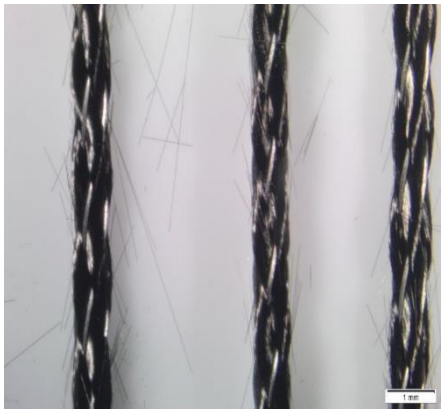

Figure 3-6 Titanium–carbon fibre hybrid braid hybrid micro-braid – 8 mm lay length.

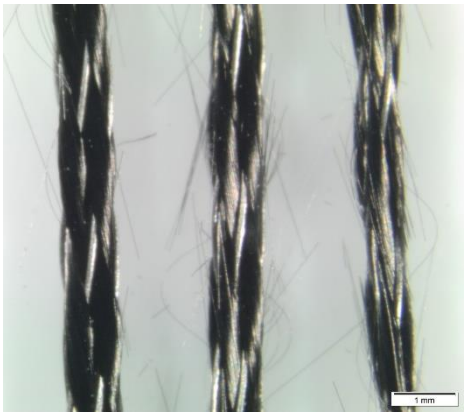

Figure 3-7 Titanium–carbon fibre hybrid micro-braid – 12 mm lay length.

The wire components in the braid increased braid stiffness. When not under tension, the hybrid threads showed little change in form and did not experience a detectable loss in length. It was also difficult to compress the braids without kinking the wires or damaging the carbon fibre tow.

The geometry of the 12 mm lay length braid was less consistent compared to the other produced braids. As the number of interlacements or picks decreased, variability in compaction of the carbon fibre tow was evident. The increase in uptake also caused some separation or slippage of the carbon fibre tow in certain areas although it was possible that this occurred before braiding as a

results of damage during winding or handling. The separation and thinning of the carbon fibre tow was more evident in the 12 mm lay length braids, suggesting that at the higher take-up speed the carbon fibre filaments were being separated by the braiding process. Braids with 8 mm and 12 mm lay lengths showed some filamentation but could be safely and consistently produced in sufficient amounts for this research.

Table 3-3 summarises the properties of the produced braids. Braid angles were determined by averaging 20 measurements taken with ImageJ software from microscopic images. As expected, braid angle decreased with increasing lay length, with angles 10.8°, 12.9° and 23.0° measured for lay lengths 12 mm, 8 mm, and 4 mm, respectively. Difficulty in assessing the images for braid angle were evident from the high coefficient of variation (CV). This was partially due to difficulty in imaging caused by the narrow nature of the braid, the contrasting material types, and splaying of the carbon fibre, which made selecting appropriate segments difficult. In addition to imaging difficulties, the inherent deviation along the braids were clearly evident; fraying, filamentation, and gaps in the carbon fibre tows occurred in all braids and selecting a definitive section of carbon fibre tow proved difficult.

Table 3-3 Summary of braid parameters

Lay length setting [mm]	**12**	**8**	**4**
Mean Braid angle [°]	10.8	12.9	23.0
CV [%]	24	15	7
Mean Linear density [tex]	304.9	414.3	428.9
CV [%]	0.21	0.34	0.01
Pick per Inch [Units per inch]			
*Machine measured output	16.9	25.4	50.8
Visual pick count [Units per inch]	23.7	29.7	36.3
CV [%]	0.2	0.3	6.1

Both the linear densities and the pick count of the braids increased with decreasing lay length. However, a variation between the expected pick per inch count, as stated by the instrument, and the visually measured result was found for all braids. This could be due to the hybrid nature of the braids and the

contrasting material properties of the carbon fibre tow and the metal wire. The interlacement placement was likely to have been affected; with the stiffer wire not being as compliant or flexible as a traditional braiding yarn.

3.4 Manufactured braid specimens

3.4.1 Produced braids

Titanium and carbon fibre braids as well as 100% carbon fibre braids were produced for tufting trials as detailed in Table 3-4. A common feature of all braids was the filamenting of the carbon fibre tow throughout the braid length. The extent of filamenting increased with shorter lay lengths. Shorter lay lengths of 2 mm and 4 mm proved not to be a feasible or practical choice to use during this research. Only the braids with lay lengths of 8 mm and 12 mm could be produced in sufficient amounts and so were deemed more suitable for continued assessment. The braid requirements for the research described in this thesis are constrained by the tufting needle eye size as shown in Figure 3-8This restricted the braid size to less than 1.0 mm in diameter. Due to the nature of braids (i.e., the diameter variations along the length, caused by interlacement points and also whether the braid was under tension or compression) it was necessary to identify a constant method for braid diameter measurement. To ensure consistency, the diameter of the specimen braid was measured under tension. The tension applied was that specified in the *British Standard BS 7658-2:1993 Carbon fibre - Part 2: Method for determination of linear density.* Ten measurements using a vernier calliper along the length of the braid were taken and the mean diameter recorded.

Table 3-4 Braids manufactured for tufting trials

Braid type	Visual Pattern	Lay length [mm]	Diameter [mm]	Production Notes	Tufting Notes
Carbon fibre & titanium	Horizontal	12	0.43 ± 0.01	No issues	Success: filamenting on stitch side - filamented more than lay length 8 mm
Carbon fibre & titanium	Horizontal	8	0.58 ± 0.01	No issues	Success: filamenting on stitch side
Carbon fibre & titanium	Horizontal	4	0.61 ± 0.01	Sporadic breakages	Failure: bunching on insertion pushing braid upwards and breaking - no tuft formed
Carbon fibre & titanium	Horizontal	2	[-]	Failed to manufacture	[-]
Carbon fibre	[-]	12	0.38 ± 0.02	No issues	Failure: overwrap bunching and breaking. No tuft formed
Carbon fibre	[-]	8	0.42 ± 0.02	No issues	Failure: bunching on insertion pushing braid upwards and breaking - no tuft formed
Carbon fibre	[-]	4	0.54 ± 0.03	Sporadic breakages	Failure: bunching on insertion pushing braid upwards and breaking - no tuft formed
Carbon fibre	[-]	2	[-]	Failed to manufacture	[-]

Figure 3-8 A Schmetz EP 11 Nm 230 tufting needle with a 1.0 mm diameter.

3.4.2 Tuftability and handling

An initial assessment of the ability of a braid to be tufted was undertaken using an automated KLS RS522 tufting head, mounted onto a KUKA KR 240 L180-2 2000 robot arm. A dry fibre automated fibre placement (AFP) quasi-isotropic preform of 40 layers of PRISM TX1100 tape from Cytec Solvay was used for this purpose. The mean preform thickness was 8 mm. Each braid was assessed by attempting to tuft a row into the preform. Three different lay lengths 4 mm, 8 mm, and 12 mm of both the hybrid braid and 100% carbon fibre braid were tested. Qualitative assessment on the braids' suitability was determined visually by comparison with a strand of Kevlar® TKT 40 yarn, and two commercially available tufting threads. These threads consisted of 2k carbon fibre, and 4k twisted carbon fibre overwrapped with polytetrafluoroethylene (PTFE). Figure 3-9shows the tufted panel with the trialled tufted rows. The hybrid metallic carbon fibre threads with 8 mm (row 5) and 12 mm (row 6) lay lengths successfully tufted whilst the 4 mm lay length (row 4) failed. Braids of 12 mm lay length had increased levels of carbon fibre damage and fraying in comparison to those of 8 mm lay length.

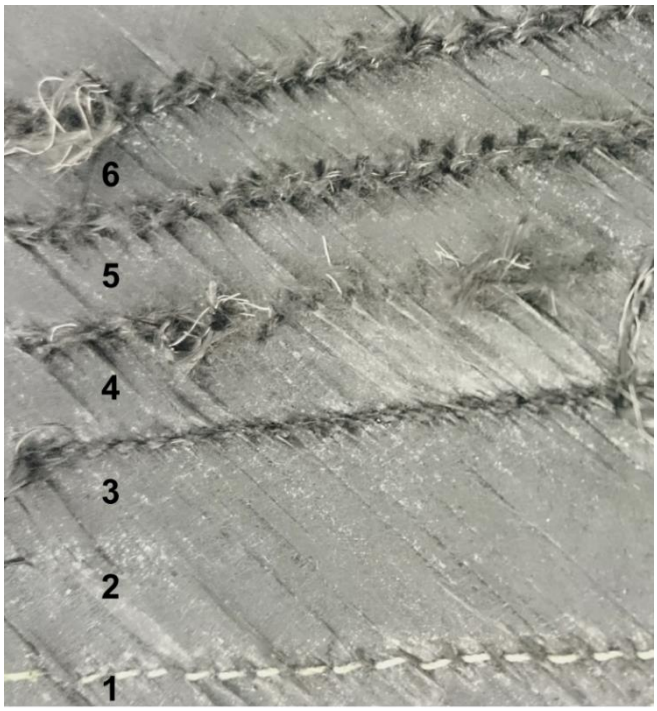

Figure 3-9 Tufted panel, (1) Kevlar® yarn, (2) failed carbon fibre braid, (3) 4K carbon fibre thread, (4) titanium–carbon fibre 4 mm lay length hybrid braid, (5) titanium–carbon fibre 8 mm lay length hybrid braid, (6) titanium–carbon fibre 12 mm lay length braid.

Unexpectedly, the successful tufts of titanium–carbon fibre thread all displayed broken loops when examined on the underside (Figure 3-10). These broken loop lengths were even in length. No precise reason for this breakage could be determined though it was speculated that the needle may have cut the braid when fully inserted into the backing foam. Compared to the commercial yarn, the braided thread tufts showed more fraying and filamenting of the carbon fibre tow. This was to be expected as the braid had inherently more fraying due to the braiding process. None of the carbon fibre braids were successfully tufted irrespective of lay length. All were immediately broken during the initial insertion by the tufting needle as it pierced into the preform.

Figure 3-10 Underside of tufted panel, (1) Kevlar® yarn, (2) failed carbon fibre braid, (3) 4K carbon fibre thread, (4) titanium–carbon fibre 4 mm lay length hybrid braid, (5) titanium–carbon fibre 8 mm lay length hybrid braid, (6) titanium–carbon fibre 12 mm lay length braid.

3.5 Finalised manufacturing parameters

Chapter 3 has detailed the assessment of the potential combinations of hybrid braids, which and established the braiding parameters used throughout the rest of the project. The initial braider limitation study determined that the most suitable hybrid braids would consist of an eight yarned braid comprising a 1:1:1 horizontal pattern. This was based on predictability of successful manufacture, final braid diameter size, and ease of handling. The tufting trial indicated that compared to a braid of 12 mm lay length, braids of 8 mm lay length presented less damage during insertion into the needle and when tufting, despite initially having a higher level of filamentation. Braids of 12 mm lay length experienced more fraying and damage during the tufting process and these braids were found to be more difficult to handle and also consistently exhibited fraying of the carbon fibre tow when inserted into the tufting needle. At shorter lay lengths, the more compact configuration of the carbon fibre and metal yarns provided a greater level of protection to the carbon fibre tow as well as making the braid stiffer and easier to handle. However, braids with lay lengths under 8 mm were

dismissed due to premature breakage of the threads within the braider and an inability to produce a sufficient amount of braid. Therefore, it was decided that the hybrid threads most suitable for this project would comprise an eight-yarn braid, a 1:1:1 interlacement, 8mm lay length and an even number of carbon fibre tows to metal wires in a vertical pattern.

Titanium was originally chosen due its high conductivity, corrosion resistance and high strength-to-density ratio, however, following this initial assessment it was determined that it was not feasible to continue its use. Difficulty in acquiring significant lengths compatible with the winder as well as the overall cost meant it was unsuitable for this research. Copper and nickel chrome wires were therefore used instead.

4 MICRO-BRAID MANUFACTURING PROCESS SIMULATION FOR VIRTUAL BRAID PRODUCTION

Micro-braid manufacturing required a time-consuming and material-intensive trial-and-error experimental assessment to determine the final braid parameters. As a result, testing a wide range of material and micro-braid combinations was both physically and economically impractical. This limited the braid configurations to ones that could be braided using the evaluated parameters. The combinations that did not braid, however, were intriguing, especially those that contained materials and interlacement patterns that had braided successfully in other configurations.

A modelling technique was developed retrospectively to the experimental development of the braid. Its intended use was to study behaviour observed during early manufacturing trials, as described in Section 3.3.3. The goal was to be able to analyse and compare the braider configurations and virtual braids to investigate trends that could be used to explain the observed phenomena. As a result, such virtual manufacturing approaches may provide a framework for the

discovery of more optimal manufacturing parameters that yield braids with superior performance characteristics, allowing them to fully realise their potential as a component within multifunctional composite materials and structures. The model results were validated by comparing the virtually manufactured braid geometry to physical specimens, both qualitatively and quantitatively, using braid formation and condition metrics such as braid angle, lay-length, thickness shape, and structure.

4.1 Simulations of Micro-braid manufacture process for virtual braid production

Braid parameters such as braid angle, lay length and interlacement pattern ultimately determine the mechanical properties of the braid. The component yarns making up the micro-braid i.e., the metal and carbon fibre tow, also influenced mechanical properties and overall quality of the produced micro-braid. With respects to carbon fibre, the filament components within each tow increased the complexity of the micro-braid architecture and as a result a high-resolution approach that considered a realistic representation of the micro-braid was required. Achieving a good correlation between the actual hybrid micro-braid and the virtually simulated micro-braid would allow for a technique of predicting poor braiding configurations, parameters and material combinations that are likely to produce defective micro-braids before they are ever manufactured. It was hoped that constructing the model that considered the manufacturing dynamics would enable a retrospective study of the braider parameters and determine why certain configurations failed to braid. The model enabled the evaluation of a number of adjustable parameters, such as, lay length and braid angle, and ‘virtually’ manufactured a representative hybrid micro-braid.

4.2 LS-Dyna® Model

4.2.1 Virtual braiding simulation

Components of the Herzog 1/16 80 micro-braider such as the carriers and yarns were constructed as model parts in the explicit dynamics solver LS-Dyna® v9.1.0. The yarn carriers were modelled as closed-ended cylinder of rigid shell elements (Figure 4-1). The horn gears and their tracks were not represented in

the model, with yarn carrier motion instead prescribed using boundary conditions as described in Section 8.3.2.The braid ring was not included in the model because it was positioned above the natural braid point during the manufacturing process and was primarily used to decrease oscillation and lateral movement of the generated braid during take-up, and consequently did not alter braid formation.

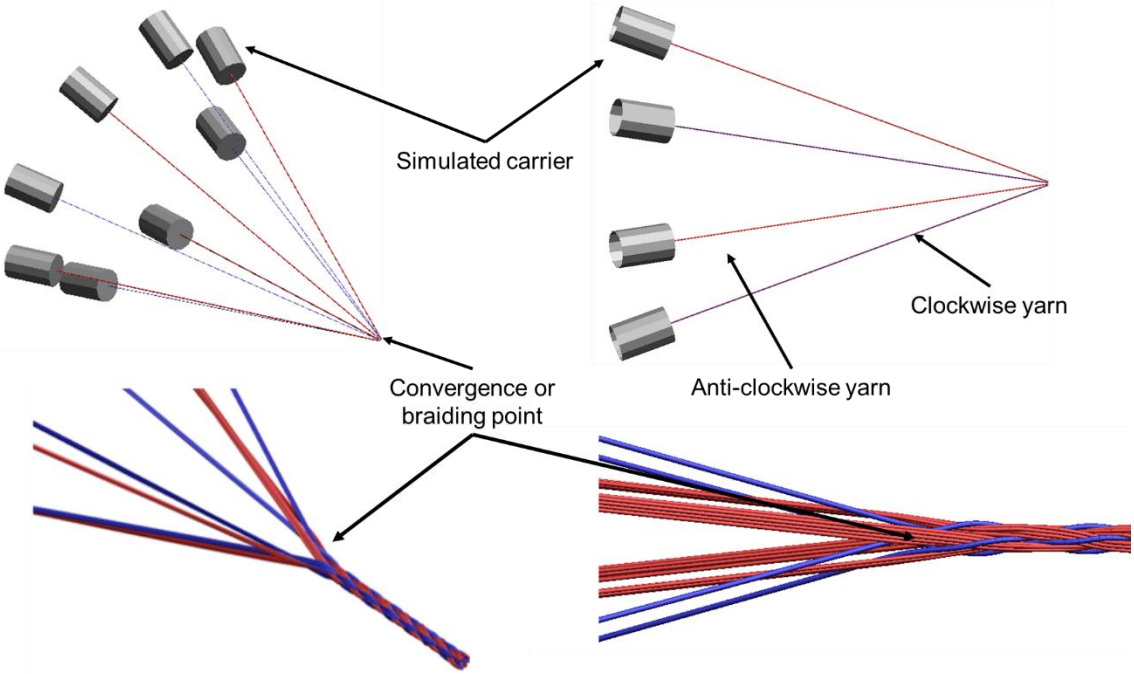

Figure 4-1 Virtual braiding in LS-DYNA®. Model yarns arranged in an initial convergence plane. Yarns are coloured red and blue alternately in their arrangement around the braid track.

Carbon fibre tows in the micro-braid were virtually represented by a multi-filament structure comprised of a bundle of virtual filaments arranged in a hexagonal packing pattern (Figure 4-2). Each virtual filament was in turn modelled as a chain of truss elements with circular cross-section (Figure 4-3).

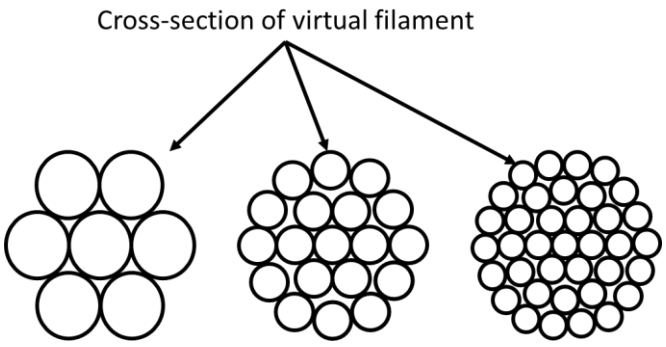

Figure 4-2 Yarn with 7, 19 and 36 virtual filaments cross-sections, arranged in a circular hexagonal packing pattern.

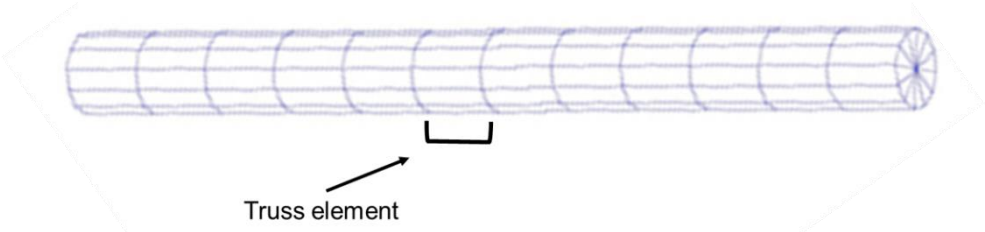

Figure 4-3 “Virtual” filament. Highlight truss element.

Subdivision of each virtual filament into individual elements of minimal length allows the filament to become fully flexible whilst maintaining high axial stiffness, thus imitating physical fibre behaviour [225] This representation of the carbon fibre yarn as a multi-filament virtual yarn, is similar to the Multi-chain Digital Element Method [226], used to model yarn level deformations during textile composite manufacture processes (e.g. weaving and braiding).

Relative displacement of the individual model yarn filaments allows for capturing of modification and deformation to yarn structure and shape due to crimping, spreading and displacement during braiding or weaving. The resulting model geometry then replicates that of the physical preform [227–229]. As previously highlighted, this approach was required in order to achieve a realistic representation of the microbraid architecture and associated braid metrics such as thickness and angle.

The cross-section diameters of the virtual filaments were determined by proportioning the physically measured diameter of the actual yarn materials. Length of the individual truss elements within each filament chain was determined by setting their diameter to length aspect ratio as 1 : 2. This ensured good contact definition (Figure 4-4 Simulated hybrid braid. Model yarns distinguished by material type and coloured according to direction travelled around the sinusoidal carrier path.).Note also, that the metal wire was represented as a single filament chain so that the model does not capture deformation induced in the wire during the braiding process (through ductility of the material for example). However, from experimental trials this was observed to be minimal and therefore not a prominent factor determining micro-braid geometry.

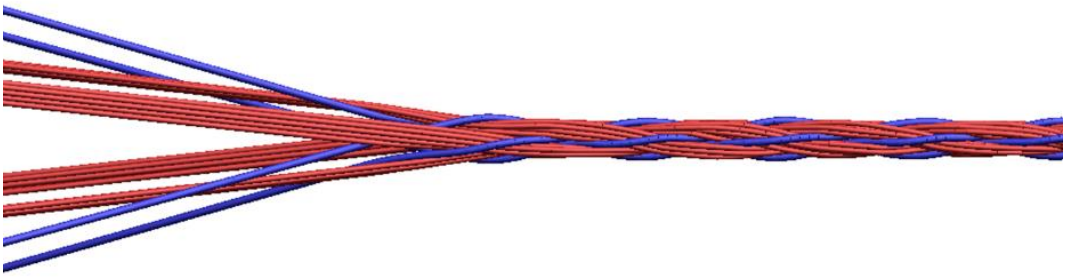

Figure 4-4 Simulated hybrid braid. Model yarns distinguished by material type and coloured according to direction travelled around the sinusoidal carrier path.

It has been observed that as the number of virtual filaments increased, so did improvement in yarn profile representation [229]. Accurate representation of the yarn profile was important in this study as yarn level distortions caused by yarn interlacement were a dominant feature in a micro-braid structure and essential for the virtual micro-braid geometry to replicate the actual manufactured braids. The yarn distortion in the hybrid braid was predominantly evident in the carbon fibre tows displayed by constant modification in the tow structure and shape along the interlaced braid. Metal wire yarns, on the other hand, were more resistant to distortion, causing the carbon fibre component to deform and undulate comparatively more.

However, increasing yarn resolution by having a higher number of model filaments per yarn, leads to consequent increases in model run time as the number of model elements is also increased. Therefore, 7 virtual filaments were used with simulations taking on average (between the two braid configurations examined in Section 4.5.5 of 57 hours (4CPu), to virtually manufacture 6 to 8 mm lay lengths within a total actual braid time of 30 seconds.

The truss elements within each virtual filament and wire are assigned elastic material properties, a modulus of 200 GPa and density of 0.001 tonne/m3. This model, like in previous work [229]), takes a purely geometric approach, so mechanical properties (moduli) were not chosen to be representative of physical material properties. Instead, material moduli are determined by the need to provide adequate contact definition, without undue increase in model runtime. Similarly, densities of 0.1 g/m^2 , 0.01 g/m^2 and 0.001 g/m^2 were trialled. Higher material densities also reduced model runtime by increasing time step size, however, addition of artificial mass (mass-scaling) to the virtual filaments was found to influence their kinematic behaviour during the simulation. This effect

was negligible for densities of 0.001 g/m^2 and lower. Finally, a global damping factor of 10 was used to stabilise contact behaviour.

Contact formulations type ‘automatic general’ was used to model interactions between the virtual filaments, with the yarn carriers excluded from the contact. A coulomb friction coefficient of 0.3 was selected. For model yarns comprising of only 7 virtual filaments, physical friction values could not be feasible employed to replicate the behaviour of physical yarns using 1000s of fibres (and their relative entanglement, for example). Instead, selection of 0.3 was made based on minimal qualitative difference in braid geometry with friction. This low observable effect of the friction value may have been attributable to the use of only 7 virtual filaments in the yarn cross-section.

Finally, as in Sun et al an Infinite Single-Strand (ISS) approach is used via the LS-Dyna® function ‘element beam source’ to add new truss elements to the virtual filament chains on-the-fly during the analysis [230]. Inclusion of beam sources at the yarn ends located at the yarn carrier positions, meant that this function replicated the action of yarn length being pulled from the bobbins during manufacture.

4.2.2 Kinematics

The sinusoidal path (Figure 4-5) followed by the carriers was defined using the equations and formulations obtained from Del Rosso et al. 2019 and used the horn gear radius r and the number of horn gears N_{h_g} to calculate the radius of the full carrier path using Equation 4-1[231]. The vector $\bar{R}$ spanned from the centre of the braiding point to the centre of a given horn gear, and $\bar{r}$ was the radius of each horn gear. Angles α_1 and$\alpha_2$were given by Equation 4-2.

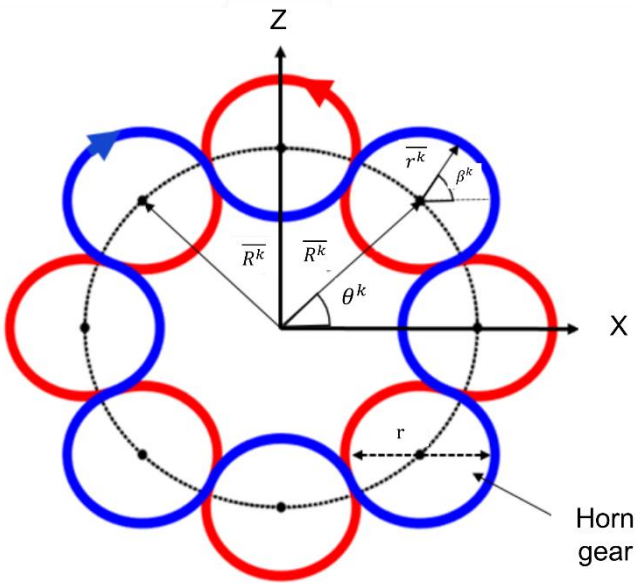

Figure 4-5 Braider track plate configuration with minor (horn gear) and major (carrier) vectors. Anti-clockwise sinusoidal path (red) and clockwise path (blue).

The initial position of each yarn carrier was situated on the radial limit of the braiding path or the major circle radial vector R determined by the horn gears k given by Equation 4-3. The minor vector (r^k) was similarly defined, using the minor circle's internal angle as defined by Equation 4-4. The angle β^k traced the sinusoidal path that traverses between adjacent minor circles replicating the yarn carrier interchanging between the horn gears during braiding.

Equation 4-5 defines the direction and angle of travel around the k^{th} horn gear for carriers moving in an anti-clockwise (ac) orientation. The initial and instantaneous position of an anti-clockwise carrier in the spool ($x - z$) plane was prescribed in the simulation as a time vs displacement curve. Clockwise yarn carrier motions were determined by reversing this path, with adjustment of the different initial position of the horn gear in the track. Finally, braid take-up at the opposing end was simulated via a prescribed y-direction velocity aligned with the physical processing rate.

$$\mathrm{R} = 2\mathrm{r}\,\frac{\sin\alpha_1}{\sin\alpha_2} \qquad \text{Equation 4-1}$$

$$\alpha_1 = \frac{2\pi}{N_{hg}}$$

$$\alpha_2 = \frac{2\pi - \alpha_1}{2}$$

Equation 4-2

$$\overline{R^k} = R[cos(\emptyset^k)\, sin(\emptyset^k)]$$

$$\overline{r^k} = r[cos(\beta^k)\, sin(\beta^k)]$$

$$\overline{r^k_{glob}} = \overline{R^k} + \overline{r^k}$$

Equation 4-3

$$\beta^k = (-1)^{k+1}\, \varphi^k + \alpha_2 - \pi + (k-1)(\pi - \alpha_2)$$

Equation 4-4

$$\varphi^k{}_{ac} = \begin{cases} [0, (2\pi - 2\alpha_2)]\ k\ odd \\ [0, (2\alpha_2)] k\ even \end{cases}$$

Equation 4-5

In an actual braider, the yarn was pulled from the carrier bobbin by a spring mechanism on the carrier, which controlled tension and feed rate. The virtual braider, on the other hand, employed the function ‘element beam source' to create new yarn material from the carrier spool using the Infinite Single Strand approach [230]. To mitigate any slack in the yarn material, a resistance force was assigned to the source node. Whilst this limited the rate of new element generation it did not generate a consistent resistive effect or tensioning on the yarns. Once exceeded at the source node, new yarn length elements were extruded from the source position resulting in an excess length and slack in yarn when the carrier reached the inside radii of the carrier path. This differed from the actual braider, where the carrier springs-maintained a relatively consistent yarn tension. Therefore, the model did contain an amount of slack which was most evident when the carriers moved between the horn gears and transitioned from the outer to the inner radii. This slack along with the non-physical mass to the model yarns, led to a dynamic effect that inhibited convergence of the virtual braid model. To counteract this effect, the carrier's movement was modified to allow motion in the y-direction, displacing the

carriers by 5 mm as they rotated along the carrier path, limiting the effect of the excess yarn length.

4.3 Model validation

The simulation model was verified using a sample of the copper-carbon fibre microbraid (Figure 4-6). ImageJ was used to measure and examine features such as micro-braid diameter, braid angle and carbon fibre tow profile. Because of the different materials used to make the braid, the natural undulating surface profile of a braid was more visible in the hybrid braid. This manifested itself as large variances in braid diameter, with the smallest cross-section being observed in regions where the copper wires were positioned externally along the braid, and highest when internally placed. The overall mean braid diameter measured using ImageJ was 0.78 mm (8% CV). The mean maximum diameter, measured when carbon fibres were internally positioned, and the mean minimum diameter, when the copper wires were externally placed, were 0.83 mm (6% CV) and 0.73 mm (5% CV), respectively. The variability caused by such contrasting yarn materials also influenced the braid angles.

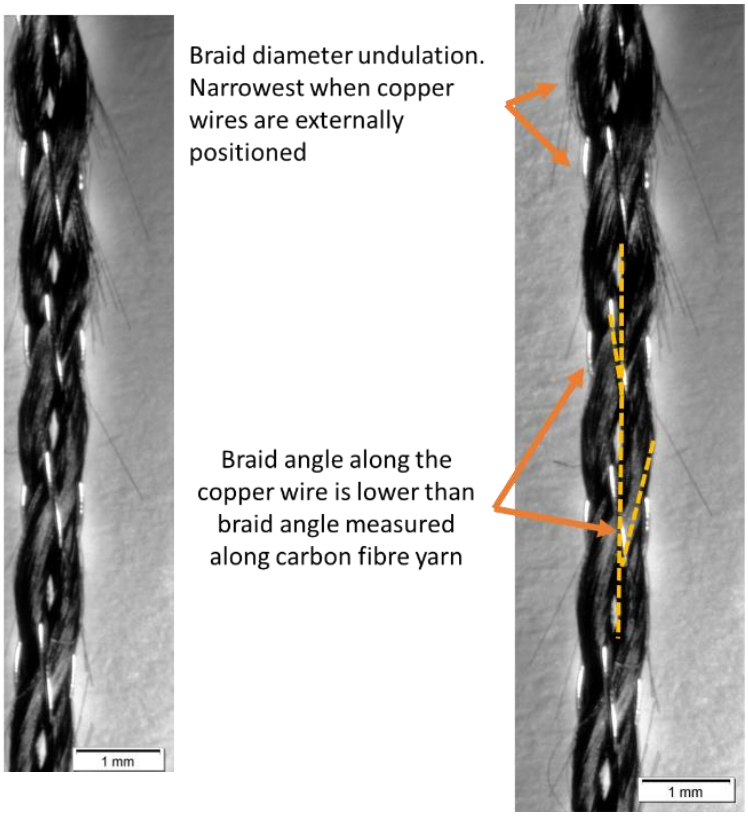

Figure 4-6 Section copper-carbon fibre micro-braid length.

When assessed along either the copper wire yarns or the carbon fibre yarns, different braid angles of 10° (10% CV) along the copper wire and 16° (18% CV) along the carbon fibre were measured. This was predominantly due to the carbon fibre yarns weaving around the less compliant copper wire. The copper wire resisted undulation during braiding and tended to maintain a straighter profile when converging at the braid point. The carbon fibre tow, on the other hand, displayed fibre displacement and spreading, as well as changes in profile and distortion throughout the braid. length.

To examine the cross-sections, a length of the micro-braid was infused in Prime27® by placing it inside PTFE tubing, securing with wire, and infus with resin using a vacuum. The tube was sealed, and the resin allowed to gel overnight. This method of infusion preserved the braid's tubular profile while limiting distortion and compression, which could have occurred if the braid had been vacuum bagged. A diamond saw was used to cut and expose cross-sections at certain positions along the micro-braid length. Final preparation involved a sequence of grinding using P400, P800, and P1200 silicon carbide pads, with a cleaning step between each. The polisher was operated at 27 N for 2 minutes with the plate rotation operating at 175 rpm. The sample was polished with TexMet® polishing solution at 27 N for 2 mins with a contra plate rotation at 125 rpm. After polishing, visual inspection of the micro-braid cross-section was undertaken with an Olympus SZX16 microscope with Olympus Stream software. ImageJ was used to measure and examine features such as micro-braid diameter, braid angle and carbon fibre tow profile (Figure 4-7).

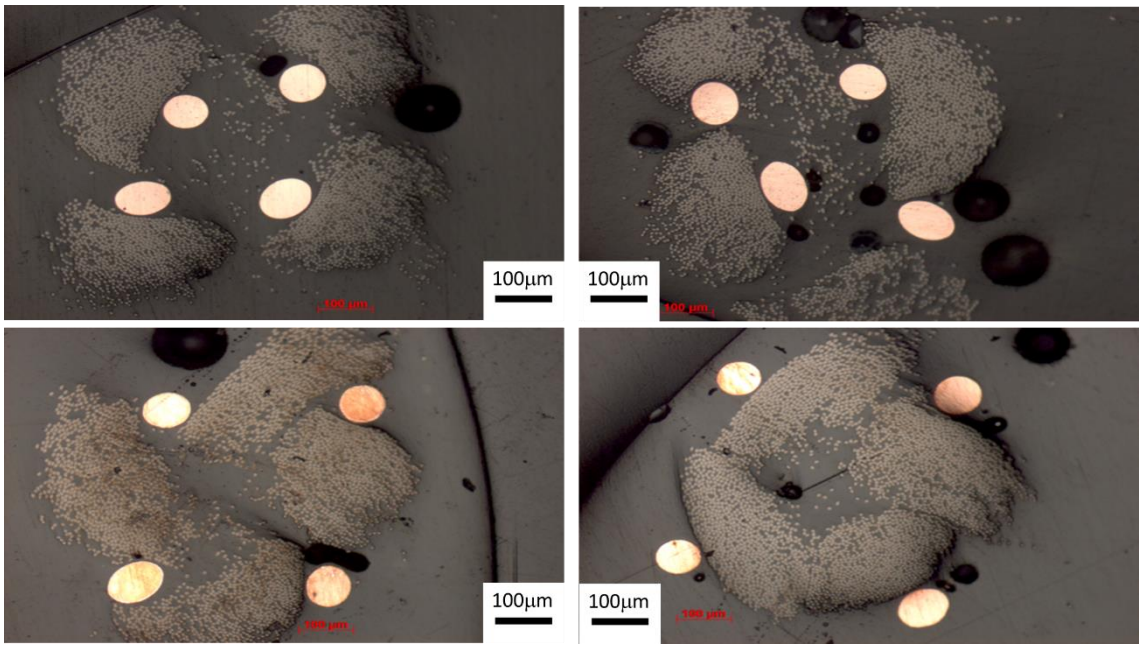

Figure 4-7 Resin infused cross sections of copper – carbon hybrid microbraid. The cross sections depict the various yarn positions along the braid length.

4.4 Braid post-processing

The components of virtual braid structure, such as braid angle, degree of undulation and braid thickness were assessed to provide a quantitative comparison to the actual manufactured braid. This was undertaken using the geometric information of the truss elements that made up the virtually braided yarns. Nodal coordinates of the simulated yarns were used to extract braid geometries, which were then processed in MATLAB. A cut section of the simulated braid comprising four lay lengths was extracted for analysis (Figure 4-8). The first and the last lay length sections were excluded due to potential for unrealistic representation caused by the model boundary conditions and yarn movement at the convergence point.

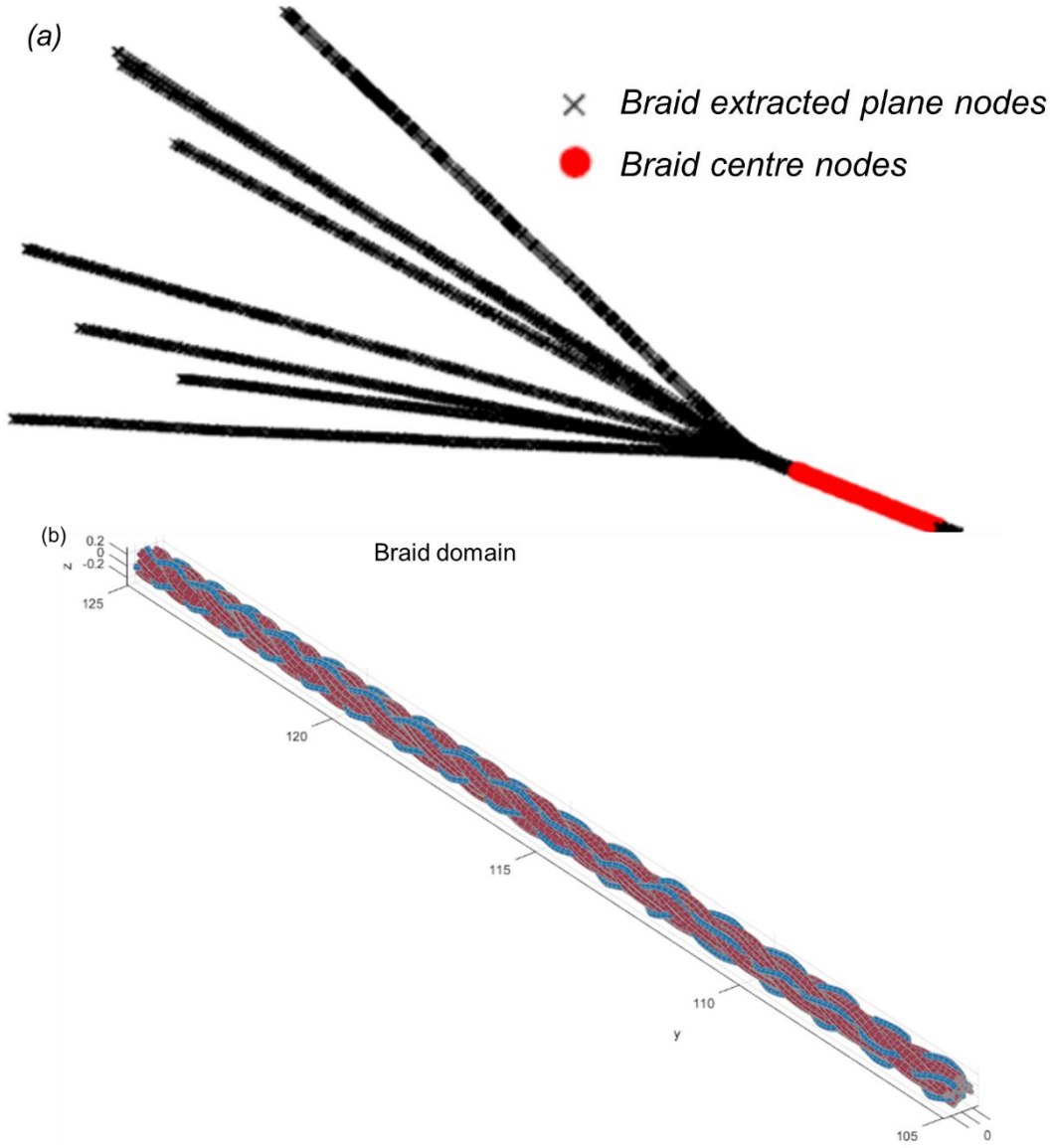

Figure 4-8 (a) Section of extracted braid after simulation (b) Domain of braid considered for analysis.

4.4.1 Braid thickness

Calculation of the braid thickness was determined by defining ($x - z$) planes at regular 1 mm intervals using a method described in [228]. An algorithm identified nodes at specific positions immediately behind (c_0) and in front of (c_1) on each plane. As shown in Figure 4-9 (a) the node pair forms the end-nodes of a given truss element connecting the virtual filament chain that intersects the plane. Interpolation along the local element vector gives a coordinate of the intersection point lying on the plane (*cp*). This process was repeated for each filament, resulting in a number of intersection points, or plane nodes, that define a cross-section of the braid at each plane location along the braid. A centre-node was then calculated for each braid cross-section plane by averaging the coordinates of the plane nodes. The braid half-thickness was calculated as the maximum distance between a plane node and the centre node plus the radius of the virtual filament.

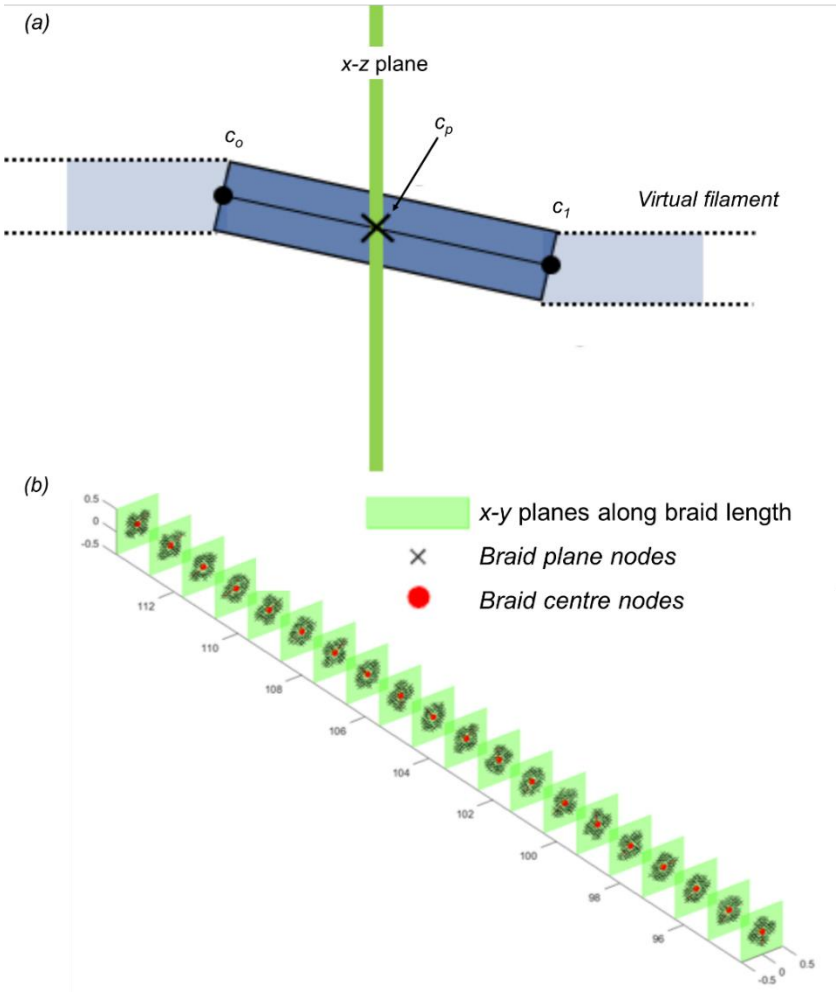

Figure 4-9 (a) Illustration of calculation of braid sections (as x - z planes) at regular intervals along its length (b) Braid section nodes and centre-nodes at each cross-section plane.

4.4.2 Braid angle and undulation

The braid angle was determined using a similar plane-intersection method as braid thickness. The plane intersection positions for each individual yarn in the braid were specified using the virtual filaments of each yarn. As illustrated in Figure 4-10, the average of these interaction sites determined the centre-node of each yarn at intervals along the braid, with the vectors ($v_i, 1 \leq i \geq N-1$, for N intervals), between neighbouring yarn centre-nodes forming the central path of each yarn within the braid. The angle between each vector (vi) and the global braid length (y) axis defines the braid angle at that position along the braid length. Additionally, the sum of the lengths of vectors v_i defines an overall yarn length L. The waviness of the yarn within the braid can then be determined by an undulation factor Uf, calculated by dividing the yarn length L by the nominal length of the braid along the global y-axis (L_y) (Equation 4-6).

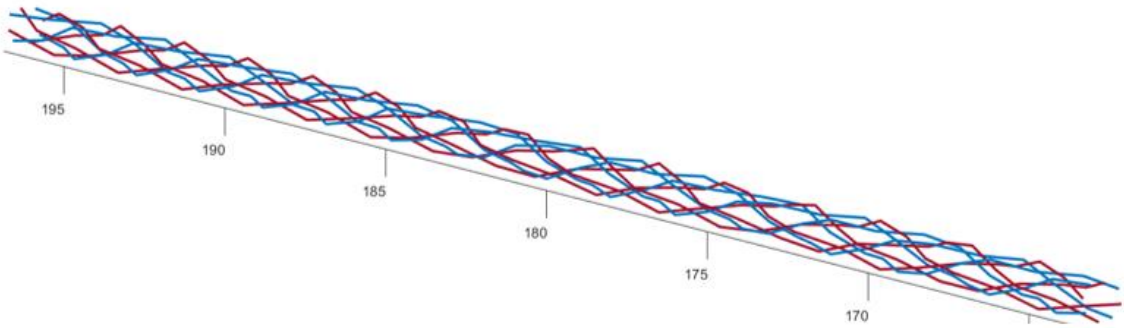

Figure 4-10 Centreline path of yarns within a microbraid, coloured red (carbon fibre) and blue (metal) alternately.

$$U_f = \frac{L}{L_y} = \frac{\sum_{i=1}^{N-1} v_i}{L_y} \qquad \text{Equation 4-6}$$

4.5 Results and model validation

4.5.1 Comparison to manufactured copper-carbon fibre hybrid braid

Figure 4-11 shows images of the physical and virtual multi-material hybrid braid, with the virtual filaments comprising the carbon fibre tow shown in red and the copper wire as a blue monofilament. The interlacement pattern, yarn undulation,

and overall surface profile of the simulated braid were visually consistent with the manufactured braid. The undulation caused by the different materials, particularly the extreme crimping caused by wire-wire interlacement, was also accurately replicated by the simulation. A notable discrepancy in the model was the lack of carbon fibre filamentation. The carbon fibre components of virtual braid specimen were each produced using yarns of 7 individual filaments. This underrepresented the actual composition of the carbon fibre tow yarn. And contributed to the lack of accuracy with respects to filamentation, yarn compression, splaying and distorting. A larger number of filaments would increase distortion accuracy but at the cost of increased computational expense.

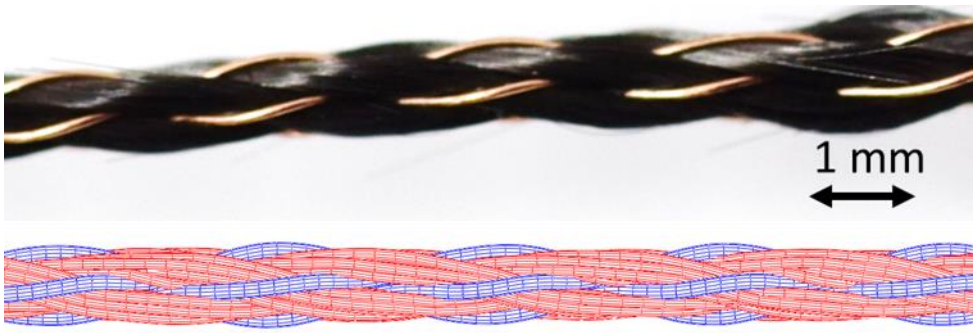

Figure 4-11 (Top) Manufactured copper-carbon fibre braid and (bottom) Finite element model of hybrid braid. Constructed with a 1:1:1 interlacement pattern and horizontal visual pattern.

4.5.2 Cross section comparison

Cross-sectional micrographs depicting three contrasting interlacement sections of the manufactured braid were analysed and compared to the simulation model (Figure 4-12). These sections depict when the wires are externally positioned, when the carbon fibre tows are externally positioned, and an intermediary position. The FE model accurately depicts local variations and reorientation of each carbon fibre tow as well as the overall braid cross sectional shape at each interlacement point. The divergence and clear change in areal profile caused by arrangement of material in the braid interlacement pattern has been accurately captured by the model.

But some difference between the model and the manufactured braid was apparent. This was particularly evident in the case of the metal wire and its proximity to the braid centre. In the physical braid, the metal wire components

tended to move and be positioned more centrally, causing carbon fibre components to be dispersed, squeezed, or relocated. The virtual braid, on the other hand, prevented the central arrangement of the wires. Again, this could be attributed to the usage of only seven virtual filaments for the carbon fibre representation, which resulted in the metal being unable to influence the considerably larger but fewer simulated filaments in the same manner that it did the genuine carbon fibre tows.

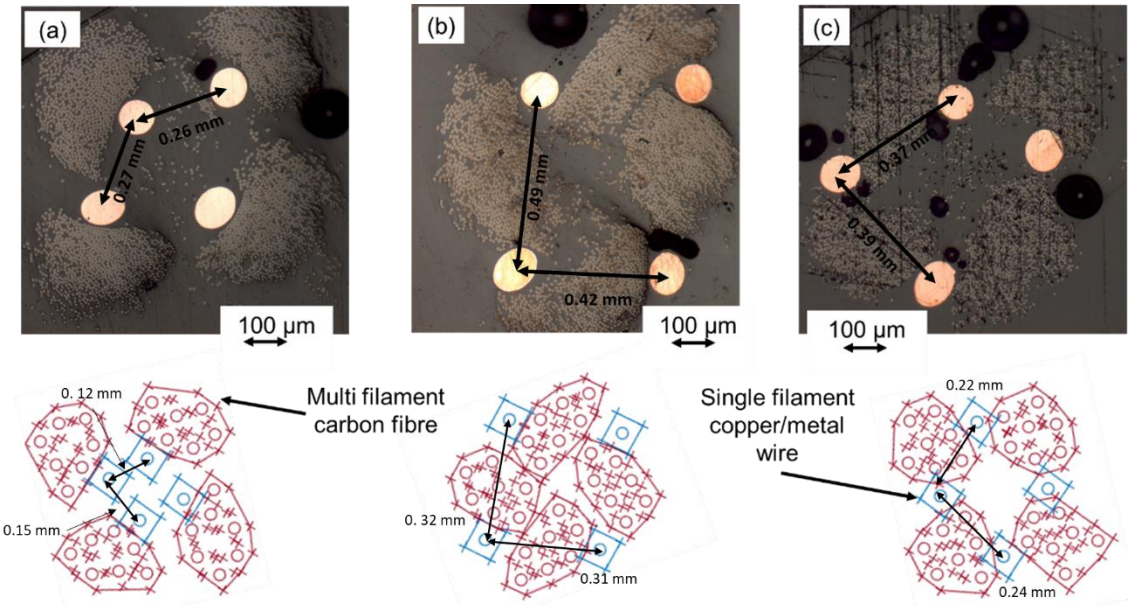

Figure 4-12 Cross-sections of manufacture and simulated hybrid braid with (a) copper wires internally positioned, (b) copper wires externally positioned and (c) intermediately placed.

Despite this limitation, the simulation accurately depicted changes in the carbon fibre tow shape caused by material interlacement. The carbon fibre cross-section shape ranged from a rounded profile when unconstrained by the wire components (Figure 4-12 (a)) to a more elongated profile with straighter sections when constrained and crimped by the externally positioned wires (Figure 4-12 (b)). A combination of these shapes was observed at the intermediate position (Figure 4-12 (c)). A comparison of the aspect ratio of the rounded and elongated profiles are provided in Figure 4-13. The difference in aspect ratios varied from 12%-35% depending on the profile of the carbon fibre yarn. The more circular profiled carbon fibre yarns being more accurately represented that the rectangularly deformed yarns.

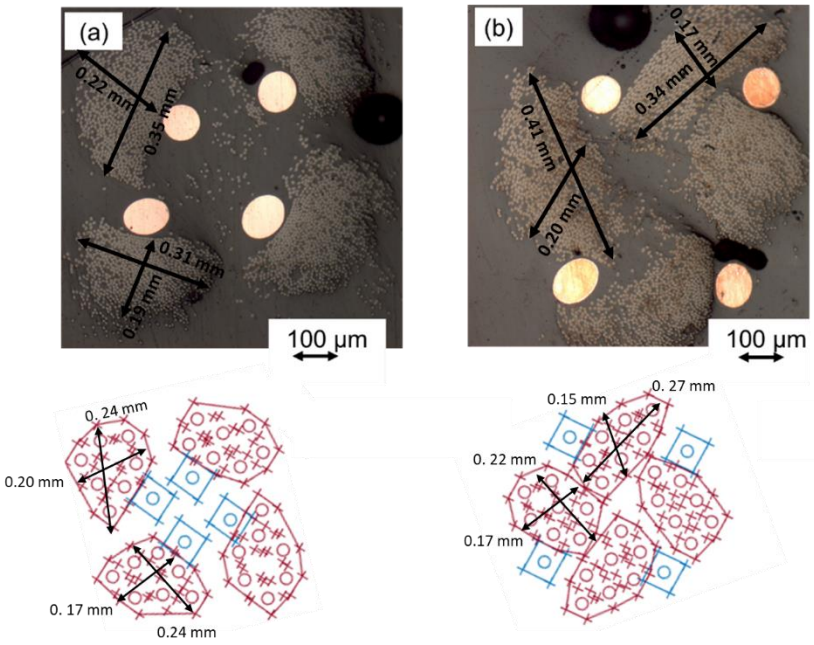

Figure 4-13 Comparison of aspect ratio profiles of braid cross sections.

4.5.3 Thickness variation

Figure 4-14 shows a plot of thickness variation along a 40 mm length of the simulated braid. Although it was not possible to obtain as full a comparative comprehensive set of braid measurements for the real braid, the mean diameter and standard deviation are provided for comparison. The calculated braid thickness along the length of the simulated braid ranged from 0.60 mm to 0.67 mm. When the mean diameters of the simulated and genuine braids were compared, the mean diameter of the simulated braid was 18% smaller. Measurements of the real braid were taken whilst the braid was still postioned inside the braider, as this is reprentive of the as manufactured state of the braid as represented by the simulation. Measurments ranged from 0.69 mm to 0.88 mm.

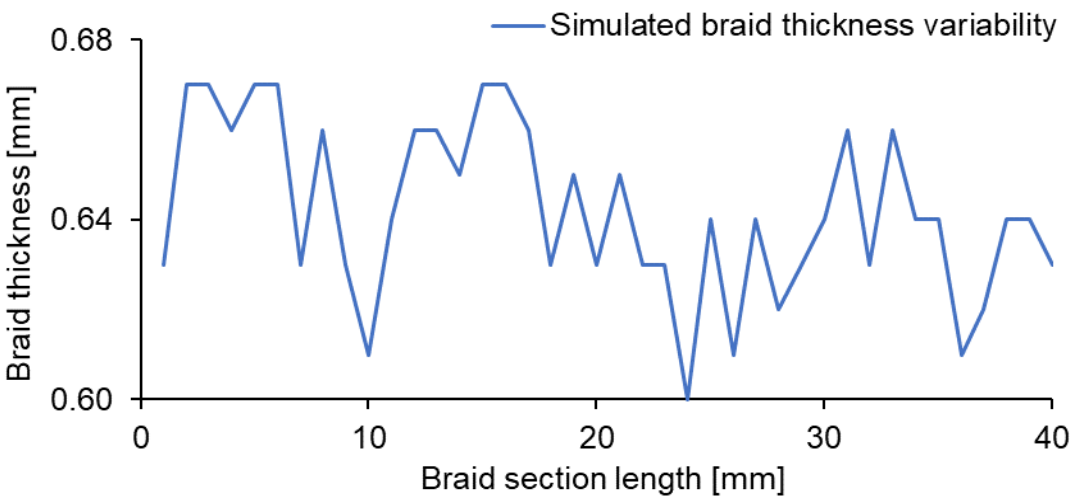

Figure 4-14 Plot of braid thickness variation.

The greatest variation was seen in the maximum thickness sections of the braid (0.88 mm vs. 0.67 mm), which equated to a 24% difference. As previously stated, this occurred when carbon fibre yarns were positioned on the outside of the braid and were less constricted by the metal components. As a result, fibre dispersion and distortion were larger in these interlacement section compared to other sections. The effects of the wire on the carbon fibre tow were less well replicated since the simulation employed fewer filaments than genuine carbon fibre. A 15% difference between the minimum thickness sections (0.69 mm compared to 0.60 mm) was measured.

Braid tension could also be a factor in the variances in braid thickness. Tension influenced the contraction and expansion of the manufactured braid, making it difficult to assure thickness uniformity when assessing the braid. Before the imagery was captured, the braid may have relaxed in the braider, causing the braid sections to expand. Physical measurements with callipers introduced the possibility of measurement error due to excessive compression. Also as explained in Section 4.2.1, it was not possible to correlate the physical and model yarn tension exactly during braiding. The model required additional carrier movement to reduce the slack along the yarn length. This method of increasing tension on the yarn might have inaccurately influenced the carbon fibre profile. Less tensioned yarns spread more than higher tensioned yarns; this effect was found during physical production where higher braiding speeds or longer lay lengths were produced.

4.5.4 Braid angle

The braid angle of the simulated braid was approximately 10° for both carbon fibre tow and copper wire, indicating a lack of correlation to the manufactured braid, which had braid angles of 10° ± 10 % along the copper wire and 16° ± 18°% along the carbon fibre. Figure 4-15 shows a plot of braid angle along yarns of each material type, as well as average braid angles measured along the real carbon fibre and metal wire yarns in the manufactured braid.

The model predicts that the metal wires undulated more than carbon fibre yarn, which contradicts physical samples. This discrepancy could be explained by the fact that the two different material types were given the same contact formulations. As a result, wire-wire, wire-carbon fibre, and carbon fibre-carbon fibre interactions were all treated the same, and the influence of the carbon fibre tow adjusting and moving around the wire components experienced in the real braid was not replicated. The graph shows two distinct sets of braid angles. These groupings could be linked to material type or braider carrier direction. What is notable, though, is that the two groups mirror each other, indicating a high level of symmetry between each component within the braid.

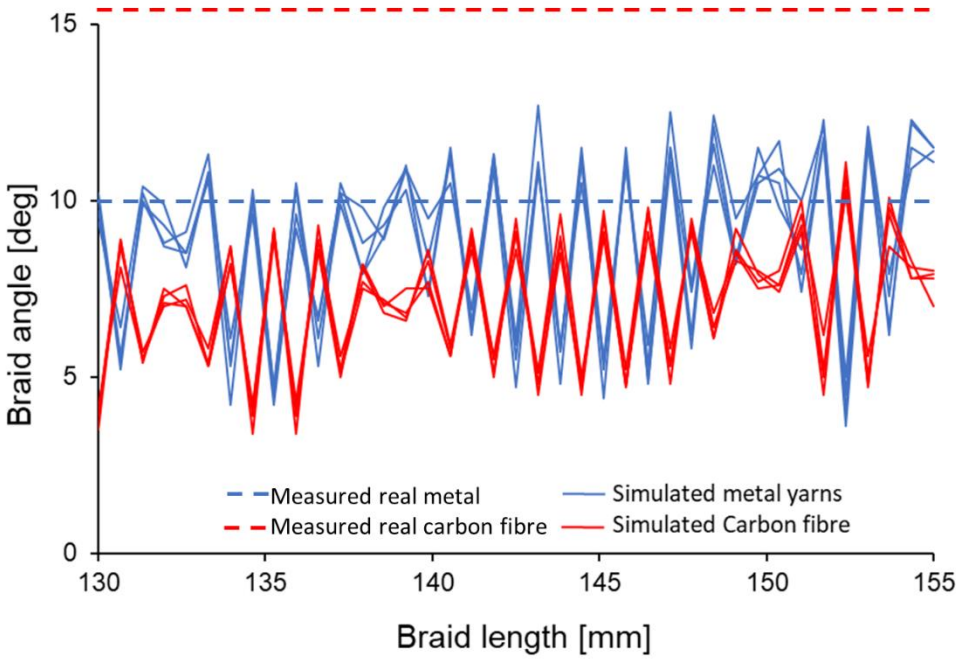

Figure 4-15 Plot of braid angles measured along each individual braid yarn.

4.5.5 Virtual investigation on the effect of material placement on braid production

As discussed in Section 3.3.3, yarn orientation and material placement had an unexpected impact on hybrid braiding manufacturing, and as a result, some hybrid configurations failed to braid. These configurations usually resulted in breakage of the carbon fibre yarns at or near the braiding point before a usable length of braid could be manufactured. Figure 4-16 shows two simulated braid configurations: on the left is the manufactured configuration used in this thesis; on the right is a braiding configuration that failed. Both comprise four carbon fibre tows and four copper wires braided in a 1:1:1 pattern. The sole variation between the two was the carrier arrangement of the materials in the braider (Figure 4-17). In the successfully produced hybrid braid, all the carbon carriers were in one direction and the copper wire carriers were in the other. In the braid arrangement that failed, both carrier directions had alternating carbon fibre and wire. The model was utilised to determine why one setup braided while the other failed.

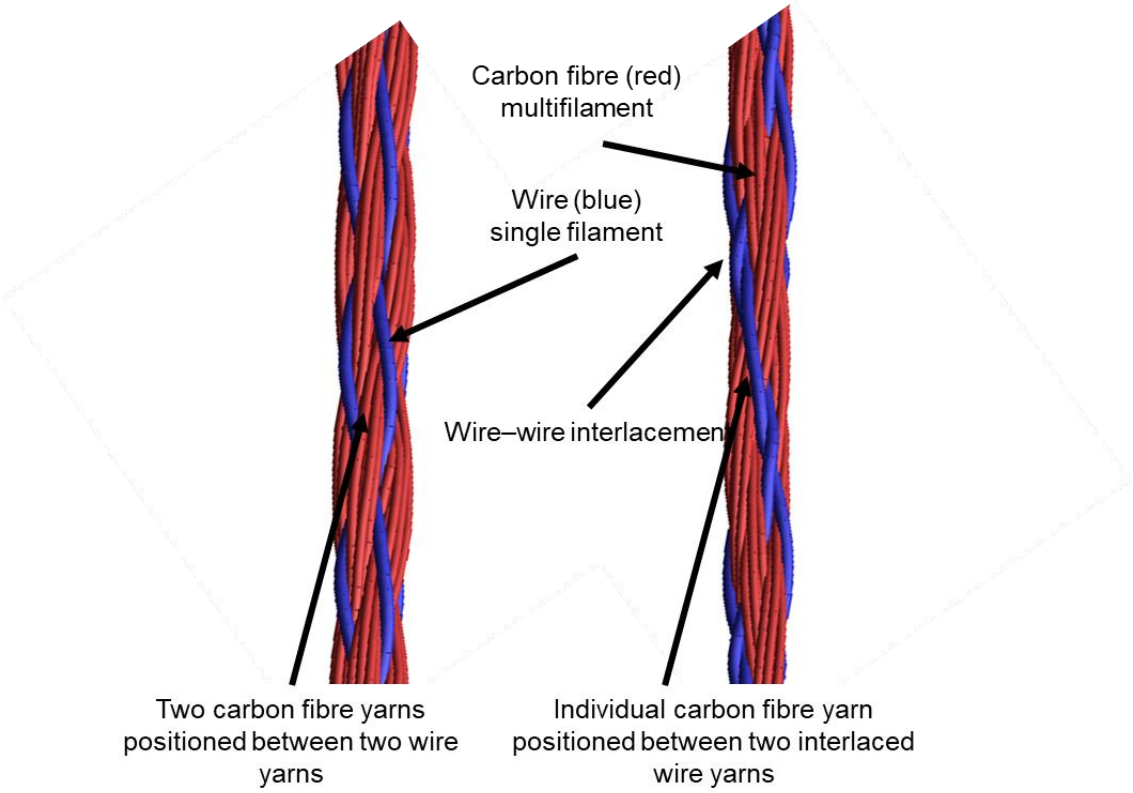

Figure 4-16 Alternative braid material configurations. (Left) A visibly vertical patterned braid was formed by keeping one material in one direction and a different material in the other, while (right) a visually horizontal braid was created by switching materials in both carrier path directions.

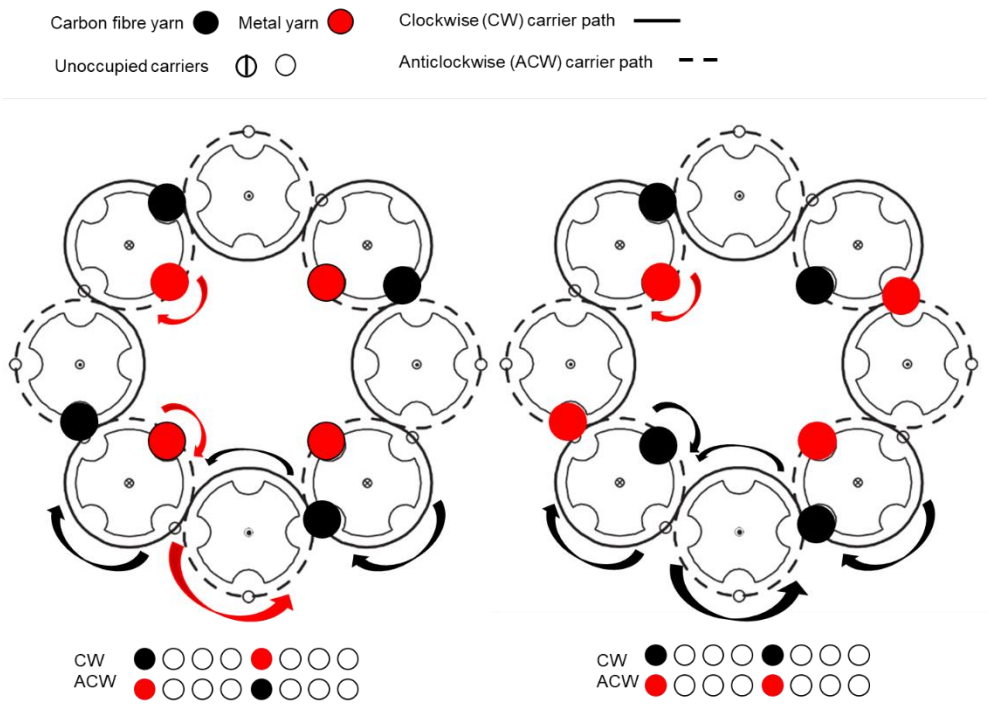

Figure 4-17 Carrier arrangements of the (left) produced hybrid braid and (right) the failed configuration. Image adapted from [298].

Qualitatively, wire-wire interactions clearly distinguish the two configurations. Whilst the interlacement patterns were identical (one-over-one under) in both configurations, the contact interactions between the two different materials were different. In the successfully braided configuration, the wires only interlaced with carbon fibre yarns, not with each other, and as shown by Figure 4-16 (left) were separated by two staggered but similarly aligned carbon fibre tows. The interlacement pattern consisted of metal wire interlaced over a carbon fibre and then under another carbon fibre and in the opposite direction the carbon fibre interlaced over a metal wire then under a metal wire.

The lack of wire-wire interlacement removed the possibility of a single carbon fibre yarn carbon being constrained or pinched between two wire yarns. As the braider up-take pulled the metal wires aligned in the up-take direction and the carbon fibre yarns adjusted around the wires. Whereas, in the failed configuration the wires intertwine, with a single carbon fibre tow positioned between the two (Figure 4-16 (right)). The interlacement pattern consisted of metal wire yarn passing over a carbon fibre yarn then under a metal wire yarn, or under a carbon fibre yarn and over a metal wire yarn in both carrier directions. Where wires are positioned externally the simulation shows that a carbon fibre yarn was pinched between two interlaced wires. When pulled by

the braider take-up drum the metal wires were likely to compress on this carbon fibre yarn and friction on the carbon fibre yarn could have led to it severing.

The profile of the failed configuration (Figure 4-16 (right)) also appears uneven from one side to the next, corresponding to parts with consecutive interlacements of either carbon fibre tows or wires i.e., where wire-wire interlacement occurs that side of the braid was narrower. This asymmetry could have caused conformance issues and dynamics, such as twisting or rotation of the braid during formation. In contrast whilst the successfully manufactured braid has variation along the length of the braid at each part the braid profile appeared even (Figure 4-16 (left)).

4.5.5.1 Cross-section comparison

Figure 4-18 and Figure 4-19 show cross-sections of the hybrid braid in both yarn pattern configurations. The profiles of the cross-sections in the unsuccessful configuration appear asymmetric, compressed, and lack the rounded tubular profile expected from a maypole braid. The wire yarns also appear to converge in pairs with the carbon fibre grouping along a central plain.

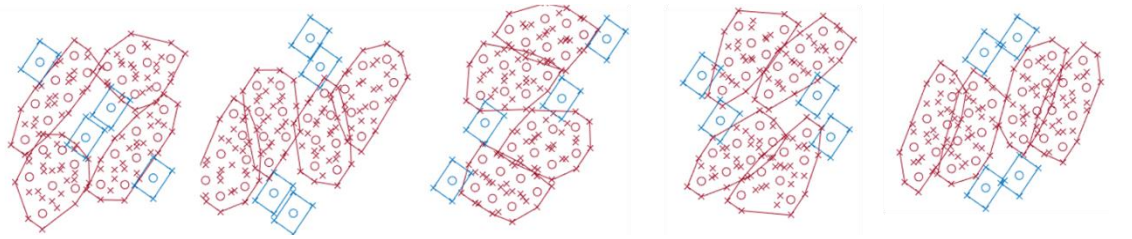

Figure 4-18 Simulated cross sections of un-manufacturable hybrid braid configuration.

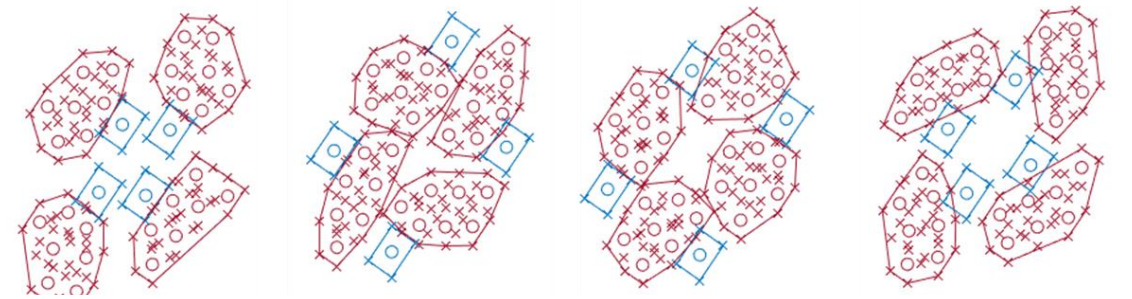

Figure 4-19 Computer-generated cross sections of manufactured braid.

In contrast the braided configuration shows higher symmetry, and uniformity with a rounded cross-sectional profile. The simulation shows the wire yarns stayed separated by the carbon fibre yarns, and the cavity in the centre remained a feature.

The lack of compression, the evident separation of each yarn in the braid, and the continuous tubular profile all showed that this configuration created a more stable structure. The wire strands appear to operate as a framework around which the carbon fibre yarn distort relatively freely into the braid interlacement pattern. Unbalanced pinch points that would have sheared the carbon fibre yarns were also avoided due to the separation and lack of wire-wire interlacements.

The real-braid possessed a symmetric and tubular profile with an undulating but relatively smooth surface. Whereas the failed configuration was asymmetric, had contrasting cross-sectional profiles, and both the shape and surface composition of the braid varied along its length. The lack of symmetry manifested as an unbalanced braid and likely caused kinking of the yarn material as it attempted to braid. This kinking increased the likelihood of material damage at the braid convergence point and potentially the cause for inevitable braiding failure.

4.5.5.2 Braid thickness

The failed configuration braid thickness possessed greater fluctuation than that of the manufactured braid, with thickness measurements varying between 0.60 mm and 0.70 mm (Figure 4-20). When compared to the manufacturable braid thickness, the thickness profile in red reveals sharply contrasting thickness changes going from maximum to minimum thickness in a short length. The manufacturable braid possessed a less dramatic sequential change with fewer sharp peaks along the braid length.

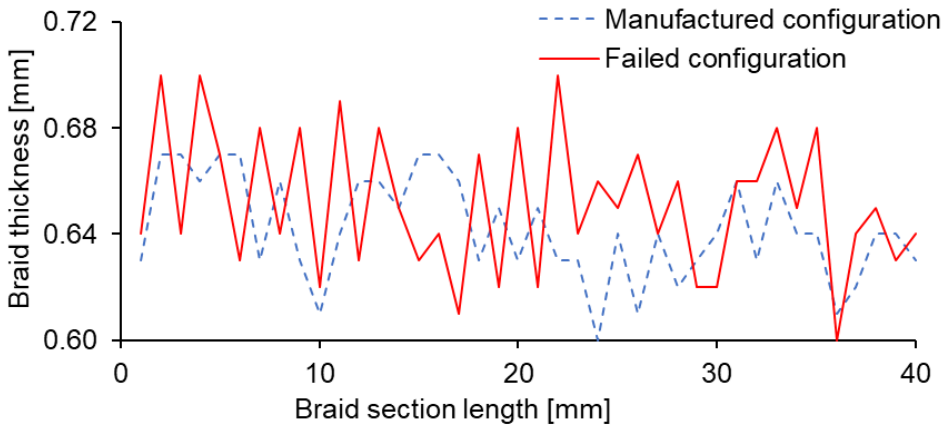

Figure 4-20 Plot of braid thickness of failed configuration (red) and manufactured configuration (blue).

This difference in braid thickness profile again indicates that the failed configuration was less uniform and the constant changing in thickness was likely to create instability in the braid structure resulting in damage to the brittle carbon fibre yarns. The thickness profile fails to capture the contrasting thinner side sections created by wire-wire interlacements. This unevenness between one side of the braid to the next was likely to result in increased residual yarn stress in the yarns, likely to result in yarn breakage especially in the carbon fibre yarns.

4.5.5.3 Braid angle

Figure 4-21 shows graphs of braid angles measured along yarn in (a) the simulated manufactured configuration and (b) the failed configuration The braid angle profiles show how the two setups produced contrasting braid structures with the lack of symmetry evident in the failed configuration. Unlike the manufactured braid configuration, the failed one shows little consistency of the braid angles between either material type or direction of travel (clockwise or anticlockwise) in the carrier path.

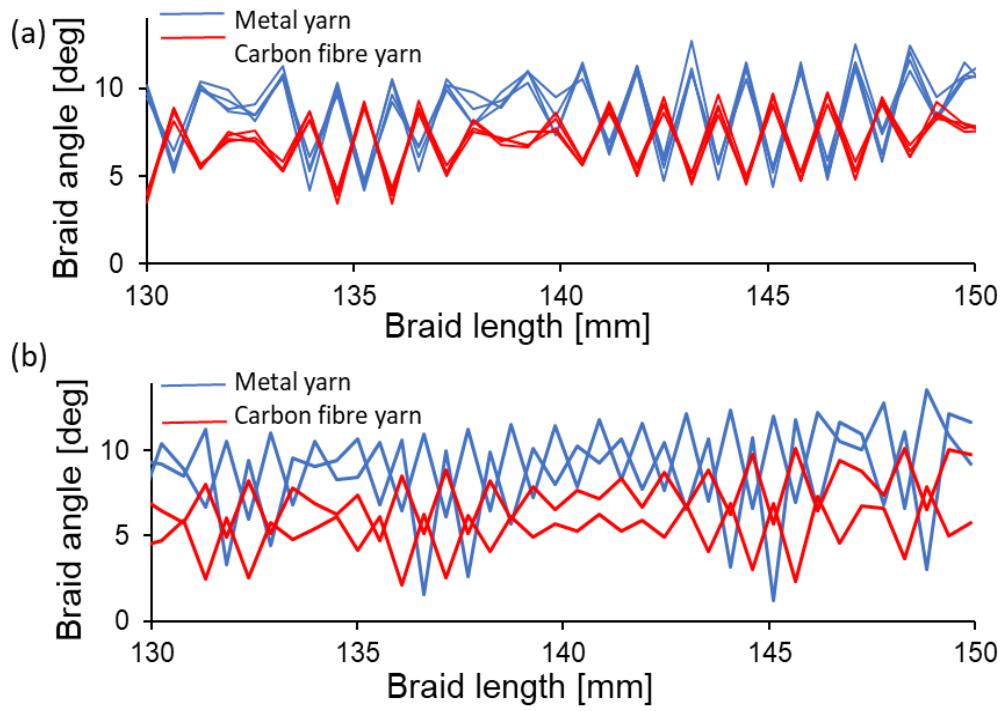

Figure 4-21 Plots of braid angles of different braid configurations. (Left) Manufactured braid configuration and (right) failed braid configuration.

The simulation shows that in the failed arrangement, two braid angles are formed by both material types moving in opposite directions, resulting in four different braid angle profiles within the same structure in contrast to the two in the successfully manufactured braid (Figure 4-22). It indicated that yarns travelling in the same direction had braid angles that were paired based on material type, for example, metal wire with metal wire and carbon fibre with carbon fibre. The braid angle profile appeared to be determined by the interlacement materials, particularly wire-wire interlacements positions.

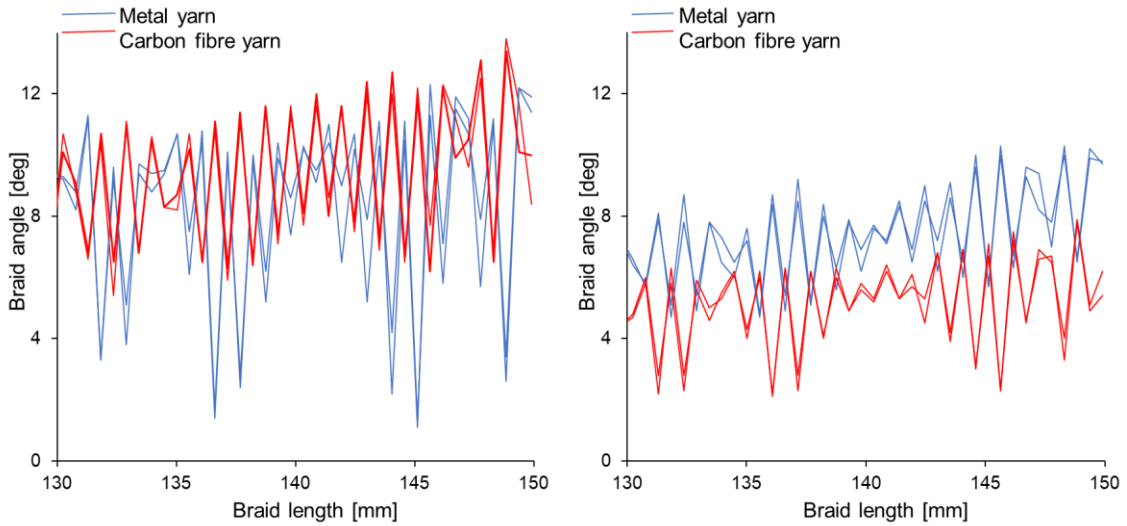

Figure 4-22 Plots of braid angle along failed configuration yarns. (Left) anti-clockwise yarns and (right) clockwise yarns.

The simulation suggests that the alternation of materials in both braider carrier directions appeared to result in an imbalance in the braid structure. Consider a metal wire going in one direction; the one-over-one under interlacement pattern caused that metal yarn to always interlace over another a metal wire running in the opposite direction.

Two separate contrasting braid angles are likely to be measured for both these two wires. In addition, the tendency of both the wires to resist bending and remain comparatively straight to the braiding take-up direction result in relatively low braid angles at that interlaced area. A similar response is likely to occur in the carbon fibre yarns although the carbon fibre yarn profile would depend on the yarns internal or external position within the braid and the level of restriction of the interlaced material to prevent deformation of the filaments. These four varied yarn responses, which were influenced by material and carrier

orientation, most likely resulted in braid instability. The contact point of the wire-wire interlacement, as well as the tendency of the wire yarns to align straight with the braiding direction, would likely exacerbate the shearing impact on the carbon fibre yarns, making this design unmanufacturable.

4.5.5.4 Yarn Undulation

The relative lengths of the yarns showed the degree of undulation within the braids, with longer lengths indicating greater undulation. It provided another way to evaluate and compare architectural differences between the two configurations (Table 4-1).

Table 4-1 Undulation of individual yarns for simulation braid configurations

Configuration	**Manufactured configuration**		**Failed configuration**
	Clockwise carrier path		
Yarn material (position)	**Relative length**	**Yarn material**	**Relative length**
Metal (1)	1.3%	Carbon fibre (1)	0.4%
Metal (2)	1.3%	Metal (2)	1.4%
Metal (3)	1.4%	Carbon fibre (3)	0.4%
Metal (4)	1.3%	Metal (4)	1.5%
	Anticlockwise carrier path		
Yarn material (position)	**Relative length**	**Yarn material**	**Relative length**
Carbon fibre (1)	0.8%	Metal (1)	1.2%
Carbon fibre (2)	0.8%	Carbon fibre (2)	0.9%
Carbon fibre (3)	0.8%	Metal (3)	1.2%
Carbon fibre (4)	0.8%	Carbon fibre (4)	0.9%

*Nominal braid lengths: Manufactured braid :38.03 mm, Failed braid 38.50 mm

The relative yarn length of the manufactured braid demonstrated repeatability and consistency in yarn length, with the only difference being material type. Metal wire and carbon fibre lengths were 1.3 % and 0.8 % longer than braided construction lengths, respectively.

Within the unsuccessful configuration, four distinct yarn lengths were determined. The length of each yarn correlated with material and carrier direction, mirroring the braid angles deviations previously discussed. The relative lengths of the metal wire components in the clockwise and

anticlockwise direction were 1.5% and 1.2%, whereas the relative length of the carbon fibre was 0.4 % and 0.9%.

Comparing the relative lengths of both configurations, the clockwise carbon fibre yarns were noticeably shorter. This reduced length would suggest that these yarns would be pulled more by the braider take-up more than the other yarns within the braid. When combined with metal wire pinching, it is probable that significant damage to these two yarns would occur during braiding, potentially resulting in braid failure.

4.6 Discussion

This chapter demonstrated a Finite Element (FE) method for simulating virtual braiding of hybrid multi-material micro-braids. It demonstrated that various material properties, such as metal wires and carbon fibre tow, may be accurately replicated by a combination of single filament and multi-filament virtual yarns. The model provided a tool for manufacturing and configuration comparison, as well as the ability for braid structure evaluation prior to actual braid fabrication. Most importantly it captures the influence of the manufacturing dynamics associated the hybrid material interlacement. It allowed for the investigation of specific combinations that proved unmanufacturable. It captured the inhomogeneous distribution of the hybrid materials at the interlacement or braid point.

Overall virtual braid composition and geometric representation were comparable to the real as-manufactured braid. However, discrepancies in certain aspects could be attributed to friction and tension differences experienced in the real braid and those assigned the in simulation. Another contributing factor was experimental measurement error, as both braid thickness and braid angle measurements are dependent on tension consistency along the braid. In practise, this was difficult to achieve due to carrier spring relaxation and the inherent tendency of a braid structure to contract and expand.

Another notable issue was the difficulty in adequately representing the splaying, dispersion, and filamentation of the carbon fibre filaments. It was evident that using only seven simulated filaments to represent a 1000 filament tow resulted in inaccuracy, but a balance of computational time and precision was

necessary, therefore, certain features were purposely omitted. It was accepted, for example, that frictional effects between filaments in a carbon fibre tow and the yarn-yarn contacts were not accurately represented. The effects of yarn material slippage within the interlacement, as well as material damage due to convergence, were also not considered. Further work could address these limitations as well as investigate the effects of twisting of both the constructed braid and the individual yarns. Despite the limitations the simulations captured the real variations in braid angle along the different material types and provided a comparable geometry of the inhomogeneous distribution of the fibre yarns. It also visually represented the actual braiding motion of the yarns and the convergence dynamics at the braid point.

The output from the simulation indicated that balance and symmetry are important for successful braiding and determined by the material placement within the carriers. Interlacement stability was especially important when using carbon fibre tow since the narrow profile of the wire in the braid dominated the braid profile, determining pinch points and undulation along the braid. A lack of symmetry generally caused to shearing of the carbon fibre by the metal.

Contrasting material combinations, such as metal and carbon fibres, also resulted in different internal and external braid architectures depending on the braider configuration. This had a significant impact on braid stability and formability since the ability or inability to rearrange, particularly for carbon fibre, influenced the likelihood of breakage. This reliance on braid symmetry and stability has an effect on a braid's ability to be tufted. Excessive asymmetry either limits production or results in a kinked braid that cannot pass through a tufting needle without snagging.

This model might be expanded to examine the material properties of the braid structure and align them to the desired final composite specifications and multi-functional capabilities. By focusing on braid construction simulation first, as opposed to manufacturing, a greater awareness of braid quality can be created and a balance between the mechanical and functional properties can be made. This would enable the creation of a tufting thread that would realise full potential of multi-functional structures.

5 THREAD PROPERTIES

5.1 Overview

This chapter details the mechanical strength measurement and electrical resistance (ER) response of the hybrid micro-braids. These characteristics were compared to two commercially available tufting threads to establish the suitability of a multi-material hybrid micro-braid as a tufting thread. The examined threads were:- a 4k carbon fibre thread comprising of four 1k carbon fibre twisted tows, a 2k carbon fibre thread comprising of two 1k carbon fibre twisted tows and a hybrid micro-braid comprising four 1k carbon fibre tows, and four copper wires. The linear densities of the threads were 268 tex, 140 tex and 414 tex, respectively. For further material details see section 3.2.1.

5.2 Tensile testing method

Breaking tenacity is defined as the ratio of breaking force to yarn linear density, and is a prominent metric used to assess the strength of a yarn material as well as for comparison and validation [232]. There appear to be no specific standards for tenacity or tensile testing of hybrid yarns in the literature; typically, the tensile strength of a dry yarn is often utilised to identify qualities and effects of damage [107, 200, 233–235]. According to research into yarn tenacity, test parameters such as gauge length and crosshead speed all influence tensile performance [216, 232, 236]. It is widely acknowledged that increasing gauge length increases the likelihood of encountering defects in a sample. The presence of a fault in the yarn causes the localization of stress which initiates

the rupture process [232]. As a result, the decrease in strength of a material with increasing test length is caused by the presence of a fault distribution of varying magnitude. Studies of tenacity in yarns also show that rate of testing also influences measurements. Generally, higher tenacity values are recorded with increasing crosshead speed [232]. The literature indicates that the mechanism of failure changes as a result of strain rate and that maximum tenacity occurs at an optimum extension rate [237]. At high rates of extension an increase in fibre rupture occurs indicating that a greater number of fibres contribute to the breaking load. Beyond this optimum extension rate the literature suggests that the resulting drop in tenacity is caused by the lack of time for the fibres to realign. At slower extension rate slippage of fibres within the yarn has been identified as the dominating failure mode with a reduction in fibre rupture [232, 238].

The research in this thesis tested tenacity according to BS EN ISO 2062:2009 [239]. Though this ISO standard specifies a method for detecting elongation at break, the standard states that measuring elongation with capstan clamps is inaccurate and is discouraged [239]. Measuring elongation is likewise discouraged in other standards relevant to evaluating yarn types, as the elongation can only be achieved using an extensometer that frequently results in specimen damage [240]. It has been demonstrated, however, that elongation at break may be measured using crosshead displacement for fine metal wires less than 1 mm in diameter [241]. Given the hybrid nature of the generated braid, elongation values are provided for completeness, though consideration must be given to the extent of their reliability. The extension was measured by grip displacement measured using a high-speed video.

5.3 Experimental procedure

The samples were tested using Shimadzu mechanical radiused clamps on a Shimadzu AGS-XSSm-DAL-10 kN testing machine using a 1 kN load cell as shown in Figure 5-1. Because the minimum length of yarn required to wrap around the two capstan grips was 320 mm, the grips were separated by 180 mm and the distance between the base was measured with a ruler. A 500 mm glass thread was also used to confirm gauge length. Using the pre-settings on

the testing machine, the return position of the grip was fixed, ensuring that the grips returned to the same 180 mm extension point after each test.

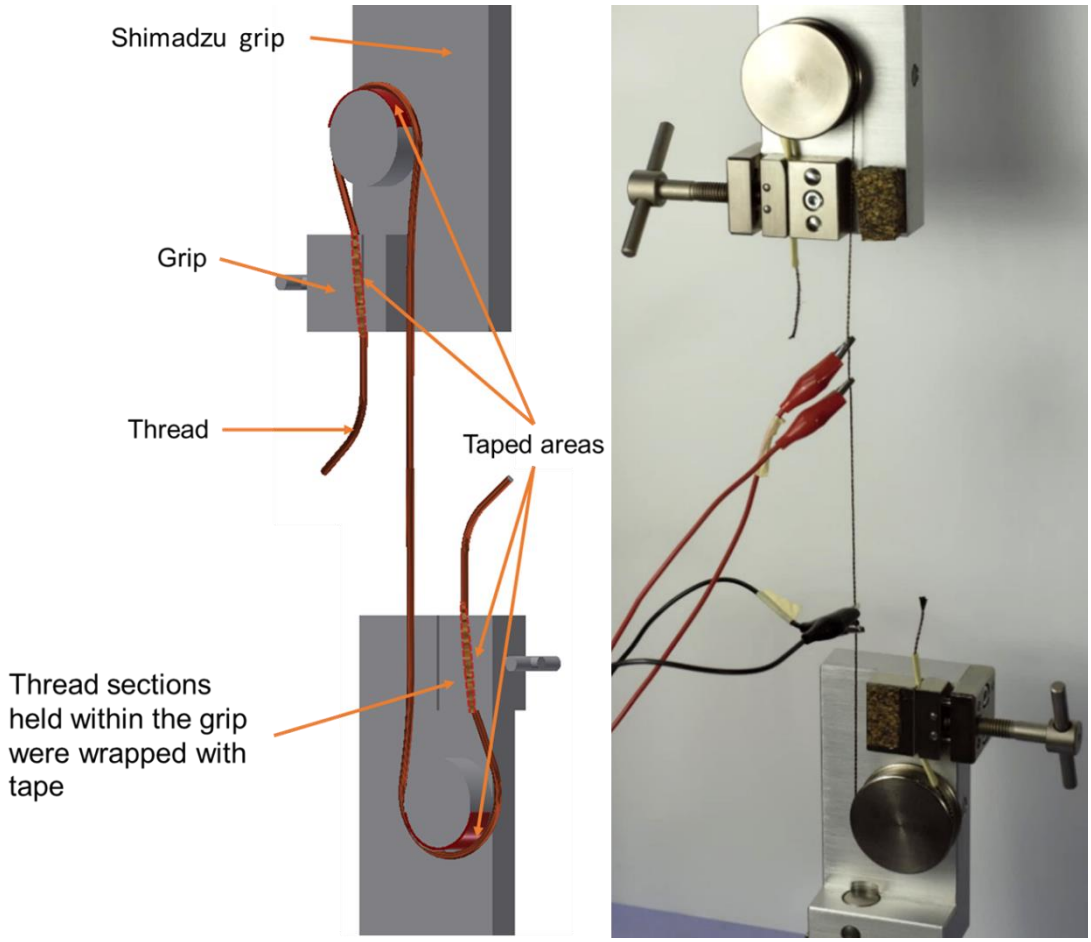

Figure 5-1 Tensile testing rig.

To prevent slippage and breakage of the threads in the grips during testing, the ends of the samples were taped with masking tape. This necessitated measuring the distance between the tapes at 500 mm, which provided additional confirmation of gauge length. This tape was also placed around the barrel of the grips to insulate the threads from the metal parts of the grips. Samples with a gauge length of 500 ± 2 mm were examined under a constant extension rate of 250 mm/min. To accommodate the recording of the ER during testing, an alternative rate of extension of 25 mm/min was used. Within the ranges utilised to measure yarn linear density as prescribed by BS 7658-2: 1993, a pre-tension of 4 cN/tex was set [242].The pre-tensions ranges were from 1.1 – 1.6 N for the 4K yarn, 0.5 – 0.8 N for the 2K yarn and 2.1 – 3.2 N for the hybrid braid. All tests were undertaken using dry threads without impregnation with any matrix material.

A four-wire Keithley 2100 digital multimeter (MM) integrated with a computer was used to record the ER. The electrode wires from the MM were attached using serrated clips as shown in Figure 5-1. The use of the four-wire method reduces measurement error by eliminating the voltage drop caused by the leads. This error is more significant when measuring resistance, as the current loop is affected by the lead resistance. The four-wire method as described comprises a set of “source” leads, or terminals that introduce a constant current supply while measuring the voltage input via a separate set of “sense” leads. As the voltmeter or “sense” leads have a high input impedance there is negligible current flowing through them to cause voltage build-up and affect the “sense” measurement. Data acquisition was achieved using National Instruments™ LabVIEW software, which synchronised the recording from the MM with the Shimadzu universal testing machine using a National Instruments™ analogue reader. The MM has a six-digit display and sampling rate capacity of 20 readings per second, however, it was not possible to achieve this reading capacity as the LabVIEW software restricted measurements to one reading per second. At a crosshead speed of 250 mm/min, as defined by the standard, the rate of recording the MM measurements was insufficient to capture enough ER measurements before the threads broke. Therefore, the ER testing was undertaken at a slower crosshead speed of 25 mm/min. The ER response was presented as the fraction change or normalised resistance ($\Delta R/R_0$), which is the difference between the instantaneous resistance (R) value and initial resistance (R_0) over time. An assessment of the effect of the crosshead speed and the serrated MM clips on the threads was undertaken to determine if any change in failure mode was observed.

5.4 Results and observations

5.4.1 Tensile strength

Initial tests with the attached MM were carried out at 250 mm/min rate of extension and resulted in breaking forces of 240 ± 17 N, 109 ± 10 N, and 94 ± 8 N for the 4k and 2k carbon fibre, and copper–carbon fibre hybrid braid threads respectively. Figure 5-2 details force elongation profiles of the threads at 250 mm/min. Table 5-1 shows the mean breaking force, extension at break and the

breaking tenacity of the respective threads at 250 mm/min testing speed along with the breaking force at 25 mm/min.

Table 5-1 Properties of tufting threads tested under constant rate of extension

	Mean breaking force* 250 mm/min	**Mean breaking force* 25 mm/min**	**Extension at break**	**Elongation at break**	**Linear density**	**Breaking tenacity**
	[N]	[N]	[mm]	[%]	[tex]	[cN/tex]
4k carbon fibre thread	240.1±6.9%	209.9±6%	6.1.±8.6.%	1.2.±0.09	268	90
2k carbon fibre thread	109.2.±8.7%	103.4±12%	4.98.±2.4%	1.0.±0.02	140	78
Cu–carbon fibre hybrid braid	93.6.±8.6%	87.1±9%	8.3.±7.4%	1.6.±0.07	414	22

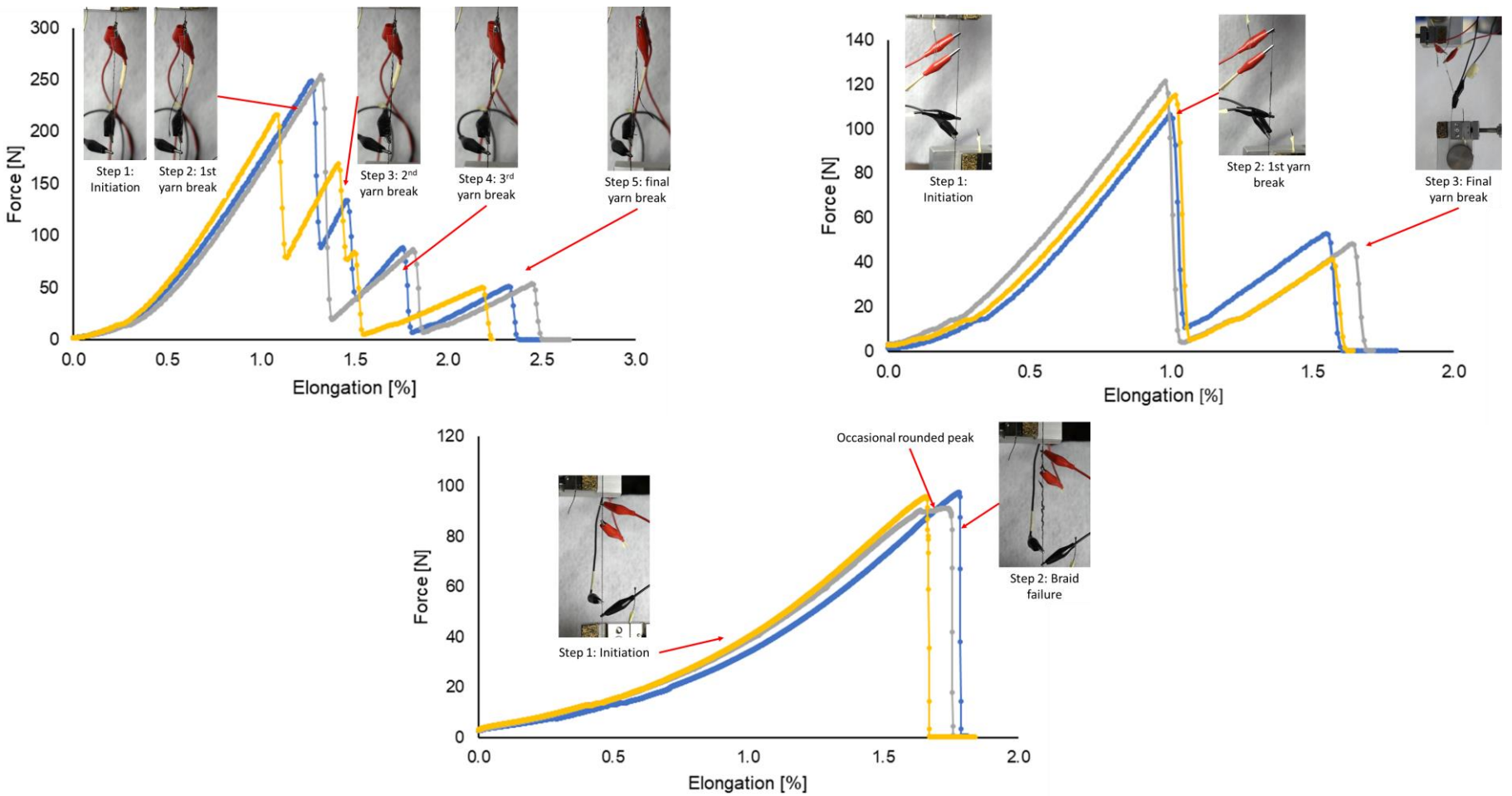

Figure 5-2 Force vs elongation profiles at 250 mm/min extension, (top-left) 4k carbon fibre thread, (top-right) 2k carbon fibre thread and (bottom) copper–carbon fibre hybrid micro-braid.

The failure mechanism of the 4k and 2k carbon fibre threads was discovered to be a progressive failure of each individually twisted 1k carbon fibre tow. A four-step failure profile was seen in the case of the 4k thread, whereas a two-step failure was recorded in the case of the 2k carbon fibre thread. Once broken, the tows of these threads unwound along the length of the unbroken sections and clustered towards the bottom grips. The 4k thread showed some continuous connection and slippage of the fibres despite the breakage of the final carbon fibres. The sequential failure of each individual yarn in the 4k and 2k threads could be due to the yarns not being under uniform tension due to their twisted profiles and the fact that each yarn is not fully integrated in the thread. The fractured thread was observed as a splayed thread with some of the previously broken yarns wrapped around it. The copper–carbon fibre hybrid braid generally failed in a single sharp step, observed as a sudden sharp drop in the profile.

Testing at 25 mm/min without clips, the force to break measurements were 251 ± 10 N, 132 ± 4 N, and 105 ± 2 N for the respective threads. Both commercial braids failed similarly at both testing rates with sequential failure of each individual carbon fibre tow. As expected, an increase in the force to break was recorded when the braids were examined without the MM clips, compared to both the higher and lower extension rate with the clips for all threads (Figure 5-3). The effect of strain rate was consistent with previous research, with an increase in strain rate being accompanied by an increase in breaking force [216, 232, 236].

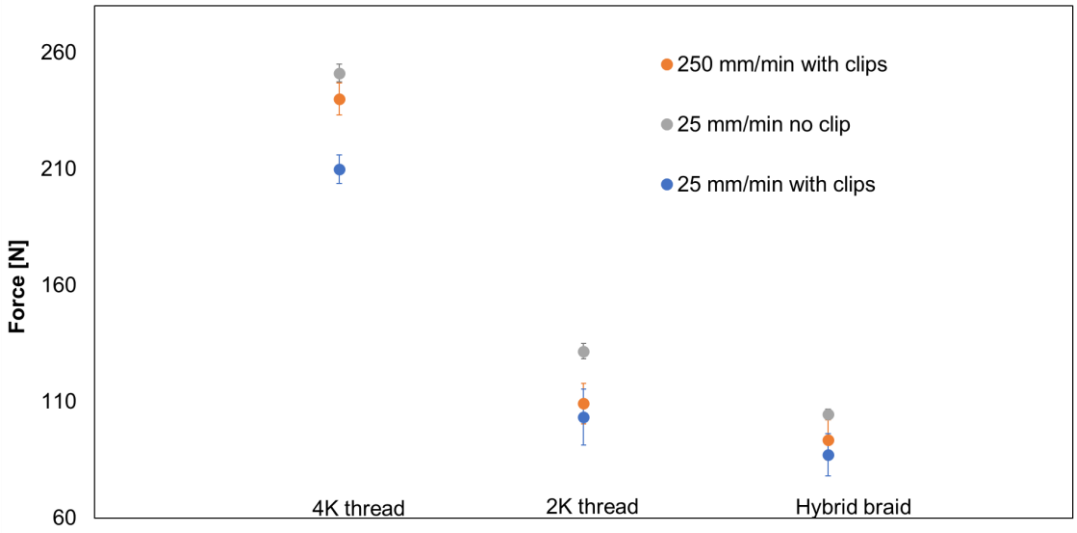

Figure 5-3 Force at break for 4k carbon fibre, 2k carbon fibre, and copper–carbon fibre hybrid threads.

The effect of MM clips dominated the failure profile of the hybrid braid. In contrast the twisted commercial threads failure profile was generally unaffected. The failure profile of the hybrid braid produced a less consistent and more complex failure profile comprising multiple drops (Figure 5-4). This could be because the clips were not uniformly attached to each of the 8 yarns of the braid. At 25 mm/min the breaking forces were 210 ± 13 N (4k thread), 103 ± 12 N (2k carbon fibre thread) and 87 ± 8 N (Cu/C hybrid braid). The mechanical properties of each thread under different testing parameters are provided in Table 5-2. Whilst the commercial 4k and 2k yarns failed in a relatively consistent manner, the behaviour of the copper-carbon braided yarn showed some deviation from the sharp and sudden fall in load to a more gradual rounded curve. This difference between the commercial thread and the braided thread could be ascribed to its unique structural interlaced features. Realignment and movement of the yarns to the jam angle and occasional slippage of wires or carbon fibres are likely to take place as the yam was extended.

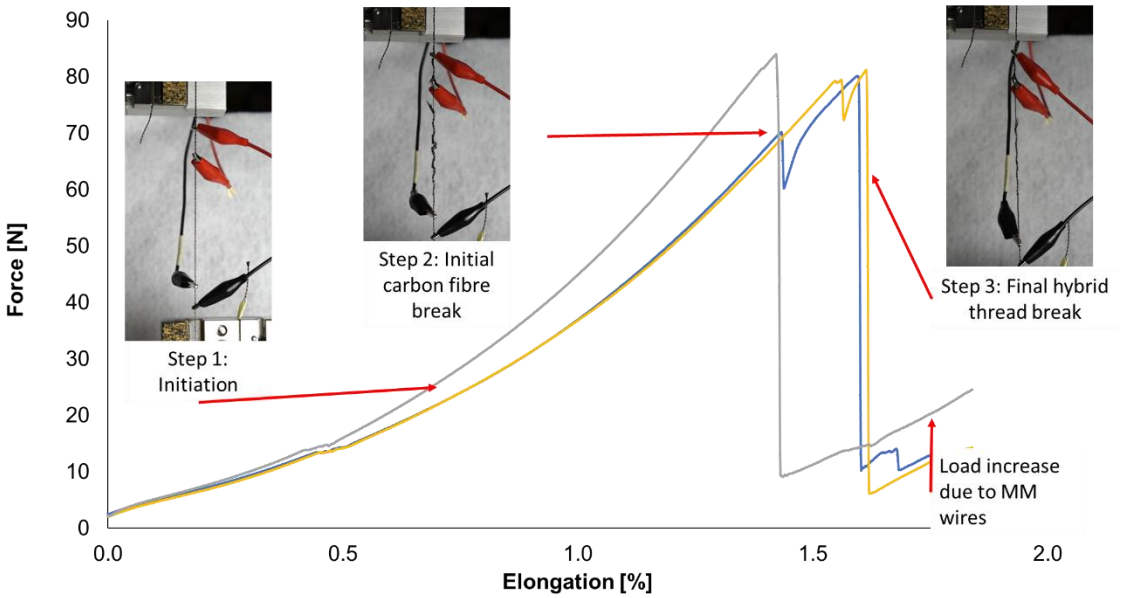

Figure 5-4 Force vs elongation profile of copper–carbon fibre hybrid braid at 25 mm/min extension rate with MM clips.

Table 5-2 Force at break, extension, and elongation at break for the 4k carbon fibre, 2k carbon fibre and copper–carbon fibre hybrid threads

250 mm/min with clips	**4k carbon fibre thread**	**2k carbon fibre thread**	**Cu- carbon fibre hybrid braid**
Breaking force [N]	240	10	94
CV [%]	7	9	9
Extension at break [mm]	6.13	4.98	8.34
CV [%]	9	2	7
Elongation at break [%]	1.23	1.00	1.67
CV [%]	9	2	7
25 mm/min with clips	**4k carbon fibre thread**	**2k carbon fibre thread**	**Cu- carbon fibre hybrid braid**
Breaking force [N]	210	103	87
CV [%]	6	12	9
Extension at break [mm]	6.07	8.82	6.87
CV [%]	9	7	15
Elongation at break [%]	1.21	1.76	1.37
CV [%]	9	7	15
25 mm/min no clip	**4k carbon fibre thread**	**2k carbon fibre thread**	**Cu- carbon fibre hybrid braid**
Breaking force [N]	251	132	105
CV [%]	4	3	2
Extension at break [mm]	7.44	6.74	6.39
CV [%]	5	4	6
Elongation at break [%]	1.49	1.35	1.28
CV [%]	5	4	6

The force to break effects highlighted that the clips, due to their angular shape and ‘cutting’ action, adversely affected the threads. In the copper–carbon fibre hybrid braids, failure occurred in one step when tested without the MM clips (Figure 5-5), however, with the clips an erratic failure profile occurred (Figure 5-4). At the point of attachment, the angular profile of the clips caused fibre separation, crushing and, on occasion, breakage of the carbon fibre tow. The damage was most evident in the hybrid braids, where filamentation was also more noticeable. This damage caused the carbon fibre tow to fail first, followed closely by the copper, and is identified by the split peak on the force elongation profile. Attempts to capture this change in failure mode using high speed video failed due to the small aperture of the camera which obscured the field of view of the failure point along the braid.

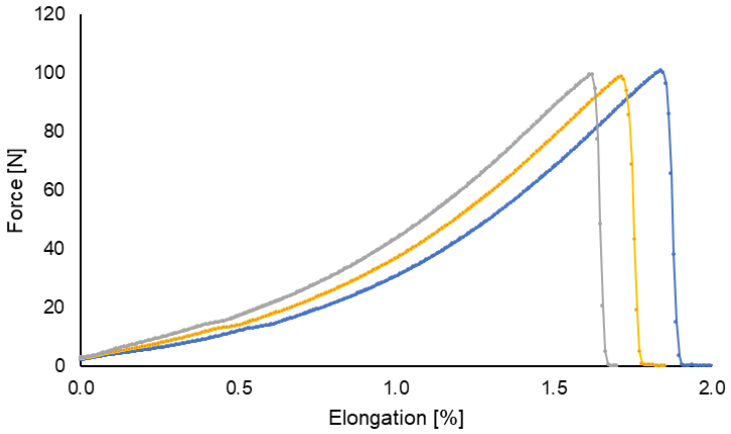

Figure 5-5 Force vs elongation profile of copper–carbon fibre hybrid micro-braid at 25 mm/min extension rate without MM clips.

The braids not failing between the MM clips generated the secondary peak in the tensile profile (Figure 5-4). The testing equipment was unable to detect the failure due to the added bulk of the clips and testing leads. As a result, the testing equipment continued to test despite thread failure.

The change in testing profile did not occur in the case of the commercial 4k and 2k carbon fibre twisted threads which were more resistant to damage inflicted by the MM clips. Their failure profiles, as shown in Figure 5-6, were consistent with the previous tests and have a characteristic stepped failure profile. The twisted nature of the commercial threads appeared to resist the crushing effect of the clips due to the consolidation of the carbon fibres. Although the clips did

cause thread degradation, the effect was less than that of the copper–carbon fibre hybrid thread.

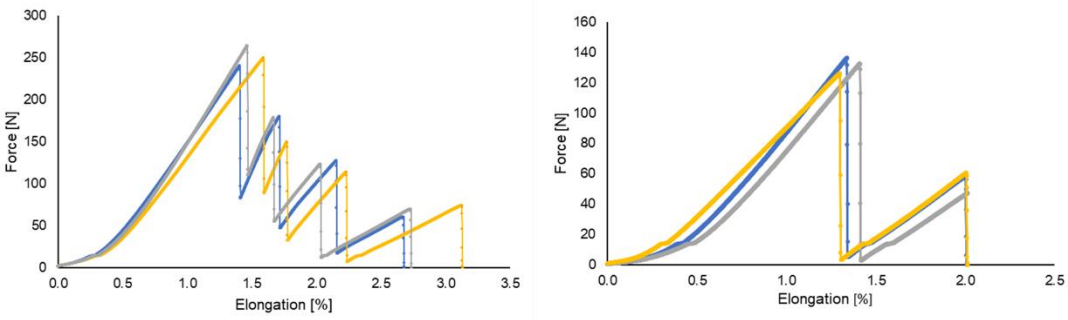

Figure 5-6 Force vs elongation profiles at 25 mm/min extension rate without MM attached, (left) 4k carbon fibre commercial thread and (right) 2k carbon fibre commercial thread.

Figure 5-7 shows images of each thread with the clips in place and after the clips were removed. The extent of thread damage is less visible on the 4k, and the 2k carbon fibre threads compared to the hybrid braid. The benefit of tufting threads possessing a twist has been previously stated. It contributes to a more homogeneous loading of the fibres along the thread as well as preventing damage during processing and manufacturing [36, 139].

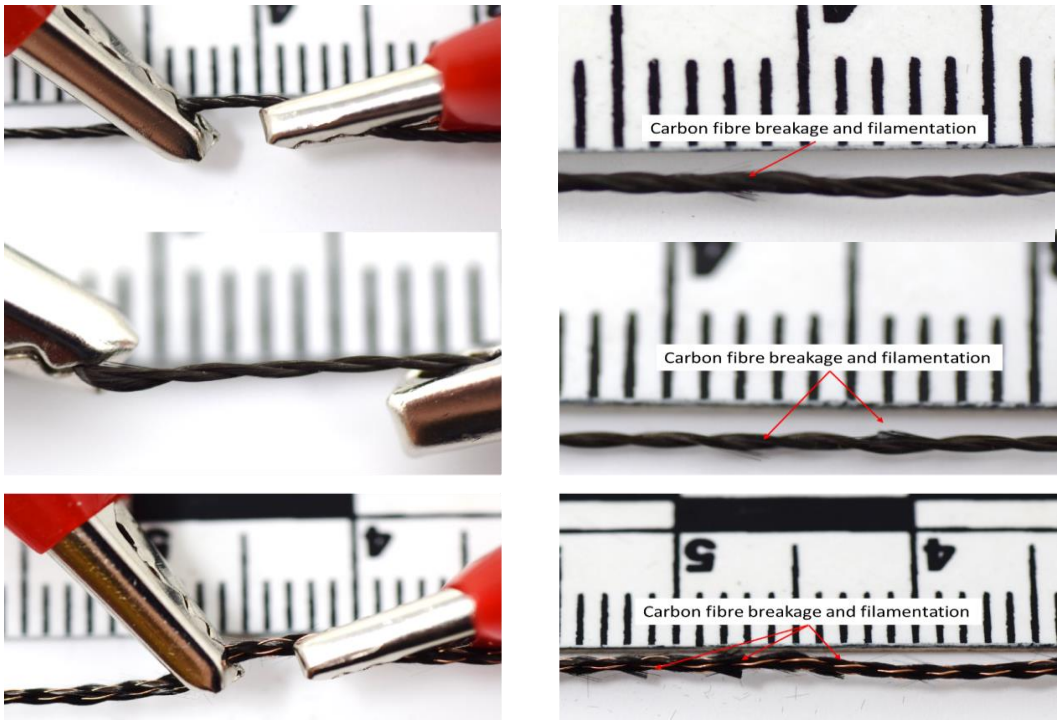

Figure 5-7 Effect of multimeter crocodile clips on tufting threads. (Top) 4k carbon fibre thread, (middle) 2k carbon fibre thread and, (bottom) copper–carbon fibre hybrid micro-

5.4.2 Electrical profile

The mean initial ER measurements of the 4k carbon fibre, 2k carbon fibre, and copper–carbon fibre hybrid threads were 9 ± 2 Ω, 12 ± 3 Ω and 0.2 ± 0.1 Ω when under pre-tension. Table 5-3.provides the mechanical and physical thread properties of each of the three threads. As expected, the metal wire components in the braided thread resulted in a much lower ER measurement compared to the commercial carbon fibre threads. The results showed that during testing the overall ER increased as damage increased. The maximum mean ER measurement for the commercial threads were 23 ± 5 Ω and, 25 ± 9 Ω for the 4k and 2k carbon fibre threads. Representative plots of load displacement and normalised ER response over time are presented in Figure 5-8, Figure 5-9 and Figure 5-10 Typical electrical resistance and failure profile of copper–carbon fibre hybrid micro-braid. On the left y-axis the blue line in each plot represents the load and on the right y-axis the orange line represents the normalised resistance. Time in seconds is on the x-axis.

Table 5-3 Physical and mechanical properties of threads

Material	**Carbon fibre yarn**	**Carbon fibre yarn**	**copper-carbon fibre hybrid braid**
Manufacturer [-]	Schappe Techniques®	Schappe Techniques®	[-]
Type [-]	Tenax® Carbon HTA40	Tenax® Carbon HTA40	[-]
Filament count [k]	2 x 1000	4 x 1000	4 x 1000 4 x wire
Linear density [g/km, tex]	140 (2 x 67)	268 (4 x 67)	414 [-]
Diameter [mm]	0.32	0.45	0.88
Cross sectional area [mm^2]	0.08	0.16	0.6
Mean breaking force* 250 mm/min [N]	240.1±6.9%	109.2.±8.7%	93.6.±8.6%
Breaking tenacity [cN/tex]	90	78	22
Extension at break [mm]	6.1.±8.6.%	4.98.±2.4%	8.3.±7.4%
Elongation at break [%]	1.2.±0.09	1.0.±0.02	1.6.±0.07
Resistivity [Ω.m]	106 x 10^{-3}	106 x 10^{-3}	1.66x10-10

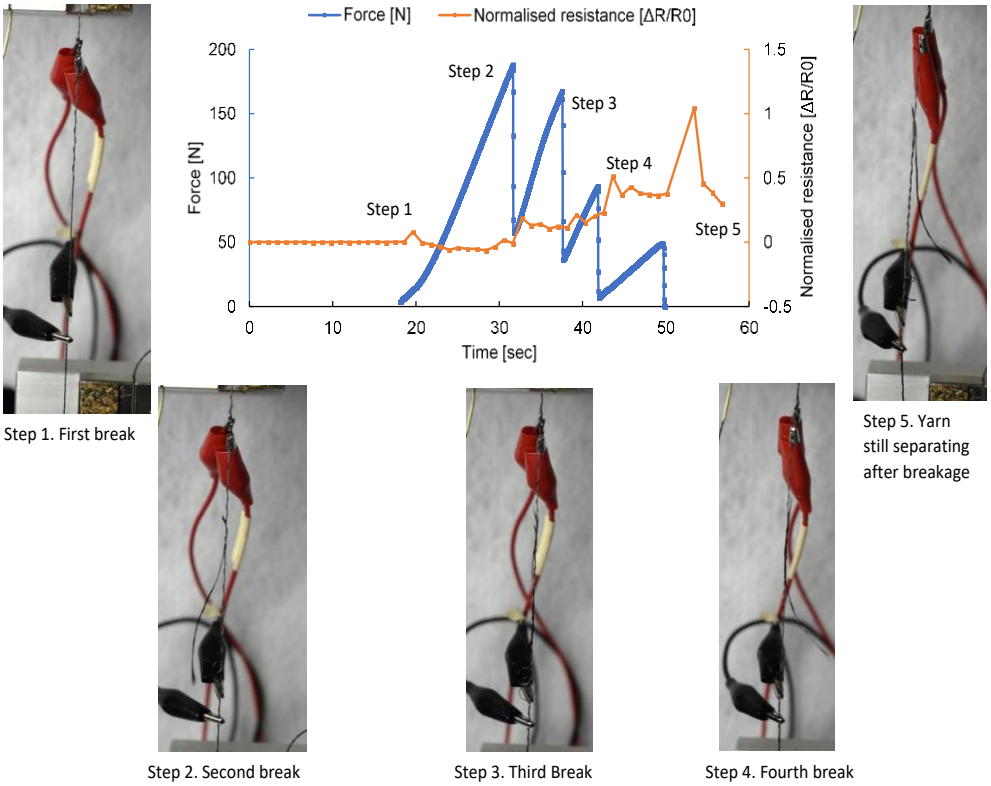

Figure 5-8 Typical electrical resistance and failure profile of 4k carbon fibre commercial thread.

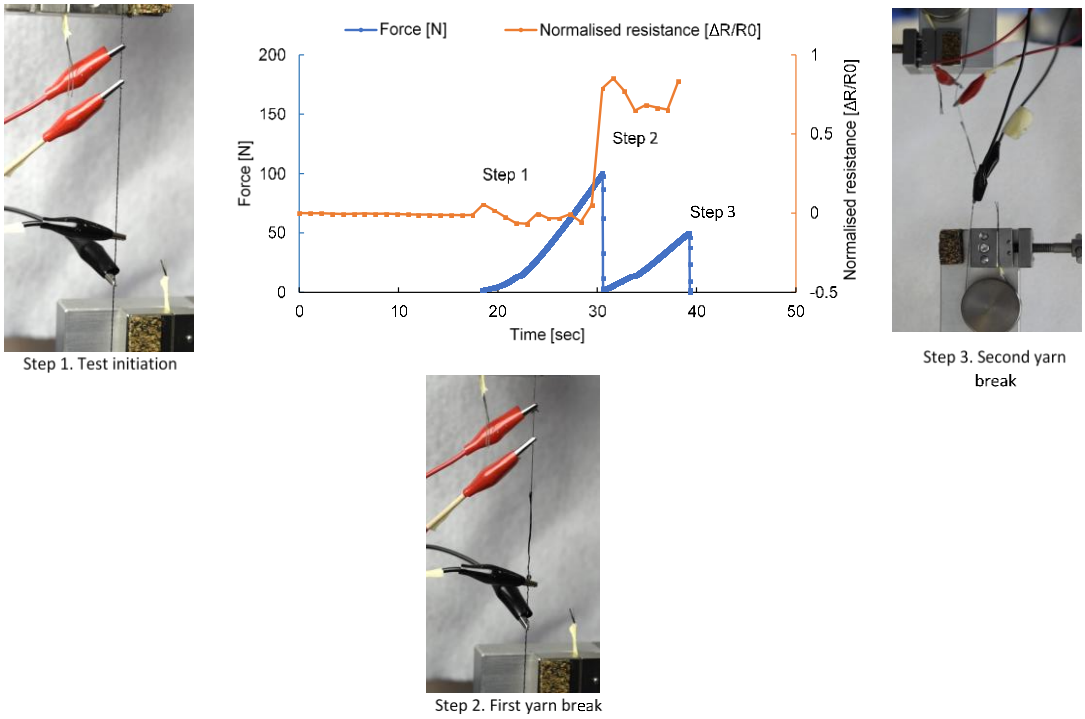

Figure 5-9 Typical electrical resistance and failure profile of 2k carbon fibre commercial thread.

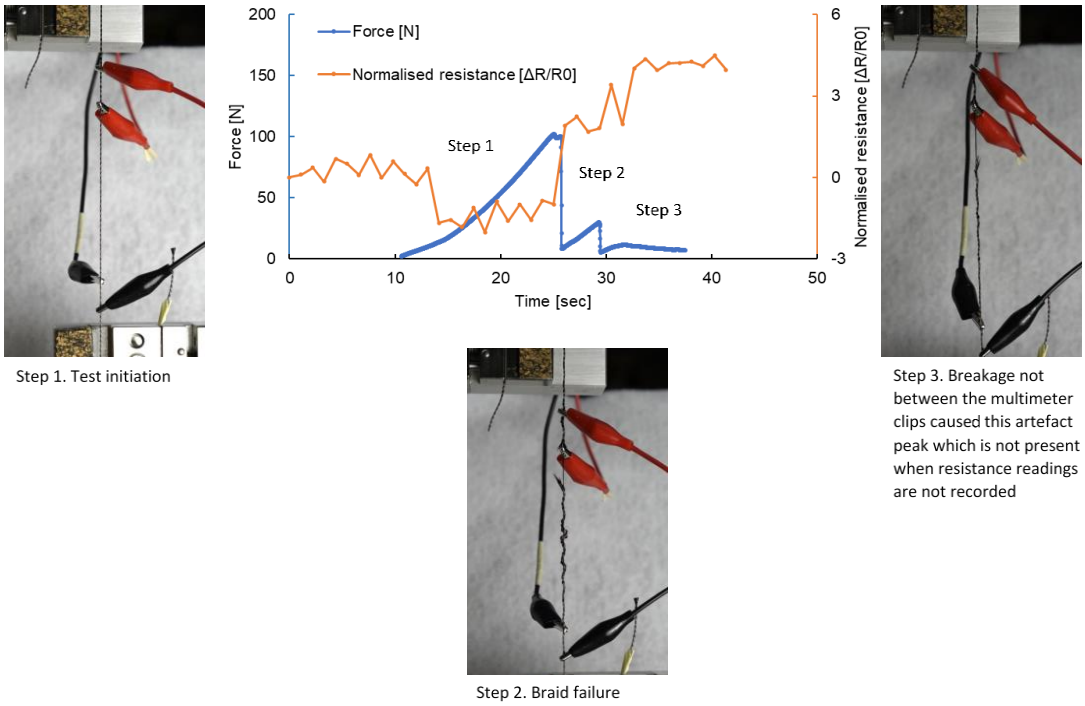

Figure 5-10 Typical electrical resistance and failure profile of copper–carbon fibre hybrid micro-braid.

A mean maximum ER of 9 ± 7 Ω was recorded for the hybrid braid. However, this does not represent a true reflection of the condition of braid after testing. The braid repeatedly broke outside of the MM monitored area therefore, despite the thread being completely broken between the grips, the MM connection was still in place resulting in an ER measurement. A more accurate ER reading for a completely broken thread would have been an ER measurement tending to infinity, represented as an overload on the MM. Irrespective of this limitation, testing the sensing capability of the hybrid braid was still beneficial as the ER still altered as the braid condition degraded.

Overall, the ER response for all the threads showed an increase in ER due to the induced strain. In addition, a slight decrease in ER occurred during the initial loading of the thread, which is consistent to previously reported studies and was attributed to the alignment of the carbon fibres [9, 243]. This increase could also be attributed to the further consolidation of the thread due to the applied load.

The normalised ER response of the 4k carbon fibre commercial thread, (Figure 5-8), shows a gradual increase as each individual carbon fibre tow breaks. The response is not as abrupt as the sharp load drops previously describe in Section 5.4.1 but at each tow failure a stepped increase is observed. As the 4k

carbon fibre thread breaks the broken thread untwists but remains loosely wrapped around the unbroken thread thereby maintaining an electrical connection and preventing a larger change in ER. A similar phenomenon occurred in the 2k carbon fibre thread but to a lesser degree. The ultimate break of the remaining carbon fibre tow of the 4k carbon fibre thread often manifested in a sharp break followed by the gradual pull-out of the carbon fibres. A decrease in ER response was recorded due to the testing machine returning to the set origin and re-establishing an electrical connection between the previously disconnected carbon fibre tows. This did not happen when testing the 2k carbon fibre thread (Figure 5-9). The failure of the 2k carbon fibre thread involved the breaking of the first yarn component, which then wrapped around the remaining intact yarn until complete disconnection occurred.

5.4.3 Discussion

This initial assessment of the copper–carbon fibre hybrid braid and its comparison to two commercially available threads was used to determine its suitability as a tufting thread. The characterisation of each thread established their response to tensile loading and provided insight into their failure modes and deformation characteristics. It provided some failure predictability and an understanding of threads ability to withstand the processes of tufting. The single point failure of the braid could be considered beneficial in the context of a sensor due to the likelihood of a large contrast in ER measurements. Conversely, the sequential non-catastrophic failure of the commercial threads did provide a gradual warning system, although this could potentially be misinterpreted or result in a lack of sensitivity.

Although the method of connecting the MM clips to the threads as presented in this study inflicted damage; this test does emphasize a potential in-process use for the ER measurement for in-line monitoring of threads to determine thread condition. An adaptation of the MM connection method would enable the continual assessment of the thread for use as a warning system to prevent miss-tufts or machinery damage due to entanglement of broken yarns.

5.5 Publications

The work carried out in this chapter led to the following publication:

O’Keeffe, C., Pickard, L.R., Cao, J., Allegri, G., Partridge, I. K., and Ivanov, D. S. (2021) Multi-material braids for multifunctional laminates: conductive through-thickness reinforcement. Functional Composite Materials Vol 2:5 (1) DOI: 10.1186/s42252-021-00018-0

6 MECHANICAL PROPERTIES AND CRACK SENSING CAPABILITY

6.1 Overview

This chapter details the influence of the thread microstructure on the mechanical properties and electrical resistance (ER) self-sensing capabilities for the commercial tufting thread, and the hybrid micro-braid thread. It also explores the failure mechanisms of single tuft coupons, array of tufts and the ER profiles associated with those failures. The mechanical characterisation of representative specimens was undertaken via "single tuft" pull-off experiments and DCB tests. Direct performance comparisons are established between untufted specimens and coupons reinforced through the thickness with a commercial tufting thread or with hybrid micro-braid thread, proving the effectiveness of the latter.

6.2 Single tuft test

6.2.1 Specimen manufacture and test method

To examine the failure mechanisms and the forces exerted by the tuft within a coupon, pre-delaminated single-tufted coupons were tested under mode I conditions. Single tuft coupons were manufactured from preforms consisting of

four layers of Formax FCIM359-PB biaxial non-crimp carbon fibre fabric (NCF) containing 24k HTS carbon fibre tows with a layup of $[0/90)]_{2S}$, held together by non-structural stitching. A 20μm thick layer of release film separated each coupon into two halves, which were only held together by a single tuft inserted in the coupon's centre. A copper–carbon fibre hybrid micro-braid thread as described in Table 5-1 was used as the tufting thread. Tufting was undertaken using an adapted 3D printing chassis, with NEMA 23 stepper motors and an Ardunio Mega 2560 controller. Tufts were inserted vertically using a Schmetz EP 11 Nm 230 tufting needle with a 1.0 mm diameter eye. Airex® R6380 foam 25 mm thick was used as backing, covered with Wrightlen PTFE to prevent contamination and aid in separating the preform from the foam layer. No tension was applied to the micro-braid thread during the tufting procedure. Nine rows of nine tufts were inserted into the preforms as shown in Figure 6-1. Two tufting profiles were examined. One preform was tufted with the copper–carbon fibre hybrid micro-braid thread with average loop lengths of 6.5 mm ± 0.6 mm (CV 8%), while the other was tufted with a minimum loop length that was just visible on the underside of the coupon (Figure 6-1).

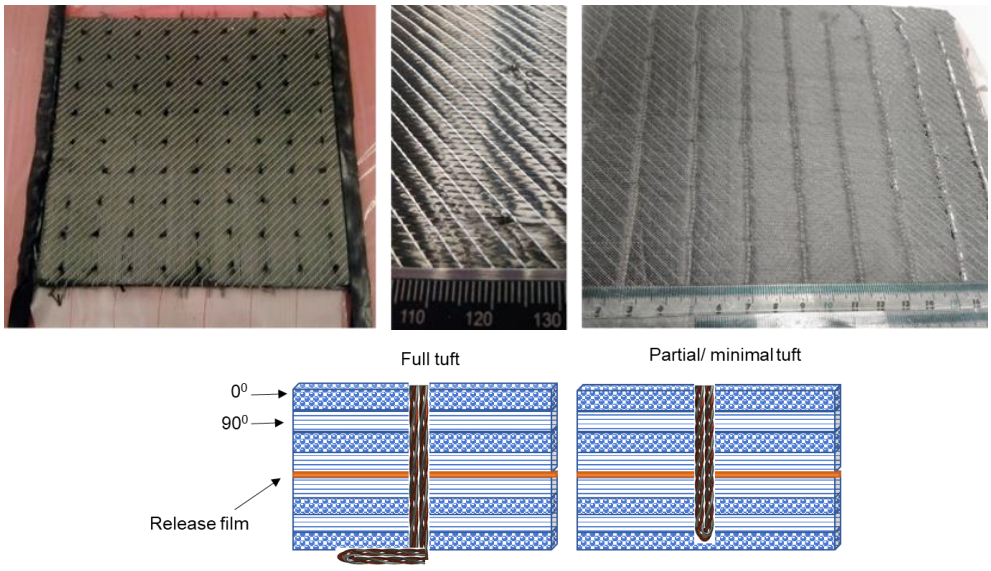

Figure 6-1 (Left) tufted preform for single tufted coupons, (middle) tuft with minimum sized loop, and (right) cured panel. Schematic representation of ply layup and fulla nd partical tufts.

Both preforms were resin infused under vacuum, using a double bagged system with Prime 27™ epoxy, at room temperature and cured at 80°C for 2 hours. Coupons with dimensions of 10 mm x 10 mm x 4 mm were cut from each panel,

each comprising a single copper–carbon fibre hybrid micro-braid tuft with a cross-sectional area of 1.30 mm^2 (equivalent to areal density of 0.003 %). All the coupons in which the tuft was not centrally placed were discarded. The average maximum thickness of each coupon was 4.20 mm ± 0.13 mm. It was evident that the presence of the tufts affected the thickness uniformity on the surface of the coupon. This also depended on the positioning of the loops on the underside. In general, the coupons appeared to have a variable thickness profile, with the highest point at the central tuft location and progressive tapering along the direction of the underside loops, as illustrated in Figure 6-2.

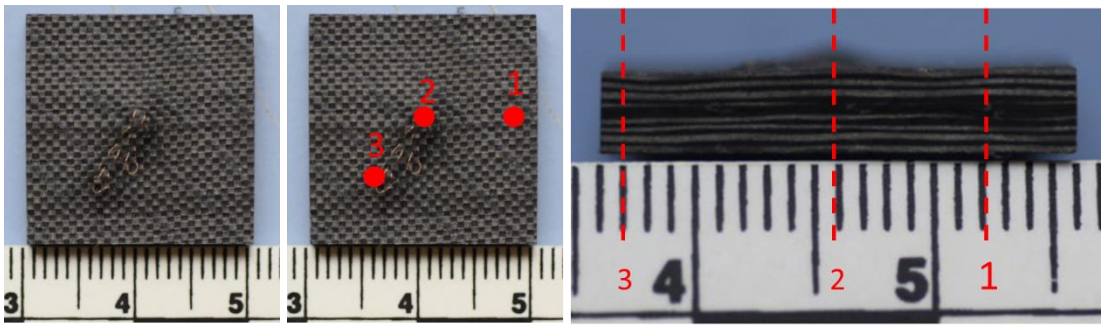

Figure 6-2 (Left) Looped single tufted coupon, (middle) photo indicating measured areas, and (right) profile photo indicating the relative positions of the thickness measurements, (1) thinnest section of tufted coupon, (2) tufted section and (3) looped section.

Table 6-1 details the dimensions of ten tufted coupons, indicating the variability in thickness. Measurements were taken at three points; the first at the edge (where no tuft was present), the second at the centre of the tuft and the third at the opposite edge, which contained the micro-braid thread length or loop. A variability of up to 22% was measured between the thinnest and thickest parts of the coupons examined.

Table 6-1 Coupon thickness measurements

	Position 1	**Position 2**	**Position 3**
	[mm]	[mm]	[mm]
Coupon 1	3.8	4.0	3.7
Coupon 2	3.5	4.3	3.4
Coupon 3	3.7	4.3	3.5
Coupon 4	3.5	4.1	3.4
Coupon 5	3.5	3.9	3.6
Coupon 6	3.8	4.0	3.7
Coupon 7	3.6	4.3	3.4
Coupon 8	3.6	4.3	3.4
Coupon 9	3.7	4.2	3.4
Coupon 10	3.7	4.5	3.6
Average	3.6	4.2	3.5
STDEV	0.1	0.2	0.1
CV [%]	3	4	4

The surface preparation of the coupons for ER measurement involved sandblasting the surface of both sides, washing with acetone, drying, and attaching tin coated copper electrical wires using Huntsman Araldite® 2014-2 epoxy adhesive to the top and bottom surfaces. Two types of terminal wire positioning were examined; one set were positioned centrally on the coupon and near to the tuft, while the other used electrodes located far from the tuft (Figure 6-3).

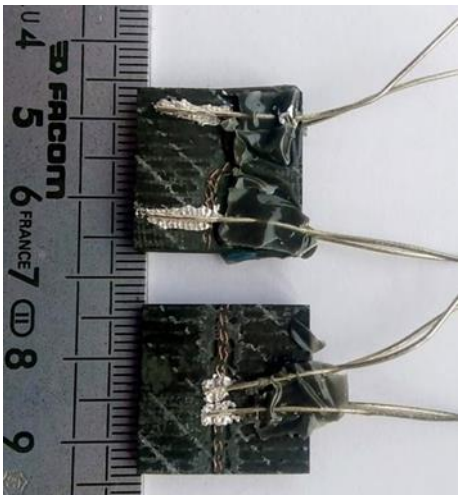

Figure 6-3 Single tuft coupons (top) wire electrode far from tuft positioning and (bottom) near tuft electrode positioning.

These two alternative configurations were tested to investigate the effect of the electrode positioning in terms of ER sensing capability. Silver paint was applied

to the surface of the wire electrodes, ensuring that the paint covered both the wires and the coupon surface, whilst not creating a short-circuit. A preliminary ER measurement was taken at this stage to ensure that good contact was made and correct for any short-circuiting errors. Once the silver paint was dry, the coupons were adhered to aluminium T attachments with epoxy adhesive, as shown in Figure 6-4.

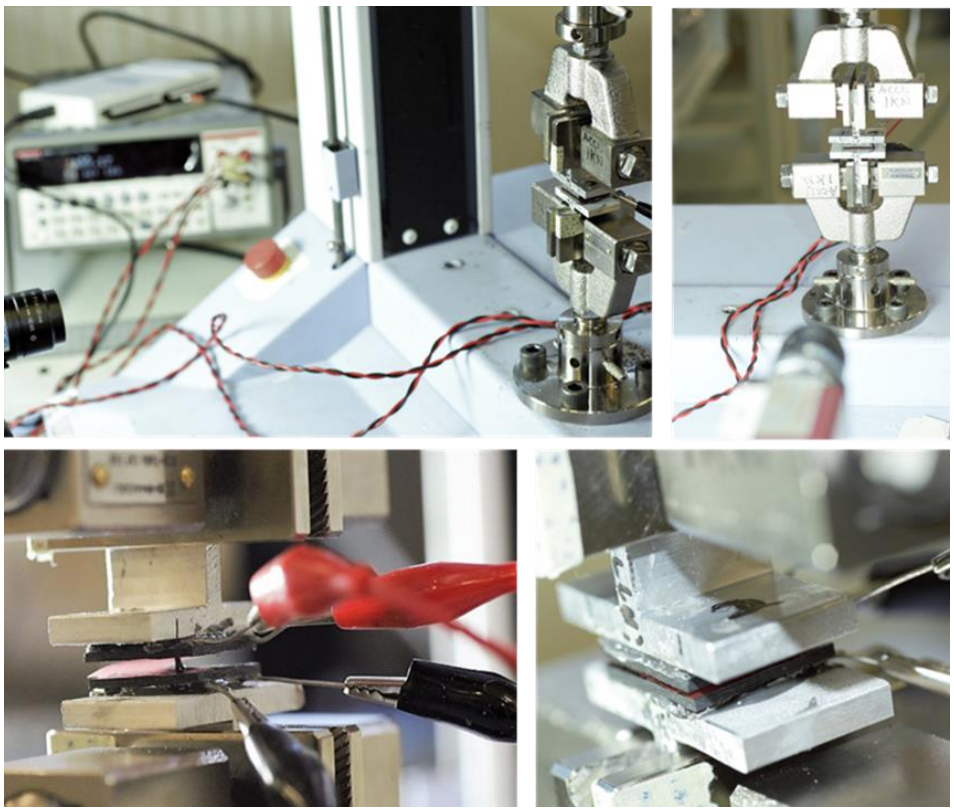

Figure 6-4 Single tuft testing experimental setup.

The coupons were tested under out-of-plane tension displacement control, at a crosshead speed of 0.25 mm/min in a Shimadzu universal testing machine. A Keithley four-wire multimeter (MM) was attached, such that the current applied through the source electrode was in the through-thickness (TT) direction. A digital video gauge was used to monitor the relative displacement of the testing fixtures. The output and data from the Shimadzu and the MM were compiled using a National Instruments™ analogue output and LabVIEW software.

6.2.2 Delamination profiles

Two sets of single tuft tests were undertaken in this study: one set examining a looped tuft and the other with a minimal loop. Figure 6-5 presents load vs. displacement curves for both categories of coupons. The mean maximum load

for the looped and minimal looped coupons was 286.7 N and 237.6 N, respectively. The failure profile is similar to that previously described in the literature where an average load of 258 N was reported in similar tensile test for coupons singly tufted with a 2k thread [244].

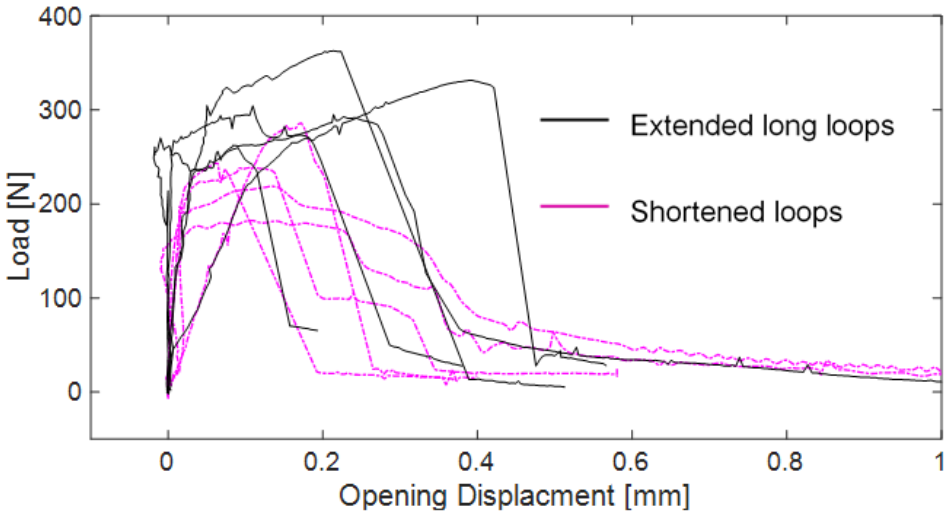

Figure 6-5 Load-displacement curves of delamination tests of single tufted coupons. Long looped coupons (solid black) and short-looped coupons (dotted pink).

Overall, three distinct load versus displacement profiles were observed for the two different coupon types. Representative responses for the Mode I single-tufted coupons are shown in Figure 6-6.

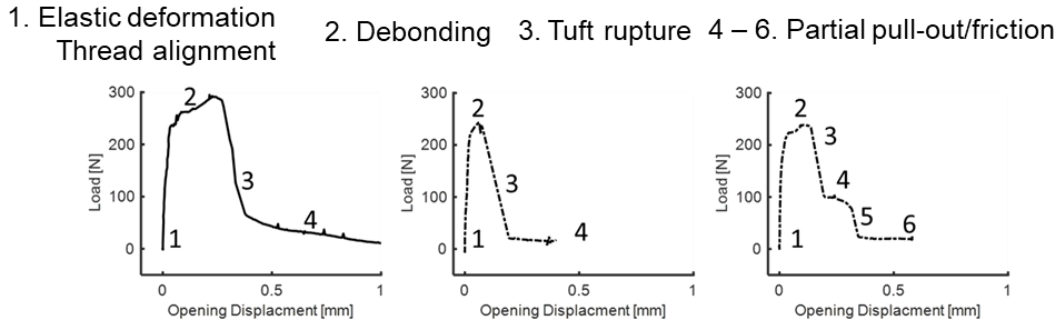

Figure 6-6 Representative load-displacement curves, (left) long-looped tuft 4-step response, (centre) minimalist-looped 4-step response and (right) 6-step response of Mode I delamination profiles.

In general, the long-looped tufted coupons failed in a more consistent sequence of events, which could be divided into four stages. Stage 1 comprised a linear profile up to a critical point, while stage 2 continued the upward trend but with a lower gradient. A rapid load drop occurred in stage 3, while the final stage 4

comprised of the gradual pull out of the tuft. In comparison, the minimal looped coupons failed in two different fashions.

Both of the associated responses, as for the long-looped tuft sample, initiated with a linear profile. After this first step, the minimal tuft either followed a four- or six-stage failure process. The four-stage response consisted of a plateau or a gradual reduction in load (stage 2), an abrupt load drop (stage 3), and then followed by gradual pull-out of the tuft (stage 4). The six-stage response consisted of a liner response (stage 1), a decrease in load or plateau (stage 2), two separate load drops with an intermittent plateau (steps 3 – 5) and then pull-out (step 6). Video assessment of the different coupons did not identify any obvious reason for the variability between the two different failure profiles of minimal looped specimens.

However, subsequent micrographic analysis of samples cut from the tested coupons revealed some variability in tuft profile, especially in terms of angle, and penetration depth. The micrographs also showed the characteristic curved profile of tufts, as well as resin-rich regions around the insertion point, which have also been reported in other studies [245]. Regarding tuft angle, it has been shown that a greater angle from the surface results in a greater volume of thread being inserted into the preform but that in comparison to loop length it has little effect on the laminate thickness [135]. Tuft angle can, however, influence the waviness of the preform fibres, the extent of compaction of the in-plane fibres that can locally increase compression but also decrease in-plane properties [35]. The degree of inadvertent tuft deviation has been reported to be dependent on the bending stiffness and compression limit of the tufting material. Copper wire is said to rotate due to preform compression, forcing preform fibres away rather than buckling [133]. The braided hybrid structure adds complexity by changing profile under compression and extension by varying the braid angle. Deviation can also occur during many stages of manufacturing, such as removing the tufted preform from the tufting support, preparing the preform for infusion, and infusion, but there is little else in the literature that addresses it further than to state that it can result in unexpectedly lower structural performance [133]. Intentionally angled tufts have some benefits if the load direction is known [23]. However, with respects to the research in this thesis the angle could negatively influence the sensing reliability.

As illustrated in Figure 6-7, some of the tufts with minimum loop lengths do extend beyond the tuft channel and through to the underside of the preform, whilst others remained flush to the preform surface. Although this might account for the difference between the two response profiles observed for the minimal-loop tufts, it does not explain the additional load drop experienced by the protruding minimal loop tufts in comparison to the long-looped ones.

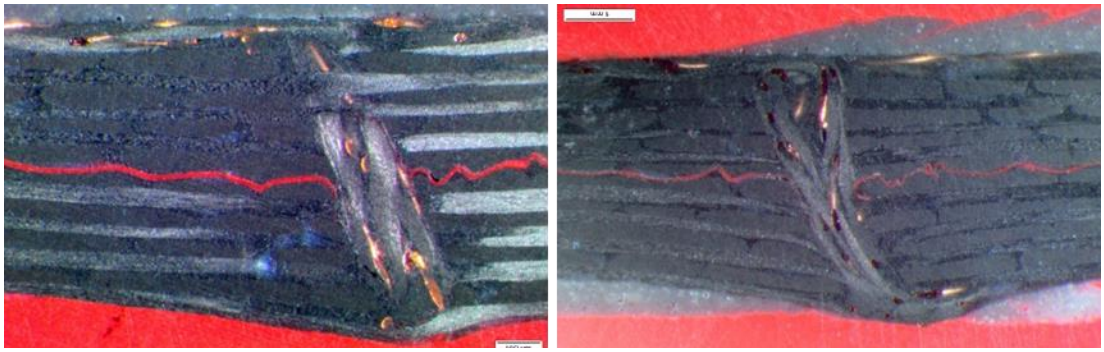

Figure 6-7 Microscopic images of minimalist tufts, (left) tuft remaining flush with the underside of preform and (right) tuft with protruding loop.

Overall observations indicated that the tufts all failed asymmetrically within one half of the coupon section and after elastic deformation. It was observed that tuft failure did not occur at the midline between the coupons. A schematic bridging mechanism is illustrated in Figure 6-8. Specifically, an asymmetric failure occurred and resulted in a tuft portion remaining within one of the two composite sub-laminates; this portion was subsequently pulled out. This asymmetric failure and pull-out occurred irrespective of the loop length.

The gradual pull-out of the ruptured tuft, shown in Figure 6-8 had significant consequences for the ER sensing capabilities of the tuft as discussed in Section 5.2.3. The presence of the asymmetric tuft also held the crack open. This was observed when the tests were interrupted, and the coupons removed from the testing machine. The broken tufts held the two halves of the coupon ajar and prevented the closing of the crack.

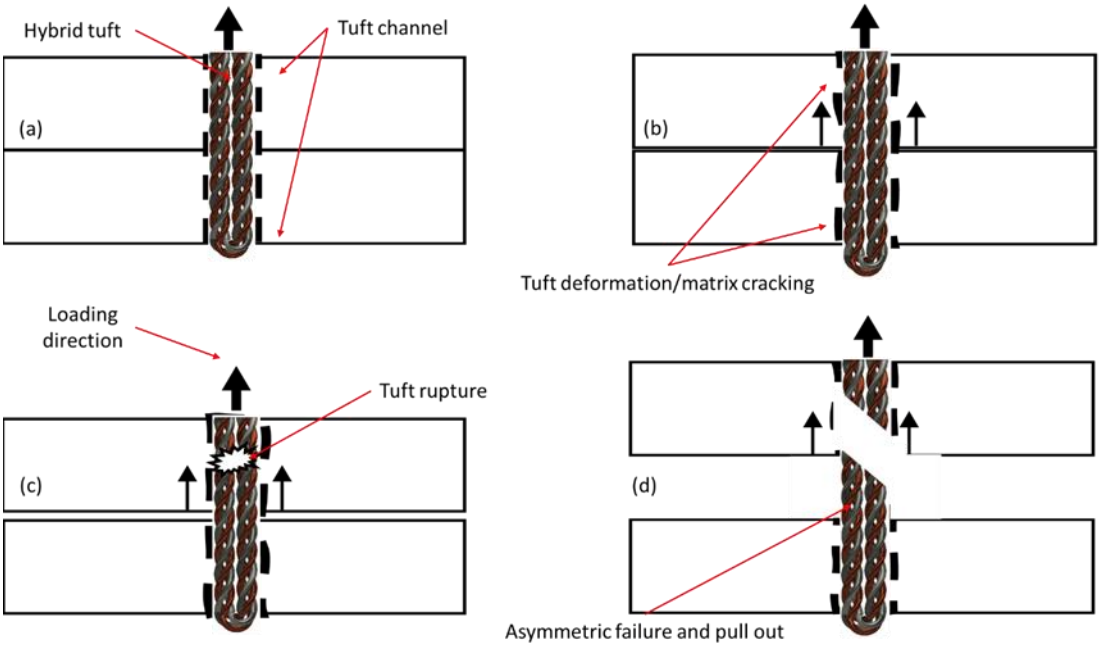

Figure 6-8 Schematic illustration of tuft bridging during Mode I displacement, (a) initial ailment, (b) tuft deformation and matrix cracking, (c) asymmetric tuft rupture and (d) asymmetric pull-out.

6.2.3 Crack sensing capabilities

6.2.3.1 Effect of electrode positioning

As previously discussed in Section 6.2.1 the sensing capability of the hybrid micro-braid thread was assessed by the measurement of the ER variation caused by the architectural change in the tuft and specimen under load. An initial assessment of the single tuft coupons was carried out with the MM electrode connection positions relative to the tuft positioning. As described in Section 6.2.1, two configurations were considered: one with contacts close to the tuft and the other with electrodes far-from-tuft. This positioning of the electrodes influenced the ER response since the tuft provides a TT current path. Figure 6-9 illustrates the potential complex electrical paths available to the applied current. The high conductive properties of the metal wire in the micro-braid, combined with the near-tuft positioning, resulted in the hybrid tuft dominating the current path. Whilst alternative current paths were possible, due to the higher resistivity associated with them, the resulting current flow had a comparatively negligible influence.

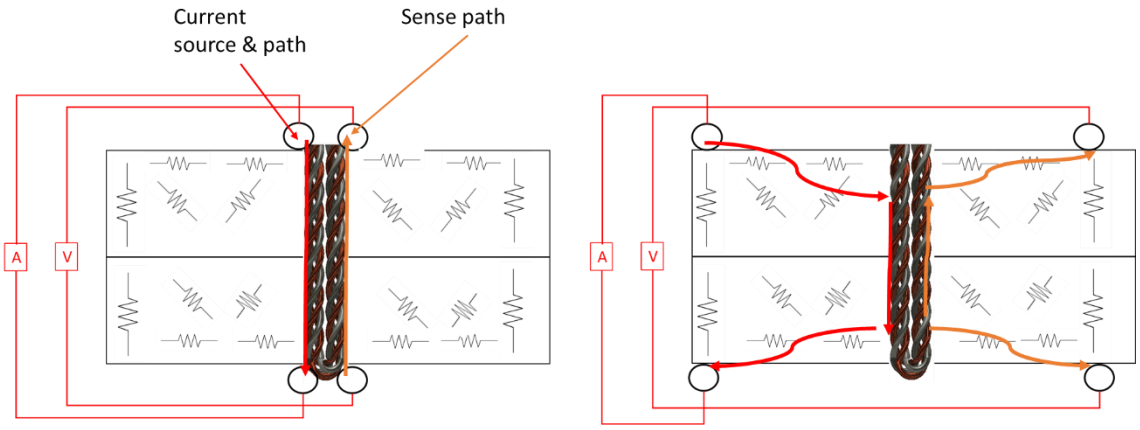

Figure 6-9 Schematic illustration of dominant current paths. Source current (red) and sense (orange). (Left) Near tuft electrode placement and (right) far-from-tuft electrode placement.

Resistance readings tending towards zero were recorded using the MM. Due to the low resistivity of the wires in the micro-braid, the limits of instrumentation sensitivity were reached, resulting in high noise levels and the inability to measure a definitive initial resistance reading. In comparison, the electrodes positioned far from the tuft generated a more complex arrangement of potential current paths, leading to an overall higher value of initial resistance. This resistance represented a "whole coupon" measurement, which was influenced by the electrical conductivity of the micro-braid, and the in-plane conductivity of the UD carbon fibre, as well as any potential indirect connections in the TT direction created by random fibre connections. This created a more complex circuit but also leads to a whole coupon characterisation method with an overall higher initial resistance. Initial starting resistances for the far-from-tuft configuration ranged between 1 – 3 Ω. Both sets of resistance readings were dependent on factors such as the qualities of the glue and the silver paint connections, as well as damage levels to the micro-braid caused by the manufacturing process, voids in the matrix, and any residual defects that were introduced during the sample preparation.

The sensing capacities of the near-tuft electrodes and the far-from-tuft electrodes are illustrated in Figure 6-10. The far-from-tuft electrode positioning showed a higher initial resistance measurement compared to the near-tuft position. On loading, the ER measurement was more responsive to the linear deformation stage (stage 1) of the loading profile compared to the near-tuft as shown in Figure 6-10. The ER response indicates that the near-tuft electrode

placement does not respond to the initial loading of the coupon. No increase in the normalised ER value was recorded until a sudden load drop (stage 3). This load drop corresponded to the tuft rupture and the subsequent increase in normalised resistance due to the gradual pull-out of the broken tuft.

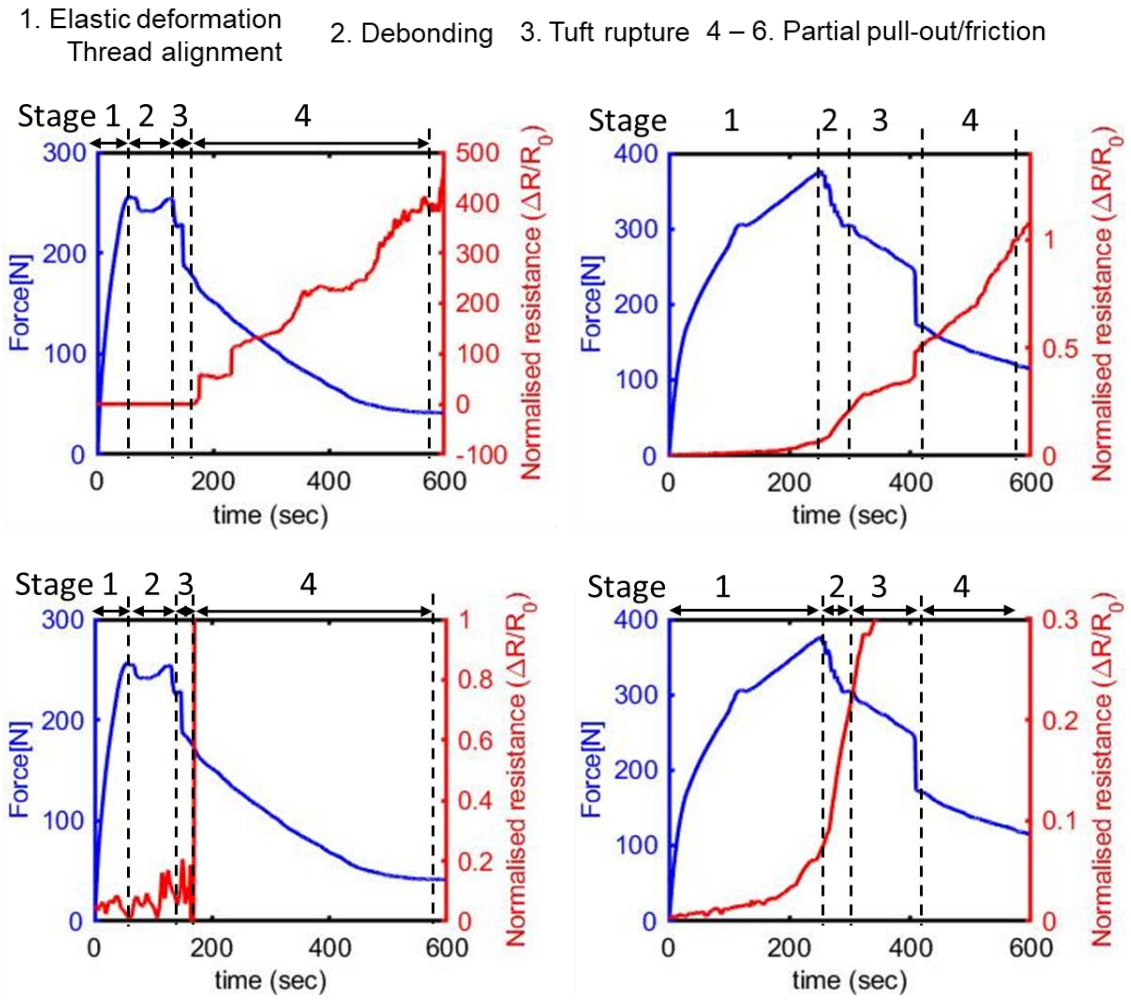

Figure 6-10 (Top) Full-range plots and (bottom) partially enlarged plots of single-tuft Mode I delamination depicting failure stages. (Left) Near-tuft electrode position and (right) far-from-tuft electrode positioning.

Variations of the loading that occurred before complete failure were not detected. In comparison, the far-from-tuft positioning enabled an almost immediate ER-based sensing of the loading of the tuft. This is true for both stage 1 and all the further load drops, which were all recorded as jumps in normalised through-thickness electrical resistance (TTER). Whilst the near-tuft resistance varied by at least two orders of magnitude from the start of the test to the end, it lacked sensitivity during the initial elastic loading stage, as evidenced when the resistance scale is adjusted. Partially enlarged plots of the single tuft

tests highlight the stages of failure for both sets of coupons. Due to the low sensitivity of the near-tuft electrode arrangement in the early loading stages, further testing was undertaken using the far-from-tuft electrode positioning. This was to ensure that events which occurred in the early stages of failure could be scrutinized by ER change monitoring.

6.2.3.2 Effect of loop length on sensing capabilities

The results of a selection of the relative ER change profiles and the synchronised load profiles for long-looped tufts and the minimal loops are presented in Figure 6-11. There were no distinguishable features that could be found to differentiate between a minimal and a long-tuft response profile. From the onset, all the coupons, irrespective of tuft configuration, yielded variable initial resistance measurements as well as variable magnitudes of ER change throughout testing. However, a clear trend relative to the applied load over time is observed for both sets.

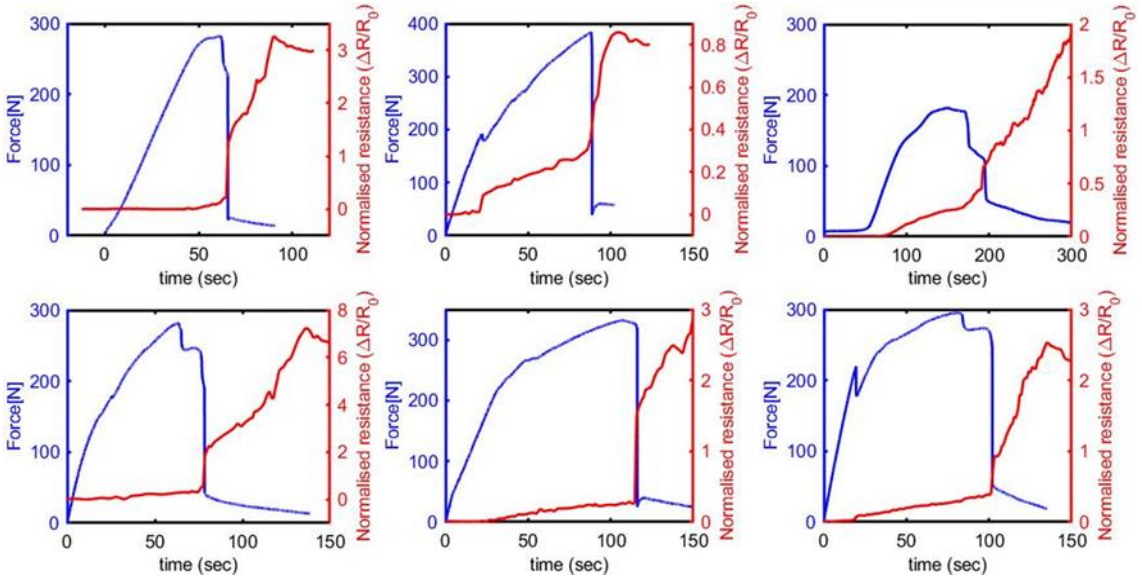

Figure 6-11 Full profiles of (top) minimal-looped tufts and (bottom) long-looped tuft in Mode I delamination with ER change response.

Overall, the trend shows an increase in relative resistance over time. The ER sensing profile corresponded to the main stages of the force vs. displacement profiles, with increases in relative ER coinciding with sudden load drops. These sudden spikes in the relative ER indicated a disruption in the electrical pathway of the coupons, resulting from a decrease in the structural integrity of the braided tuft or the composite laminate. The displacement was halted once a

clear visual separation of the coupons was observed. The frictional pull-out of the tuft (stage 4) can be discerned in the graphs as a progressive decrease of load, which was accompanied by an increase in relative ER, with the latter tending to infinity. Testing was stopped before the complete pull-out of the broken tuft. This was done to reduce experimental time and to preserve the coupon for microscopic examination. In addition, extending the test yielded no useful information because the high resistance reading caused by complete detachment of the broken tuft made the results unreadable. The ER and the corresponding load profiles of the single tuft coupons indicate that several failure processes occur during loading. The linear (stage 1) section corresponded to the elastic deformation of the braided tuft, which showed a gradual increase of relative ER. The sudden load drops corresponded to matrix cracking, fibre breakage, disbanding and rupture of the braided tuft. Gradual ER increases corresponded to the final pull-out of the tufts. As stated previously, manufacturing variability affected the tuft insertion angle, the extent of the resin-rich regions, and caused local disruption to the fibre architecture. These could have resulted in uneven loading of the composite constituents.

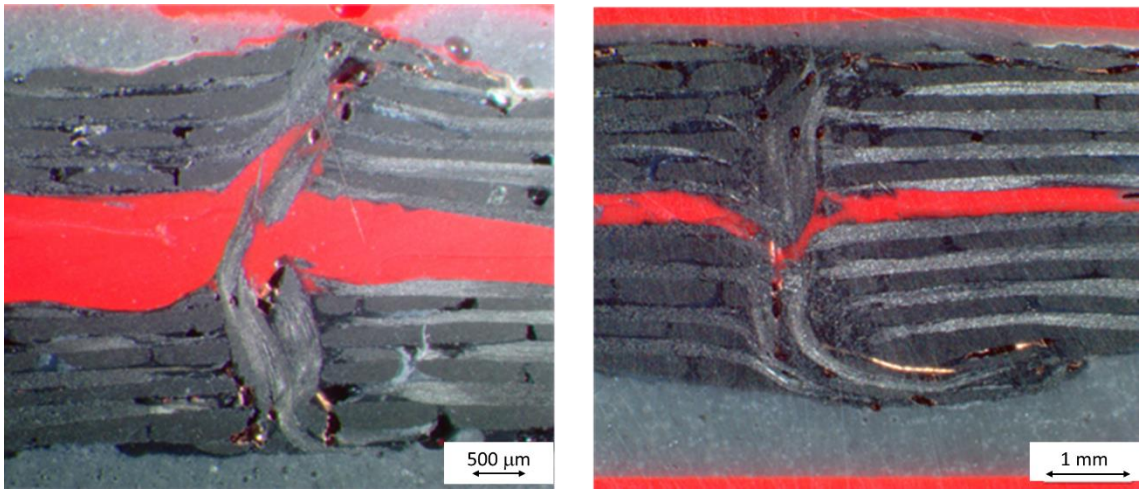

Figure 6-12 Macroscopic images of Mode I delamination partially de-bonded tested single tuft coupons, (left) minimal-loop tuft and (right) long loop tuft.

The hybrid nature of the braided tuft caused sequential failures that induced multiple load drops in the displacement profiles. The difference in mechanical properties between the carbon fibre and the copper wire promoted a complex failure mechanism within the micro-braid. Micrographic analysis was used to assess the tufts' post-test condition and to support the hypothesis that the various components within the braided tuft failed in a sequential order. The

uneven separation of components following rupture is visible in micrographs of the tuft's cross section (Figure 6-12). Remnants of broken carbon fibre and copper from the micro-braid thread are evident within the tuft channel of partially loaded tufts. The failure profile of the hybrid micro-braid thread also affected the response of the MM reading. Micrographs of fully dislocated tufts show splaying of the micro-braid thread components (Figure 6-13).

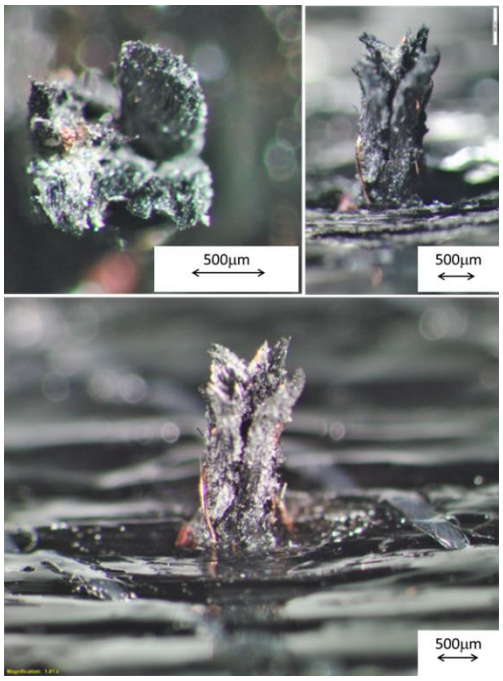

Figure 6-13 Micrographs of fully dislocated ruptured tufts.

The position of the tuft within the channel as it was pulled-out influenced the response of the MM. As shown in the micrographs of partially ruptured and fully dislocated tuft, the micro-braid thread components are separated, and the extent of this separation varied from tuft to tuft. As the ruptured tuft was pulled-out from the composite, a combination of different current pathways could be generated or inhibited depending on the positioning of the micro-braid components. The continued connection of the wire component of the micro-braid thread would result in a lower reading from the MM and, as a result, any subsequent break would have resulted in a larger relative ER jump.

In addition to this, there was the potential for further pathways to be created, which would explain fluctuations and noise within the signal. Figure 6-14 shows the results of a minimal-looped coupon under Mode I. The initial response showed an ER trend similar to those discussed so far, with an overall increase in relative ER and a gradual increase throughout stages 1 and 2. On closer inspection, the relative ER decreased with the rapid load drop in stage 3. This

was opposite to that observed in the other single coupon tests, but it is consistent with other reported TTER tests in the literature [9, 246]. This has implecations for the use of the ER monitoring method for SHM although any variation in ER should be concidered an indication of damage events.

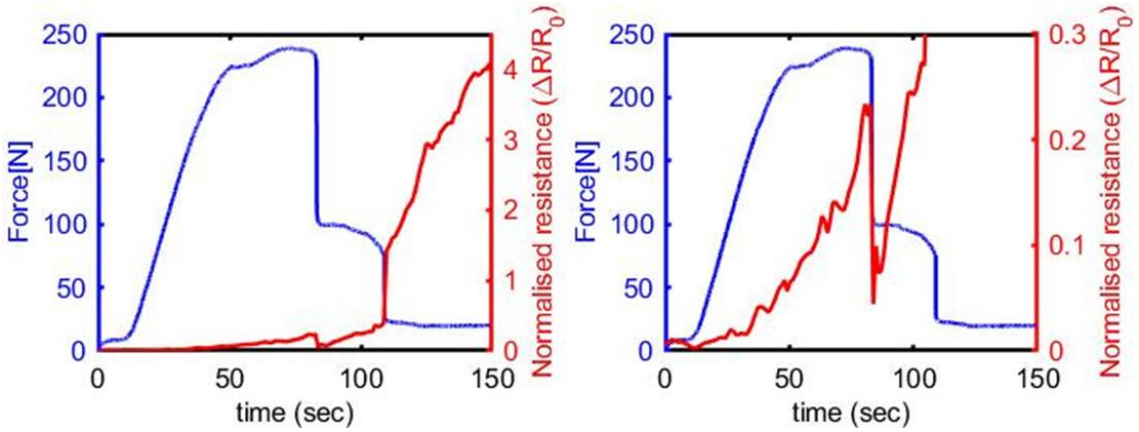

Figure 6-14 (Left) Full-range plot and (right) partially enlarged plot of single minimal tuft in Mode I delamination with ER change response.

6.3 Double cantilever beam (DCB) test

6.3.1 Specimen manufacture and testing methods

Double cantilever beam (DCB) coupons were manufactured according to ASTM D5528 – 13 Standard Test Method for Mode I Interlaminar Fracture Toughness of Unidirectional Fiber– Reinforced Polymer Matrix Composites specifications [247]. This test was used to further assess the SHM capability of the tufting thread and used to compare the untufted and the tufted specimens. it was not intended to provide material properties. It should be noted that, due to the presence of the tufts and to avoid the coupons breaking at the arms, some deviation in thickness and the length of the coupons from the standard were necessary. Preforms comprising twenty-four plies $[90]_{24}$ of Sigmatex 5011X carbon fibre PC414X UD fabric were used. The fabric was made of 12k HTS 5631 carbon fibre yarn and an epoxy sizing with a 37 tex E-glass weft at 300-500 picks per metre. The total fabric areal weight was 330-350 gsm. The fabric contained a blue X-ray tracer fibre evenly placed along the ply, for which no further specifics were provided by the manufacturer. In accordance with the standard, a 20µm thick PTFE release film was inserted along the mid plane of the preform at a length of 60 mm. No tufts were present within the release film

region. The tufting was carried out using an automated KLS RS522 tufting head, mounted onto a KUKA KR 240 L180-2 2000 robot arm as shown in Figure 6-15.

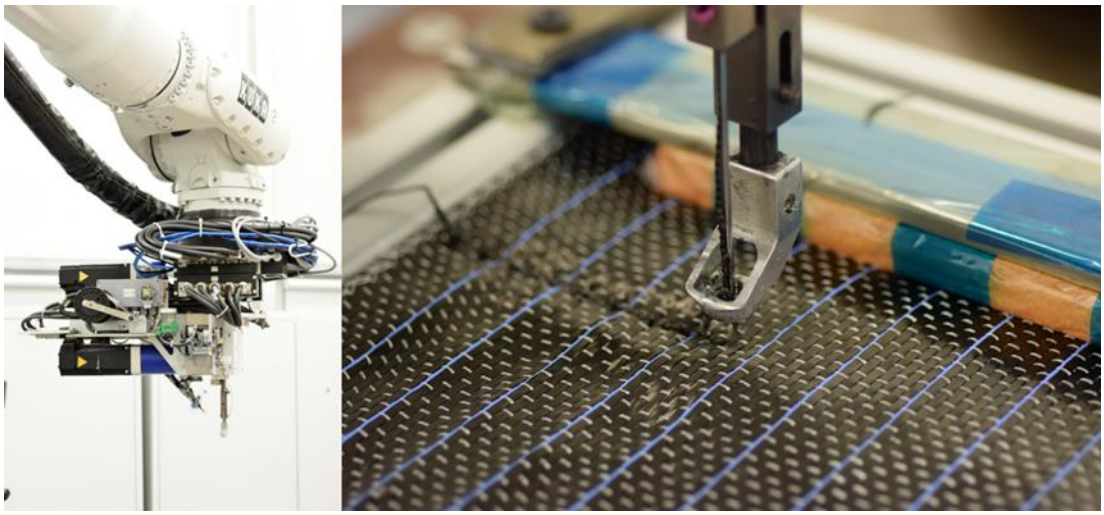

Figure 6-15 (Left) KSL tufter and (right) tufting needle and UD dry preform in tufting clamp.

Each panel was tufted with seven rows of tufts, using two different sets of spacings. The dimensions chosen were 10 mm x 15 mm and 10 mm x 10 mm tufting patterns. The tufts were inserted vertically using a Schmetz needle with a 1.0 mm diameter eye (Figure 6-15). The backing foam was a 25 mm Airex® R6380 foam covered with Wrightlen PTFE to prevent contamination and aid in separating the preform from the foam layer. The resulting areal tuft densities were 0.8% and 1.3%, respectively. For comparison, untufted control panels were also produced. Initial tufting trials of the micro-braid thread resulted in the removal of the tensioning function on the tufting head. This produced more consistent tufts, but it meant any variability that might have occurred during insertion and retraction went undocumented. The tufting rate was 0.0008 m/s, equating to approximately seven tufts per minute.

During initial trials it was observed that the UD fabric was susceptible to movement and bunching, something not experienced with the biaxial fabric used in the single tuft coupons. To avoid extensive distortion of the fabric material, the foot pressure was set to minimum and to assist in the debulking, deionised water was sprayed on the preform. The water acted as a binding agent and restricted ply movement. When tufts were inserted perpendicularly to the ply orientation, bunching, or crimping of the in-plane fabric tows occurred,

as seen in Figure 6-16. Once dry, this crimping was less pronounced but still present as typical of tufted preforms. The looped ends on the back of the fabric and embedded into the foam were 5mm ± 0.5 mm (CV = 9%) long. These were manually flattened in the direction parallel to the UD fabric. The preforms were left to dry at room temperature for several days. To ensure the preforms were completely dry, each was weighed and then placed in an oven at 100°C for 2 hours, then re-weighed and returned to the oven for another 2 hours. If the weight decrease was less than 1% the preforms were considered dry.

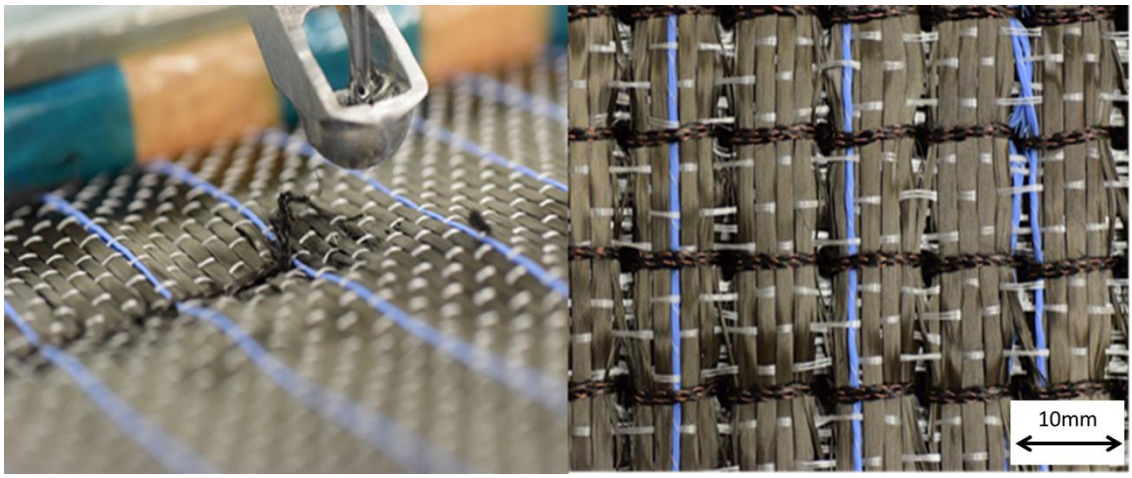

Figure 6-16 Tufting of UD ply, (left) curvature of the carbon fibre fabric when tufted and (right) temporary bunching of carbon fibre when wet.

The tufted preforms were infused under vacuum by a double bagged vacuum assisted resin transfer mould method. The resin was Momentive Infusion resin MGS® RIM 935 and MGS® RIMH 936 hardener with a mixture ratio of 100:29 parts by weight. The plates were cured at 80°C for four hours. Prior to infusion two panels had the external loops cut using scissors so that the ends were flush with the preform. This was done to examine the different effect of external loops and no loops on failure mechanisms. Figure 6-17 compares the flatted loops and the cut loops. The loops remained a feature of the preform and were present as flattened loops enclosed in a resin rich layer.

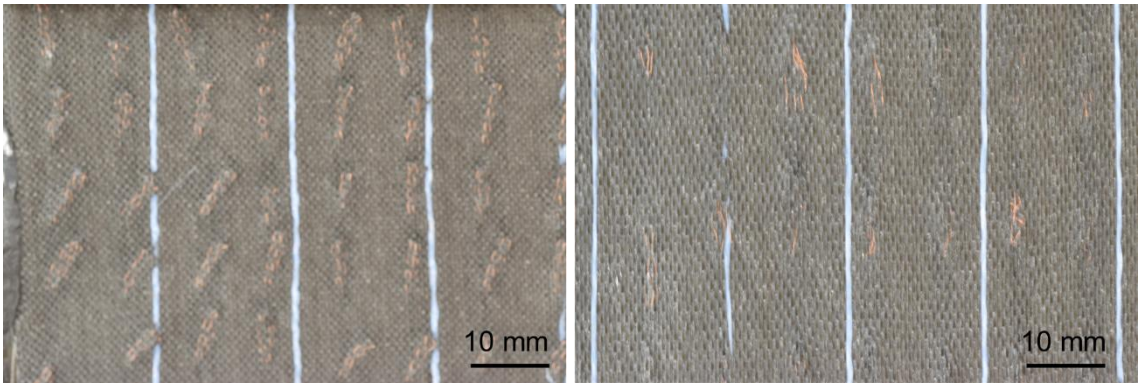

Figure 6-17 (Left) Underside of cured panel with loops and (right) underside of cured panel with loops cut.

Whilst every effort was made to ensure that the loops lay parallel to the fabric, the process of infusion caused some variability, as seen in Figure 6-17. Infusion of the untufted UD panels resulted in more dry patches on the outlet side due to ‘fast tracking’ caused by compaction of the UD fabric. Repeated attempts to achieve proper impregnation were required. The presence of the tufts aiding in the resin propagation and impregnation within the panels. The tufts provided channels where resin was visibly seen propagating up from the lower plies, this appeared to aid in infusion quality.

After cure, DCB coupons with dimensions of 20 mm x 180 mm were cut using a diamond saw, ensuring that two tufts were present along each row. Each tufted coupon had seven rows comprising two bridged tufts. The distance between each row was 10 mm or 15 mm depending on the tufting pattern, as illustrated in Figure 6-18. Where the loops diverged from parallel along the UD fabric, there were instances where the ends were trimmed as a result of coupon cutting.

The purpose of this study is to determine the suitability of the copper–carbon fibre hybrid micro-braid thread for use in tufting as well as its ability to introduce a multifunctional component into a composite structure. Coupons tufted with a commercially available 4k thread were also produced to compare the hybrid thread properties to those of more conventional threads. Table 6-2 shows the combinations of parameters that were examined, including untufted coupons as a benchmark.

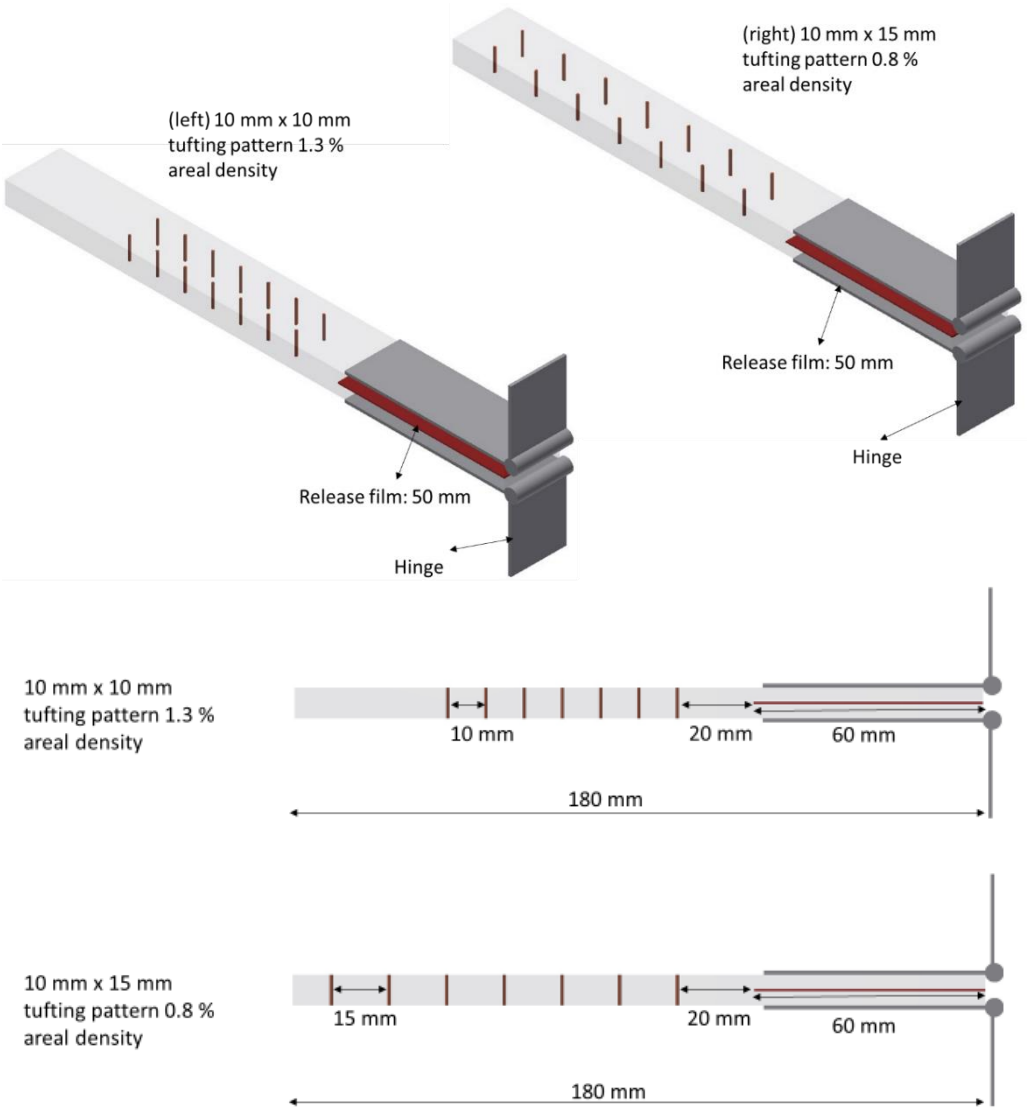

Figure 6-18 DCB coupon dimensions and configuration for 0.8% and 1.3% tufting densities.

Table 6-2 DCB testing parameter variation

Thread type	Tuft areal density (pattern)	Loop condition
Control reference None	[-]	[-]
Copper–carbon fibre hybrid micro-braid thread	1.3% (10 mm x 10 mm)	Looped Unlooped
	0.8 % (10 mm x 15 mm)	Looped Unlooped
4k carbon fibre thread	1.3% (10 mm x 10 mm)	Looped

As expected, a thickness variability was apparent along the length of the tufted coupons, due to the unconstrained vacuum infusion. This meant that the panel thickness was not restricted by a closed mould and the loops on the underside increased the thickness of the specimen in the tufted area. A thickness variability of up to 2.9% was measured for the untufted coupons. Whereas the coupons tufted with the 4k carbon fibre thread and the copper–carbon fibre hybrid thread exhibited a variability of up to 4.7% and 12.3% respectively. Measurements of the coupon thickness were taken along three points for the untufted samples and four points for the tufted coupons. Untufted coupons were measured at the two ends and the central point, whilst the tufted coupons were measured at the two ends, on the tuft and between two tuft rows, as shown in Figure 6-19. This variability and thickness increase has previously been examined by several studies and determined to affect in-plane behaviour, as well as aerodynamic and aesthetic properties. Whilst this is an important consideration in manufacturing and composite structural design, the effect of this variability is not examined in this study. Previous studies have shown that the extent of the thickness variability is primarily determined by tuft areal density with loop length, with thread size having lesser effects [23].

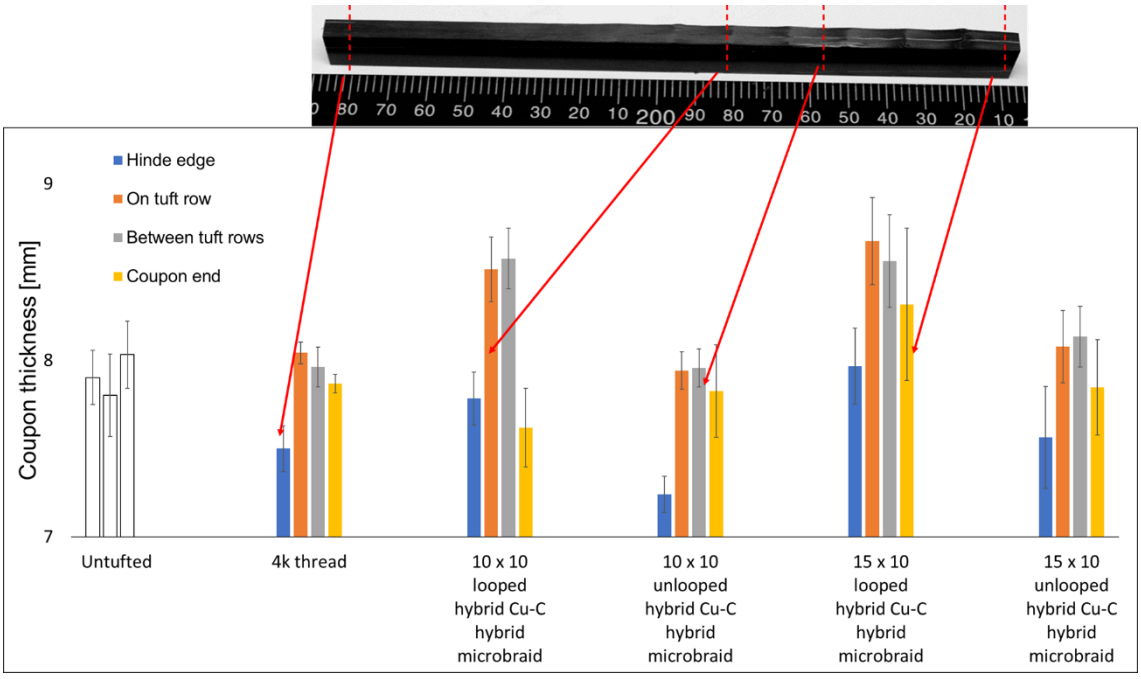

Figure 6-19 DCB coupon thickness variability.

To enable the measurement of the ER change during testing, tin coated copper electrical wires were attached, as described for the single tuft tests in Section 5.1.1. These wire electrodes were positioned on the first and third tuft rows. Prior to attachment, these areas of the coupons were prepared by sanding to remove surface resin and expose the tufted micro-braid thread. The coupons were further prepared following the guidelines given in the standard, with hinges adhered to the ends using Huntsman Araldite® 2014 – 2 epoxy adhesive following surface treatment in the relevant area (Figure 6-20).

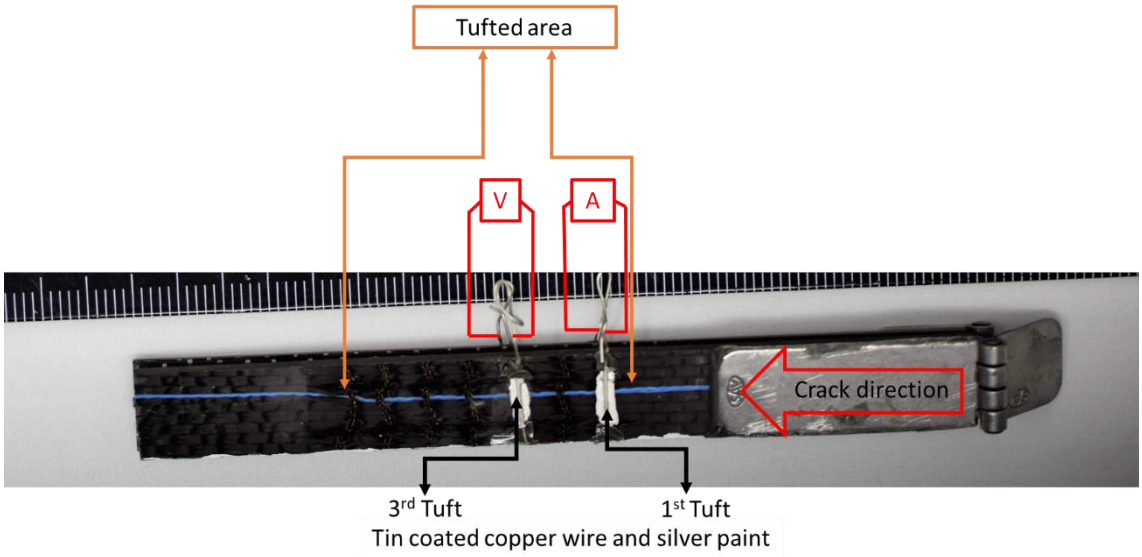

Figure 6-20 DCB coupon with ER electrodes attached.

White correction fluid marked with black pen every 1 mm was applied to aid the measurement of the crack growth. A video gauge was used to measure crack length during testing and was manually verified after testing by visually assessing the video. Testing was undertaken according to the standard specification at 2 mm/min displacement rate. The initial plan was for testing to be halted before complete separation of the two halves of the coupons. Unfortunately, this was not consistently achievable, as often the crack propagation occurred unexpectedly during the last stages of testing. It was therefore decided to continue the testing until complete rupture of the coupons. This had the additional benefit of ensuring that multiple rows of tufts failed and enabled a determination of their influence on ER measurement. The ER change was measured using a Keithley four-wire MM, as discussed previously in Section 6.2.1. The source and sensing electrodes were attached to the bonded wires so as the current flowed in the TT direction, as illustrated in Figure 6-21.

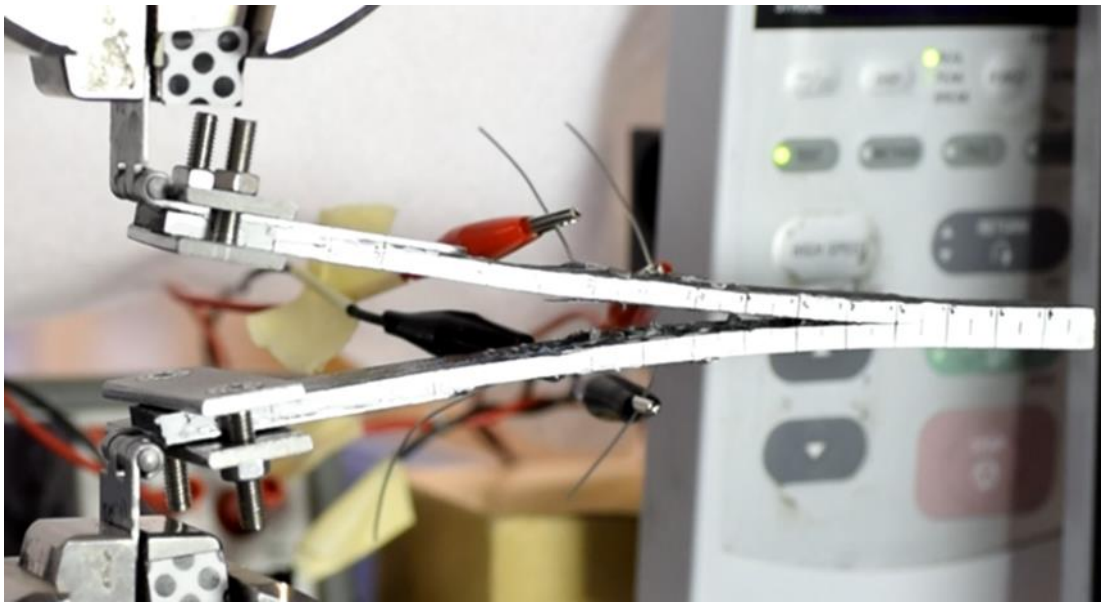

Figure 6-21 DCB experimental setup.

During testing, due to the extensive force required to achieve the crack propagation through the tufted sample, reinforcement of the hinges was required to prevent debonding due to glue failure. This was achieved by opening up the specimen, attaching two sets of screw clamps and resuming testing.

6.3.2 DCB Mode I delamination response

Figure 6-22 depicts a typical load displacement curve and crack length propagation for an untufted control DCB specimen. The typical response of an untufted coupon was a linear increase through the pre-cracked release film region of the coupon, up to an average critical maximum load of approximately 131.1 N ± 12.1 N. After crack initiation, the load plateaued and monotonically decreased until complete delamination. The crack growth propagated gradually with stable delamination. Some minor fluctuations did occur during testing, corresponding to fibre bridging beyond the crack front. Intact bridging fibres absorbed energy and resisted crack progression. Longer crack lengths resulted in the increase of the number of bridging fibres and complexity of the delamination mechanism, thereby, increasing the scatter in test results. As the crack propagated, the lever arm length increased and consequently the load required to propagate the crack decreased.

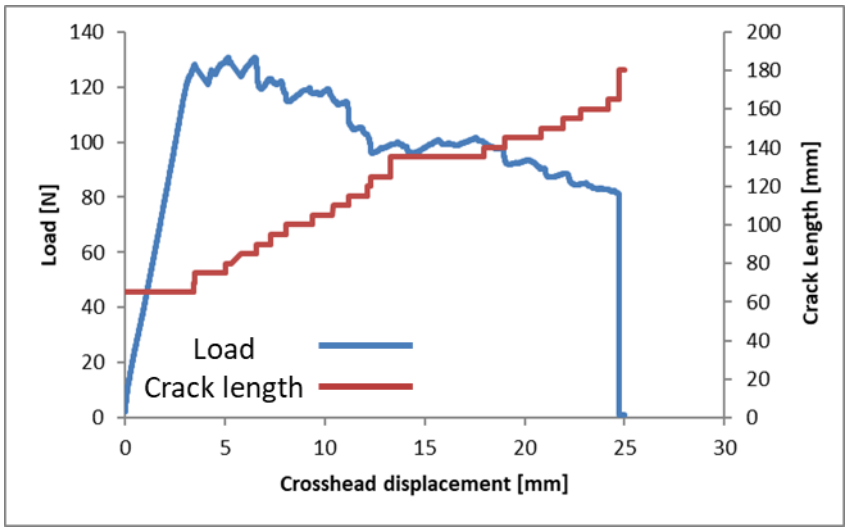

Figure 6-22 Typical load displacement profile for untufted coupons

In this study, the DCB tests were carried out until the specimen arms were completely split, i.e., the delamination crack extended the length of the specimens. This was done to ensure that a sufficient number of tuft rows ruptured, but it introduced additional forces into the DCB coupon. For example, arm bending and some compression at the crack tip were clearly observed as testing progressed. More scatter and deviation were introduced because the test was paused to attach the hinge reinforcements. Despite this, delamination growth was consistent and progressed gradually down the coupon.

The tufted samples produced a more complex and unstable delamination than the untufted coupons. The initial profile was linear through the unreinforced zone until the crack progressed into the reinforced tufted sections where the load increased significantly compared to the untufted coupons. All the tufted coupons showed a characteristic stick–slip behaviour that coincided with rapid crack growth followed by crack arrest. Both the 4k tufted coupons and the hybrid micro-braid tufted coupons had stepped responses, with each load drop corresponding to the failure of a tuft row. As the crack propagated through the tufted area, the crack was arrested, the applied load then increased until tuft rupture and a rapid jump in crack length ensued. As the crack moved beyond the first row of tufts, the subsequent tuft rows were engaged in resisting delamination. For all the tufted coupons it was observed that crack closure occurred due to arm bending. This was most evident for the coupons tufted with the 10 mm x 10 mm pattern, where the tuft rows were closer together and

therefore more tuft rows were employed in bridging. This closing and opening of the crack front added to the experimental difficulties by hiding the exact location of the crack tip. Typical load-displacement curves for the 10 mm x 10 mm tufted 4k carbon fibre coupons and the hybrid micro-braid tufted coupons are shown in Figure 6-23 and Figure 6-24. The full load-displacement results are provided in Appendix A.

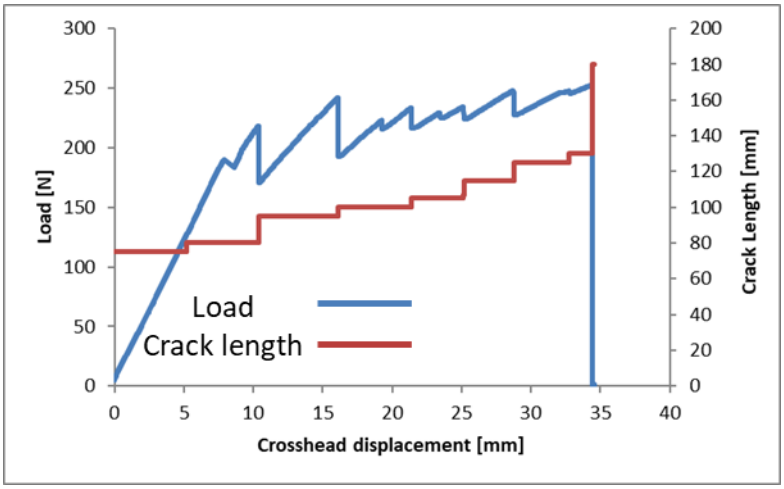

Figure 6-23 Typical load–displacement curve for 4k tufted coupons with a 10 mm x 10 mm pattern.

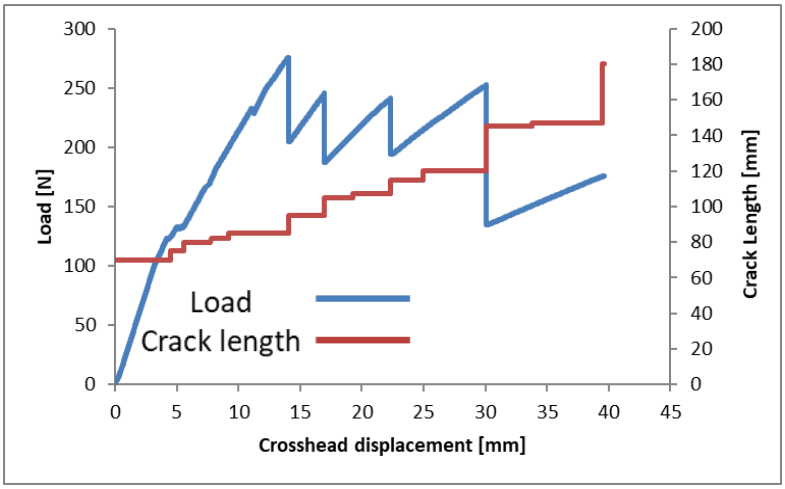

Figure 6-24 Typical load–displacement curve for coupons tufted with the hybrid micro-braid with a 10 mm x 10 mm pattern.

The 4k tufted coupons and a set of hybrid micro-braid tufted coupons were tufted with a 10 mm x 10 mm pattern. Crack progressions in these coupons were seen to occur in increments of approximately 10 mm between two adjacent tuft rows. Observations of the 4k coupons test indicated that more gradual undetected failure of the tufts occurred; cracking was heard prior to crack progression, with some limited advancement (less than 1 mm) of the

crack front, before a larger jump of up to 10 mm beyond the original arrest. In comparison, the tuft rows in hybrid coupons tufted with a 10 mm x 10 mm pattern appeared to fail in one step; less cracking was audible, and less incremental advancement of the crack was observed.

It should be noted that often the crack progressed beyond the first row, without resulting in tuft failure or a measured load drop. This was predominantly observed in the coupons tufted with the 10 mm x 10 mm patterns, where the rows were closer together and more rows were engaged in bridging the crack. However, as the first row failed, the crack advanced quickly, and occasionally caused the second row to fail in the same phase as the first.

For the samples with a 10 mm x 15 mm patten, the influence of additional rows was less prominent. An example load-displacement graph for coupons tufted with a 10 mm x 15 mm pattern, with the copper-carbon fibre hybrid braided thread is provided in Figure 6-25. Crack propagation in the 10 mm x 15 mm tuft coupons appeared to be influenced by two rows of tufts. The crack propagated beyond the first row of tufts, halting approximately midway between two rows until the rupture of the first row. At this point, the crack rapidly progressed beyond the second row until influenced by the third row. The crack progression in the more separated 10 x 15 mm coupons was more predicable in its stick-slip response.

During the testing, there was no discernible difference in the failure profiles of

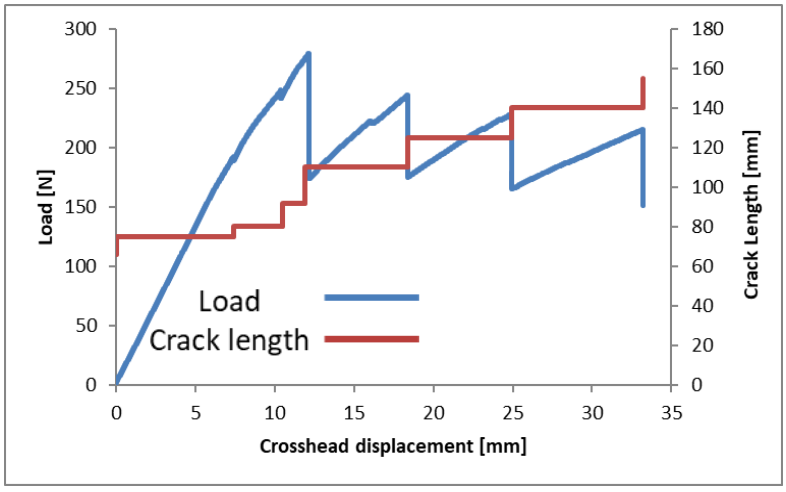

Figure 6-25 Typical load–displacement curve for coupons tufted with the hybrid micro-braid with a 10 mm x 15 mm pattern.

looped and un-looped coupons. A valid comparison cannot be made since the hinges on a number of these examples failed prematurely. Figure 6-26 shows

the un-looped coupons for both the 10 mm x 10 mm and 10 mm x 15 mm designs tufted using the hybrid micro-braid thread. It was speculated that the removal of the external loops would introduce a pull-out failure profile similar to that seen in z-pins, although, this was not conclusively observed.

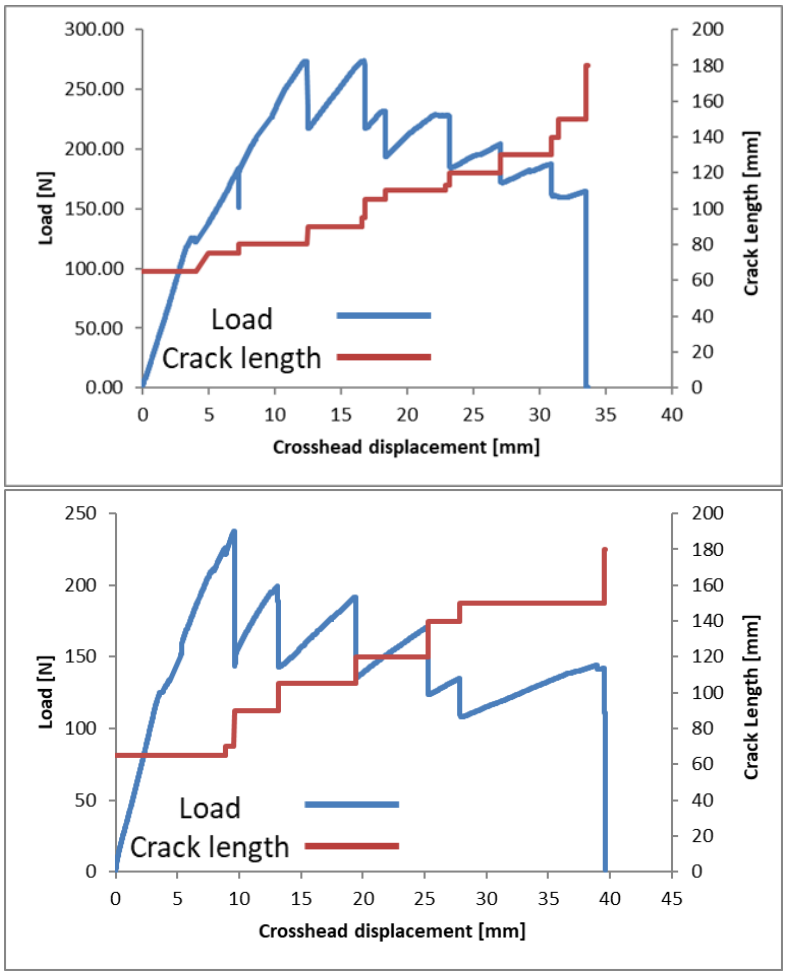

Figure 6-26 Load – displacement curves for coupons tufted with hybrid microbraid thread with cut loops (top) coupon tufted with 10 mm x 10 mm pattern (bottom) 10 mm x 15 mm pattern.

It is evident from the load–displacement curves that the presence of the tufts increased the delamination resistance of the specimen in comparison to the untufted coupon, irrespective of the tufting thread type. As shown in Figure 6-27 the maximum loads applied to the tufted coupons is almost double that of the untufted specimens. The maximum load of 275 N ± 18 N was achieved by the use of the tufted 4k commercial thread. whilst the hybrid tufted coupons achieved similar maximum loads of 274 N ± 11 N, 265 N ± 17 N, 260 N ± 21 N, and 238 N ± 12 N.

Both the looped and un-looped coupons tufted with a 10 mm x 15 mm pattern showed a slight decrease in maximum load compared to the 10 mm x 10 mm

patterned coupons, indicating that the closeness of the tuft rows enabled engagement of more than two rows and improved the initial delamination resistance. It is apparent from the load displacement curves that the hybrid micro-braid thread achieves a similar delamination resistance to the commercial thread but that tufting pattern and positioning influenced the mechanical properties.

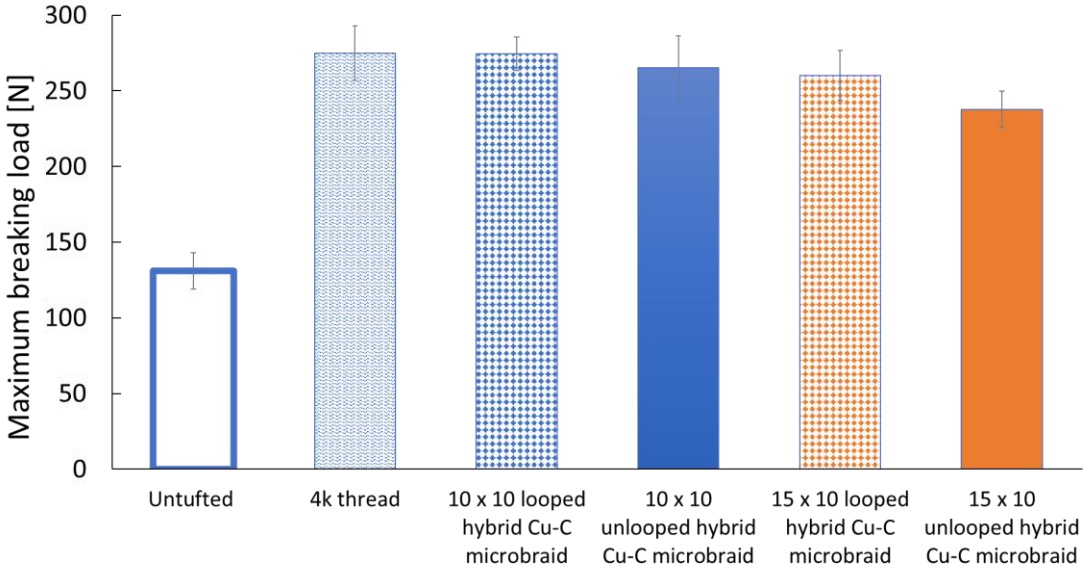

Figure 6-27 Maximum breaking DCB loads.

The standard assessment of DCB testing involves the calculation of the fracture toughness (G_I) values of the tested samples. The modified beam theory fracture toughness is calculated using Equation 6-1.

$$G = \frac{3P\delta}{2b(a-\Delta_I)} \qquad \text{Equation 6-1}$$

where P is load, δ deflection, b sample width, a delamination length and Δ_I is the crack length correction factor which mediates for the effects of rotation at the crack front. Δ_I is determined experimentally by generating a plot of the cube root of compliance, $C_{1/3}$, as a function of delamination length [247]. The standard ASTM procedures assume linear elastic behaviour, steady state failure and are not easily adaptable to coupons reinforced with TTR. The calculation of Mode I G_I assumes a load-displacement curve that contains a single peak followed by a gradual decrease unlike the stepped drops associated with the stick-slip failure of tufted coupons. As fracture toughness is a structural

rather than a material attribute in a TTR specimen, it was the “apparent” fracture toughness (G_{app}) of the tufted specimens calculated using Equation 6-1.

Table 6-3 and Figure 6-28 provide the mean G_{app} and mean maximum breaking force of the tested samples. Similarly, to the load-displacement curves, tufted coupons were more resistant to delamination than untufted coupons. The hybrid thread appears to be less effective than the commercial thread. During testing it was observed that one of the 4k tufted coupons underwent a different failure mode in the final stages of testing. This was caused by the bending moment and the stress concentration in the upper arm, which then failed as its flexural strength limit was reached. Even after eliminating this sample from the data, the 4k tufted coupons values still have a higher mean compared to the hybrid micro-braid coupons

Table 6-3 Mean fracture toughness for DCB samples.

Sample	Mean G_{app} [J/m^2]	SD [J/m^2]
Untufted	**689**	**41**
4k	2823	888
4k (eliminating sample with arm failure)	2324	233
10 x 10 mm looped hybrid micro-braid thread	1708	261
10 x 10 mm unlooped hybrid micro-braid thread	1934	896
15 x 10 mm looped hybrid micro-braid thread	1988	639
15 x 10 mm unlooped hybrid micro-braid thread	1556	610

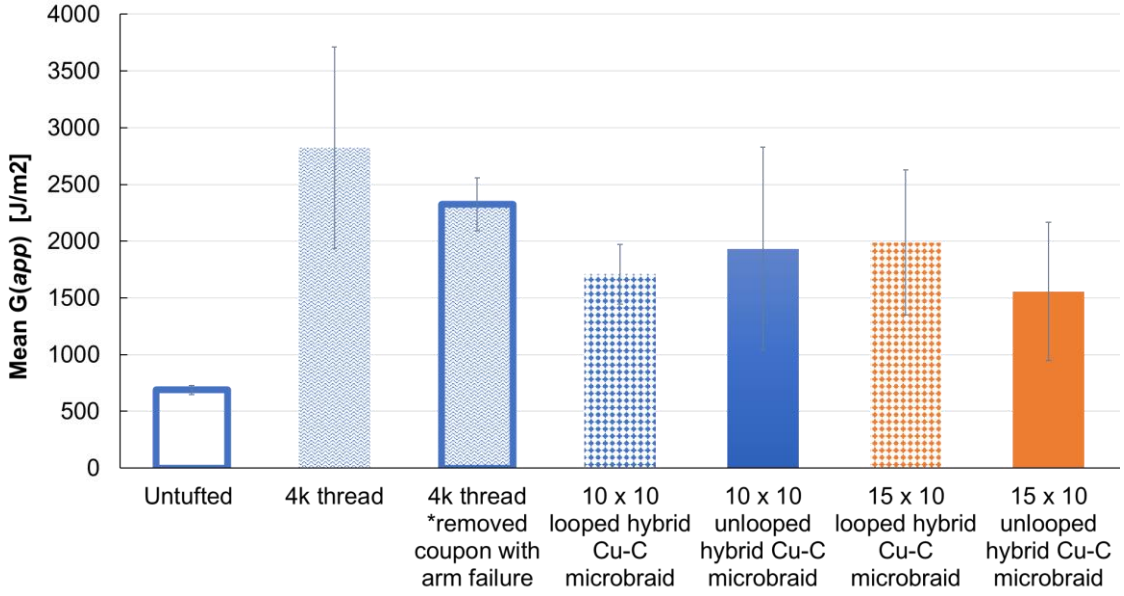

Figure 6-28 Mean Mode I inter-laminar fracture toughness.

The R–curve behaviours of the DCB specimens are shown in Figure 6-29. As stated previously, the delamination crack length was extended beyond the normal testing procedures for DCB tests to assess the influence of an array of tufts. The complexity of the delamination behaviours of the tufted specimens is evident in the large amount of scatter in the R-curves. These are therefore not to be considered "material" properties, but rather metrics to compare similarly between consistently tested specimens. In addition, coupon thickness variation, dynamic effects introduced by the stick-slip behaviour, experimental error due to arm bending (Figure 6-30) and difficultly in precisely measuring the crack tip also increased the difficulty of interpreting G_{app} values.

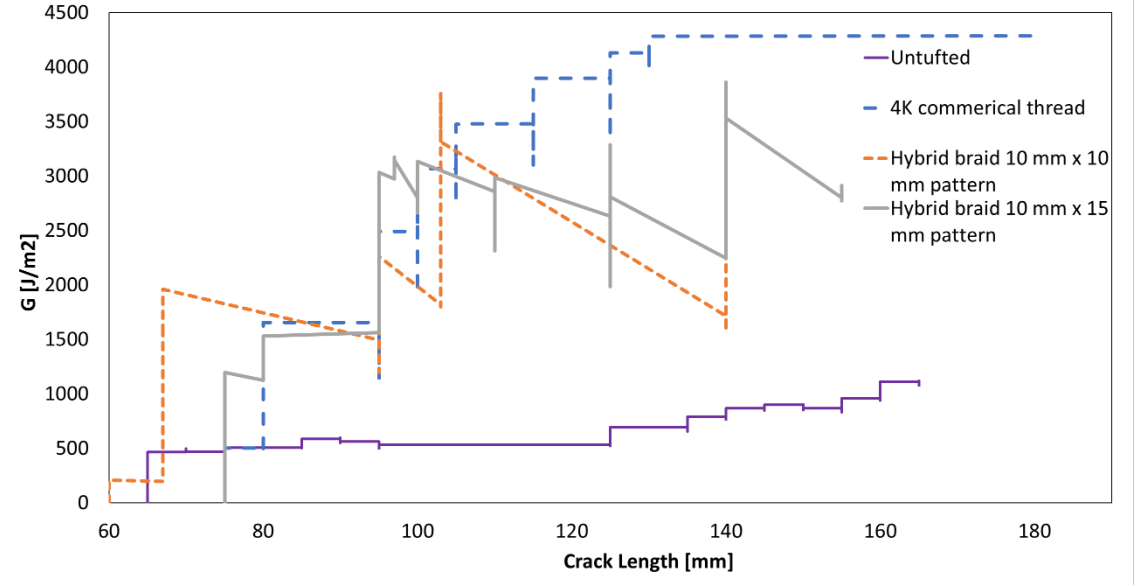

Figure 6-29 Representative R–curves for each DCB coupon configuration.

Notwithstanding these limitations, the R–curves still provided an insight into the capabilities of the TTR types, and their trends are representative of the failure processes that occurred in composites reinforced with tufts. The R–curves showed that tufting increased the mode I delamination resistance. Whilst the hybrid micro-braid thread has a slightly lower capability than the 4k commercial thread, the resulting apparent toughness was still three times higher than for the untufted specimen. The key result from this study was that the hybrid micro-braid thread increased delamination resistance compared to the untufted specimens.

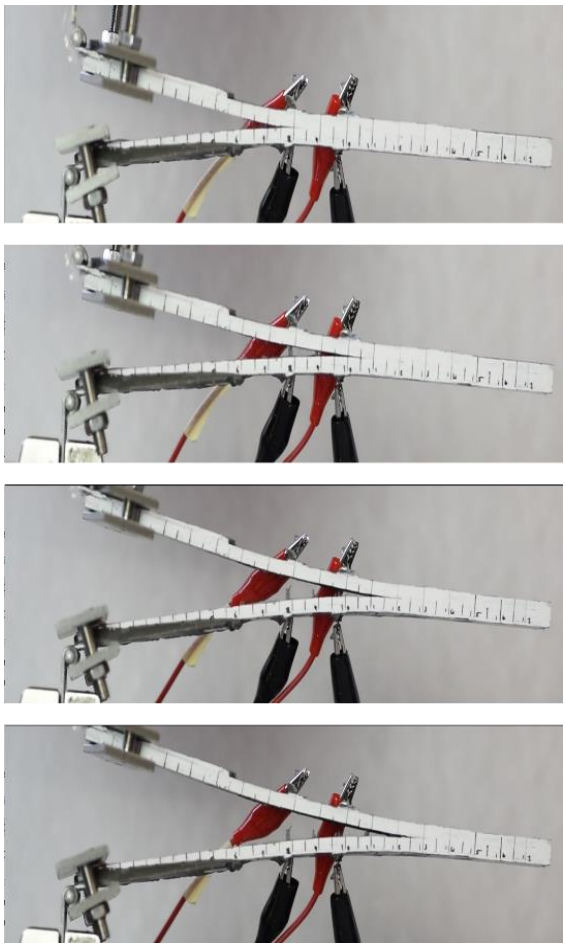

Figure 6-30 Video stills from DCB testing indicating the crack progression steps and arm bending in a coupon tufted with a 10 mm x 10 mm pattern with hybrid micro-braid.

Tufting density and location had a significant influence on crack propagation and, whilst crack initiation is not prevented by tuft insertion, the TTR does provide crack arresting properties.

Examination of the tested DCB coupons indicated a similar failure pattern to those experienced in the single tuft tests discussed in Section 6.2.2. The tuft rows showed asymmetric failure within one half of the coupon (usually the upper half), followed by bridging and pull-out before complete separation. Where the crack progression was abrupt and progressed through two rows, as observed in the 10 mm x 10 mm coupons, the profile of the broken tufts was uneven, with the bypassed tuft row appearing to be sheared at a more central point compared to the other tuft rows. All the ruptured DCB tufts had an oval aerial profile that was relatively flat in comparison to the ruptured single tuft test which had splayed copper-carbon fibre components (Figure 6-31).

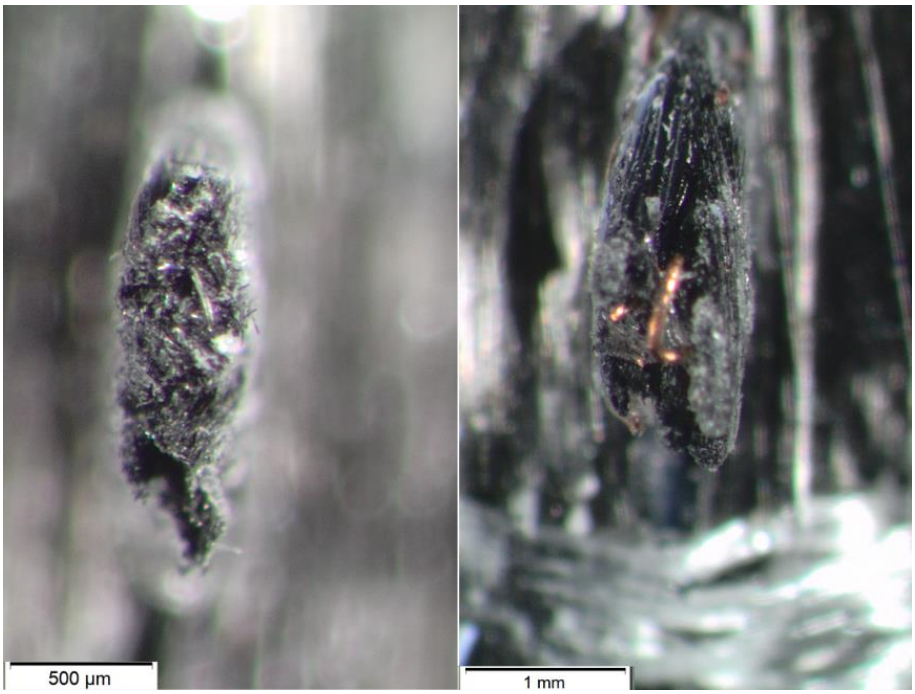

Figure 6-31 Aerial profile of ruptured DCB tufts. (Left) 4k tow commercial tuft and (right) hybrid carbon copper tuft.

The ruptured DCB tufts also had triangular or “dorsal fin” side-profiles, whereas the profiles of the ruptured single tufts were cylindrical and maintained the original micro-braid thread profile (Figure 6-32). This side fin profile appeared to be influenced by the UD fabric tow waviness and the lack of constraint provided by the UD tows, compared to the biaxial fabric used in the single tuft test. The profile of the ruptured 4k tufts showed more fracturing and unevenness compared to the hybrid tuft. Under load, more cracking sounds could be heard from the 4k tufted coupons than from those tufted with hybrid micro-braid thread suggesting fibre failure occurred within the specimens. The splintered profiles of the ruptured 4k also suggest that the four individually twisted 1k tows that comprised the 4k tufting thread failed sequentially under loading, as occurred during the yarn tensile test described in Section 3.2.2. The fracture profile of the 4k commercial thread and the more confined profile of the hybrid micro-braid thread had implications for the crack sensing capabilities of the specimens as discussed in Section 6.3.3.

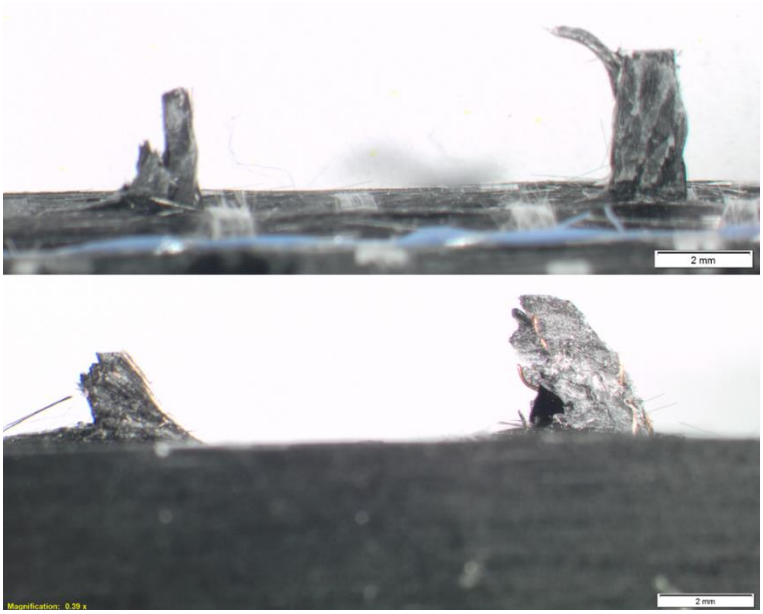

Figure 6-32 Side profile of ruptured DCB specimens (top) 4K commercial thread and (bottom) copper–carbon fibre hybrid micro-braid.

6.3.3 DCB specimen sensing capacities

Figure 6-33 shows the typical ER response of the DCB specimens to a propagating crack. The graphs present the normalised crack length ($\Delta Cl/Cl_0$), the difference between the initial cracklength (Cl_0) and the instantaneous crack length during testing (ΔCl) and the normalised resistance ($\Delta R/R_0$). Measurements of the ER using the MM yielded a high level of scatter due to both high conductivity and the available complex current paths along the in-plane carbon tow. The tufted DCB coupon creates a complex electrical network comparative to a system of resistors in both series and parallel.

The MM electrode wires were adhered directly to the DCB coupons at first and third tuft rows, which were unconnected to each other in the in-plane direction. The electrodes for the untufted specimens were attached at positions 80 mm and 100 mm along the specimen, resembling those of the 10 mm x 10 mm tufted specimens. The anisotropic conductivity of the carbon fibre tow meant that the source current in the untufted specimens was predominantly flowing in-plane direction, with the TT-direction conductivity dependent on an unknown number of fibre-fibre connections between UD plies. As a result, the initial ER was high compared to the tufted samples. As the crack propagated through the specimens, a weak increase in the TTER was observed as shown in graph (Figure 6-33).

In contrast, the tufted specimens provided a more direct TT current path, which was affected more by the crack progression. Therefore, as the crack moved through the tufted areas and caused rupture of the tufts, a larger change in TTER is observed.

All the tufted specimens showed a changed in TTER two to three orders of magnitude larger than the untufted specimens. In the case of the 4k commercial thread, whilst the change in TTER corresponded to each tuft row break, it was observed that there were instances when the crack progressed beyond the tuft row, which did not result in a TTER increase. A possible cause for this lack of response could be the carbon fibre thread having a similar conductivity as the UD carbon fabric. The conductivity of the specimen and tuft are dependent on fibre-fibre contacts and clearly multiple current pathways were available within the specimen. Damage to the 4k thread during tufting and coupon manufacture meant it is likely that the dominant current flow was in the in-plane direction. Despite an ER variation being observed, this was only clearly discernible once a substantial separation was achieved.

Another reason for this lack of sensitivity to crack progression was the sequential failure of the four individual 1k tows that made up the 4k thread tufting thread. Sequential failure of the individual tows was observed in the thread tensile tests (Section 3.2.2). It is possible that this failure also occurred during DCB testing and caused an asymmetric splintered shape of the ruptured tuft. As the delamination and separation of the two halves of the specimen progressed, the splintered part of the tuft maintained a connection or created additional conductive pathways despite the tuft breakage. It was also likely that partial failure of each 1k strand within the thread simply did not cause a sufficient TTER change that was measurable by the MM.

The response of the hybrid micro-braid thread tufted specimens was similar to the 4k thread, with a stepwise increase of ER with cracklength, although one order of magnitude higher. Unlike the 4k tow, copper components of the hybrid micro-braid thread increased the specimen TTC. Therefore, the source current predominantly flowed through the tuft in the TT direction and then between tuft rows through the in-plane UD fibre. The higher TTC of these specimens meant that any breakage of the wire components in the micro-braid thread caused a

significant increase in the TTER, thereby demonstrating the increased sensitivity of the hybrid braided tuft TTER to measure crack detection.

It should be noted that the electrode placement influenced the ability to detect cracks. This was observed during testing of the coupons with a 10 mm x 15 mm pattern, as shown in Figure 6-33. No TTER response was observed for an initial section of crack progression and corresponded to the area between the first and third rows.

This lack of sensitivity was unexpected as it did not occur in the 10 mm x 10 mm specimens, it is possible that because of the increased distance between the sense and source electrode, the influence of the UD in-plane tow was greater, thereby reducing the significance of the second row of tufts to the current path. It highlighted that in addition to the tuft thread types and materials, the tuft density and pattern, as well as electrode positions, must be considered during the design stage to ensure an optimum response.

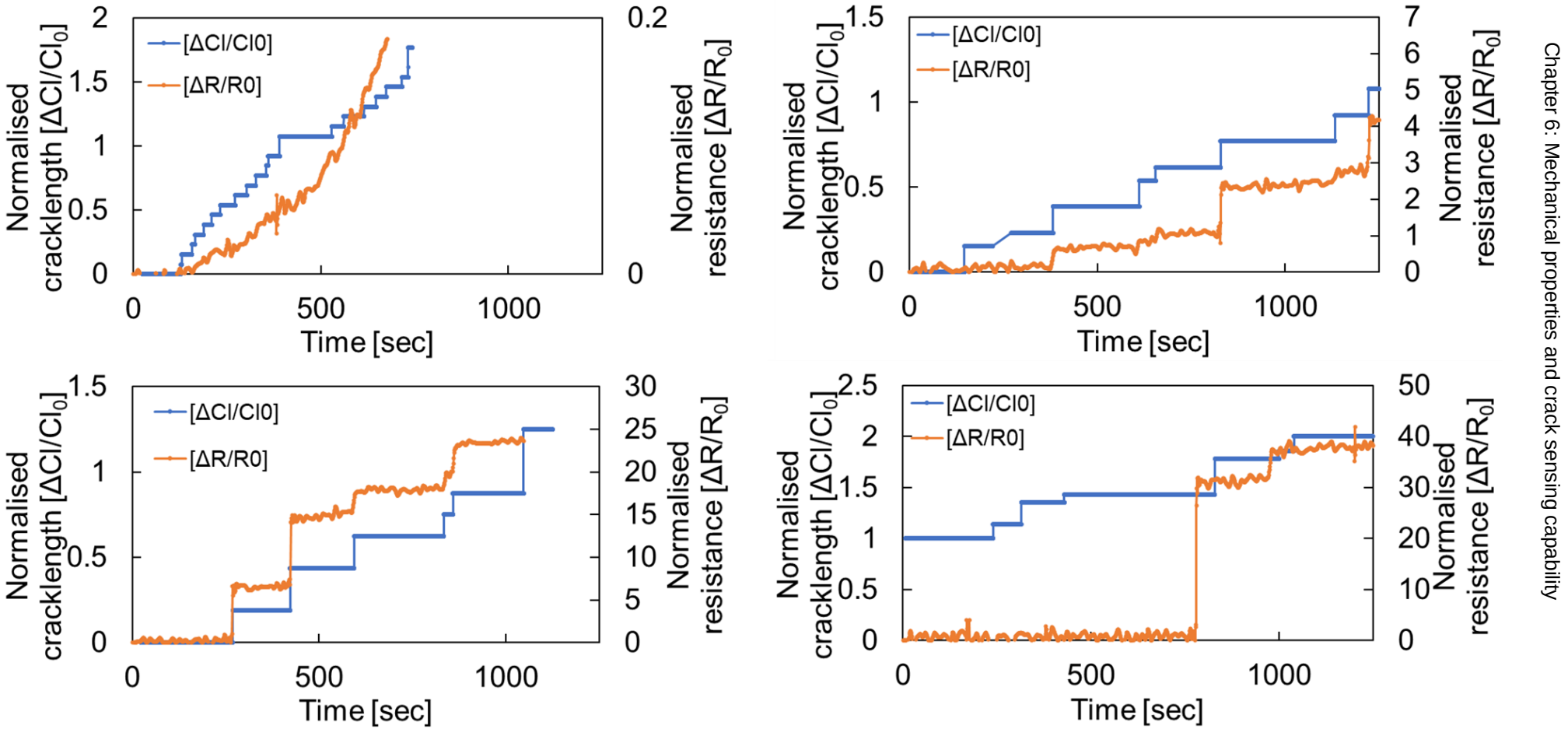

Figure 6-33 Normalised electrical resistance and crack length progression in DCB specimens. Top: (left) untufted, and (right) 4k commercial thread. Bottom: (left) hybrid micro-braided thread 10 mm x 10 mm pattern and (right) hybrid micro-braid 10 mm x 15 mm pattern.

6.4 Discussion

This study demonstrated that specimens tufted with both a hybrid micro-braid thread and 4k thread can effectively monitor delamination progression in tufted specimens via ER measurements. In addition to a monitoring capability, the tufts also increase the TT delamination resistance in comparison the untufted baseline, thereby creating a multifunctional composite. The TTER of the tufts increased with increasing crack length, with the hybrid micro-braid thread experiencing a greater increase in TTER due to tuft breakage in comparison to both the untufted and commercially tufted 4k thread.

When choosing thread material, whether hybrid or not, a balance must be achieved between manufacturing process adaptability and mechanical performance in the cured composite. Tufting reduces in-plane properties, although as other research have demonstrated, this is compensated for by increased delamination resistance [33, 95, 143]. The use of a hybrid braid does not change this compromise, but the improved conductivity may compensate for it further, depending on the application and situation. Manufacturing considerations when implementing this technique must involve parameters such as tuft areal density, micro-braid, or tuft thread materials, as well as extent of tufted areas. These should be considered to ensure optimised mechanical properties and to enable crack detection in areas susceptible to failure, in order to provide both structural reinforcement and health monitoring capabilities. Attention should also be paid to changes in laminate thickness and variations as well as potential changes in failure modes due to reinforcement.

Another factor to consider is the ply layup and fabric type. As seen in the single tuft test, the failure manner of the tuft might vary, resulting in variances in the ER response. This was due to the continued contact of the broken tuft within the tuft channel of the composite. This variability was not seen in the DCB tests, where the tufts failed similarly within the UD fabric. Increases in ER were achieved mainly by thread rupture, however, where decreases in ER did occur it still provided an indication of damage.

The MM electrode placements influenced the extent of the monitored area and ideally should be placed to enable a whole specimen assessment. The source and sense electrodes should be configured so that the sense electrode is as

close to the source as possible but in line with the potential direction of crack growth. This requires prior knowledge of failure modes in addition to any potential changes in failure mode caused by the introduction of TTR. The approach presented enables in-service structural health monitoring using in-situ electrical response assessment while also improving out-of-plane mechanical properties. By avoiding the need for additional sensors, it removed the parasitic weight penalties associated with current damage detection methods. In terms of the materials used and the extent of insertion, this method has the potential to be highly customised. However, more research is needed to fully comprehend the composites' complex current path. This would allow for a reduction in scatter in the recorded TTER, making crack propagation easier to identify.

7 STRUCTURAL ELEMENT DEMONSTRATOR

7.1 Overview

This chapter investigates the parameters encountered when attempting to upscale the SHM method and the intricacies involved in utilising a hybrid micro-braided tufting thread as a structural health sensor. The purpose of the chapter was to determine if the SHM method using ER could be applied to a more complex architecture and determine what configuration of electrodes would be needed to achieve whole structural assessment. T-joint sections were employed as the structural element demonstrator and pull-off experiments with untufted, and two differently tufted specimens were carried out. The chapter discusses T-joint fabrication, mechanical performance, and the potential of hybrid micro-braids to serve as crack sensors in a more complicated composite structure.

7.2 T-joint section manufacture

Formax FCIM 359-PB biaxial non-crimp carbon fibre fabric (NCF), containing 24k HTS carbon fibre tows held together by non-structural stitching was used for this demonstrator. The T-joints were manufactured using back-to-back ‘Ls’ on top of a carbon fibre skin base. The web comprised of two angled sections each of six plies bonded to a base plate of ten plies. Each section had a layup of $[(0/90)_6]$ such that the left and right sections of the web were symmetrical (Figure 7-1). The deltoid regions of the T-joints were filled with 28 ± 1 grams of

12k carbon fibre tow running along the length of the T-joint, that were extended beyond the plies to ensure they remained taut and straight.

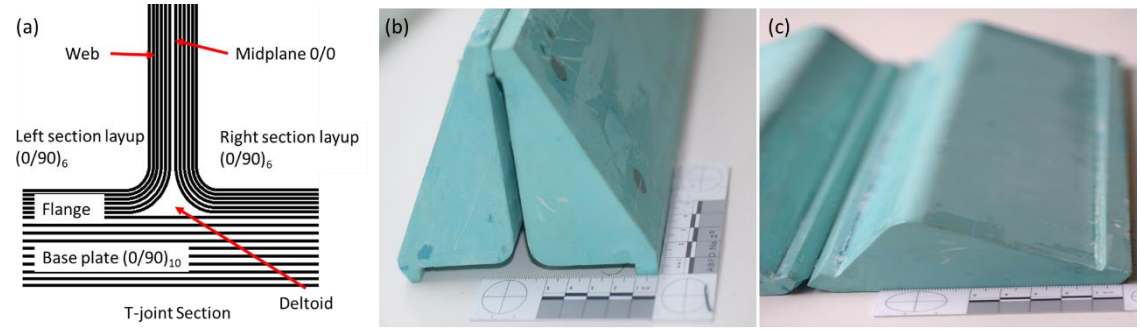

Figure 7-1 (a) Ply layup and T-joint technical nomenclature (b) Assembled T-joint forming tool, (c) disassembled T-joint forming tool.

The tufted preforms were produced using a bespoke 3D printed frame which restricted movement of the plies and facilitated tufting. The frame was made up of four angular 'L' sides, two supporting lengths and a laser cut Perspex base plate assembled and held together using bolts. The base plate of the preforming jig was manufactured with two cut-out sections to facilitate the tufting process (Figure 7-2).

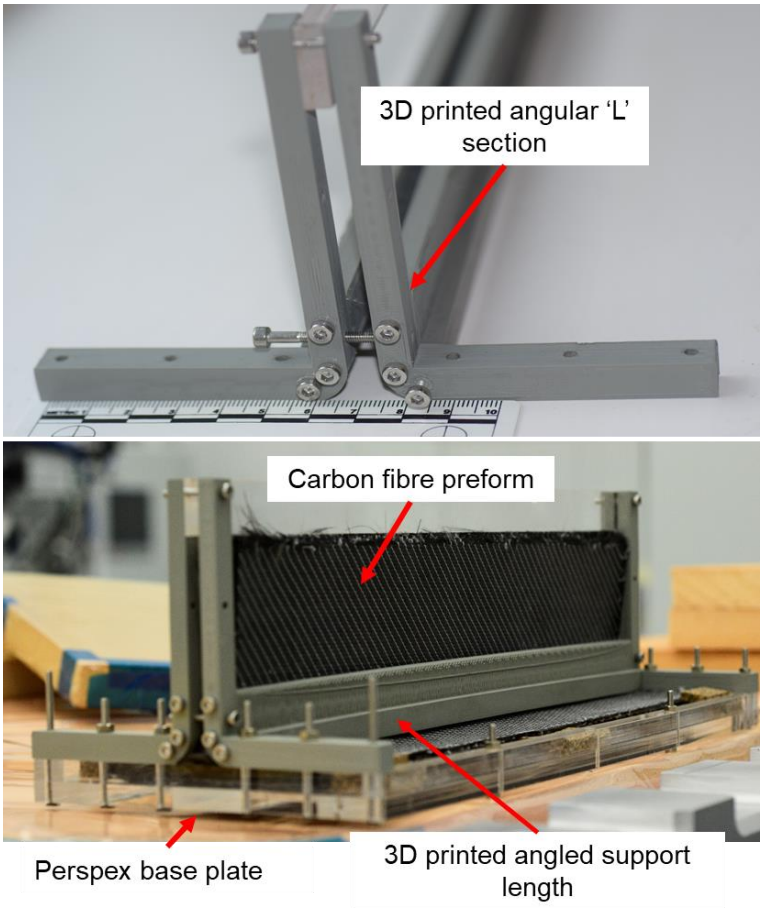

Figure 7-2 3D printed T-joint frame (top) without and (bottom) with preform.

The preform was made by inserting the web plies into the angular ‘L' sections, curving the plies around the radius, and inserting the carbon fibre tow along the deltoid section, after which the skin section was placed down and the frame baseplate was mounted and screwed secure. During tufting, the frame was secured using G-clamps and tufted using a RS522 tufting head, mounted onto a KUKA KLR 240 L180-2 2000 robot arm as previously described in Section 5.3.1 (Figure 7-3). Two parallel rows of tufts with a line spacing of 10 mm and tuft spacing of 10 mm were inserted through the stiffener flange and the adjoining composite skin preform, for a total of six rows of tufts into each T-joint, two in the vertical web section and two on each side of the flange.

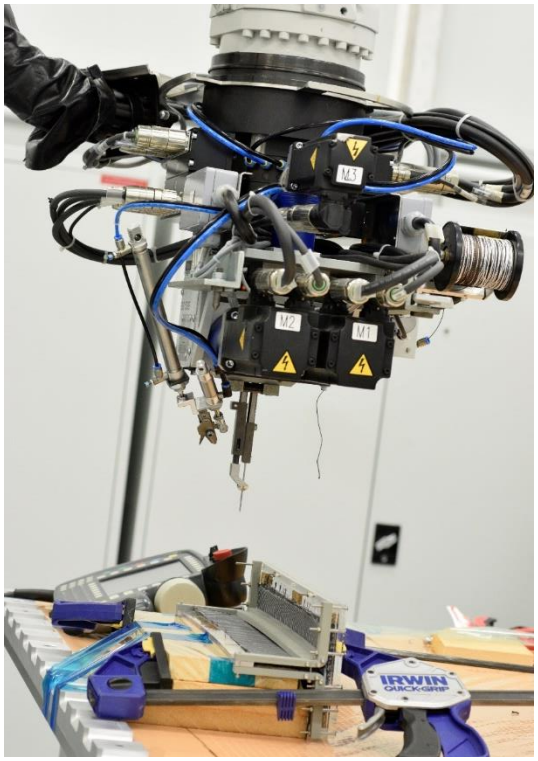

Figure 7-3 KUKA KLR robot with RS522 tufting head with preform restrain in 3D printed frame in clamp.

Compared to the untufted preform, the resulting tufted T-joint when removed from the frame was self-supporting. This increased the ease of handling during subsequent stages. The foam backing was removed before the preform was placed within the rigid tooling and infused using vacuum assisted resin transfer moulding system in a double bag (Figure 7-4). Control specimens containing no tufts were also produced and were manufactured by direct placement of plies into the T-joint tool with 28 ± 1 grams of 12k carbon fibre tow in the deltoid. All preforms were infused using Prime 27™ epoxy resin, allowed to gel at room

temperature for 12 hours before post cure in an oven at 80°C for two hours. The T-joints were allowed to cool at room temperature after curing, the infusion bagging material was removed, the edges were trimmed, and sections were cut from the cured composite piece with a diamond saw.

The T-joint specimens measured 150 mm ± 0.1 mm in length and 100 mm ± 0.1 mm wide with a mean thickness of 6.8 mm ± 0.7 mm and 6.9 mm ± 0.3 mm for the tufted and untufted specimens, respectively (Figure 7-5). A total of nine measurements were taken on each specimen, three on each side of the flange and three on the web. The measurements were taken on the tuft (position 1), 10 mm from the centre of the deltoid (position 2) and the 5 mm from the edge of the T-joint as described in Figure 7-6. The untufted control specimens were measured at points equivalent to the tufted specimens (Table 7-1)

Table 7-1 T-joint specimen thickness measurements

	Specimen type	**Position 1 [mm]**	**CV [%]**	**Position 2 [mm]**	**CV [%]**	**Position 3 [mm]**	**CV [%]**
Web	Tufted	6.0 ± 0.2	3	5.7 ± 0.2	3	6.3 ± 0.1	2
	Untufted	6.9 ± 0.7	10	6.9 ± 0.5	7	6.6 ± 0.3	5
Flange (left)	Tufted	7.3 ± 0.4	5	7.5 ± 0.2	3	7.0 ± 0.3	5
	Untufted	6.6 ± 0.9	14	7.5 ± 0.6	9	6.6 ± 0.5	7
Flange (right)	Tufted	7.3 ± 0.4	6	7.4 ± 0.4	5	7.1 ± 0.1	2
	Untufted	6.9 ± 1.0	14	7.3 ± 0.7	10	6.7 ± 0.7	11

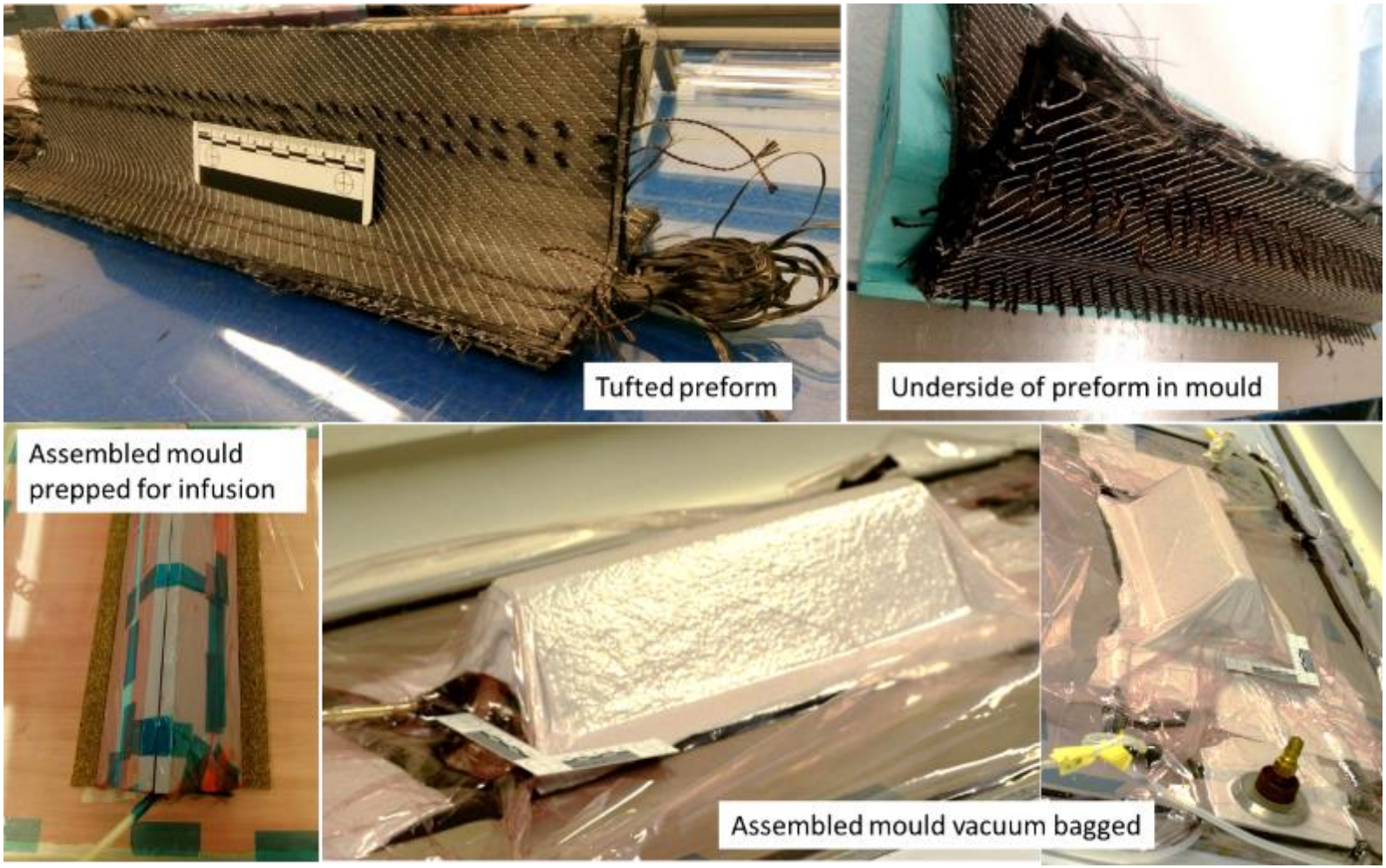

Figure 7-4 Post tufting T-joint preparation, vacuum bagging.

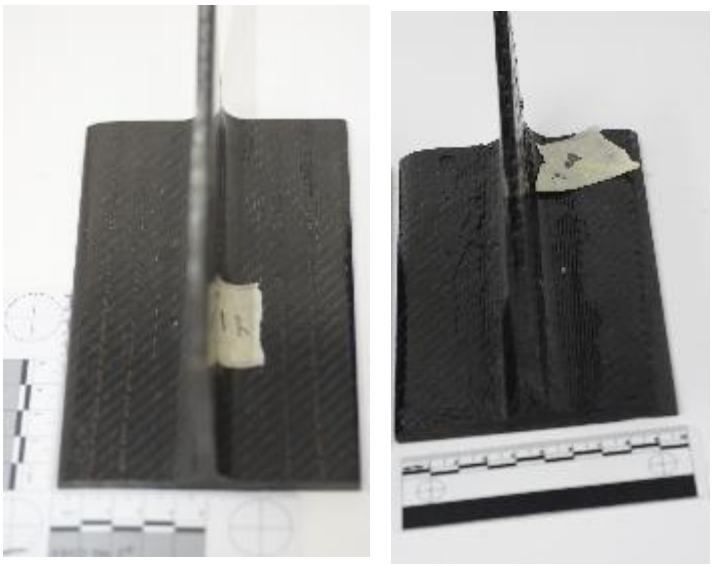

Figure 7-5 (left) tufted specimen, (right) untufted control.

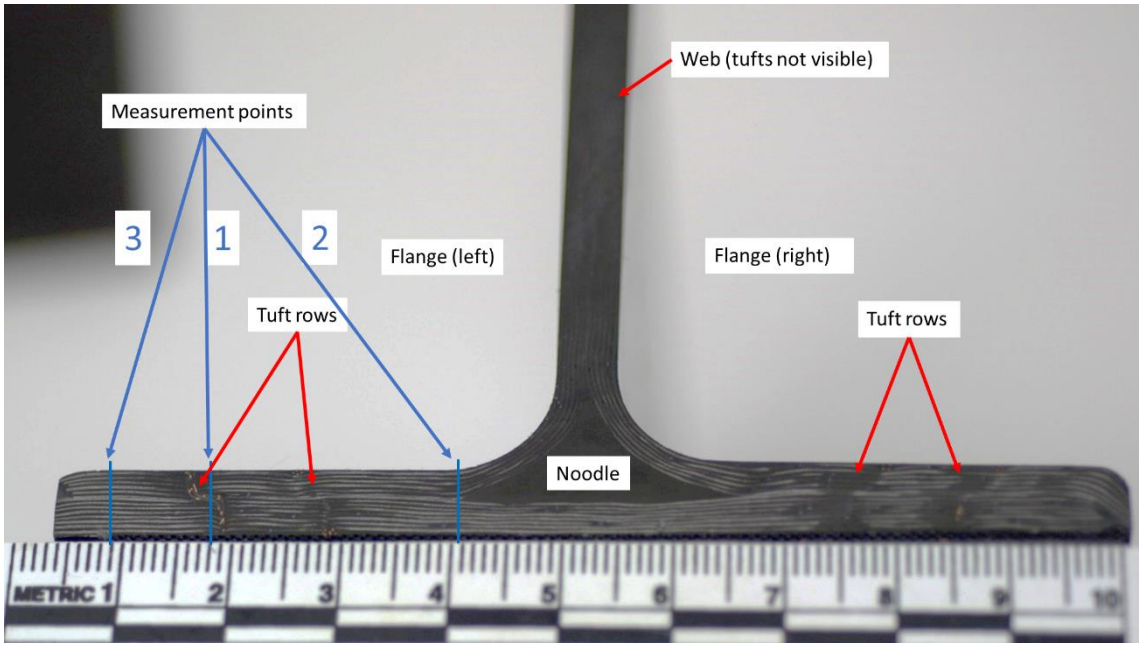

Figure 7-6 T-joint thickness measurement positions. Indicated are the three areas taken on the left-side flange.

The presence of the tufts caused undulation in the specimen thickness, but it was not as apparent as in the DCB samples (Section 5.3.1). The variability over the length of the T-joints from the edge, into the tufted area, and up to the deltoid was less than 1%, compared to 20% in the DCB specimens. This improvement in thickness uniformity was caused by the employment of the multi-part ‘L' tool, which increased the restriction of expansion in the preform, as previously seen in earlier studies. [23]. This restriction resulted in a more pronounced curvature of the tuft profiles in the T-joint compared to that seen in both the single tuft and the DCB specimens (Figure 7-7).

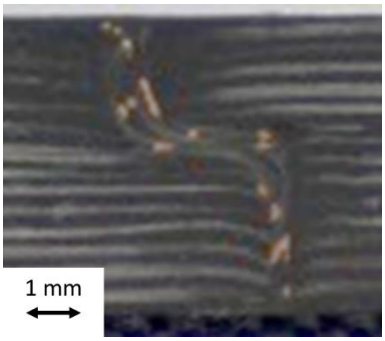

Figure 7-7 Curved tuft profile.

Between T-joint specimens, the coefficient of variation (CV) in thickness at each point for the tufted specimens ranged between 2% and 6% whilst the untufted specimens showed greater variability of up to 14%. The increased variability in non-tufted specimens was most likely caused by the plies lack of constraint during lay-up. Untufted specimens were more difficult to produce than tufted specimens. During the lay-up and infusion stages, ply slippage was difficult to prevent, resulting in increased flaws and thickness variability. The manual placing of the tool sections was particularly problematic during the untufted preform preparation, resulting in more noticeable movement of the plies. A visual examination revealed defects, most notably voids in the deltoid area, and resin shrinkage on the surface of the untufted specimens. Tuft insertion aided in restricting ply movement, removing issues during the preform assembly stage of manufacturing. The underside loops of the tuft specimens were manually flattened in one direction, however, following curing it was evident that some overlapping occurred (Figure 7-8).

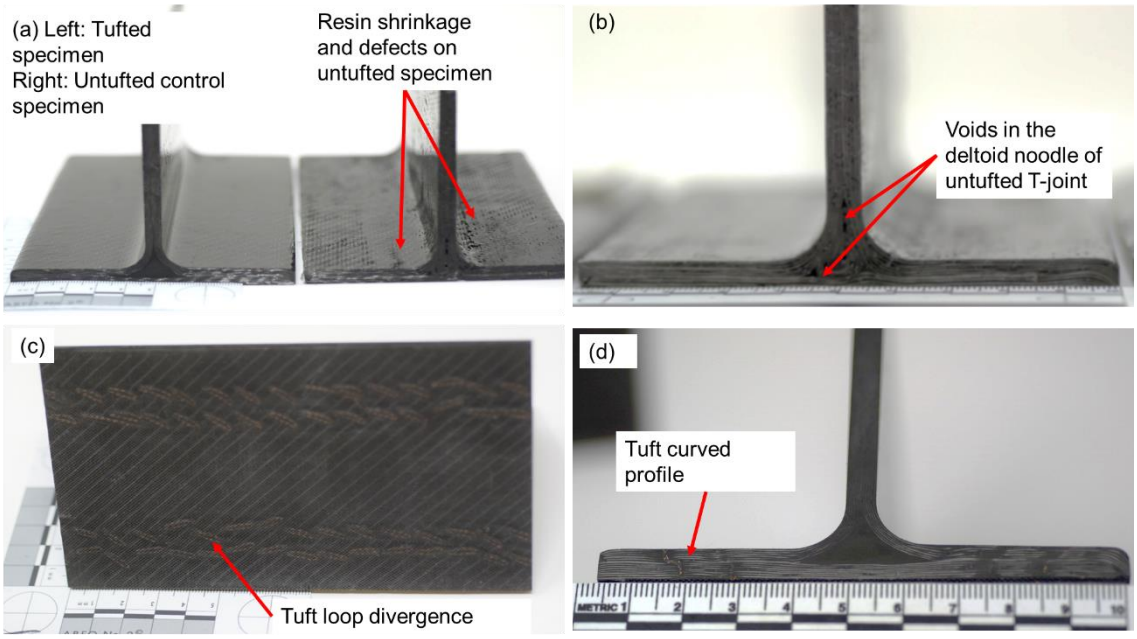

Figure 7-8 (a) Tufted and untufted T-joint specimens, (b): tufted specimen indicating loop overlapping, (c) untufted specimen profile view, (d) tufted specimen profile view and (d) curved profile of tufts.

7.3 Sample preparation

7.3.1 Electrode connection method

In a similar manner to the specimen testing in Sections 6.2.1 and 6.3.2, the T-joint demonstrators were examined to assess the ability of the microbraids to sense crack propagation. The T-pull loading system was designed to test the delamination sensing capabilities of the tufted multi-material microbraid. As described in Section 5.2.1, the electrode connections for the single tuft and the DCB tests were comprised of copper wire coated with silver paste, glued to the surface of the specimens. The cylindrical profile of these wire electrodes was not a concern during the single tuft and DCB coupon testing because neither test caused the electrodes to become caught in grips or compressed. However, because the restriction bars of the testing rig are positioned directly over the surface of the T-joint, they would have impacted the electrodes during this pull-off test. Compression of the wire electrode would have either damaged the electrode connection, resulting in erroneous electrical resistance (ER) measurements, or created stress concentration spots, and changed the failure mode. Therefore, for the T-joint pull-off tests, an alternative electrical connection method in the form of conductive matting was investigated. See Appendix B

The lack of consistent ER measurements and the surface preparation made the conductive matting unsuitable for this application. The solution was to use flat conductive copper tape instead of cylindrical wire.

The copper tape had a conductive adhesive backing with an overall through thickness electrical resistance of 0.001 Ω [248]. The T-joint surface was sanded to ensure electrical contact between the conductive copper tape and either a hybrid tuft or the carbon fibre of the T-joint. To aid with electrical connectivity silver paint was also applied to the sanded surface, and the tape placed on top. Araldite epoxy adhesive was applied to the edge of the copper tape to fully secure it and prevent movement during testing (Figure 7-9).

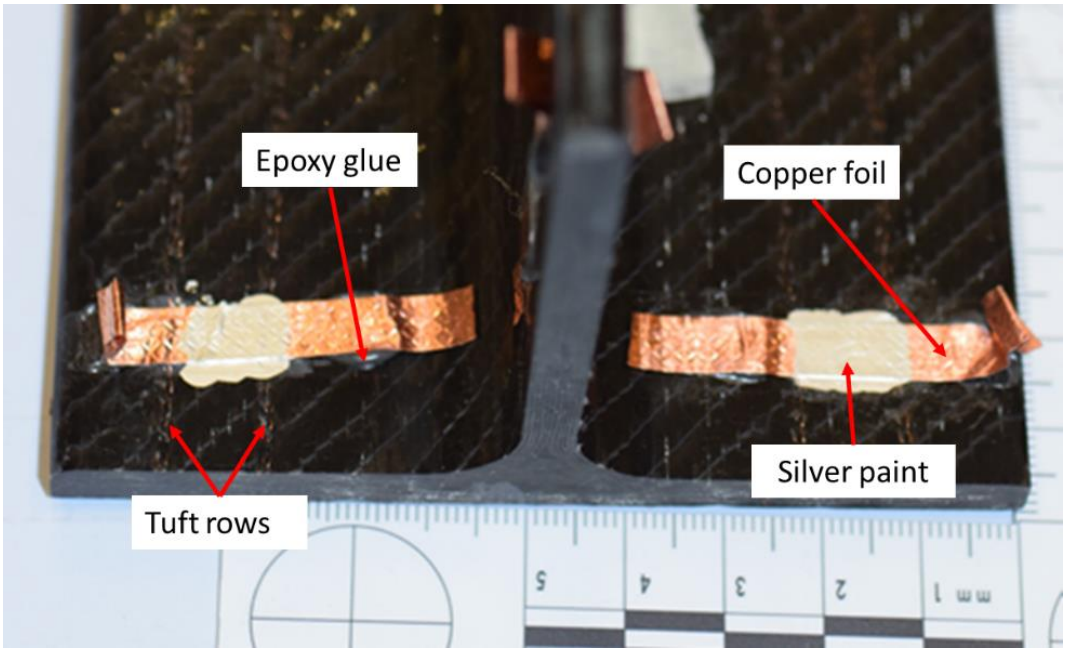

Figure 7-9 Electrode configuration.

7.3.2 Electrical response measurement method

In previously studied specimens, the failure initiation point and delamination were well-defined and progressed over a single flat panel. The electrode connections in these tests were made in such a way that the input and output electrodes were connected in the TT plane, and a single MM using a four-wire approach was sufficient to monitor changes in an electrical connection network. Testing the T-joint structure would result in the onset of failure at many locations inside the T-joint structure. When compared to previously examined coupons, crack propagation during a pull-out test was more complicated and likely to take a less predictable path. Therefore, a method of simultaneously assessing different parts of the structure was required. Utilising several MMs at once was unsuitable due to interference between the respective input currents. Therefore, a single current input was connected centrally to the web whilst individual output measurement electrodes were attached to three different areas as depicted in Figure 7-10. The output electrode positions were attached 10 mm from the edge of one side of the T-joint: one on each flange and another on the web. The current input was supplied using an Iso-tech power supply IPS303A unit set to a maximum voltage of 9 volts and an input current of 0.2 amps.

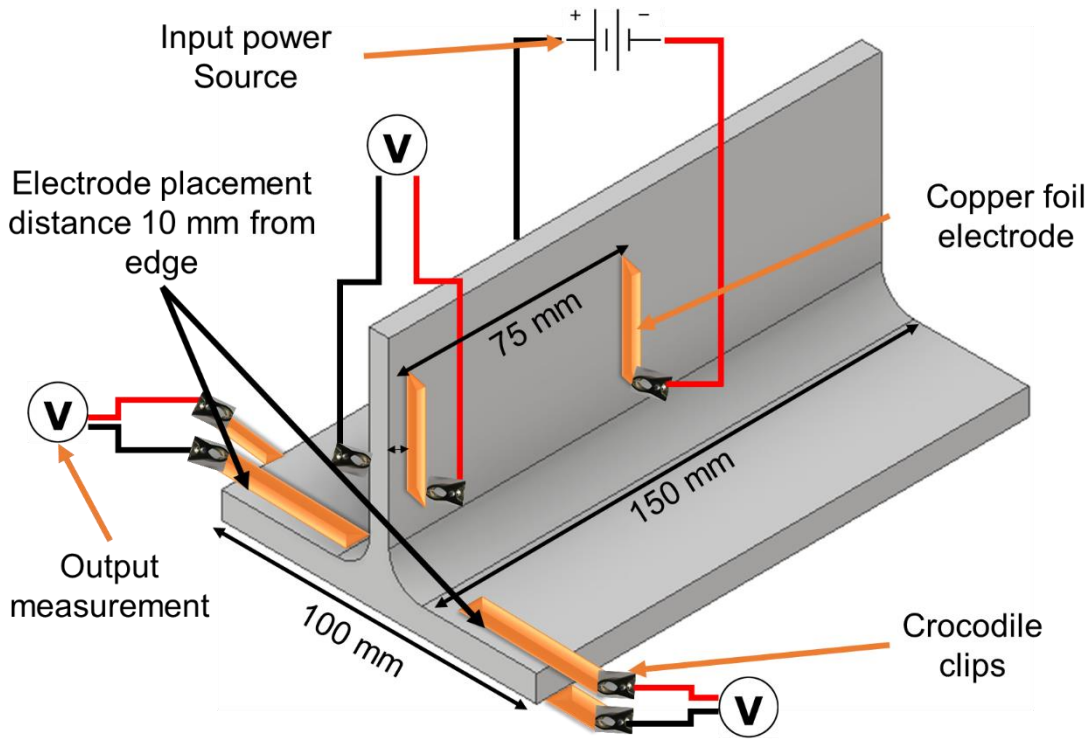

Figure 7-10 Schematic of power input electrode position and output electrode positions.

An electrically conductive network created within a carbon fibre structure could be represented as a system of resisters in both parallel and series. The predicted current path in the untufted specimens was dominated by carbon fibre ply direction. The biaxial fibre determined that the current would propagate vertically and horizontally along the respective plies. A small but comparatively limited current was likely to flow between plies along random carbon fibre-carbon fibre connections caused by consolidation, carbon fibre misalignment, and damaged tows. The TT carbon fibre connects are arbitrary and unquantifiable due to their sporadic occurrences.

The tufted specimen had three main electrical pathways; the first along the tufted rows, the second along the carbon fibre plies and finally between the tufts and the carbon fibre fabric. The tuft rows extended through the thickness of the T-joint increasing the electrical conductivity in the TT of the specimen. The in-plane electrical network, comparable to the untufted T-joint, was still present in addition to the three major electrical routes formed by the tuft. Due to its higher resistivity than the tufted zones, this in-plane network is anticipated to provide a minor contribution. A schematic representation of the electrically conductive pathways is depicted in Figure 7-11.

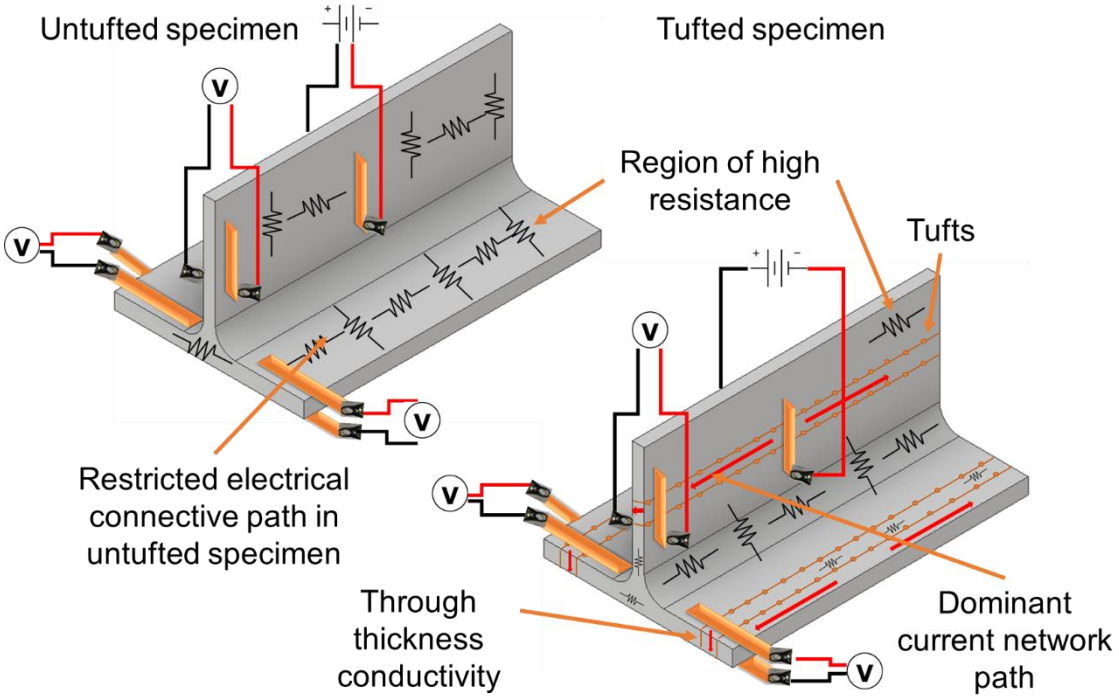

Figure 7-11 Electrical connectivity networks of untufted and tufted T-joint specimen.

The damage monitoring concept was based on the breakage of the tufted copper-carbon fibre hybrid thread, disrupting the electrical pathway and causing a fluctuation in the recorded output voltage within the specimen. In a fully intact undamaged tufted specimen, the electrical current would predominantly flow along the metal components of the thread and spread evenly between three output areas. The result of many output measurements was that if one area broke, the current path that was originally on that path would divert along other paths, potentially increasing another output reading. As a result, the overall trend and variations in output are more important than the specific numerical result.

7.4 Mechanical testing rig

The absence of a standard testing method for the examination of a T-joint specimens meant that tests were carried out using a bespoke loading rig (Figure 7-12). It comprised a steel base, two steel spacer blocks and steel half bars to restrain the specimen. The rig was designed to hold T-joint web directly within the testing machines grips and the flanges were restrained by the bars as depicted in Figure 7-13. The restriction bars were secured loosely with bolts in order to have the T-joint base suspended off the rig when tested. This prevented the ER measurements being affected by compression effects and guaranteed linear contact along the specimen surface.

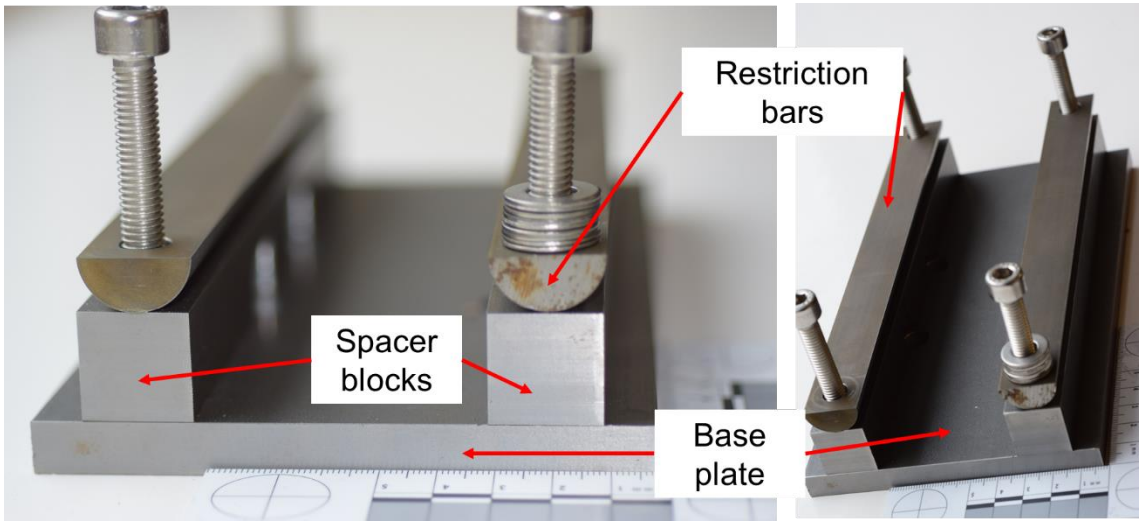

Figure 7-12 Image of the T-joint testing rig.

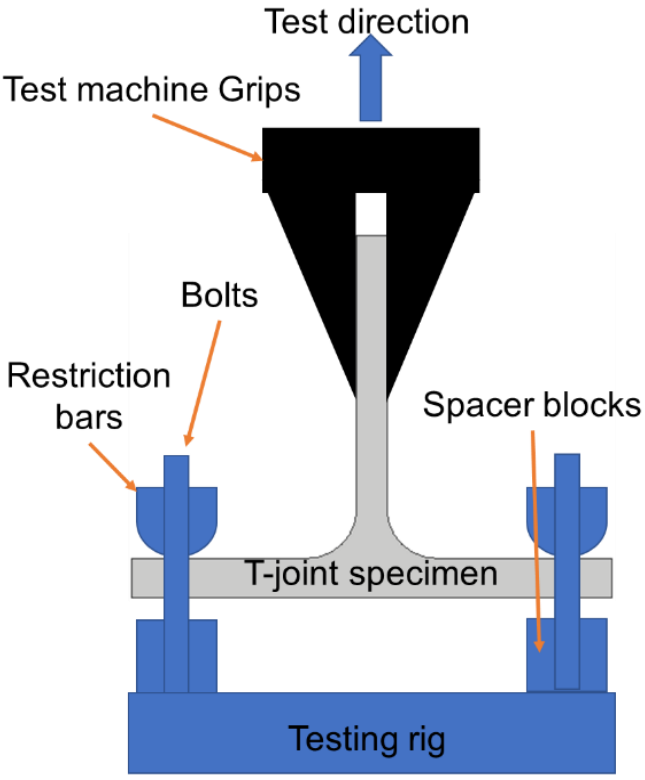

Figure 7-13 Schematic of T-joint pull-off testing setup.

7.5 Experimental setup

Mechanical testing was performed using an Instron 8875 hydraulic testing machine equipped with a 25 kN Z742-301 load cell and the testing rig mounted centrally within the lower grips. The flange and skin were secured in the testing rig with the load points approximately 35 mm from the centreline of the T-joint. The vertical web of the T-joint specimen was positioned centrally in the testing rig and secured in the upper grips.

The T-joint was raised within the testing rig enough to engage the restriction bars and ensure that clear space was achieved between the T-joint base and the testing rig. This reduced the likelihood of electrical interference from the testing rig and enabled easier attachment of the crocodile clips. To further isolate the T-joint from electoral interference two sheets of paper were placed between the restriction bars and the specimen (Figure 7-14). The electric connections were attached using crocodile clips and a current input of 0.2 amps was applied using an Iso-tech IPS303A power supply. The ER was indirectly measured by monitoring the voltage output at three points. These were recorded using a National Instruments™ analogue instrument and a LabVIEW program. The load output from the Instron was synchronised with the voltage

output from the specimen. The relative displacement of the four areas of interest were tracked using a Digital Image Correlation system as showing in Figure 7-15.

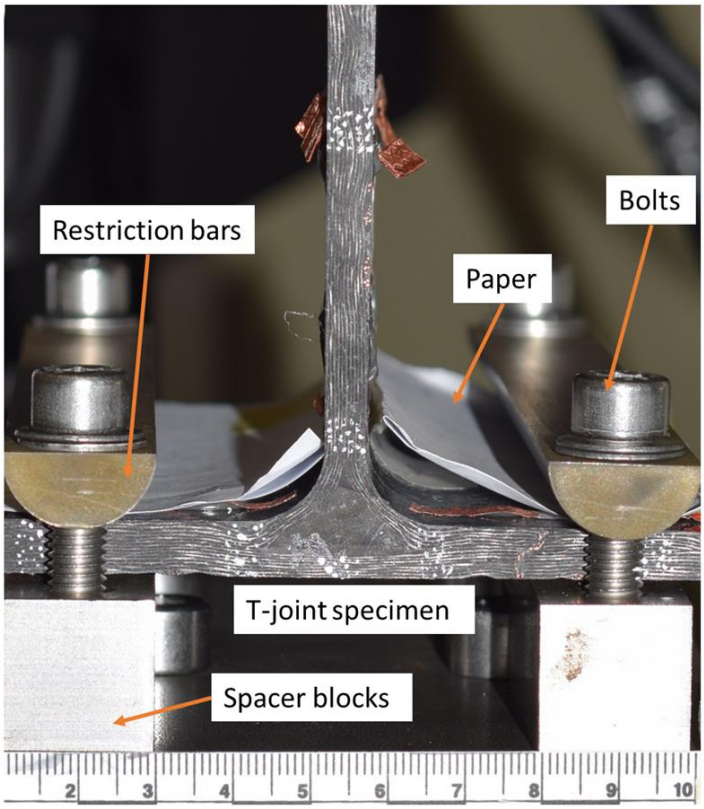

Figure 7-14 T-Joint specimen in testing rig.

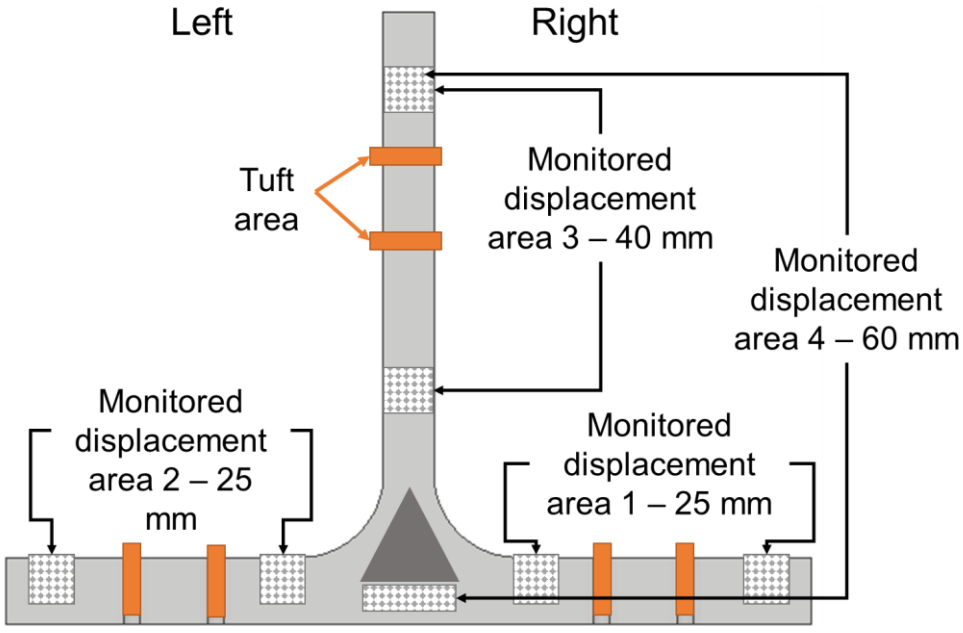

Figure 7-15 Areas monitored by the image correlation video gauge camera.

These four areas were the three tufted areas and the fourth included the deltoid region of the T-joint. The crosshead displacement rate was set to 2 mm/min to be consistent with the DCB test. The displacement was maintained beyond the first point of failure to the point where the central web failed, or until it was deemed that further displacement would not produce useful results. The experimental setup is pictured in Figure 7-16.

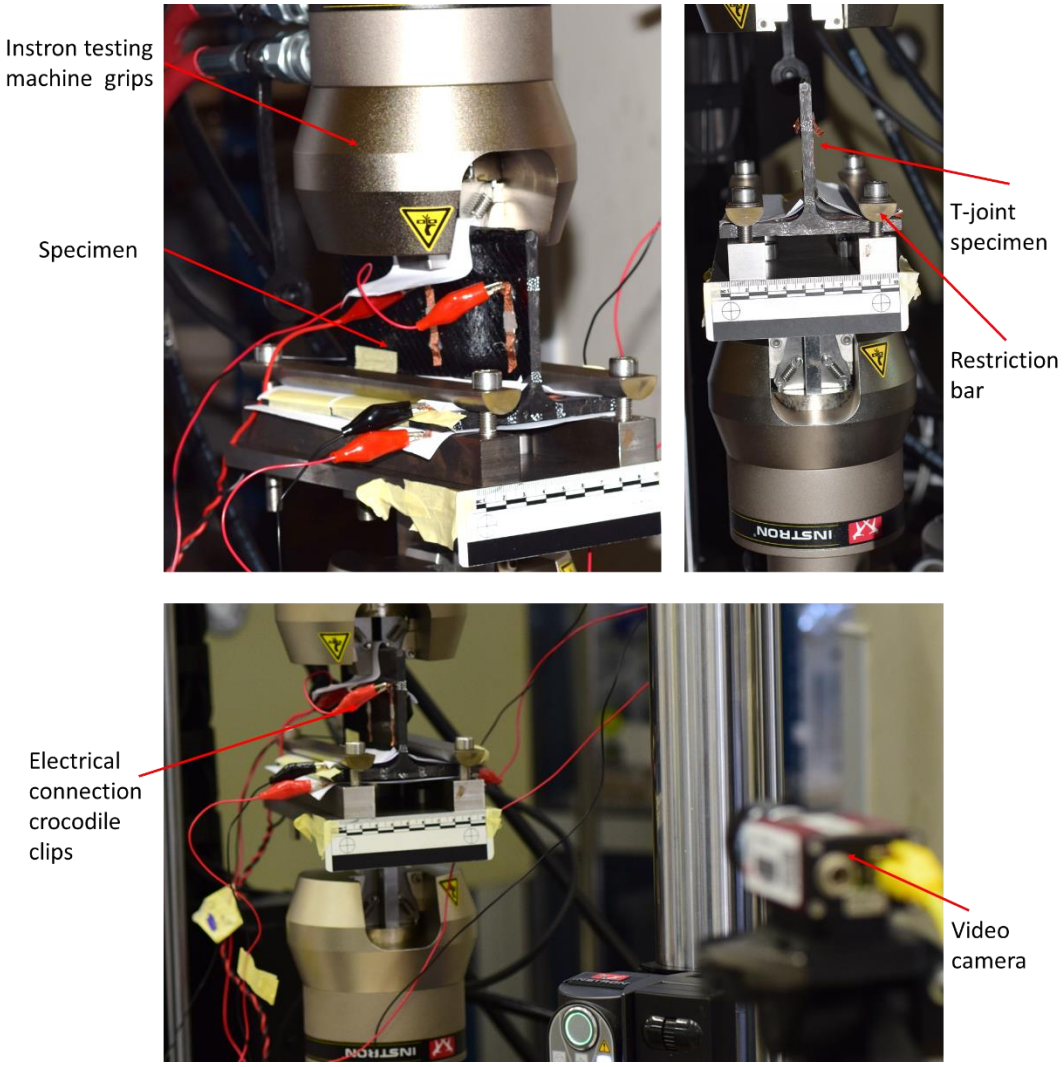

Figure 7-16 Experimental apparatus for T-joint pull-off test.

7.6 Results

7.6.1 Mechanical response

The load-displacement curves for the tested T-joint specimens are provided.in Figure 7-17. A total of four T-joints specimens were tested: two tufted T-joints

and two untufted controls (Results from all specimens tested provided in Appendix C).

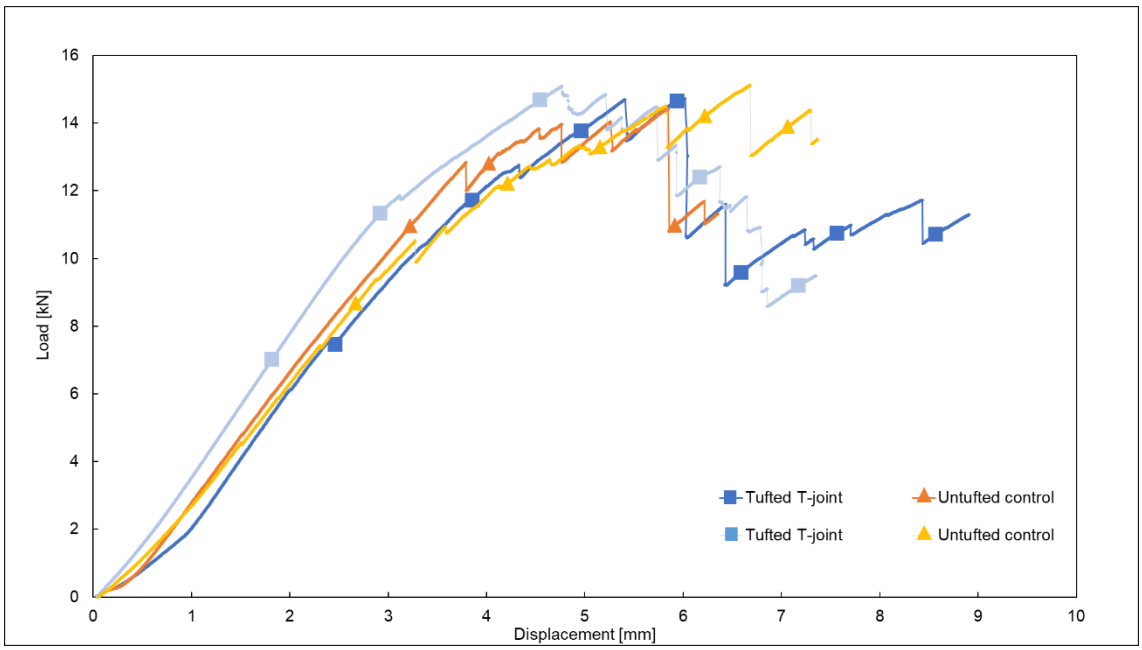

Figure 7-17 Load-displacement curves for untufted control and tufted T-joints.

The plot depicts similar pattern in failures for all four specimens irrespective of the presence or absence of tufts. In general, crack initiation occurred in the deltoid region of the specimens and propagated along the ply edges. For both specimen types there was a build-up in stress concentration at the crack front, followed by a sudden load drop and a subsequent increase in delamination length. Three stages can be identified in the failure profiles. The first presents an elastic loading before crack initiation. The second, begins at the point of crack initiation and are seen as relatively small load drops. The final stage contained larger irregular load drops. The testing was continued until the separation of the web or the separation of flange from the deltoid region occurred. The recorded maximum force of the tufted and untufted specimens were also similar (Table 7-2).

Table 7-2 T-joint specimen maximum force

Category	**Tufted**	**Untufted**
	kN	kN
Test 1	15.1	14.4
Test 2	14.7	15.1
Average Max. Load [kN]	14.9	14.8
CV [%]	1.3	2.4

Figure 7-18 shows the final condition of the two T-joint types. The lack of discrepancy in the load-displacement curves between the two types of T-joints specimens indicates that the tuft rows were not sufficiently engaged to fully influence or increase the delamination resistance compared to the untufted specimen. The still images from the videos (Figure 7-19 and Figure 7-20) indicated that the crack initiation was closer to the deltoid region and had substantially increased before reaching the tufted rows.

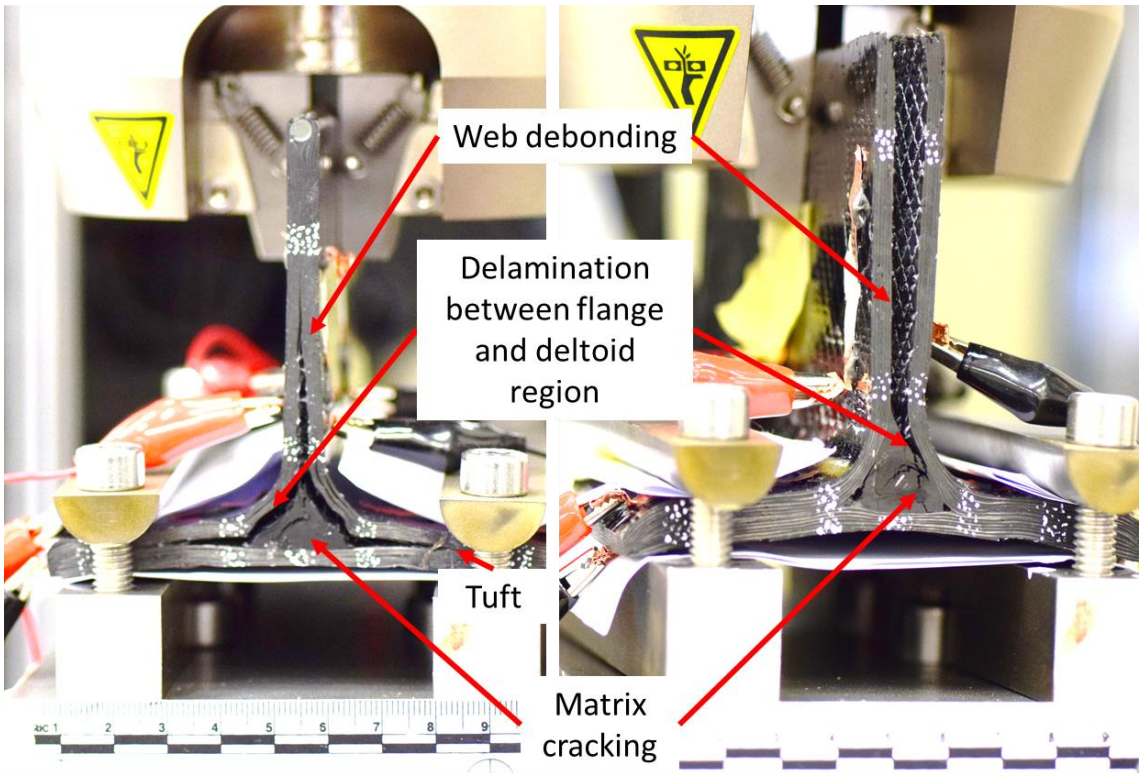

Figure 7-18 Images of tested (left) tufted and (right) control untufted T-joint specimens.

Despite this oversight in tuft location, video assessments (Figure 7-19 and Figure 7-20), provided an insight in failure progression and highlighted some slight variations between the two different specimens which was not immediately apparent. Delamination occurred between the deltoid and flange plies in the tufted specimen, and fracture propagation appeared to be evenly distributed between the web and both flange sides. In the untufted control, the crack propagated through the deltoid and up into the web and was generally less uniform and unpredictable.

The three stages of failure of the tufted specimen can be characterised :

Stage 1: Initial linear increase in load - no visual defects (Figure 7-19(a))

Stage 2: Minor load drops correlating with crack initiation within the deltoid region propagating around the ply-deltoid boundary and web centre (Figure 7-19(b)). Further, but limited, crack advancement around the edges of the deltoid region and along base (Figure 7-19 Video stills of tufted T-joint testing. Stage 1(a), Stage 2(b) and (c) and Stage 3(d) and (e).(c)).

Stage 3: The final stage was characterised by larger load drop corresponding to significant crack growth between the base and delamination into the web ((Figure 7-19(d)). Final failure occurred with the debonding of the base from the web section but, despite the extent of debonding the tufted area remained intact Figure 7-19(e)).

In comparison, the untufted control comprised:

Stage 1: Linear load increase – manufacturing defects evident (Figure 7-20(a)).

Stage 2: Larger initial load decrease compared to tufted specimen (Figure 7-20(c)). Crack initiation in the untufted specimens occurred within the deltoid region, but unlike the tufted specimen, crack propagation took the form of matrix cracking within the centre of the deltoid as well as debonding upwards into the web. The plateau region of the load-displacement curves corresponded to percolating cracks within the matrix of the deltoid.

Stage 3. Multiple points of matrix cracks within the deltoid with delamination in the web. (Figure 7-20(d)). The maximum load point and subsequent drop corresponded to the point that full debonding of the ‘L’ sides of the web (Figure 7-20(e)).

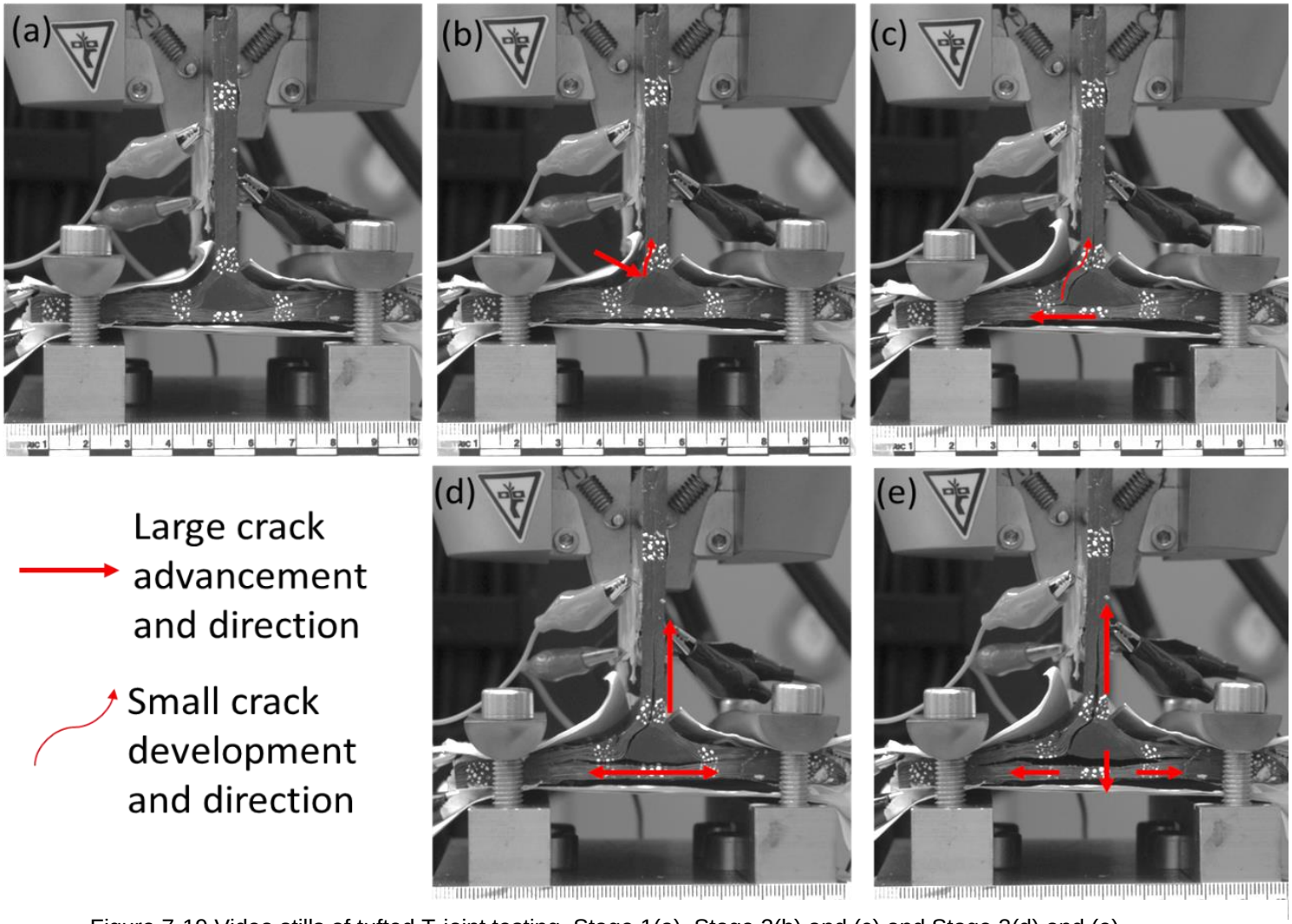

Figure 7-19 Video stills of tufted T-joint testing. Stage 1(a), Stage 2(b) and (c) and Stage 3(d) and (e).

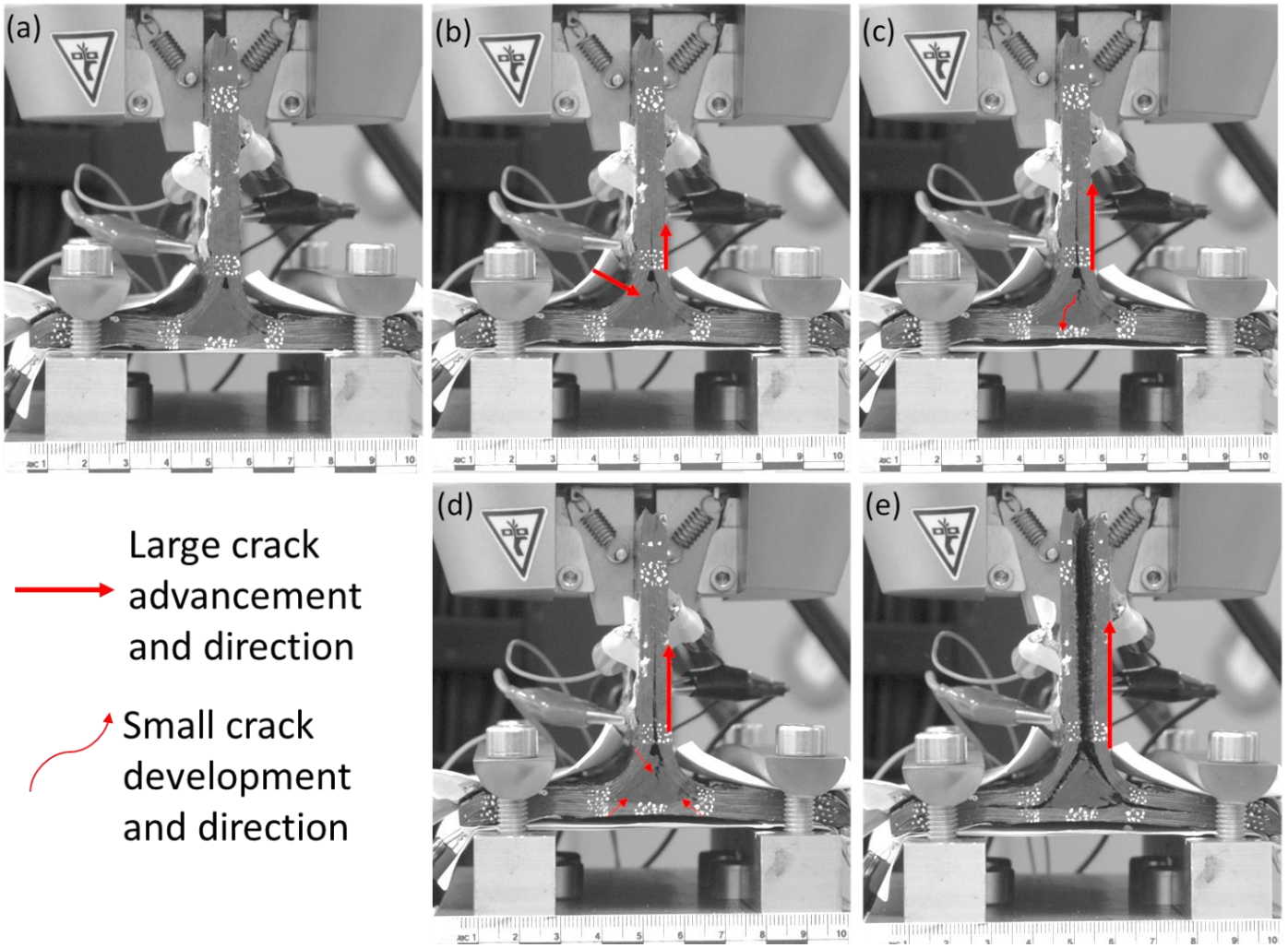

Figure 7-20 Video stills of untufted control T-joint testing. Stage 1(a), Stage 2(b) and (c) and Stage 3(d) and (e).

Limitations in utilising the video gauge were experienced due to the run-arrest failure profile of the specimens. The rapid movement resulted in the video gauge losing tracking and creating an erratic profile that was not representative of the testing events. The displacement monitoring of the tufted regions provided little insight in the dynamic response of the tufts due to crack growth. This was mainly due to the advanced crack length prior to reaching the area. Figure 7-21 shows close-up images of visible tuft rows between the flange and base of the T-joint specimen. The advancement of the crack beyond the tuft results in some debonding and fibre breakage but essentially the tufts remained intact.

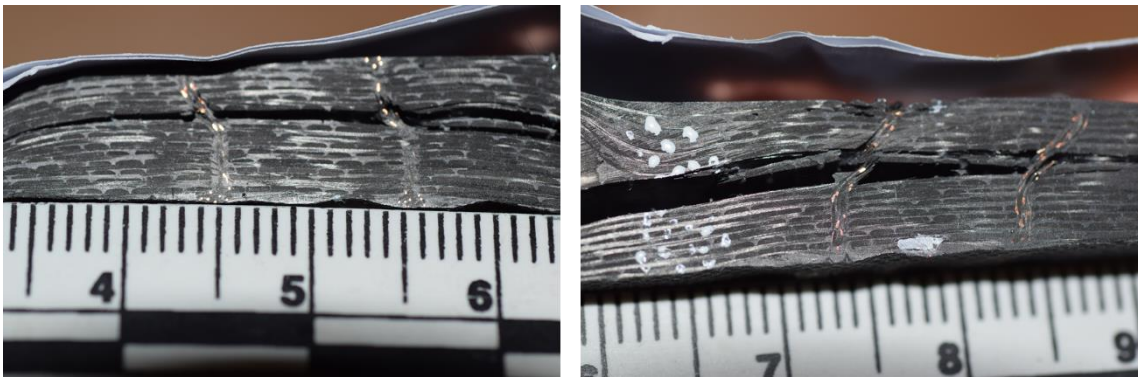

Figure 7-21 Tuft rows after testing.

7.6.2 CT scans

CT scanning of two specimens, an untufted control and tufted specimen was undertaken to determine the internal condition of the tufts within the composite part. Scans were taken at the National Composite Centre using a Nikon XTEK 320H platform with a reflection target mounted using a flat panel detector. Images were acquired, without a filter, at a voltage of 124 kV, 142 micro amps and exposed for 500 ms. Each scan was 2600 projections with an average frame rate of 4, and a resolution of 88 microns. Figure 7-22 shows the whole specimen scans of the untufted and tufted T-joints. Damage and debonding are indicated by the dark grey along the deltoid region, while the paler grey indicates undamaged regions. The tufts are identifiable due to the copper wire component (purple). The carbon fibre tows with the hybrid thread are indistinguishable from carbon fibre of the composite. The other coloured areas

(blue and purple) are the areas where electrodes were attached and caused by residual silver paint.

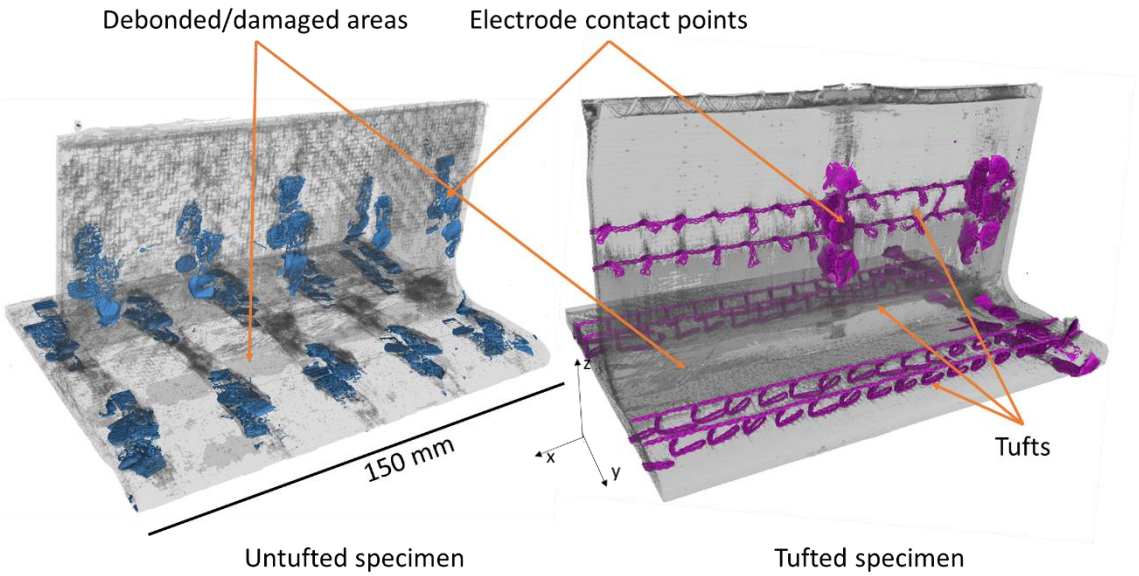

Figure 7-22 CT-scans of untufted and tufted specimen.

Figure 7-23 shows the copper wire component of the tufts with the carbon fibre digitally removed. The tuft architecture within the preform was accentuated and highlights the compressed condition of the thread in the TT direction caused by restriction during infusion using a semi-rigid tool.

The sectioned images of the T-joints were also examined and confirmed that the tufts did not break during testing despite the crack propagation. Figure 7-24 (a-d) shows images of the sectioned assessment through the specimen of all three tufted areas. No indication was found that the tuft rupture occurred within any the areas. Figure 7-25 (a-b) show similar images of the untufted specimen where voids and manufacturing defects were evident throughout the deltoid region.

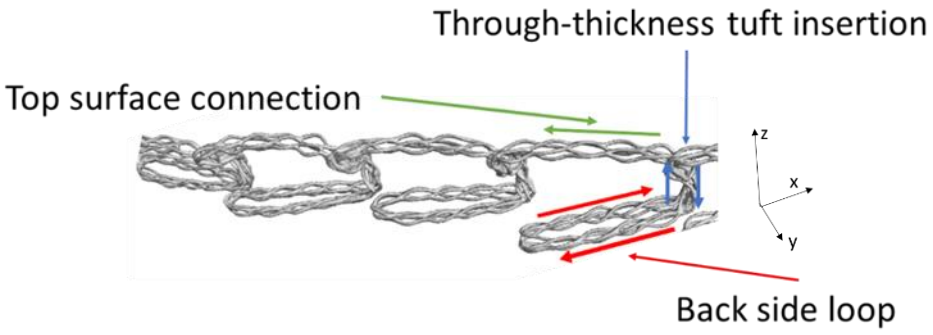

Figure 7-23 CT scan: copper wire component.

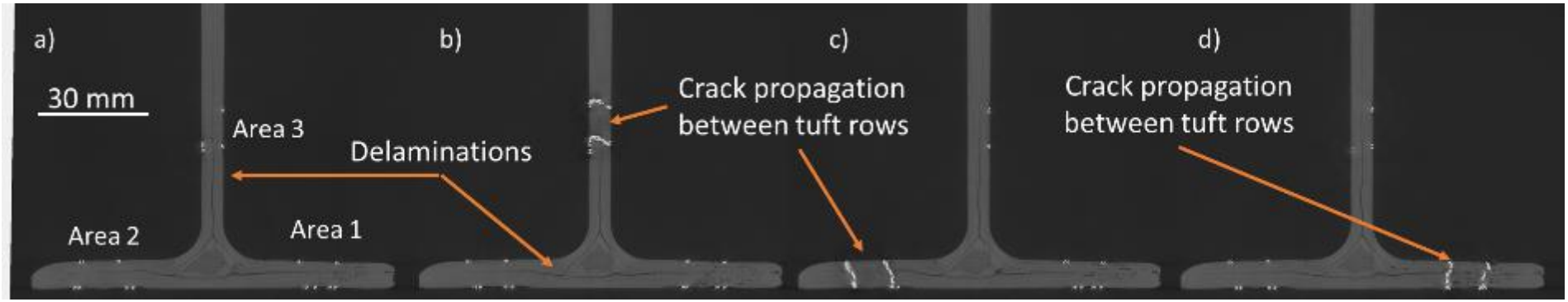

Figure 7-24 CT-scans tufted specimen - sectioned along specimen.

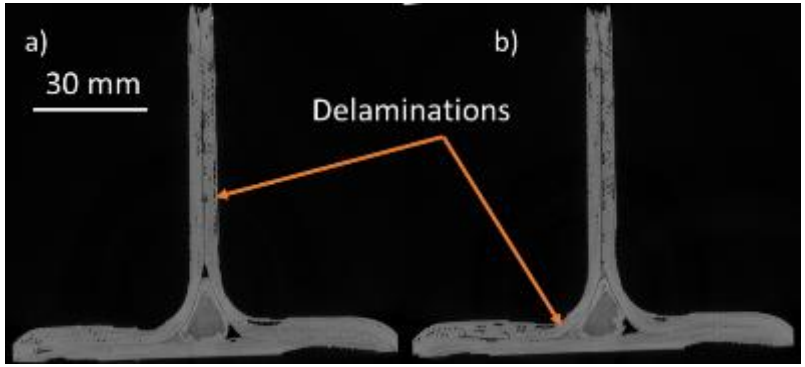

Figure 7-25 CT-scans untufted specimen.

7.6.3 Electrical response

Three positions of each T-joint were monitored to establish if changes in ER corresponded with crack propagation in the structure. The data acquired contained a high degree of noise and scatter caused by local variability of electrode contact construction, placement, and the complex electrical network. In general, the electrodes positioned on tufts had good connectivity with ER measurements two orders of magnitude lower than those electrodes on the untufted specimens. The refractive index, which represented a moving average of the zeroed normalised resistance of the recorded data, was used to illustrate the ER change over time. Measurements of visible crack developments were measured using ImageJ from synchronised video gauge images.

Figure 7-26 provides an illustration of visible failure in an untufted sample along with a plot of resistive index and load profile. Each image details the visible crack length on each monitored side corresponding to the load drops labelled (a) to (e) on the plot. As shown in the schematic, crack initiation in this specimen occurred along the web (position 3) and moved along the deltoid (position 1). Subsequent delamination progressed along both flanges (positions 1 and 2) and resulted in the complete debonding of the web. The plot of resistance index over time shows no response from either of the two electrodes at positions 1 or 2. The electrode at position 3 shows a sharp spike which was in response to partial detachment of the crocodile clip with the copper electrode rather than by delamination.

In contrast, the tufted specimens presented a different sensing behaviour. Failure began and spread more significantly along position 2 than position 1, as shown in the schematics and plot (Figure 7-27). During the last stages of testing, the crack caused an increase in resistance index at position 2 corresponding to images (e) and (f). Prior to this stage, no response was recording despite crack propagation into the all the tufted regions. Video gauge image analysis revealed that crack development at position 1 resulted compression and crack closer at position 2.

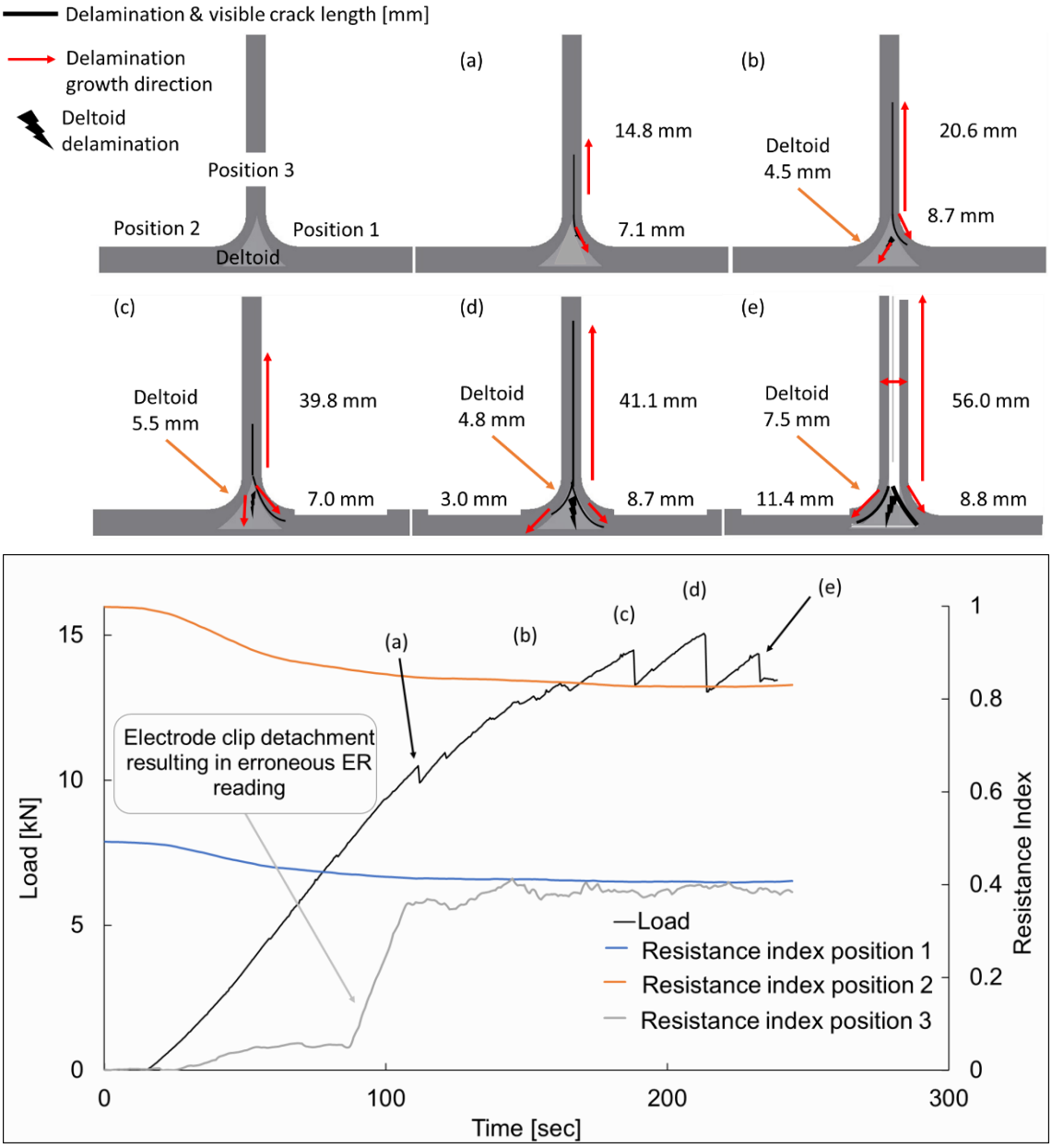

Figure 7-26 (Top) Schematic of visible crack propagation at front of T-joint and (bottom) plot of resistance index and load over time of an untufted specimen.

Crack bridging by the tufts also occurred which maintained the electric pathway. An ER response was only achieved once substantial separation or tuft rupture occurred in respective areas. The separation of the base from the flange eventually influenced the tufts sufficiently to generate a response from the position 2 electrode. In position 1, despite the crack eventually propagating into the tufted region, the delamination did not result in a response, owing to tufts remaining intact. Similarly, the advancement of the crack along position 3 did not propagate into the tufted region and therefore no ER response was measured.

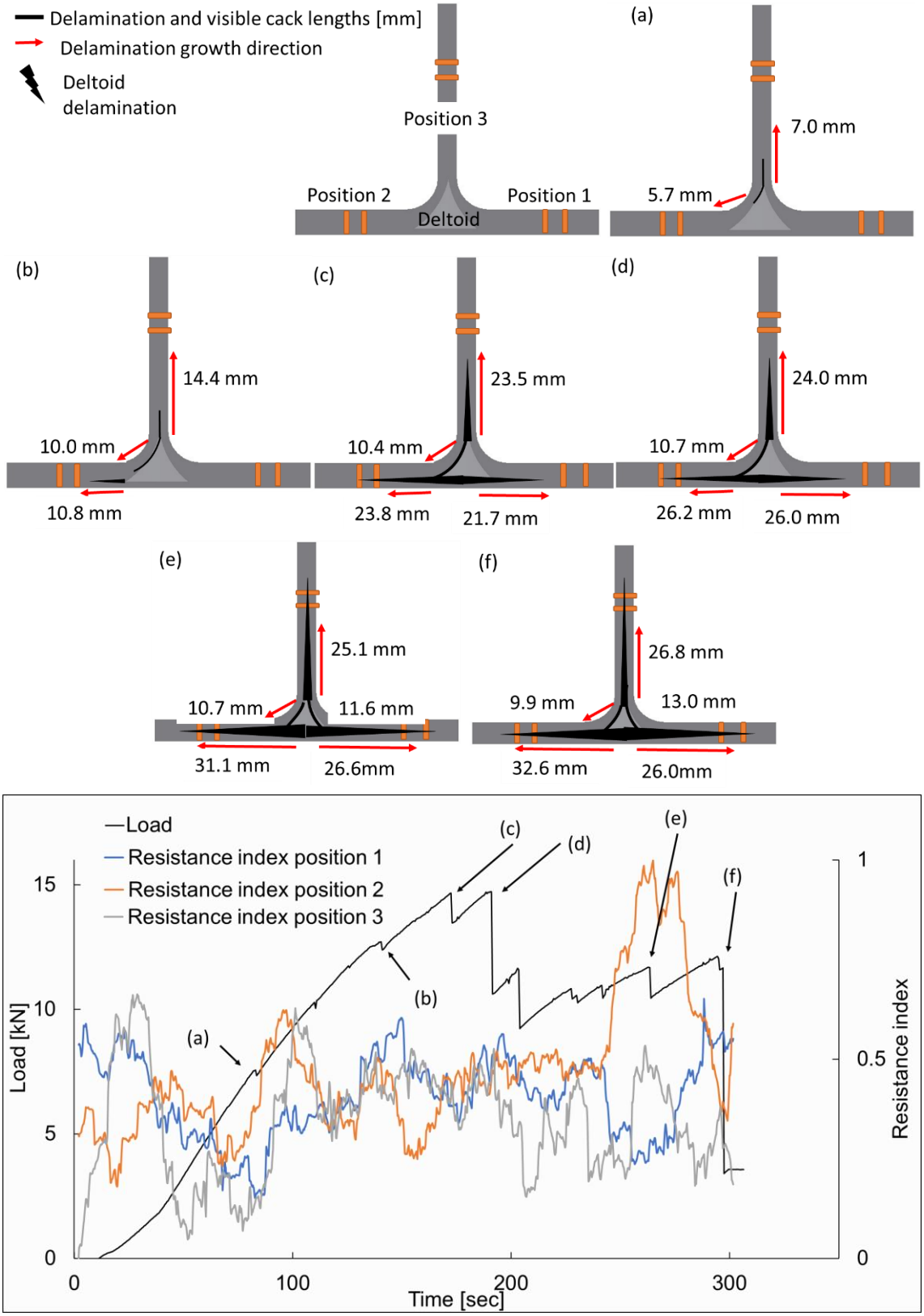

Figure 7-27 (Top) Schematic of visible crack propagation at front of T-joint and (bottom) plot of resistance index and load over time of a tufted specimen.

7.6.4 Discussion

As expected, design challenges arose when progressing from flat rectangular composite specimens to more complex T-joint structures. This complexity in upscaling centred on determining the positioning of the electrodes in relation to failure progression. Electrode position and other variables such as tuft placement, density, and pattern, were all based on results from single tuft and DCB test results. It was evident from the lack of ER response from the T-joint, that determining such parameters from the flat coupons were not sufficient. There was a lack of sensitivity experienced in implementing ER monitoring for structural health monitoring (SHM).

Despite this, a response was measured in a number of positions but these were due to substantial failure at the tuft sights. As expected, the untufted specimens did not evoke a response during testing. This indicated that without the tufts the lack of a TTC network was insufficient to enable ER measurement. Conversely it was possible that a sufficient set of carbon fibre conductive pathways resulted in an undirected current flow. As progressive delamination occurred alternate current pathways were made available and therefore no measurable ER changes were detected.

The obtained results indicate that the tufts do enable a crack detection method however, several aspects of the experimental design and structural response considerations need to be addressed. Determining the optimum position for the electrodes for a whole structure assessment was challenging. Positioning of the of the source current and sense electrodes influenced the monitored areas and ER measurement sensitivity. Proximity of the electrodes to the crack initiation point and propagation direction determined whether a localised or whole structural assessment was undertaken, although due to the greater number of potential electrical paths within the structure the extent of the monitored area was uncertain.

Compared to a flat coupon, the T-joint structure creates a multidirectional electrical network that flows along the in-plane carbon fibre, propagates between the two flange sides, along the web and also percolates in the TT direction. In the above experiments, an assumption that the electrical current would flow evenly between the three areas was made, and that any disruption to any one network would result in an equalised rearrangement of the current

between the remaining paths. Based on this assumption, the source was positioned in the centre of the web and that the current propagated through the web, then evenly between the two sides and any TT percolation would occur predominantly through the conductive tufts if present. However, as crack initiation occurred within the deltoid area, this may not have been the optimal position for current input. This was especially relevant in the tufted T-joints, where the tufts maintained the electrical circuit despite crack advancement. The electrical flow propagation in the structure propagates outward towards along multiple pathways towards the deltoid region. Because the crack initiated within the deltoid, the electrical current was not sufficiently affected until the delamination progressed towards the input electrode. A better position for the input current would have been closer to sight of crack initiation and the deltoid area.

The sensitivity of measuring ER variations in the presented study was compromised by tuft density and high conductivity of the hybrid thread. The tufted areas whilst limited to two rows equated to 1.3% areal density in those regions. This was possibly too dense, and the close proximity of the tufts to one another made it difficult to break the tufts, allowed the electrical current to travel along multiple routes, and resulted in a negligible ER increase. Also, the tuft pattern on the top surface and any overlapping loops on the underside created a conductive network that was completely unaffected by the delaminations. The high conductivity of the thread offered a “path of least resistance” to the electrical current consequently obscured the overall diminishing structural integrity of the composite. A disconnected or unlinked tuft pattern would have increased the probability of measuring an ER change due to crack propagation, although this would increase tuft manufacturing complexity.

Crack detection was dependent on tuft deformity or rupture in the TT direction as seen in the DCB and single tuft tests. The curved profile of the tufts in the T-joints appeared to enable the tufts to align in the direction of the applied force without rupture or significant distortion. This realignment of tufts enabled the electrical network to be maintained despite the crack propagation. Therefore, to avoid an excessive curved profile of the tuft, shorter loops or partial tufts would have likely offered a better alternative.

Compared to a flat composite panel, the parameters that affect ER measurement sensitivity were more complex and dependent on electrode positioning, tuft areal density and composition, and crack propagation relative to the monitoring electrodes. Tailoring tuft insertion to obtain optimum mechanical performance must be balanced between achieving structural performance and enabling effective SHM. Determining whether a whole structural or local monitoring requirement must also be considered.

7.7 Parameter adjustments

Another T-joint demonstrator was created in response to the observations in Sections 7.6.1 7.6.2 and 7.6.3. Construction of the T-joint was similar to that described in Sections 7.2, with the exception of the tufting pattern and the source electrode connection positions. Tufting was again undertaken using a RS522 tufting head, mounted onto a KUKA KLR 240 L180-2 2000 robot arm as described in Section 5.3.1. Two parallel rows of tufts were inserted through the stiffener flange and the adjoining composite skin preform. In contrast to the previous T-joints with a 10 mm x 10 mm tufting pattern, this T-joint was tufted with a line spacing of 10 mm, and a tuft spacing of 20 mm. The tufts were placed as close to the deltoid region and the site of crack initiation as possible, 15 mm from the centre.

There was concern that during tufting the needle may hit the base of the T-joint frame therefore it was decided that the tufts would be inserted through the underside rather than the top (Figure 7-28). Six rows of tufts were orthogonally inserted into the T-joint, two in the vertical web section and two on each side of the flange. The tufts were inserted in pairs giving the appearance of staples. The T-joint was bagged and infused under vacuum using a double bagged system with Prime 27™ as previously described in Section 7.2. The edges were trimmed, and two T-joints of 150 mm in length were cut using a diamond saw. Figure 7-29 depicts both the original T-joint and the T-joint with the revised tufting pattern. For simplicity, the tufts inserted in the new T-joints are depicted in the same orientation as the previous T-joint. In reality, the looped ends would be visible on the top side of each flange side. Changing the tuft pattern in this way reduced the tuft aerial density from 1.3% to 0.6%, lowering the overall TT conductivity. However, the ‘staple-like' profile of the inserted tufts also reduced

electrical interconnectivity in the in-plane direction, implying that any tuft rupture should have a greater impact on ER. Tuft insertion nearer to the deltoid region also promoted earlier engagement of the tufts during the testing.

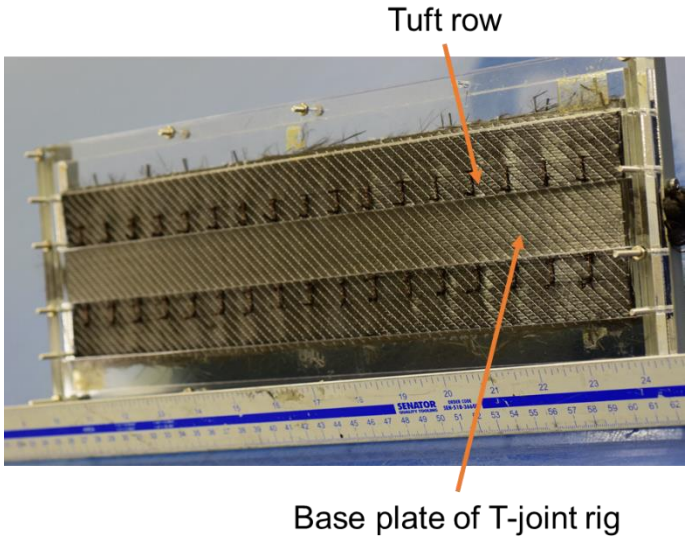

Figure 7-28 Underside of tufted preform in T-joint rig.

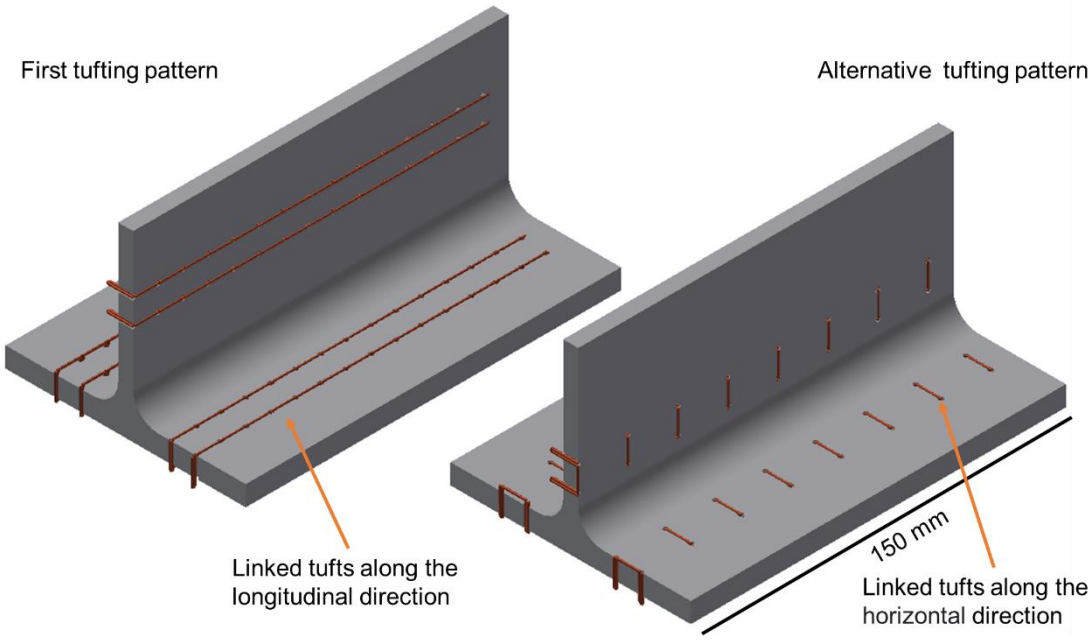

Figure 7-29 T-joint tufting profiles, (left) Original tufted T-joint and (right) revised tufted T-joint.

The T-joint specimens also contained a thickness variation in their profile similar to that described in Section 7.2. Table 7-3 details a total of nine measurements taken on each specimen, three on each side of the flange and three on the web. The measurements were taken on the tuft (position 1), 10 mm from the centre of the deltoid (position 2) and the 5 mm from the edge of the T-joint.

Table 7-3 T-joint specimen thickness measurements

	Specimen	Position 1 [mm]	Position 2 [mm]	Position 3 [mm]
Web	T-joint 1	5.5 ± 0.2	4.7 ± 0.2	6.4 ± 0.0
	T-joint 2	5.9 ± 0	4.8 ± 0	7.1 ± 0.1
Flange (left)	T-joint 1	7.4 ± 0.1	7.9 ± 0.2	6.9 ± 0.1
	T-joint 2	7.6 ± 0.2	8.2 ± 0.1	7.2 ± 0.1
Flange (right)	T-joint 1	8.0 ± 0.1	7.3 ± 0.2	7.1 ± 0.0
	T-joint 2	7. 2 ± 0.1	7.6 ± 0.1	7.2 ± 0.0

Electrodes of copper foil and silver paint were prepared and attached as previous described Section 7.3.1. The positions of the electrodes were altered for this study. The input source electrode was placed on the web near the deltoid to the front of the T-joint, closer to the point of initial crack development. The number of outputs was also doubled in order to establish a localised and overall structure assessment of the T-joints. Figure 7-30 provides a diagram of the six output electrodes and the source current input positions. The two sets of output electrodes are described as “near” and “far” electrodes depending on their position relative to the current input. The “near” electrodes labelled 1, 2 and 3 in the diagram are positioned close to the current input. 1 and 2 are specifically placed on the first tuft row on each flange while 3 was positioned on the web between the first and second tufts as the input current was placed on the tufts. Electrodes 4,5 and 6 positioned at the far end of the T-joints on the final set of tufts of each respective side.

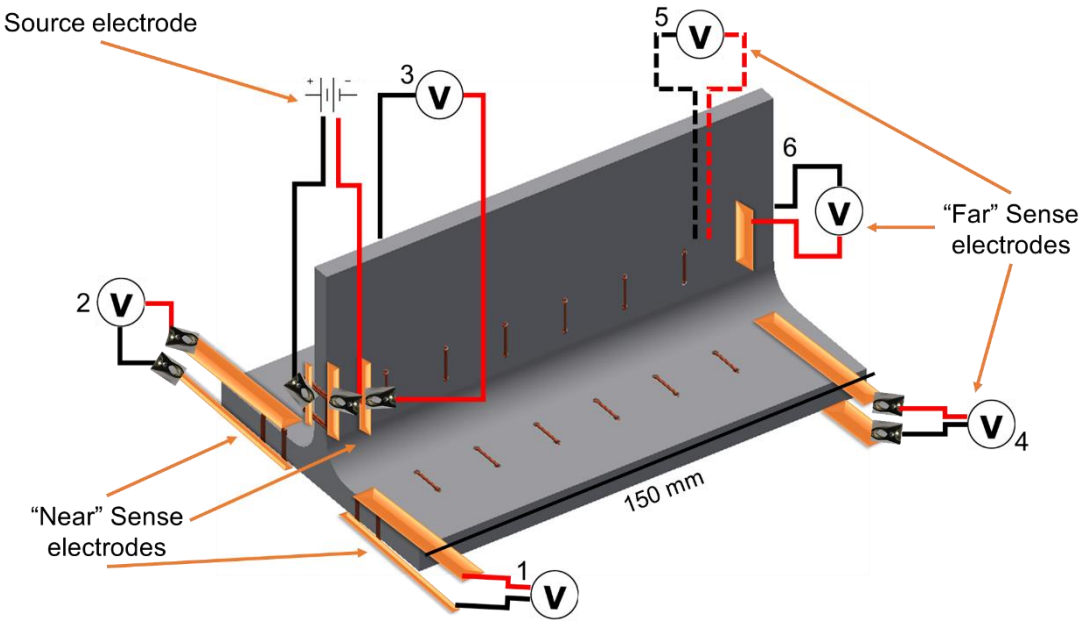

Figure 7-30 Schematic of power input electrode position and output electrode positions.

7.8 Results and observations

7.8.1 Mechanical response

Figure 7-31displays the load–displacement curves of the T-joint sections with the alternative tufted specimen. The mechanical result of one test sample was dismissed due to failure of the testing rig and slippage of the T-joint which resulted in compression and uneven loading. It was acknowledged that drawing conclusions from a single data set was limited, however, the dismissed test did not accurately replicate the previous tests and therefore its exclusion from the mechanical comparison was justified. The load-displacement curve of the alternatively tested T-joint exhibited a failure profile simlar to that of the other tufted specimens, but with fewer large drops. Crack initiation occurred at 11.1 kN versus 7.8 kN and 11.8 kN in previous tufted specimens, and maximum load reached was 14.3 kN versus 14.7 kN and 15.1 kN in previous samples.

Initial failure manifested as delamination between the deltoid and the left flange (Figure 7-32 (a)). Crack propagation progressed first into the web where it appeared to be arrested by the tufts (Figure 7-32 Video stills of tufted-joint testing.(b)). The crack then deviated left and right along the Figure 7-32(c)). The final three load drops occurred due to crack jumps along the base plate and bending of the radius, with final failure resulting in separation of the baseplate and tuft pull-out (Figure 7-32 (d)-(f)).

Tuft rupture was evident following testing, and two types of failure profiles were observed (Figure 7-33). The tufts at position 1 failed asymmetrically within the composite, resulting in material pull-out when the base plate separated from the specimen. The tufts at position 2 appeared to have been equally ruptured by the crack propagation, with no projecting material. It was not possible to determine the condition of the tufts at position 3 on the web. Compared to previously tested tufted specimens, engagement of the tufts occurred earlier, was more extensive, and it was clear that tuft failure occurred at positions 1 and 2.

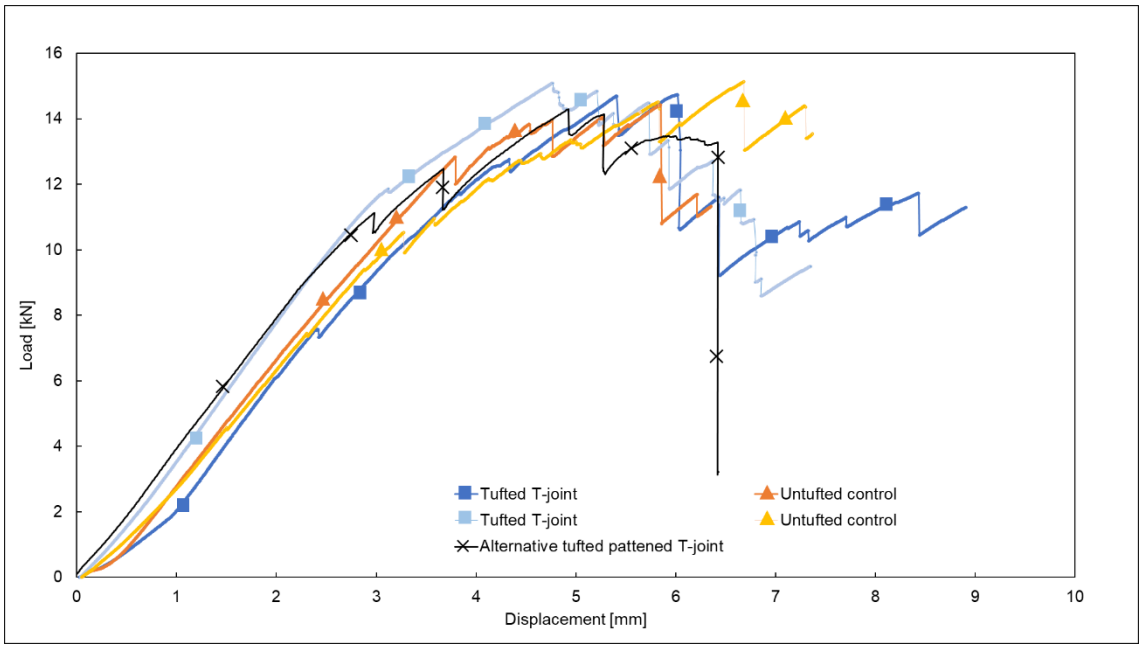

Figure 7-31 Load displacement curves with alternately tufted sample.

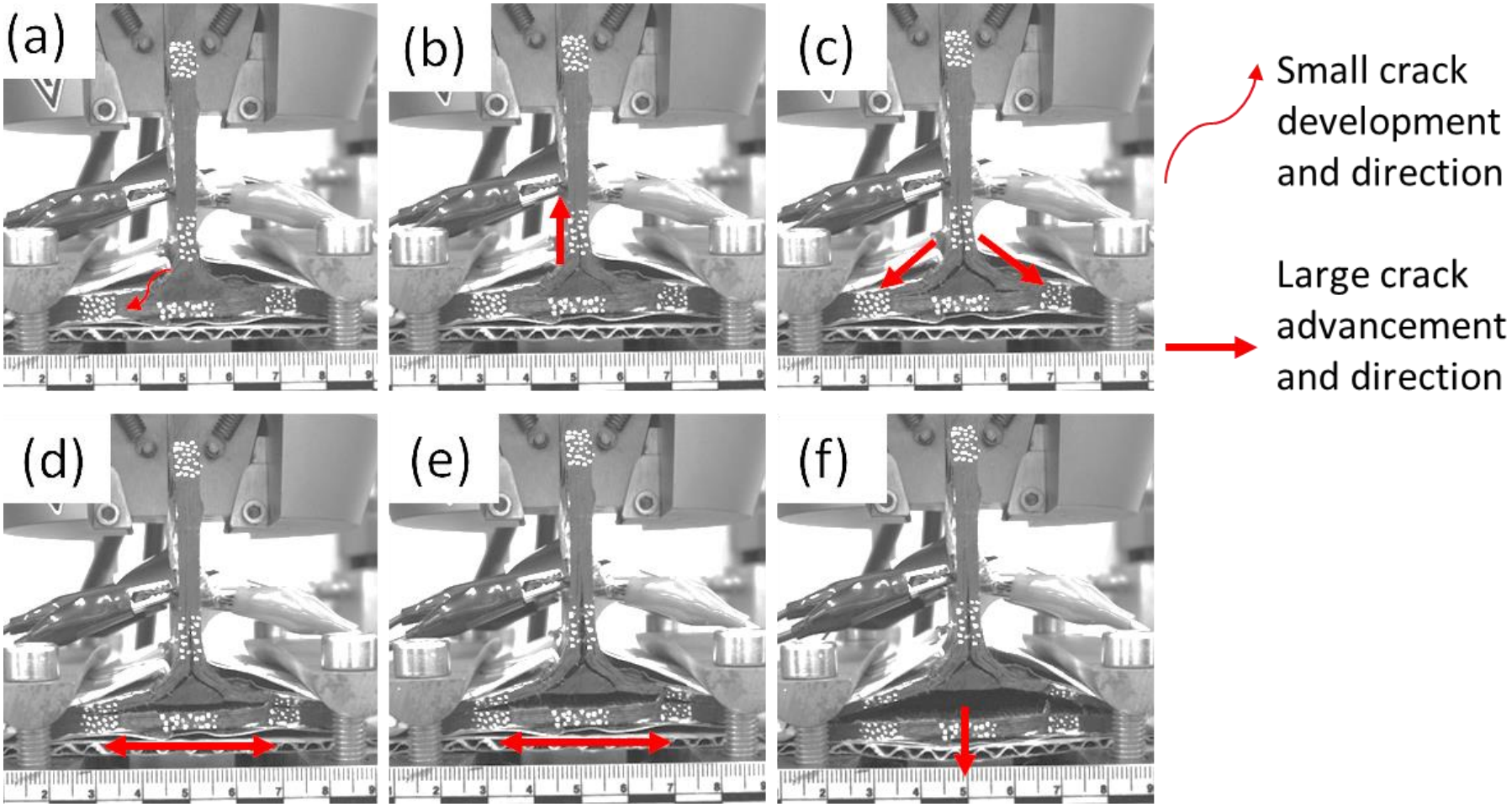

Figure 7-32 Video stills of tufted-joint testing.

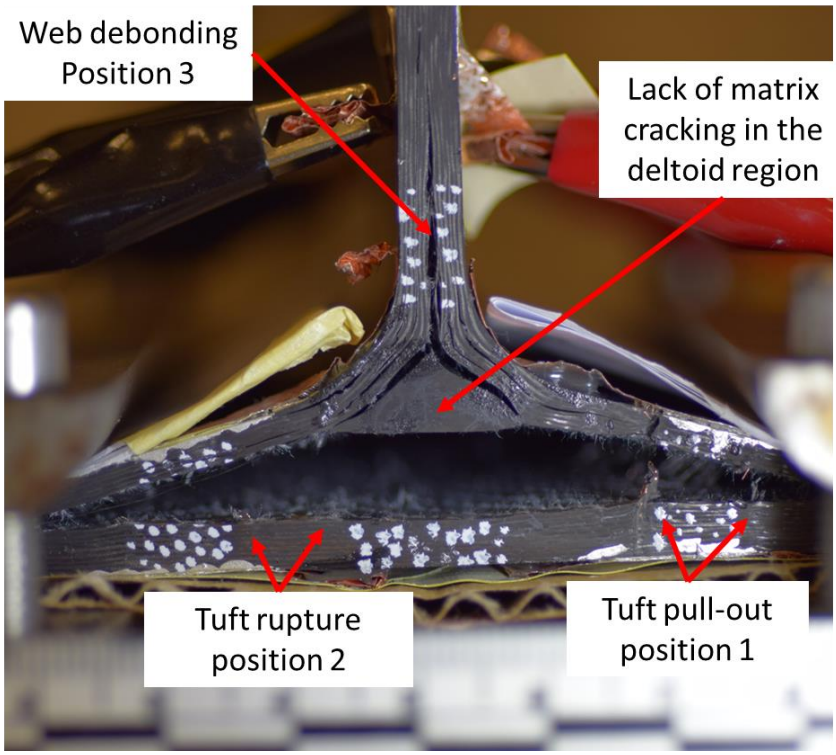

Figure 7-33 Image of tested T-joint specimen.

7.8.2 Electrical response

Figure 7-34 shows the resistance index plots of the six sensing electrodes over time. Figure 7-35 is an illustration of visible crack progression at the front facing section of the T-joint. The resistive index plot indicates a response from the electrodes at positions 2 and 3. In the case of position 2, the initial ER response coincided with the crack propagation at position 2 on the T-joint (Figure 7-35 Schematic of visible crack propagation at front of alternatively tufted T-joint. (d)) until complete detachment of the base of the specimen. The response of the electrode at position 3 begins before the final load drop at stage (e) but rises sharply compared to the position 2 electrode. No response was observed at either position 1 or any of the “far-sense” electrodes.

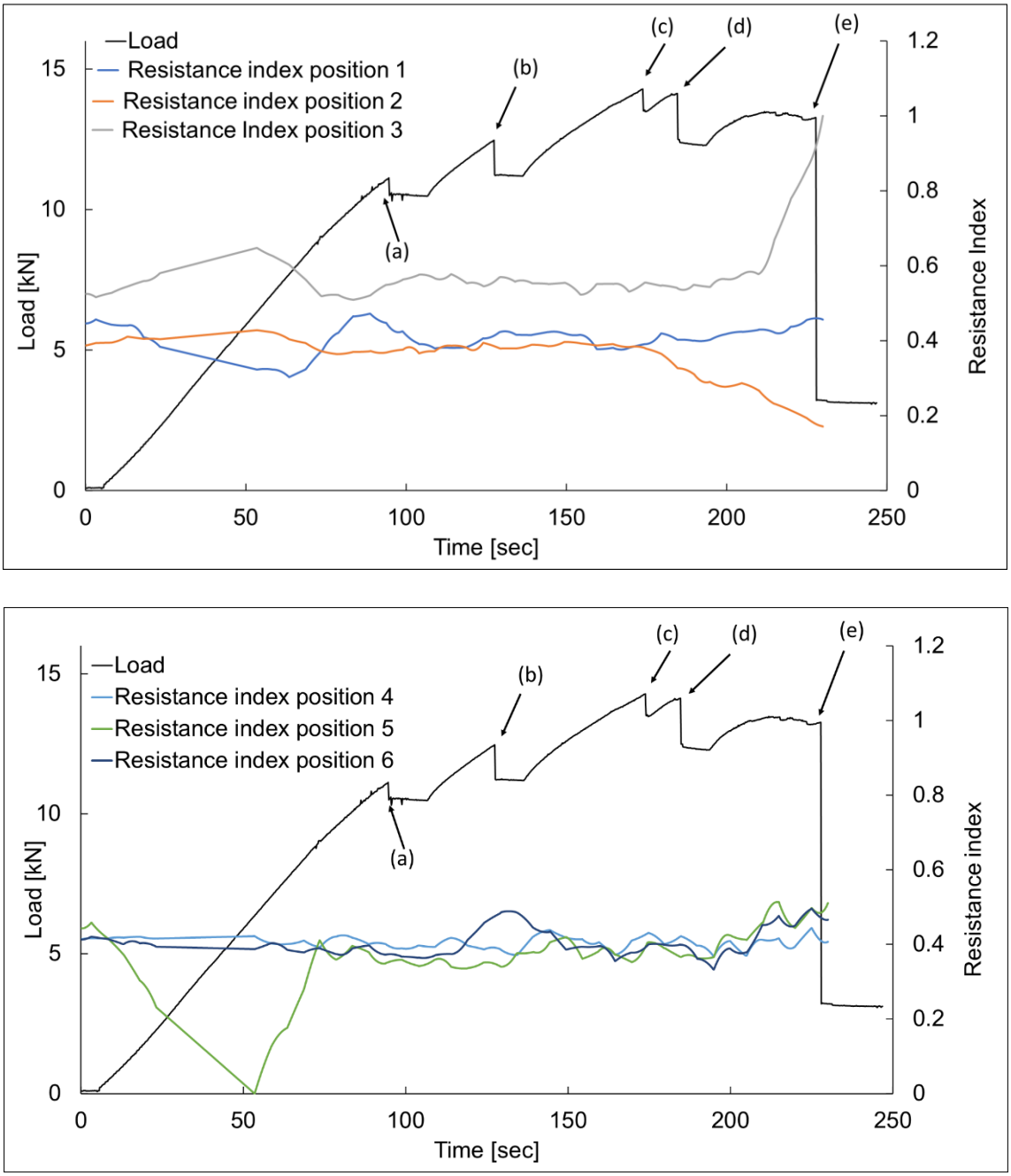

Figure 7-34 Plots of plot of resistance index and load over time of alternatively tufted specimen. (Top) “Near-sense” electrode response and (bottom) “far-sense” electrode response.

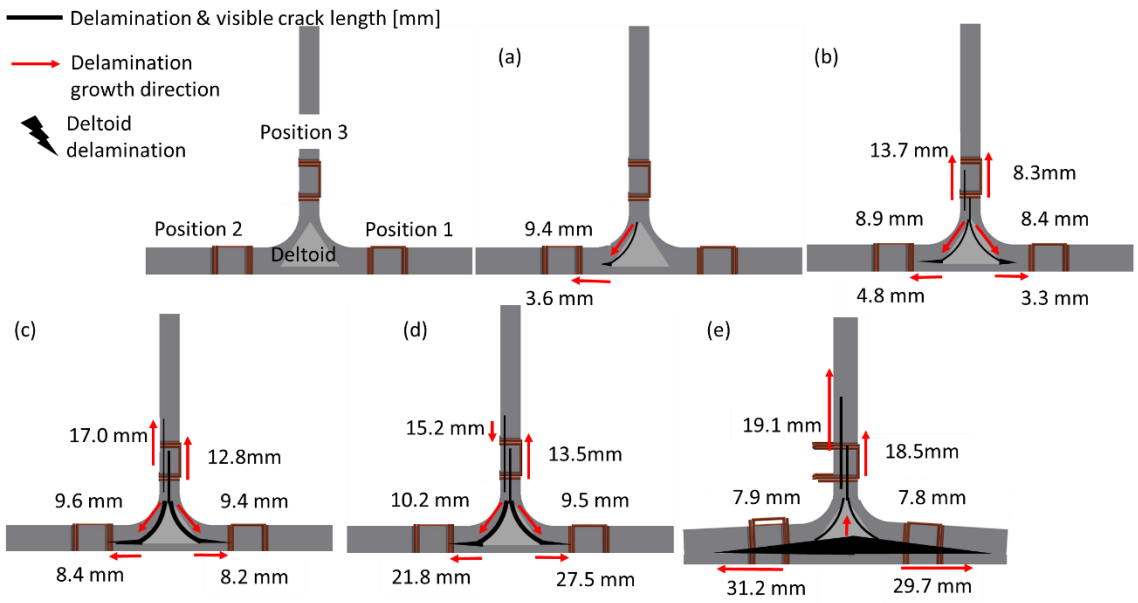

Figure 7-35 Schematic of visible crack propagation at front of alternatively tufted T-joint.

7.8.3 Discussion and conclusions

Undertaking an ER assessment in a complex architecture such a T-joint presented a number of challenges not experienced in previously examined DCB specimens. Overall, the results are promising, however, limitations in sensitivity were an issue. The increased complexity in upscaling this technique was predominantly associated with electrode placement and construction. Predicting the current direction in the labyrinth of conductive pathways was not possible especially in the untufted specimens. The location of the sense electrodes in relation to the current path, the three-dimensional form of that path, and the electrode architecture all contributed to differences in initial ER values between samples. Increasing the current input would have increased sensitivity, but it would also have had heating effects on the specimen.

T-joint failure mechanisms were more varied than those observed in single tuft and DCB testing, where a single crack front and crack path were predictable. While initial failure appeared to occur at a single spot in the T-joints, numerous crack fronts later proceeded. Detectable ER changes occurred only in the final stages of testing, when structural damage was substantial, indicating that tuft rupture or significant disruption to the conductive channels was required to obtain measurable results. This lack of responsiveness to early stages of failure may be due to several delaminations on separate sides of the specimens. Following the detachment of the baseplate, there was compression and bending

of the radius, as well as fracture closure in the web. It was observed that the increasing size of the fracture on one side typically resulted in the crack on the other side being artificially closed, thereby maintaining, or re-establishing the electrical pathways on the closed side. Tuft pull-out whilst beneficial from a mechanical performance perspective, appeared to negatively affect sensing capability as the protruding material maintained the conductive network.

The final demonstrator, with both “near” and “far” electrodes highlighted limitations of whole structure sensing and the single input source. The positions were based on the previous DCB tests where the ER increased as each set of tufts broke. The combination of the “staple” shaped disconnected tufts created an indirect whole structure sensor relying on the conductivity of the in-plane carbon fibre to complete the network in the specimen. Whilst this configuration was successful for the DCB specimens it did not respond similarly in the T-joints. The “far” electrodes, positions 4–6, did not respond, indicating that either the current did not reach the probes or was insufficiently altered to be detected. Positions 3 and 2 on the "near" side did detect the final delamination. As a result, proximity to the source current was a significant criterion for ability to detect.

A number of observations and considerations from the demonstrator experiments can be taken to aid addressing some of the limitations of this sensing technique. Refinement of the electrode construction technique would increase the reproducibility of the sensing method and possibly increase sensitivity.

A more direct form of monitoring could be undertaken by examining individual tuft threads as opposed to the “whole structure” assessment in a method similar to that described by Bing *et al* [171, 246]. This would create a more localised sensing method and require the use of individual input source currents. This would improve sensitivity, but each set of local measurements would have to be done separately to avoid interference between the different current inputs.

8 THESIS CONCLUSIONS, AND FUTURE WORK

8.1 Overview

This thesis set out to determine if it was possible to demonstrate multifunctionality in carbon fibre composites by integrating a novel hybrid tufting thread and enhancing through-thickness conductivity. It aimed to develop a hybrid tufting thread to achieve multifunctionality, to increase through-thickness conductivity without reducing structural capability and demonstrate multifunctionality in the form of an SHM system for crack detection by monitoring of electrical resistance changes.

8.2 Conclusions

This section provides an overview of the main conclusions from this work in reference to the research questions.

Can micro-braiding be used to manufacture a metal-carbon fibre hybrid tufting thread?

- A tuftable multi-material micro-braided thread was manufactured and shown to be a viable way for producing customised threads.
- The method effectively integrated metal wire and carbon fibre tow in an inherently interlaced configuration to improve tuftability.
- Tufting thread or braid quality was determined by the symmetry of the material in the interlacement pattern.

What braid parameters have an impact on the manufacturability of a metal-carbon fibre braid?

- The success or failure of the braiding operation predominantly depended on the choice of braid materials and by the symmetry of the material in the interlacement pattern.
- Lay length, and braid angle mainly influenced the final braid structure.
- Too high a lay length resulted in carbon fibre slippage and tow separation along the braid whilst lower laylengths resulted in higher filamentisation.
- Braid pattern combinations also had a much greater influence on hybrid braids than on single-material ones. This was caused by interaction of the metal and carbon fibre yarns. This was caused by high “contrast” in the interaction of the metal wire and the carbon fibre tows at the braiding point. In particular, carbon fibre is very stiff, while copper is more compliant and yielded around the metal wires.
- The complexity of design parameters was increased by braiding contrasting materials. Combining materials with mismatched elastic properties may compromise the mechanical architecture of the braid but achieving multifunctionality was dependent on merging these contrasting materials.

Does the addition of the wire yarns improve the tuftability of the tufting thread?

- Throughout the tufting process, the metal wires prevented the carbon fibre yarns from breaking. It was not possible to tuft untwisted carbon fibre or a completely carbon fibre braided thread.
- These hybrid multi-material braids were used successfully as tufting threads. The metal wire provided protection for the carbon fibre by reducing filamentation and preventing the carbon fibre filaments catching in the needle eye during the insertion process.

Can MF in the form of SHM be demonstrated using a system to monitor changes in ER caused by crack propagation?

- The hybrid multi-material tufting thread increased inherent through-thickness conductivity (TTC) and increased delamination resistance.

- Using a multi-material hybrid microbraid as a tufting thread complicates the final composite architecture. The mechanical and functional qualities of the final composite were defined not only by the hybrid thread composition, but also by the tuft areal density, tuft placement, and tufting pattern.
- The “apparent” fracture toughness of the hybrid multi-material tufted composite, performed similarly to commercially available tufting thread in a double cantilever beam test, with the added benefit of increasing through-thickness conductivity (TTC)
- A balance or compromise must be made regarding mechanical and functional requirements. A combination of mechanical and functional (conductive) threads could be implemented within the same structure.
- Managing tuft insertion level and loop length necessitates optimisation. Overlapping loops resulted in an increased electrical network, which, depending on the application, may be advantageous. Although, it would be preferable to have consistency in avoiding or assuring overlapping loops.
- The increased TTC permitted crack sensing by the measurement of changes in electric resistance (ER). The breakage of the hybrid tuft showed greater changes in ER compared to the carbon fibre thread.

What effect does the placement of electrodes have on the capability to detect crack propagation?

- Electrodes positioned in close proximity to the tuft provide an individual tuft or localised assessment.
- Assessment of the crack initiation site can be achieved if the electrode placement is such that the source and sense electrodes are as close to the initiation site as possible.

What are the implications for up-scaling the SHM technique?

- Up-scaling increases the complexity of the electrical network making whole structural assessment difficult.
- In larger or more complex structures, it is recommended an electrode placement that achieves localised monitoring be used.

- Implementing an ER sensing capacity in a more complex structure necessitates additional research into data gathering and post-processing approaches.

8.2.1 Overall thesis research question

Is it possible to demonstrate multifunctionality in carbon fibre composites by integrating a novel hybrid tufting thread and enhancing through-thickness conductivity?

The micro-braiding of tufting threads provided a means of incorporating multifunctionality into CFRP. Through-thickness conductivity and delamination resistance were inherently increased by integrating both metal and carbon fibre in a tufted thread. When compared to the untufted specimen, there was an increase in “apparent” fracture toughness of up to 189% and changes in ER orders of magnitude higher due to crack propagation. Therefore, a multifunctional composite with increased structural and conductive capability has been manufactured and multifunctionality in the form of SHM method has been demonstrated. This addressed the industrial desire for integration of a sensor during manufacture that enables weight savings and less conservative structural designs [19, 20].

8.3 Future work

Further manufacturing development of hybrid braided threads could be achieved by examining braid parameters and combinations such as core yarn, axial yarn, and polymer yarn inclusion. Resin infusion would be improved by the presence of polymer yarns, however, the increase in braid diameter would increase preform damage caused by tuft insertion. Similarly, inclusion of core and axial yarns are likely to increase braid diameter and stiffness, potentially increasing difficulty in tufting. One other thread parameter not addressed in this study and worthy of further investigation is the introduction of a twist in the carbon fibre tow.

Examining the feasibility of creating a length of braid that contains conductive and non-conductive sections could lead to further advancement. The effect could be easily manufactured by replacing yarn carriers at planned stages during braiding. Care would be needed to ensure the external profile of the

braid is not distorted, and consideration given to the tuft pattern and placement of the respective conductive and non-conductive braid sections.

The use of normalised ER has proven to be effective, however additional refinement in data post-processing would be required for in-service demands. It would be preferable to have a more comprehensive interpretation of the signal to provide a more complete condition status of the structure.

The development of an electrode construction technique would improve reproducibility, reduce noise, and possibly increase the output signal sensitivity. But, as the electrical current flow was dictated by the placement of the source and sensor electrodes, careful positioning is required to detect initial crack development. This necessitates comprehensive research into the failure mechanisms of each structure, as well as any potential alterations to those failure modes as a result of tuft insertion. An alternative setup of the electrodes could be undertaken by examining individual tuft threads as opposed to the “whole structure” assessment. This would create a more localised sensing method and require the use of individual input source currents. Individual source and sense electrodes increase sensitivity, but each set of local measurements would have to be separately taken to avoid interference between the separate current.

Effects of corrosion and galvanic effects of metal wire inclusion and material hybridisation into these tufted composites was not undertaken in this thesis. This would provide useful insight into material degradation and environmental effects within a part.

9 APPENDIX

Appendix A Results of DCB Tests

9.1 Load displacement profiles

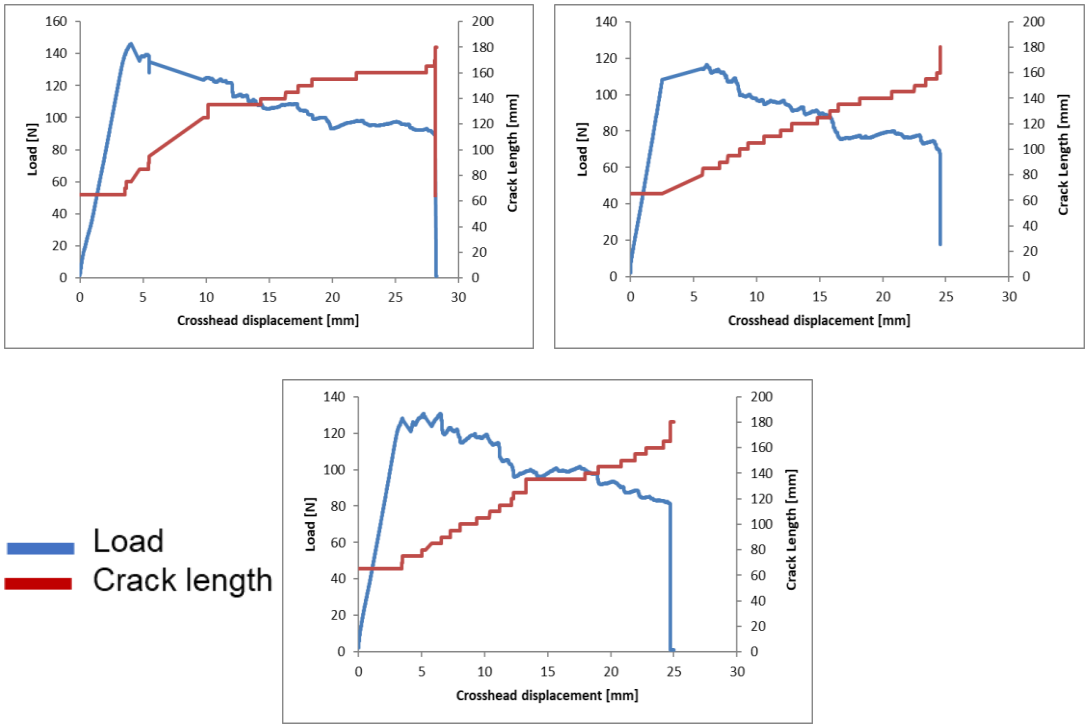

Figure 9-1 load displacement profile for untufted coupons

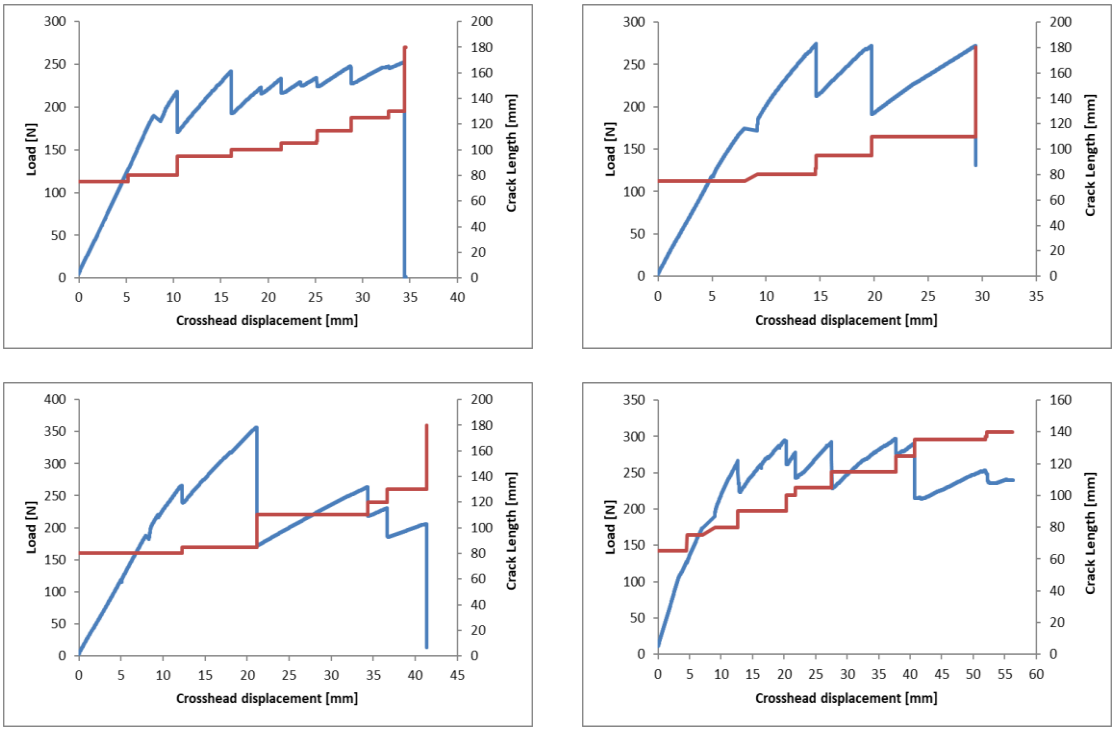

Figure 9-2 Load–displacement curves for 4k tufted coupons with a 10 mm x 10 mm pattern.

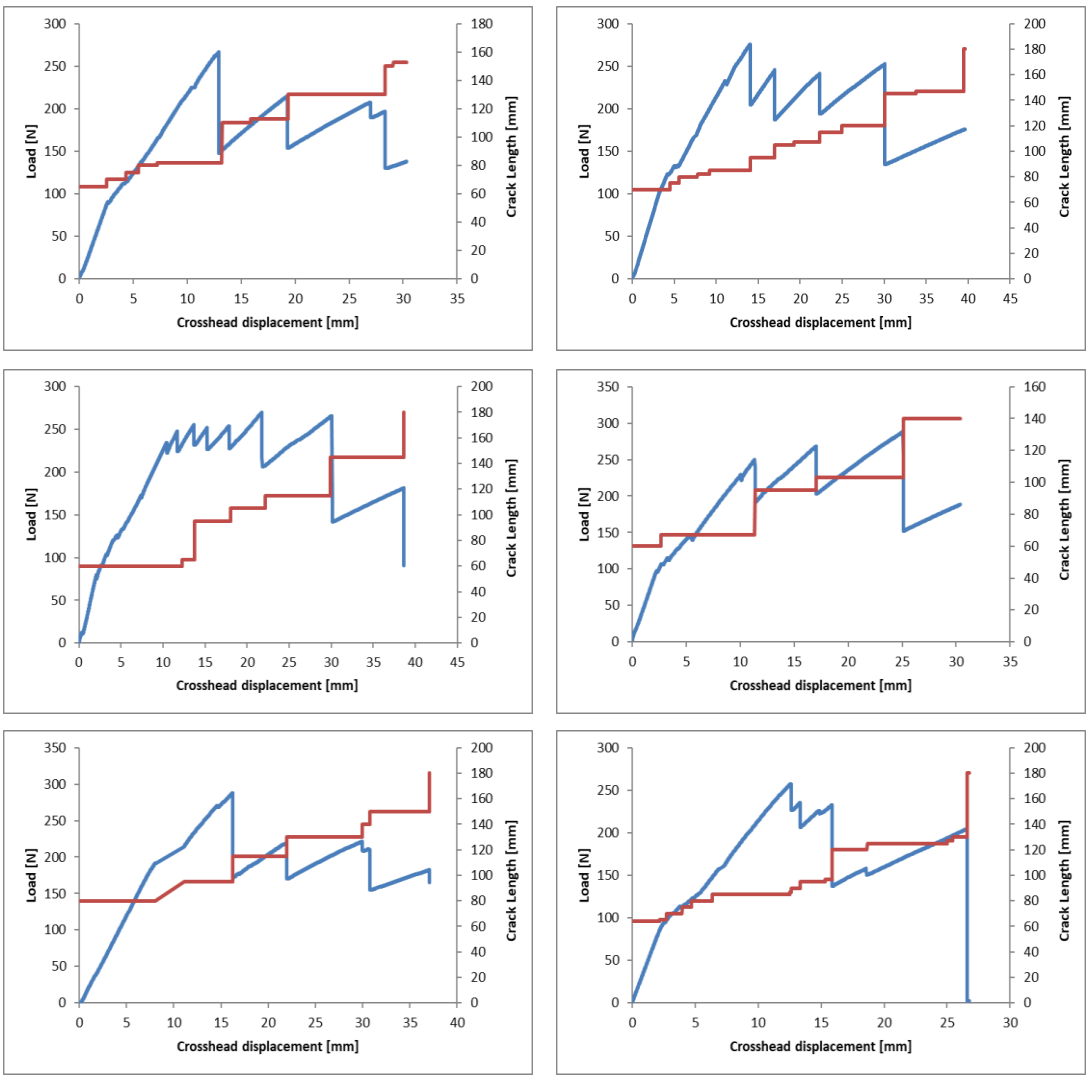

Figure 9-3 Load–displacement curves for coupons tufted with the hybrid micro-braid with a 10 mm x 10 mm pattern.

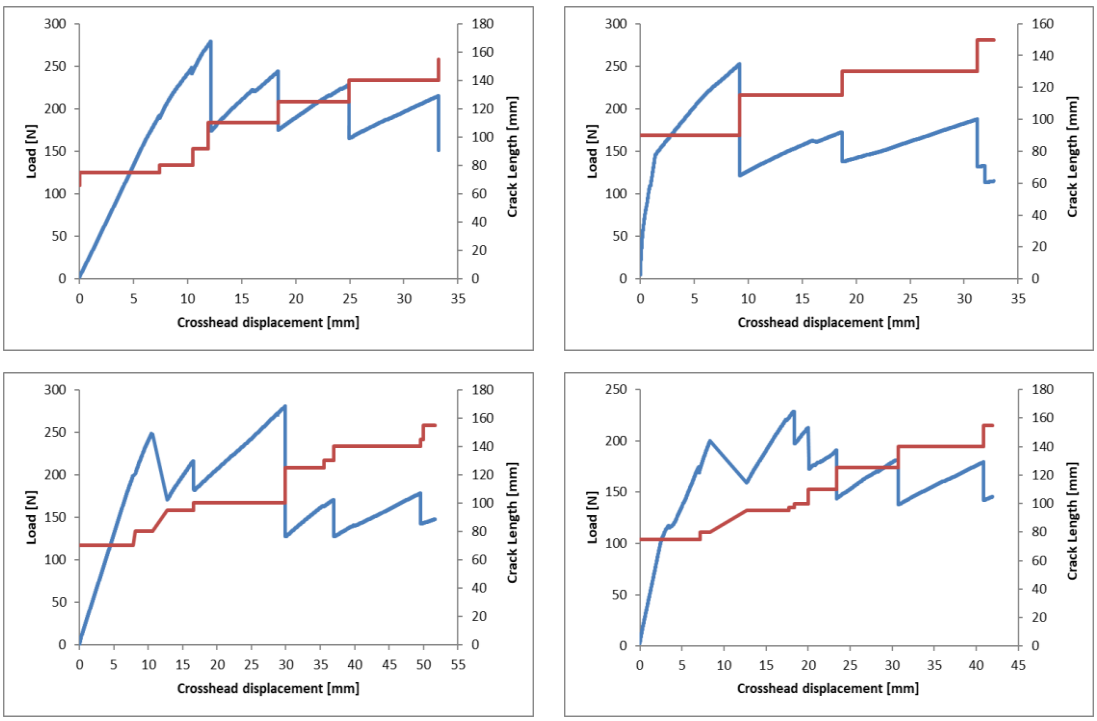

Figure 9-4 Load–displacement curves for coupons tufted with the hybrid micro-braid with a 10 mm x 15 mm pattern.

9.2 R–curves for each DCB coupon

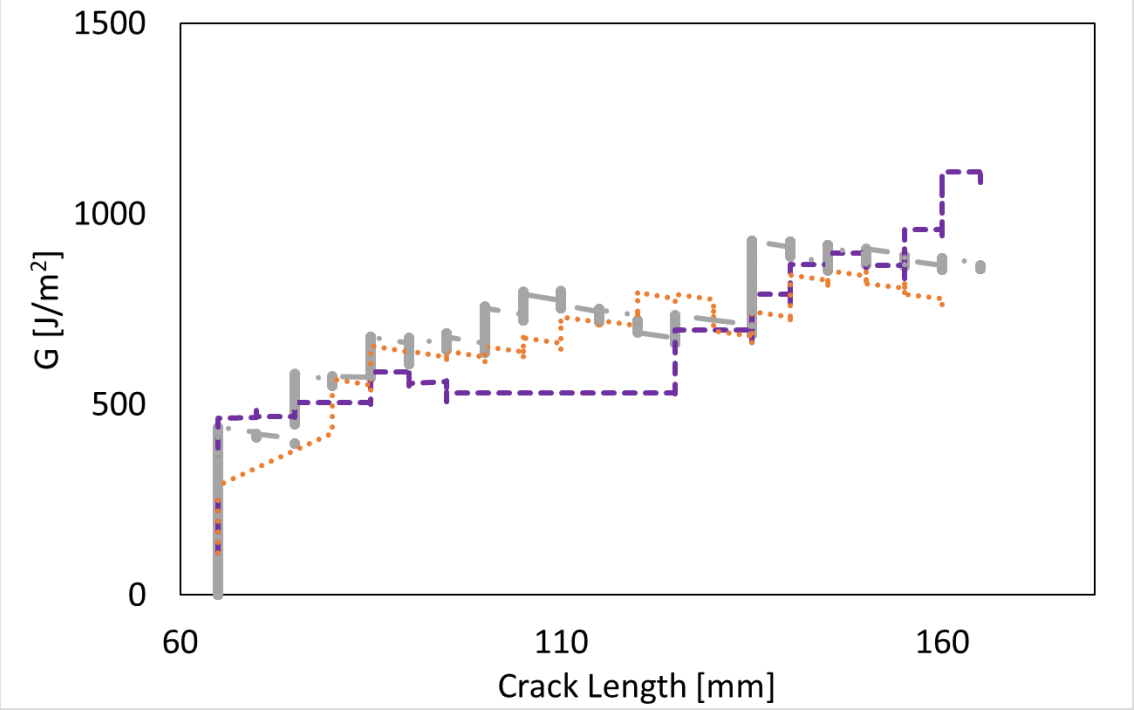

Figure 9-5 R–curves of untufted DCB specimens

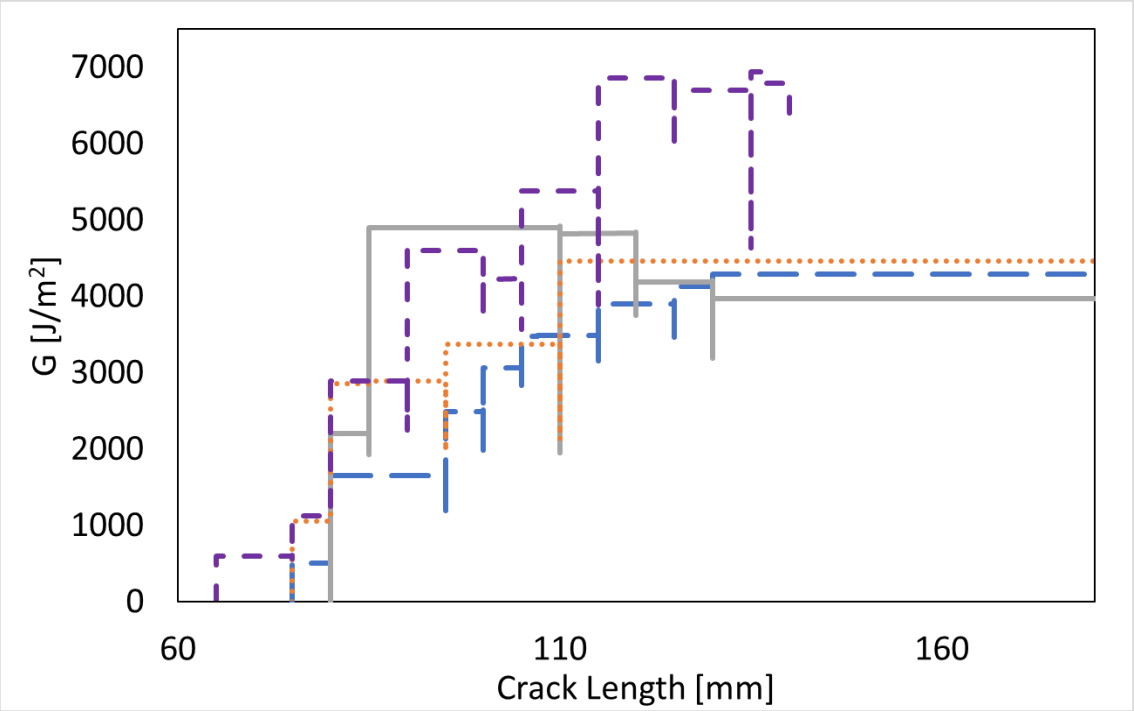

Figure 9-6 R–curves of 4k carbon fibre tufting thread: 10 mm x 10 mm pattern DCB specimen.

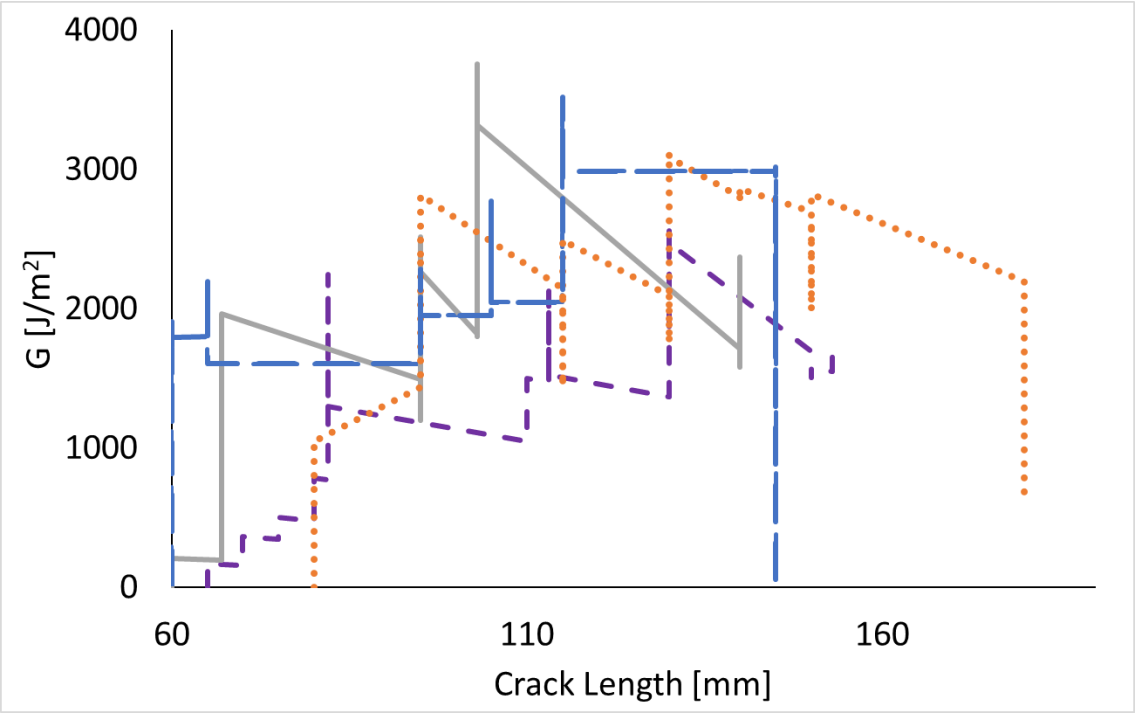

Figure 9-7 R–curves of hybrid tufting thread: 10 mm x 10 mm pattern DCB specimens.

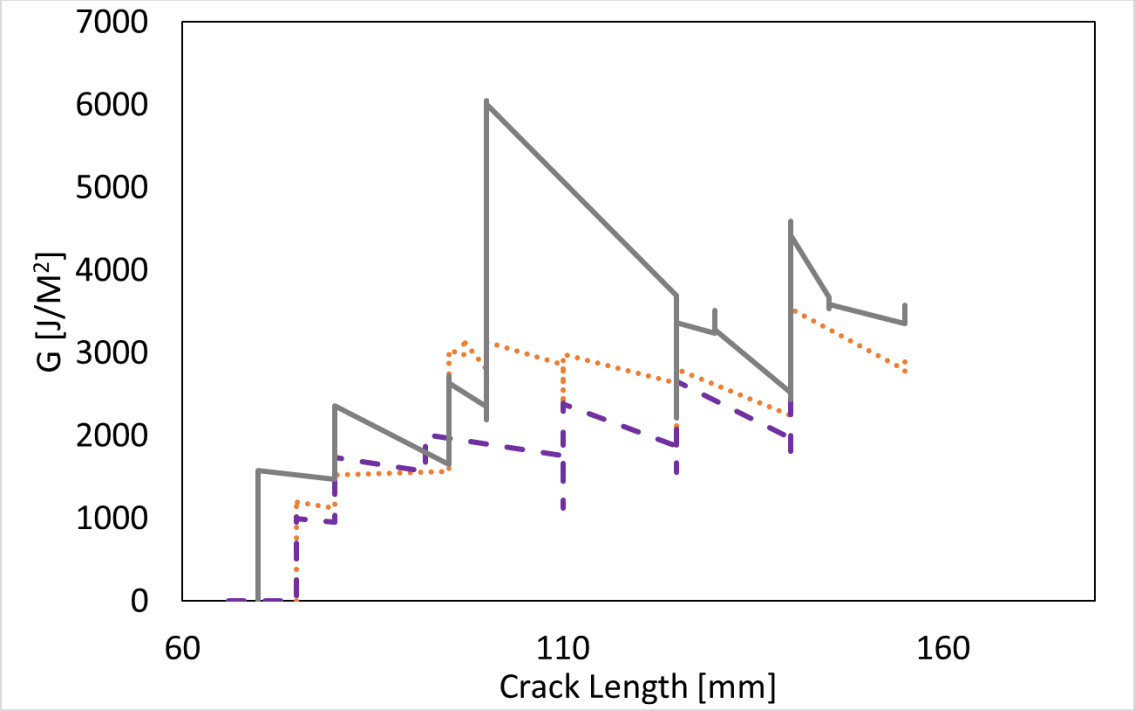

Figure 9-8 R–curves of hybrid tufting thread: 10 mm x 15 mm pattern DCB specimens.

9.3 Electrical response of DCB coupons

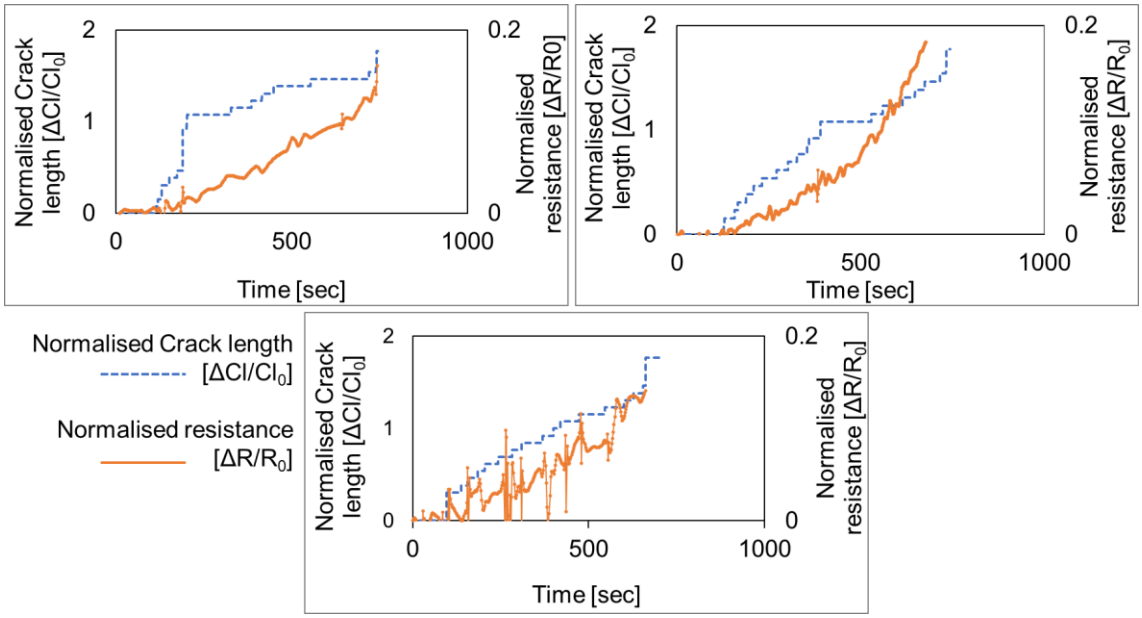

Figure 9-9 Normalised electrical resistance and crack length progression in DCB specimens- untufted specimens.

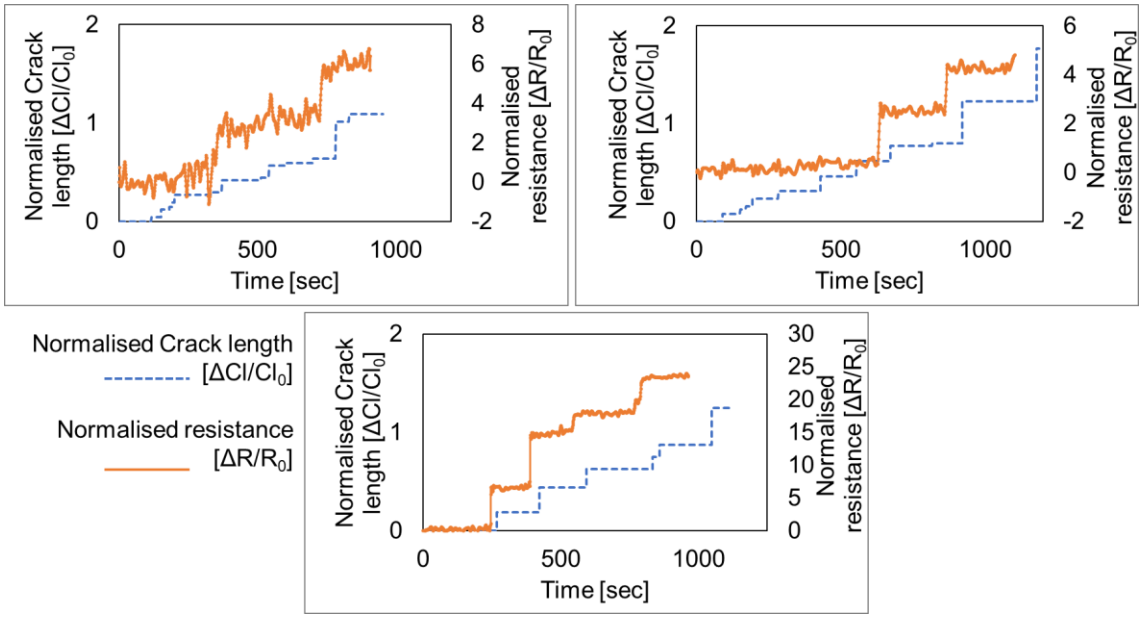

Figure 9-10 Normalised electrical resistance and crack length progression in DCB specimens – 4kcommercial thread

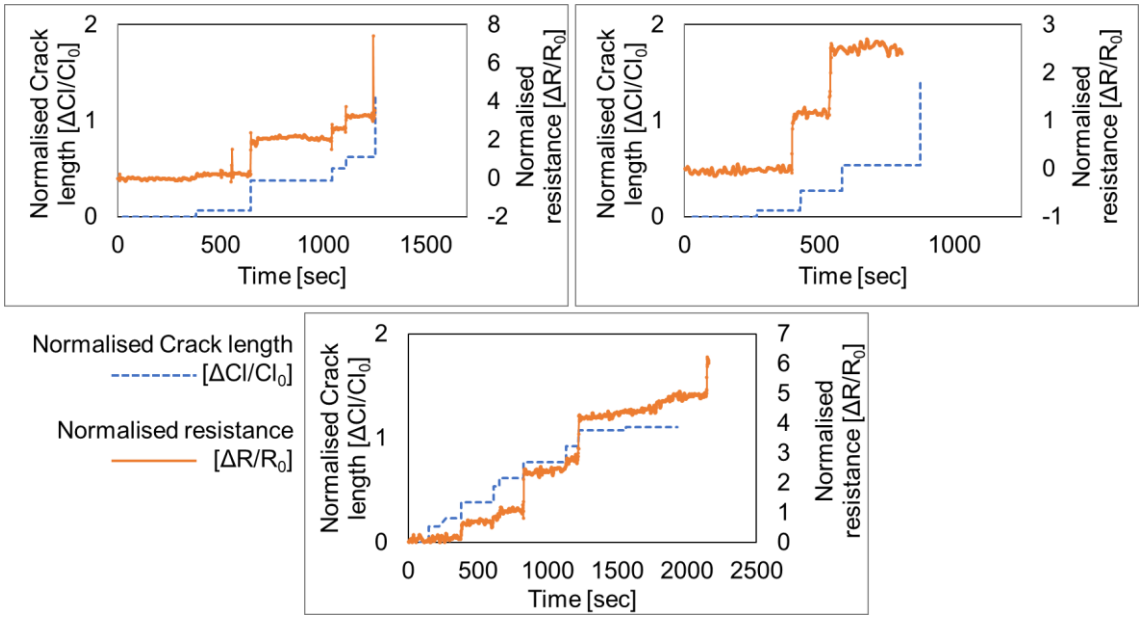

Figure 9-11 Normalised electrical resistance and crack length progression in DCB specimens- hybrid micro-braided thread 10 mm x 10 mm pattern

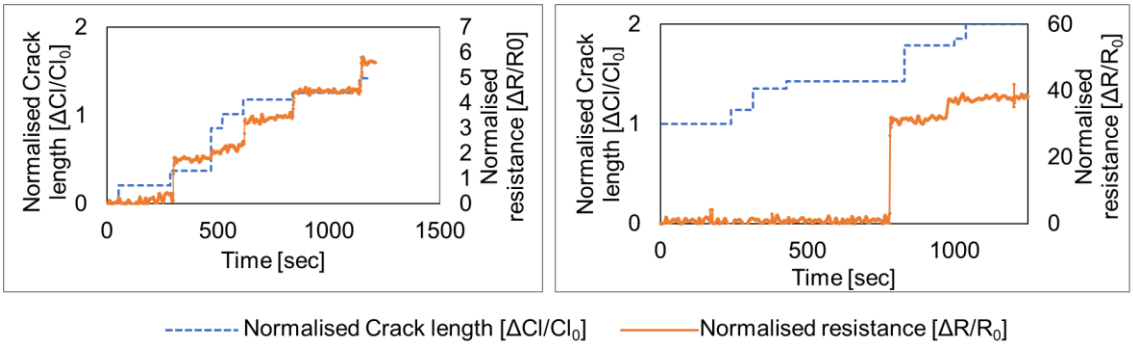

Figure 9-12 Normalised electrical resistance and crack length progression in DCB specimens- hybrid micro-braided thread 10 mm x 15 mm pattern

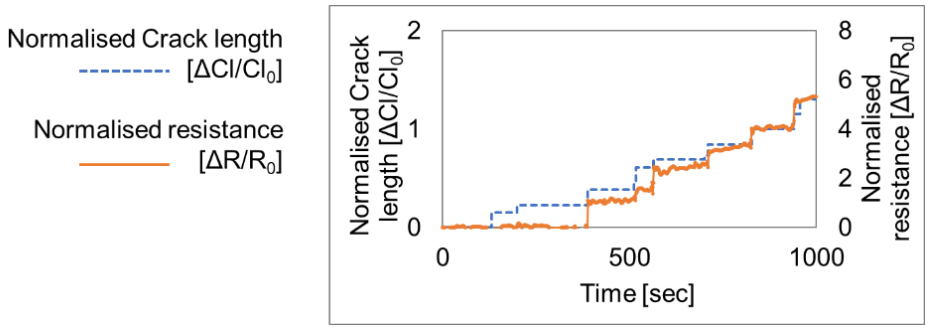

Figure 9-13 Normalised electrical resistance and crack length progression in DCB specimens- Un-looped hybrid micro-braided thread 10 mm x 10 mm pattern

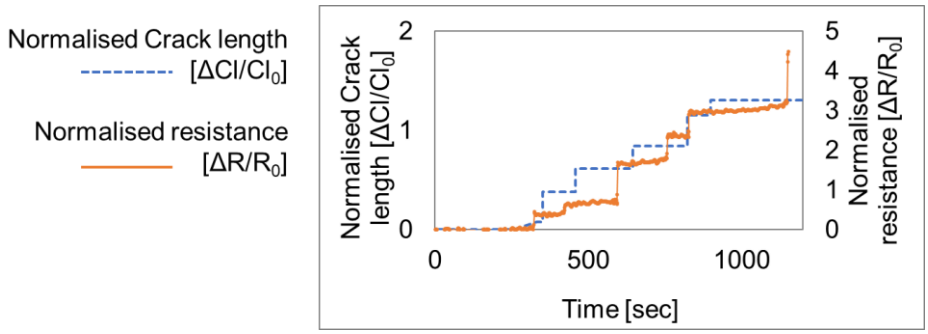

Figure 9-14 Normalised electrical resistance and crack length progression in DCB specimens- Un-looped hybrid micro-braided thread 10 mm x 15 mm pattern

Appendix B Investigation of conductive nonwoven materials as alternative electrodes

9.4 Method

Conductive nonwoven materials composed of copper and nickel coated carbon fibre supplied by Technical Fibre Products Ltd. were examined for their suitability as an alternative ER surface attachment method [249, 250]. Six mats with different aerial densities were examine. Table 9-1 details the technical data of the different mats with areal densities 75, 50, 34, 20, and 10 g/m^2.

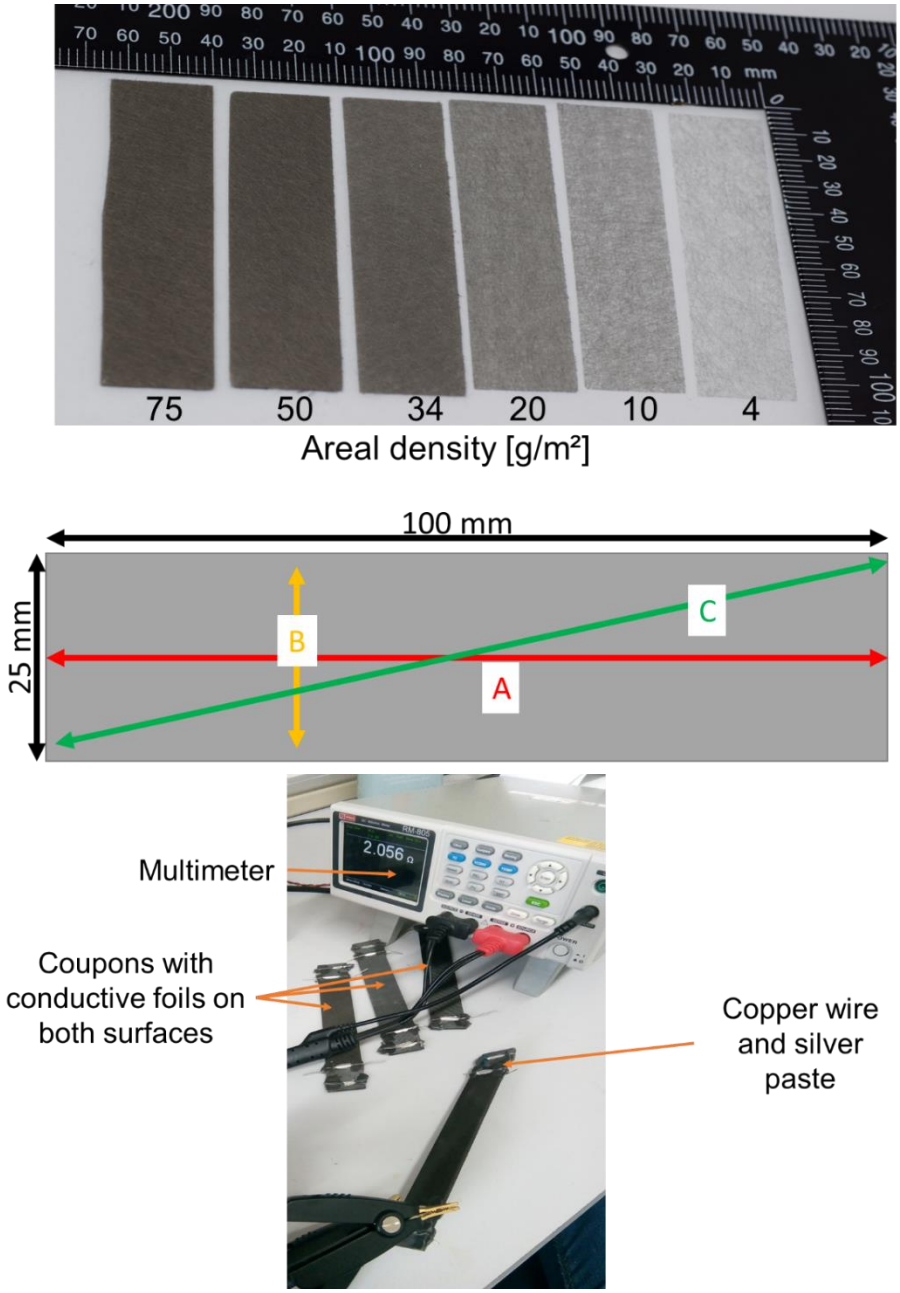

Figure 9-15 TFL conductive mats and diagram of directions for measured ER.

Table 9-1 Technical data for TFP conductive mats

Areal density [g/m²]	**75**	**50**	**34**	**20**	**10**	**4**
Reference number	20444A					20444B
MD Surface Resistivity [ohm/sq]	0.1	0.1	0.2	0.2	0.3	0.6
Description	Wet-laid nonwoven copper & nickel coated carbon fibre mat					Wet-laid nonwoven copper & nickel coated carbon fibre veil
Fibre type	Copper & nickel coated carbon fibre					
Fibre Length [mm]	12					
Fibre diameter [mm]	8					
Binder type	Cross-linked polyester					

[249, 250]

A preform made of four plies of biaxial carbon fibre was constructed with matching strips of each mat type on the top and bottom surfaces, resulting in a "multi-mat" preform. It was infused using the vacuum assisted resin infusion technique described in Section 5 with Prime 27 epoxy™ resin and cured in the oven at 80˚C for two hours. Coupons were cut from the resulting composite using a diamond saw and three 25 mm x 100 mm coupons were made for each conductive mat. Initial examination of the ER, using the four wire Keithley multimeter (MM) method, established that the resin infusion resulted in the electrical insulation of the conductive material. It was therefore not possible to measure ER from the coupons without further surface preparation. This surface preparation involved the sanding of the surfaces using a Dremel to expose the conductive layers, painting with silver paint and attaching copper wires to create a clipping point.

Resistance measurements were highly dependent on surface sanding level, and a repeatable surface treatment that did not damage the matting was not possible. As shown in Figure 9-15 surface measurements were taken along the length, width, and diagonal directions. The material with lowest aerial density had the highest resistance of 2.9 Ω along the horizontal direction. Overall, the resistances of the materials ranged from 0.1 Ω - 2.9 Ω (Table 9-2). The lack of consistent ER measurements and the surface preparation made the conductive

matting unsuitable for this application. The solution was to use flat conductive copper tape instead of cylindrical wire.

Table 9-2 Electrical resistance measurements of conductive mats

Areal density [g/m²]	**75.0**	**50.0**	**34.0**	**20.0**	**10.0**	**4.0**
A [Ω]	0.9	0.5	0.5	0.5	1.8	2.7
B [Ω]	0.2	0.2	0.1	0.2	0.6	1.2
C [Ω]	1.0	0.6	0.6	0.9	2.3	2.8

Appendix C Structural element demonstrator results

9.5 Untufted specimens

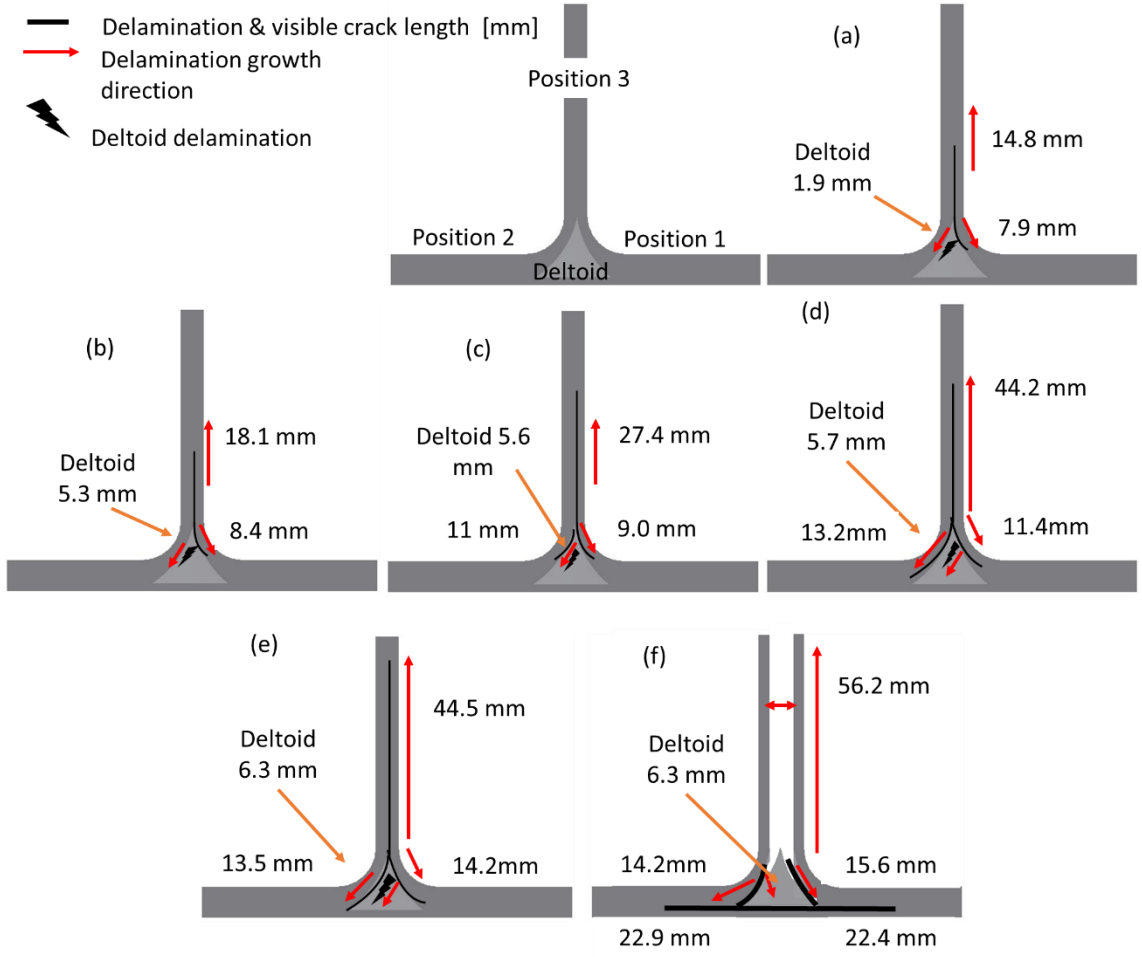

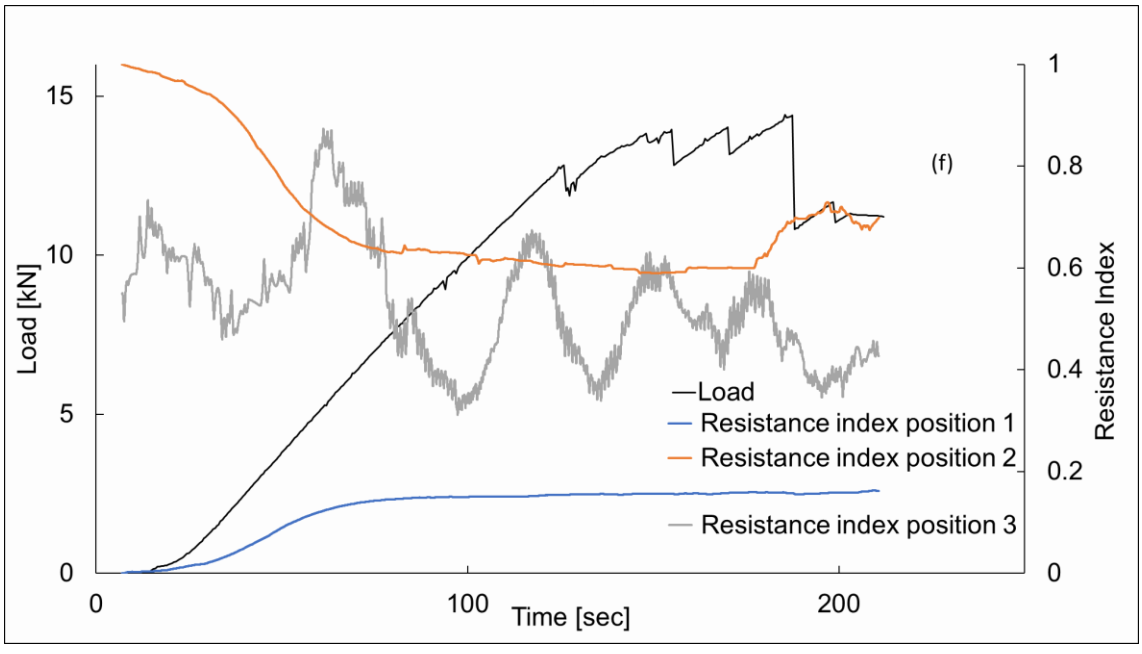

Figure 9-16 Schematic of visible crack propagation at front of T-joint and (bottom) plot of resistance index and load over time of an untufted specimen.

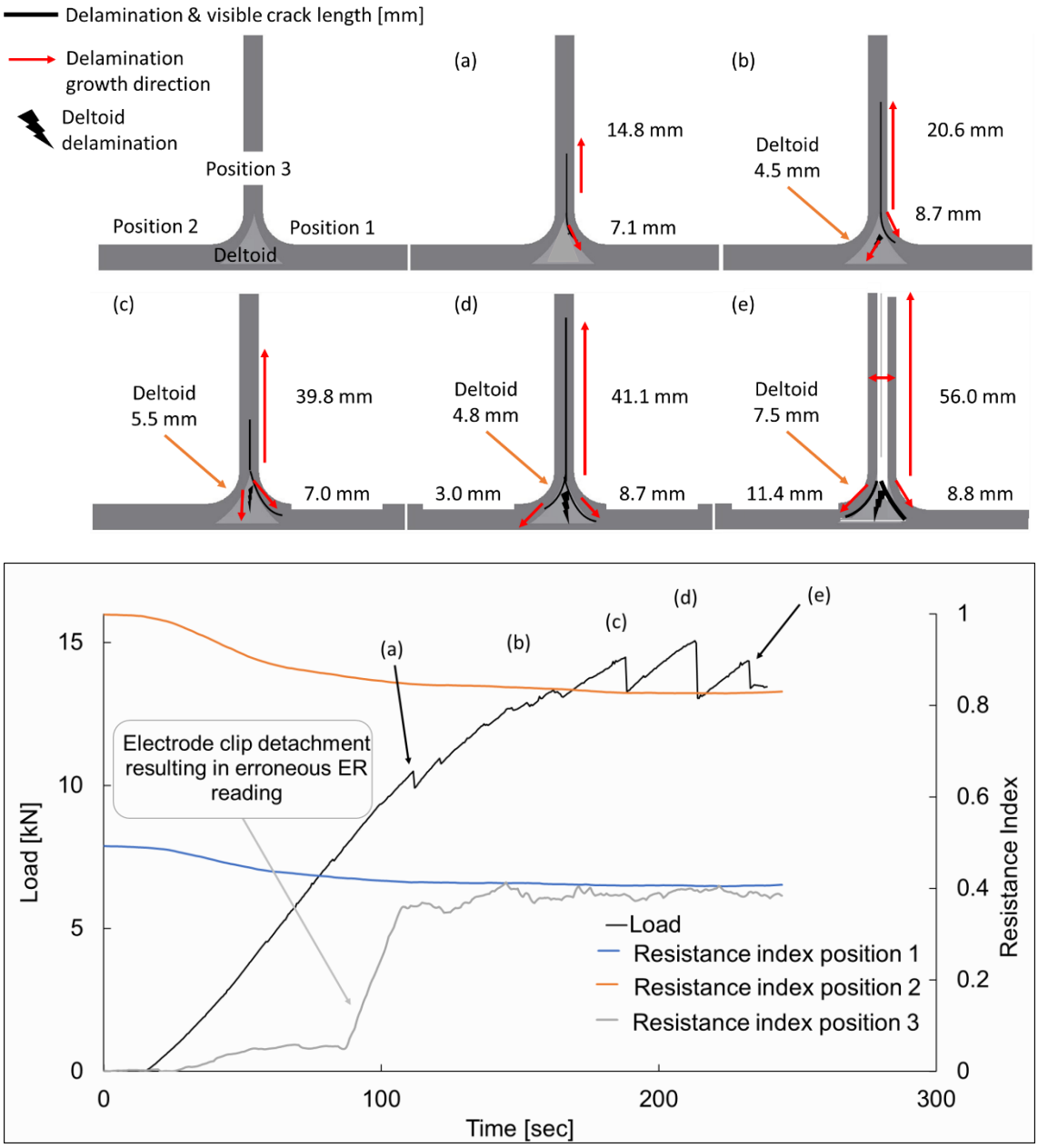

Figure 9-17 Schematic of visible crack propagation at front of T-joint and (bottom) plot of resistance index and load over time of an untufted specimen.

9.6 Original tufted specimens

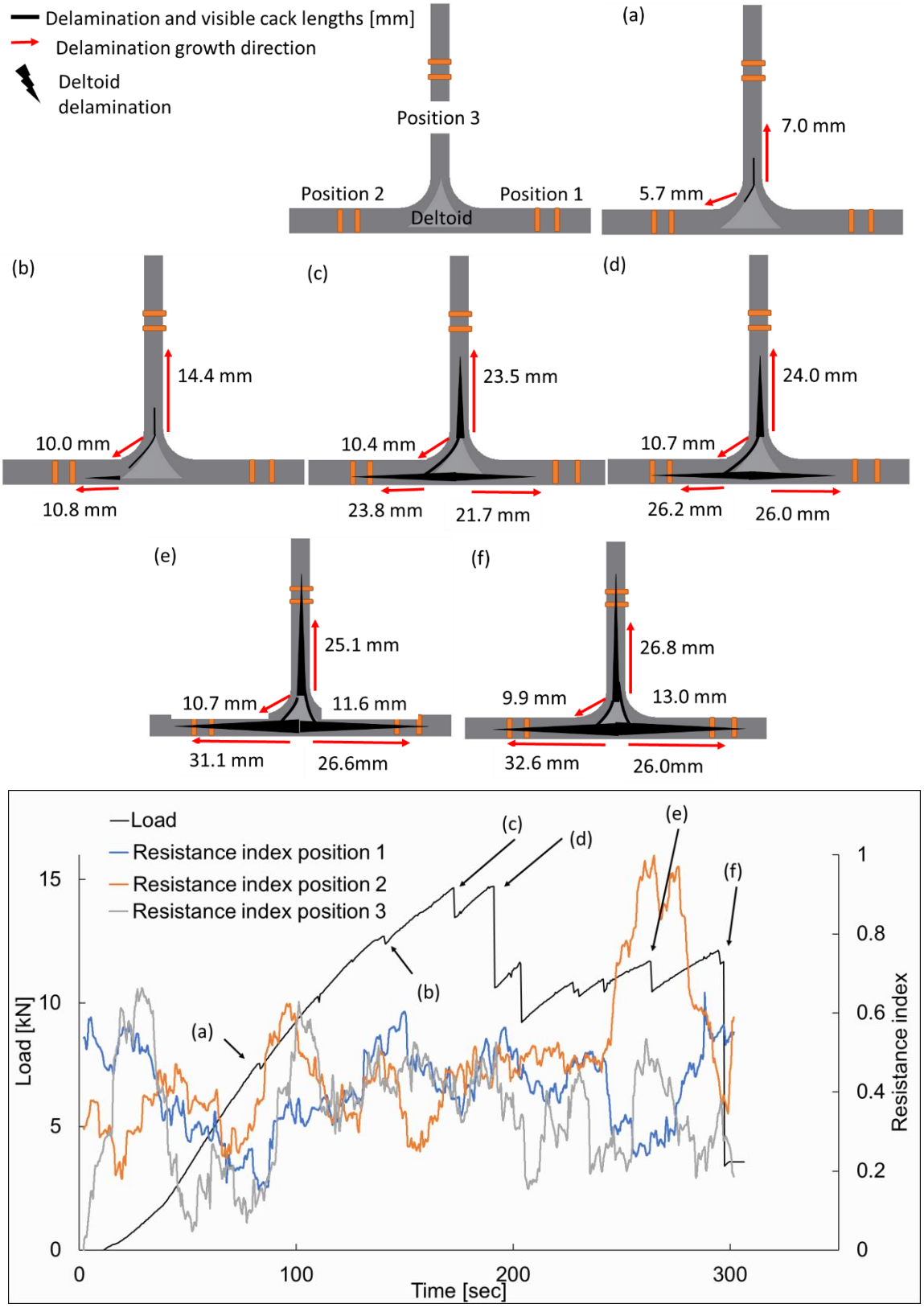

Figure 9-18 Schematic of visible crack propagation at front of T-joint and (bottom) plot of resistance index and load over time of a tufted specimen.

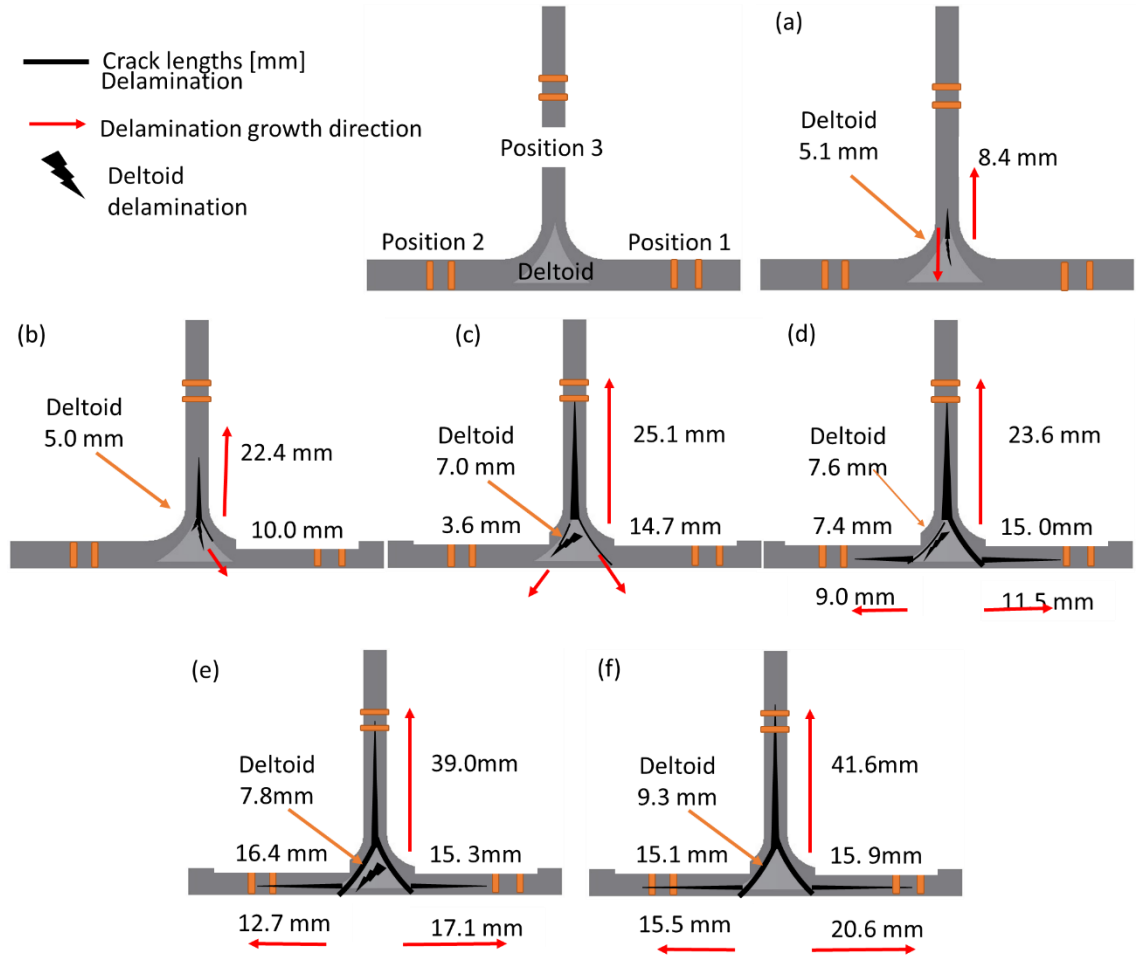

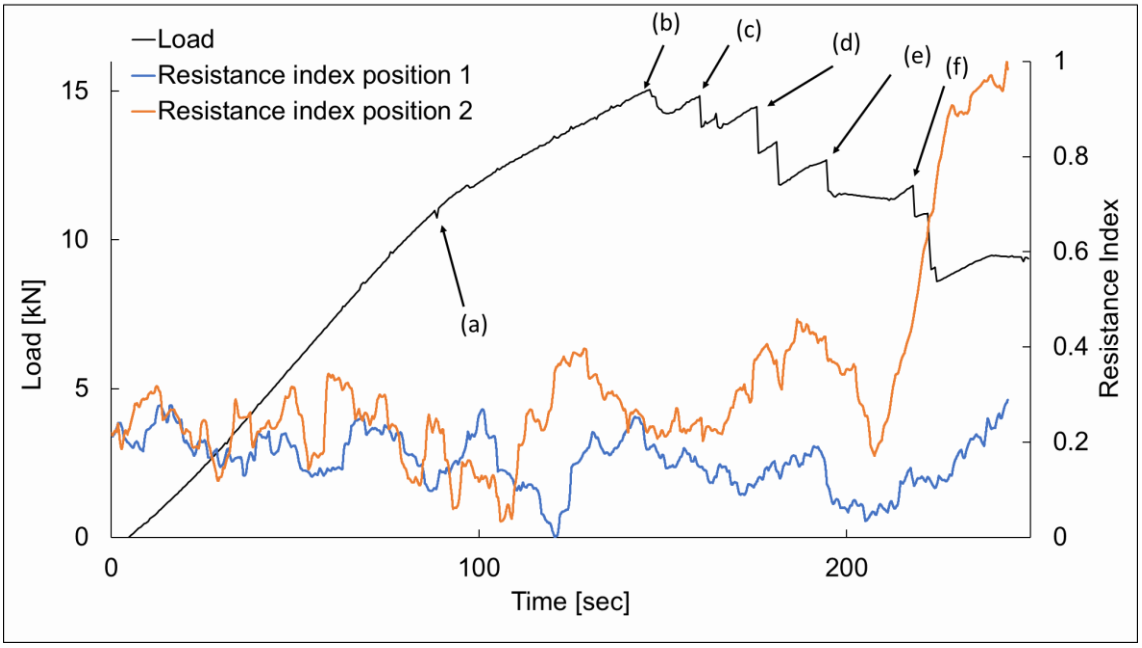

Figure 9-19 Schematic of visible crack propagation at front of T-joint and (bottom) plot of resistance index and load over time of a tufted specimen.

9.7 Alternatively tufted specimen

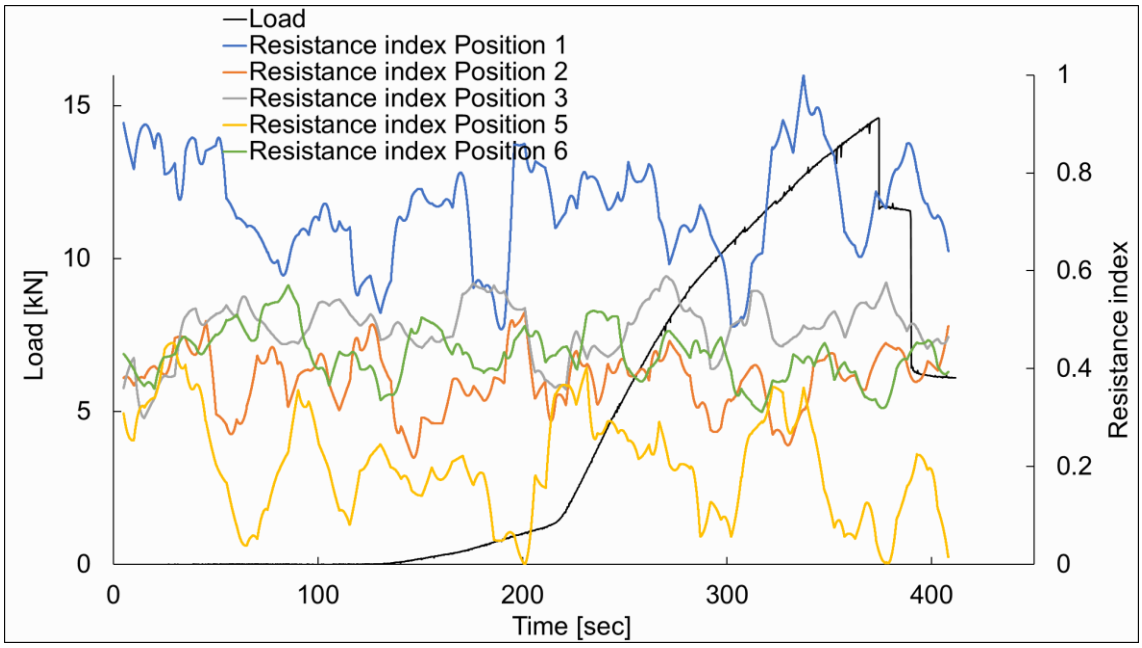

Figure 9-20 Plot of resistance index and load over time of an alternatively tufted specimen tufted specimen. Because tuft rupture did not occur due to asymmetric failure of the specimen in the grips, there was no electrical response measurement.

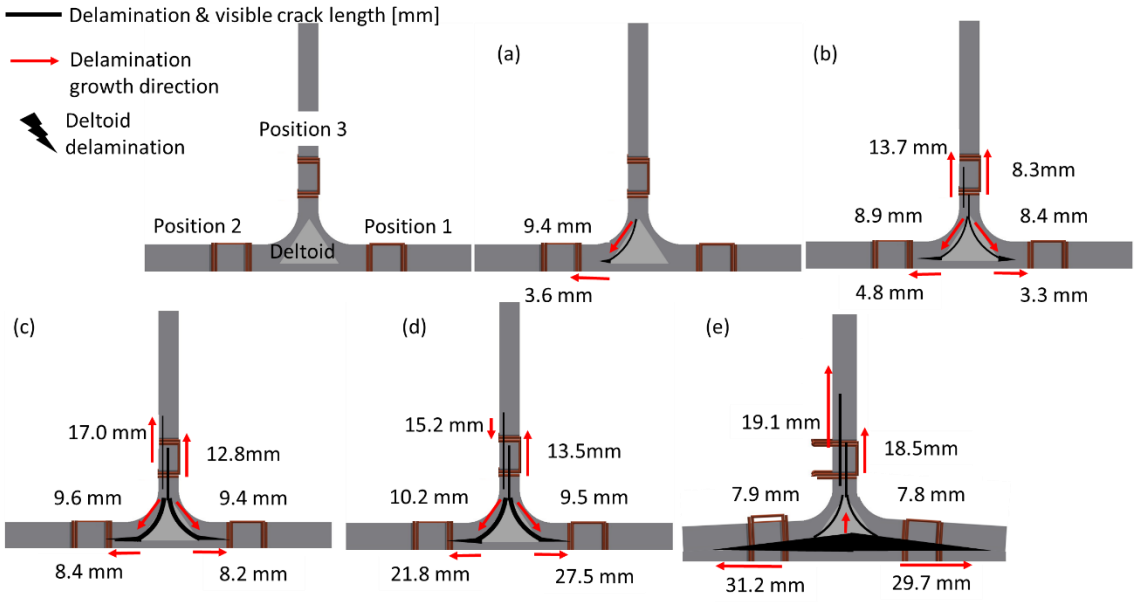

Figure 9-21 Schematic of visible crack propagation at front of alternatively tufted specimen

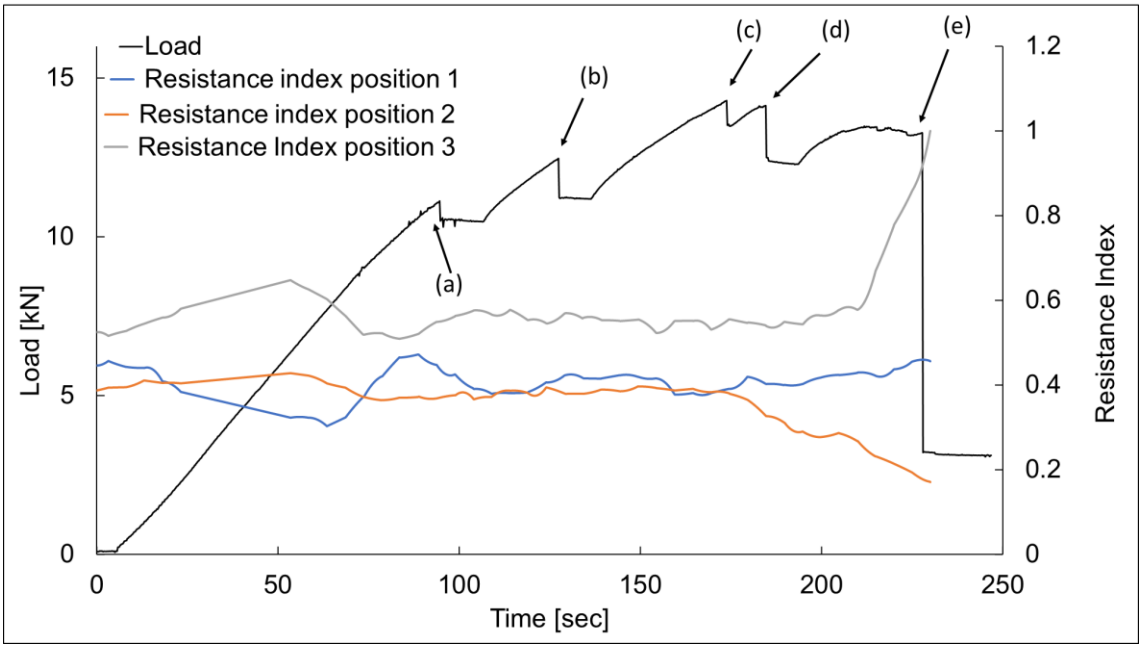

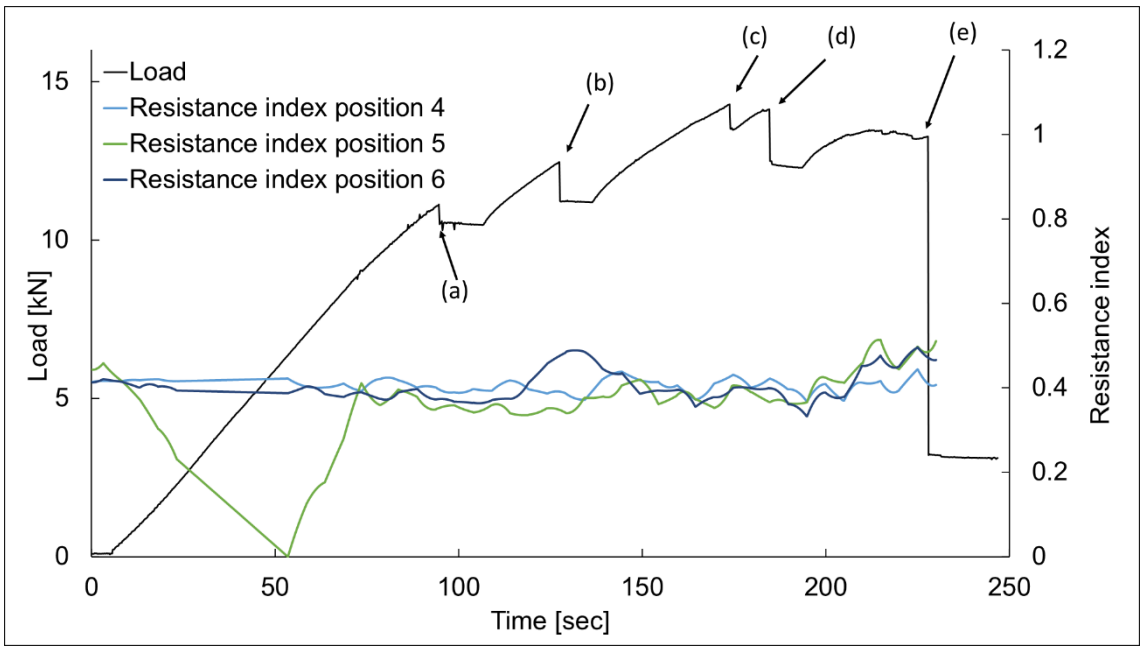

Figure 9-22 Plots of plot of resistance index and load over time of alternatively tufted specimen. (Top) “Near-sense” electrode response and (bottom) “far-sense” electrode response.

Appendix D A pilot study: Achieving cure by inductive heating using hybrid microbraids

9.8 Overview

The following section describes a pilot investigation into an alternative application of the hybrid braided thread and its ability to promote induction heating within composite materials. It introduces another functionality of the incorporated hybrid braid and the benefits of increased through thickness conductivity (TTC). More specifically, the study focused on the ability of the orthogonally inserted hybrid microbraid to increase TTC and improve the susceptibility of the composite laminate to heat by induction. The benefit of better inductive heating in composites has the ability to address industry limitation and issues in repair and maintenance scenarios.

The work is intended to be a standalone section within this thesis and has separate background and objective sections. It includes a description of the relevant induction heating theory as well as information of the apparatus, settings, and experimental methodology. The experimental focus was to determine the feasibility of generating heating in the functionalised material. The effects of hybrid tuft materials, tuft pattern modifications, and composite lay-up on the heating profile were examined in this pilot study.

9.9 Introduction

9.9.1 Objectives

Previous chapters in this thesis showed how improvements in electrical properties could be used for structural health monitoring (SHM) through the use of a hybrid microbraid tufting thread to increase the TTC. This pilot study expands on the previous multifunctional chapters and examines how the improvements in TT thermal properties increased the susceptibility of the composite materials to inductively heat. It was hypothesised that the insertion of the hybrid braid by tufting would increase TTC and increase interply fibre connections within a preform. In so doing, the prerequisites for efficient induction heating should be achieved through electrically closed loops as discussed in Section 9.9.3. This would allow for a quick and energy-efficient carbon fibre structure curing procedure. Furthermore, increased TTC lowers

current and frequency demands on the system, resulting in energy savings. By reducing the demands on the induction system, it would be possible to reduce the size of the equipment and would make the process more realistic for in-field applications.

9.9.2 Background

The increase in composite use over the past decades has predominantly been driven by environmental, cost and energy efficiency savings. However, in comparison to their metal counterparts repair and maintenance of composites presents several challenges resulting from processing sensitivity requirements such as temperature and humidity [251–253]. Initial manufacture of composite parts is usually undertaken within autoclave and industrial settings, however, remedial maintenance and repair of fully assembled structures within identical settings is costly and often not practical. Scarf repairs are the usual and preferred method of repairing composite structures and are considered to be a cost-effective method for extending service life and maintaining high structural efficiency [254]. Scarf repair involves removal of the damaged area, tapering the edges of the cutaway section and the insertion of either prepreg, wet layups or dry fabric followed by localised infusion. In-situ repairs usually involve vacuum bagging systems [255, 256]. Achieving controlled cure temperature and pressure during the curing stage of an in-situ repair is an important consideration. The repair quality is often dependent on the quality of the cure and temperature control [251, 257]. The use of large scale autoclaves or ovens for localised repair of composites would not be practical, as they are slow and energy intensive processes due to ineffective heat transfer, temperature lags and variability, and the time taken to load (and unload) the oven and achieve target temperatures [253, 258–260].

Instead, the composite industry uses localised heating methods such as heat blankets or heat lamps to target the area of interest to avoid heating the entire structure. These external heat sources are placed on or near the surface of the area being repaired and heat the target area gradually from the outside [261, 262]. As composites materials have poor TTC, there are several disadvantages to external methods of heating including excessive or over heating on the surface causing thermal damage, and undesirable temperature gradients through the thickness of the part. Therefore, internal heat generation methods

such as induction heating, offer advantageous alternatives for maintenance and repair [261–263].

There is a clear industrial need to address the constraints of current manufacturing practices and create a cure process that promotes high-rate manufacturing and reduces industry's large ecological and financial footprint [264].

One such method is microwave curing [265–267]. Several studies have described the potential advantages offered by microwave methods compared to conventional heating [268, 269]. These include quick heating rates, fast starting and stopping times, targeted energy efficient heating, increased heating uniformity, and reduced processing time [270]. Research has shown significant reductions in cure cycle time without a reduction in mechanical and physical properties [268]. Conversely, degradation to the epoxy matrix and the carbon fibre due to thermal and microwave exposure has been documented carbon fibre reinforced polymers (CFRP) [269]. A further significant disadvantage is that microwaves are hazardous to health and as a result specialist vessel designs are required. This limits part size and complexity due to the increased cost associated with bespoke tailoring and health and safety considerations [267, 269].

Another alternative to autoclave heating is the direct application of an electrical current to carbon fibres [271]. This method has an advantage over microwave and induction methods due to its simplicity and low current requirements [272]. The studies investigating this method described cure processes that progressed similarly to those experienced in standard oven conditions, avoided overheating, and resulted in similar mechanical properties in the final component [262, 271]. However, the authors acknowledged some limitations in the method caused by the contact arrangements resulting in non-uniform heating and temperature gradients. However these studies were limited to laboratory examinations and not expanded to industrial scale [271].

In the aerospace industry, induction welding of thermoplastic composite parts is slowly replacing adhesive bonding, resistive bonding, and joining with fasteners due to advantages such as mass reduction, ease of automation and lower production costs [273, 274]. An advantage of using induction is that it is able to rapidly heat the compromised area internally without relying on gradual thermal

heating from the surface and avoids whole structural heating [260]. It is therefore a more efficient and energy conservative heating process suitable for curing resins used in repair patches. In addition, part complexity can be increased as induction coils can be operated remotely over a part and need not be attached to the structure as is the case for heat blankets

A study, undertaken by Boeing, examined a full-scale wing composite to demonstrate the technology and involved an in-depth evaluation of equipment, tooling, and inherent processes such as consolidation involved in manufacture [258]. Energy savings of up to 90% were achieved from increased efficiencies attributed to avoiding excessive heat loss to the tooling. The manufacture of the Fokker Gulfstream G650 (Figure 9-23) aircraft employed induction welding to the joints of the torsion box and achieved a 20% cost reduction and a 10% mass saving due to design optimisation [274, 275]. Developed by the KVE Composites Group, inductive welding technology was reportedly easily automated and offers improved part quality with no voids or contaminants detected [275].

Figure 9-23 (Left) Induction welded G650 rudder torsion box. (Centre) First flight of G650 prototype aircraft. (Right) Induction weld robot and weld jig [275].

The majority of published research on inductive heating of composite materials focuses on inductive welding and part fusion. However, the process requirements and optimisation needs in these studies are also applicable to inductive curing [259, 276–281]. Similar to large scale welding scenarios, composite manufacturers require a curing process which is energy and cost efficient whilst improving temperature control, avoiding exothermic responses, and increasing manufacturing flexibility for part geometry. Environmental health and safety are also important additional requirements [258, 267, 282]. Induction

heating has shown promise as a potential method to address these manufacturing aspirations [258].

9.9.3 Theoretical background

The workpiece is the industrial word for the target material that needs to be heated; in this thesis, the workpiece is the carbon fibre composite. In general, an inductive heating apparatus comprises of a looped wire coil with an alternating current flowing through the circuit [282]. This current in the coil produces a magnetic field that is the same frequency as the coil current. When another conductive material, the workpiece, is placed within range of the electromagnetic field (emf), secondary currents are induced. These induced currents in a workpiece are called eddy currents. In most industrial applications, metal parts are placed directly within the coil which are usually solenoidal or circular in shape (Figure 9-24) [267].

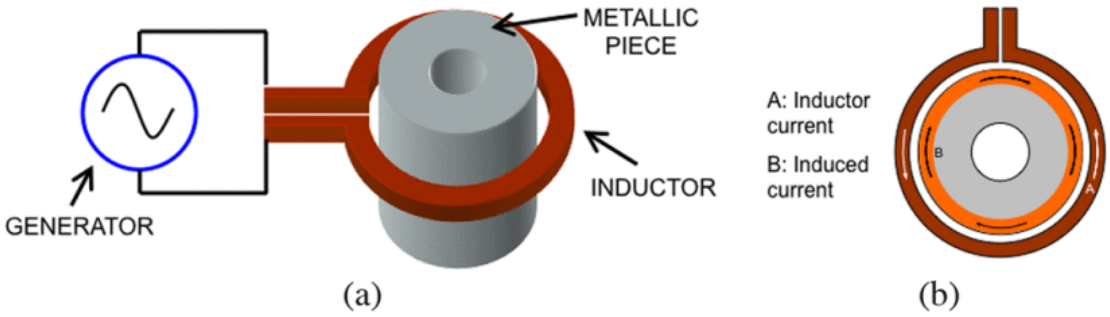

Figure 9-24 Typical arrangement of an induction heating system in a longitudinal flux configuration: (a) general view and (b) top view (Lucia et al., 2014).

The relative magnetic permeability and the relative permittivity of the material influence the inductive heating process. Magnetic materials or ferromagnetic materials such as iron, cobalt and nickel are heated using induction by magnetic hysteresis [267, 282].

In the case of composite materials, only conductivity or relative permittivity applies because carbon fibre is not magnetic [282]. The literature identifies three mechanisms for heat generation in carbon fibre, with some inconclusiveness as to which one dominates [282] These are Joule losses from within the fibre [283], dielectric hysteresis [284] and contact resistance [285] as depicted in Figure 9-25. They can be separated into two types: fibre heating and fibre junction heating mechanisms [279]. As stated previously, Joule loss is

dependent on fibre electrical resistance along the length, with heat generated due to the voltage drop across the fibre (Bayerl et al., 2014). Fibre-fibre junctions have been shown to generate maximum temperature on a carbon fibre composite when placed directly over an inductive coil [285]. Interply junction points generate heat due to contact resistance between the fibre, whilst dielectric hysteresis occurs due to matrix-fibre separation [279, 282, 285].

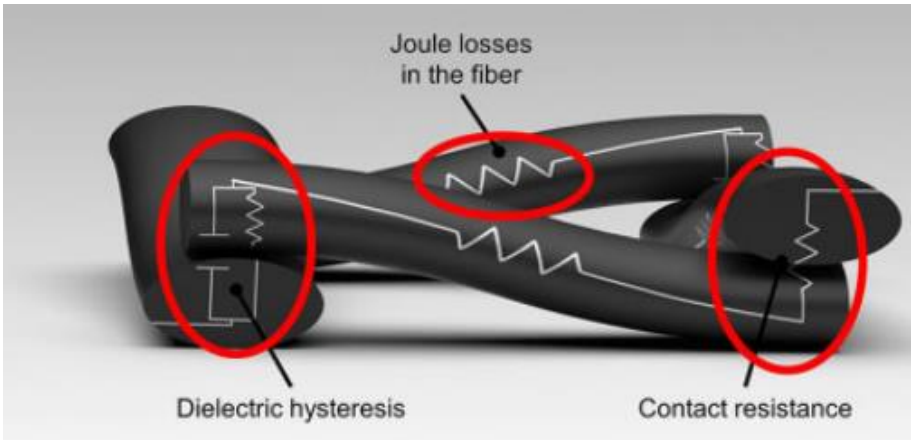

Figure 9-25 The three heating mechanisms which affect heat generation during the induction heating of CFRPC. CFRPC: carbon fibre-reinforced polymer composites [279].

The capability of a workpiece to be heated is determined by the presence of electrically closed loops to enable eddy current generation. [273, 282, 286]. Carbon fibre is sufficiently conductive to enable inductive heating, however, the extent and efficiency of this heating is dependent on the density of these closed loops. The significance of these loops is highlighted by the fact that a single ply of unidirectional (UD) fabric cannot be efficiently inductively heated due to low transverse conductivity [276].In woven fabric reinforcements, the closed loops are inherently present due to fibre-fibre connections within and between plies with different fibre orientation. It is evident from the literature that the interply connections within a carbon fibre laminate and the composition of the lay-up have a significant effect on the heat distribution, especially for UD reinforcements. The importance of junction heating dictates that the highest heat intensity was achieved by a lay-up possessing the most cross fibre junctions [276, 282]. The effect of ply lay-up on heat distribution is depicted in Figure 9-26. For nonconductive materials such as glass, inductive heating has been achieved through indirect heating in additional materials called susceptors [259, 281, 282, 287, 288]. Susceptors in the form of metal meshes or resin

matrix modifiers have been widely used to induce heating in non-conductive materials [280, 282, 289]. The workpiece is heated indirectly via the inductively heated susceptors. Susceptors have been utilised not only to permit heating of non-conductive composite materials, but also to aid in heat dispersion. The characteristically low TTC of UD carbon fibre laminates makes them unsuitable for inductive heating, however, the addition of a susceptor can facilitate and improve heating [273].

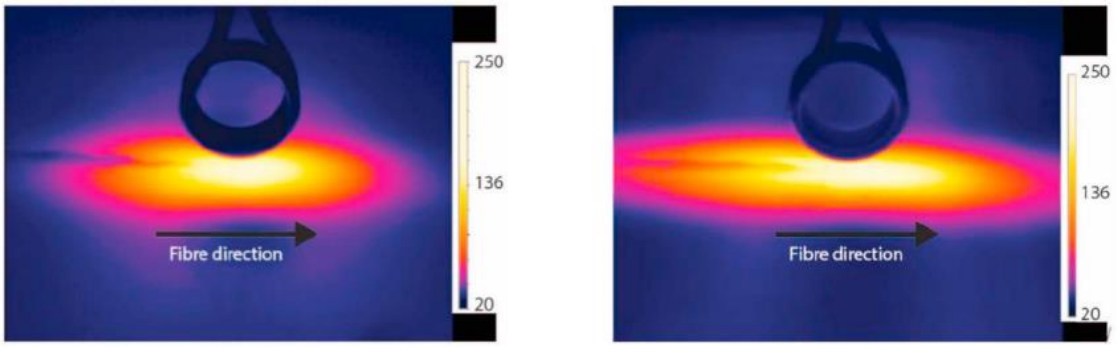

Figure 9-26 Effect of ply lay-up on heat distribution (left) Laminate with the dispersed lay-up, i.e. $[0/90]_{3s}$. (Right) laminate with the grouped lay-up $[0_3/90_3]_s$ (Grouve et al., 2020).

A number of reviews on induction heating highlighted a wide range of factors such as ply lay-up, ply orientation, material type, matrix, and other experimental design factors which greatly influence the perceived results. It is also likely that heating mechanisms vary across experimental examinations due to changes in the material compositions [259, 276, 278, 279, 281, 282, 287].

9.9.4 Heating management and optimisation

Recent studies are predominantly concerned with addressing limitations experienced whilst using inductive heating to increase industrial capacity. One such limitation is non-uniform heat distribution through the cross section of a conducting part caused by the skin effect. This causes a concentration of eddy currents at the surface of a workpiece and an imbalance in heat generation between the core and the outer edge. The extent of the skin effect is dependent on the frequency of the alternating current, the material properties (i.e., conductivity) and the thickness of the part [278]. Research in the optimisation of inductive heating has focused on increasing eddy current density and temperature distribution. The aim has been to better understand the physical manufacturing parameters, to produce more predictable model demonstrators and remove wasteful trial and error testing. Parameters such as fibre volume

fraction, fibre diameter, fabric compaction, ply orientation, part geometry, contact pressure or debulking of the material, and matrix composition have all been studied in the literature. However, there is a clear lack of understanding that would allow for definitive optimization. [273, 276, 278, 279]. The number of experimental variables also makes comparison among studies difficult.

One industrial method used by KVE INDUCT® involves the use of a cooling heat sink to dissipate the heat from the top surface, focusing induction heating at the target weld zone (Figure 9-27) [274]. This concentrates the heat in the desired areas but avoids overheating of other parts. Another method implemented to control the surface temperature of the workpiece uses an air blowing system for cooling. Several researchers have adapted similar methods so that the area cooled by the air is unaffected by the heat generated by the induction heater [287, 290, 291].

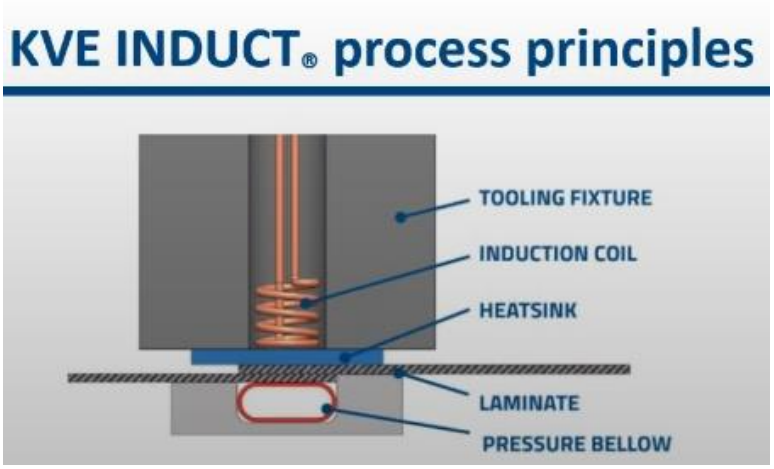

Figure 9-27 KVE INDUCT® induction welding process.

9.9.5 Instrumentation effects

Coil geometry is an easily modified but important part of the inductive heating process. It determines the magnetic field shape, which the induced eddy currents and subsequently the heating pattern tend to mirror. Ideally, the coils are designed specifically to consider the geometry of the workpiece and the desired area to be heated. However, numerous coil designs, such as pancake, helical, single-turn, butterfly multiturn solenoids, or double pancake coils, are widely accessible off-the-shelf (Figure 9-28). The choice of which to use is dependent on the industry sector, heat distribution requirements and cost. For

most induction scenarios involving carbon fibre composites, single-sided coil heating is desirable for ease of accessibility.

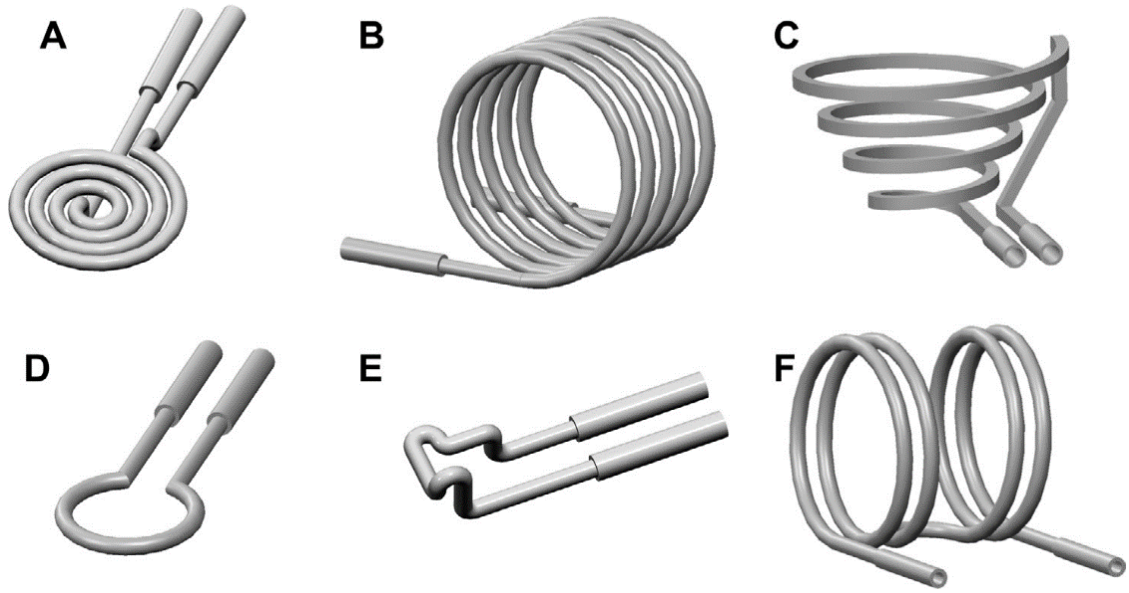

Figure 9-28 Common coil designs applied for the inductive heating of composites (A) pancake coil, (B) helical coil, (C) conical coil, (D) single-turn coil, (E) irregular coil adapted to the workpiece shape, (F) double-helical coil (Helmholtz coil) [282].

A solenoid multiturn (Figure 9-28 (B)) coil is the most conventional type for heat treatment of piping, and bars, whilst pancake coils are common in domestic worktops. As demonstrated in Figure 9-29 the effective magnetic field of a pancake coil is greatest at the outer edge but drops significantly or completely in the centre. This influences current distribution within the workpiece and causes non-uniform heat distribution. Workpiece positioning also influences the heating distribution and must be taken into consideration during processing. The electromagnetic field distribution can be easily manipulated depending on coil type, however, the heating area and temperature profile along the part are also affected by field distortions on the end and edge of the field. These end and edge effects are more obvious in flat panel parts compared to cylindrical workpieces within a solenoid coil. The extent of this distortion is dependent on a number of variables including the skin effect, coil overhang, part positioning, and coil geometry. These factors can result in overheating or underheating of the workpiece if not properly considered [267, 281, 283].

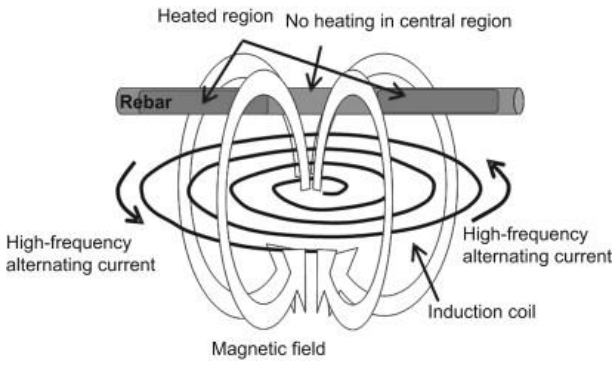

Figure 9-29 Magnetic field and region heated by electromagnetic induction

9.9.5.1 Effects of ply lay-up on heat generation

As previously stated in Section 9.9.5 the heating pattern within a workpiece is determined by and mirrors the coil geometry. However, the anisotropic conductive properties of carbon fibre have been shown to cause a disruption to this mirrored heating effect. This is due to the electrically conductive paths of carbon fibre being predominantly in the in-plane direction [283]. The effect of ply lay-up on heat generation and distribution is therefore an important parameter to consider when attempting to achieve temperature homogeneity. Depending on application, this deviation from the heat generated mirroring the coil shape, could be an advantage or a disadvantage. However targeted precision heating this the desired optimum.

Several studies have investigated the effect of ply lay-up and the extent to which the heating pattern is dispersed from the coil shape. They highlight the importance of the quantity of cross-ply interfaces which complete closed loops between ply layers [276, 282, 292]. This is most apparent in UD fabrics where heating is solely along the in-plane direction and results in high thermal gradients through the thickness direction and inhomogeneous heat dispersion [283]. In comparison the crimped fibres of woven fabrics are sufficient to create a closed loop between layers and subsequently heating occurred between the layers of the fabric [276, 283, 291, 292].

9.10 Aims and objective

The induction cure of resin infused composites has not been undertaken previously. The aim of this pilot was to investigate induction cure of resin infused composites and the effect of the tufted hybrid braid on the induction

heating profile. It was thought that the hybridisation would aid in increasing through-thickness conductivity and increase heating uniformity in the infused preform.

9.11 Materials, method, and apparatus

9.11.1 Induction heater

The Ambrell Easyheat® induction heater comprises a spiral pancake coil (Figure 9-30) with an integrated water-cooling system and an electronic digital control. Two methods of operation and temperature control were available: an optical pyrometer (closed-loop temperature control) and an external controller (current control). The equipment operated within a range of 150-400 kHz with power monitoring displayed on the front LCD panel. The resolution power control was to within 50 W. The closed-loop operation utilised a proportional–integral–derivative controller (PID) that received sample surface temperature measurements from a thermal laser monitor. Once a pre-set temperature was achieved, the induction heater pulsed to maintain the sample at the desired temperature. Instrument training of the coil was undertaken using composites similar to those for the main study. This training calibrated the PID and induction heater to match the power input to the coil with the desired temperature of the workpiece sample. A manual constant current could also be set using the front control panel with the thermal laser simply recording the temperatures reached.

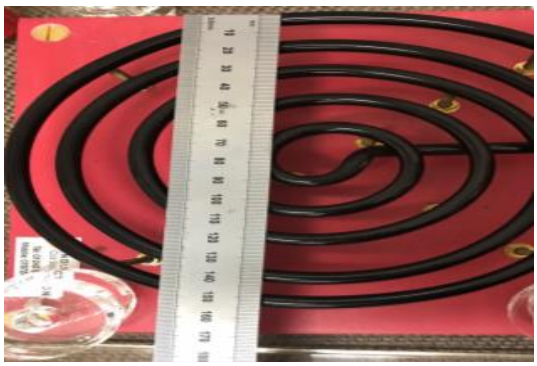

Figure 9-30 Induction heater pancake coil.

As a safety measure the unit was enclosed in a bespoke Perspex® box with a portable Labcat ULTJUMBO filter extractor used to contain any potentially released vapours during sample heating. During testing, samples were placed on a glass plate over the coil with Perspex® spacers. A hole in the front allowed

for infrared (IR) thermal surface assessment using a FLIR T650 thermal camera. The IR camera was angled to achieve a surface view of the panel through the Perspex® box opening. Figure 9-31 is a schematic diagram and photograph of the induction heating equipment used in this study.

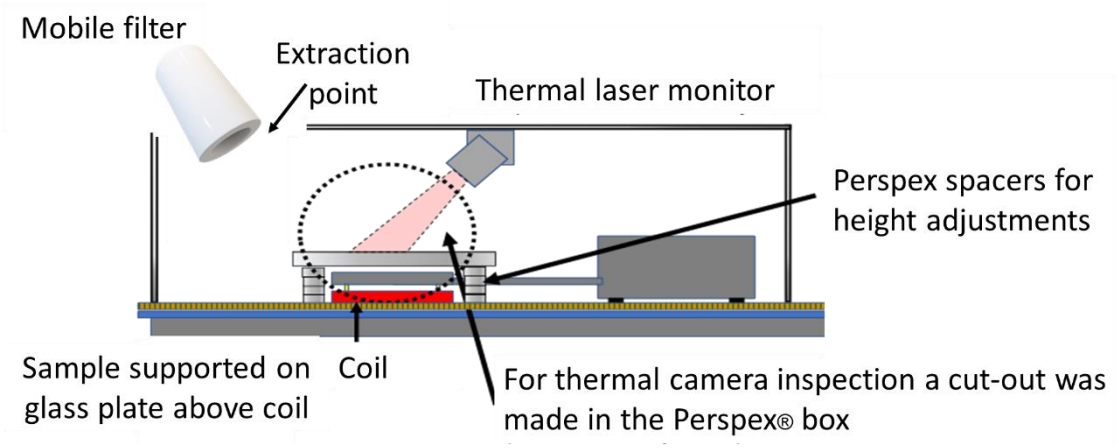

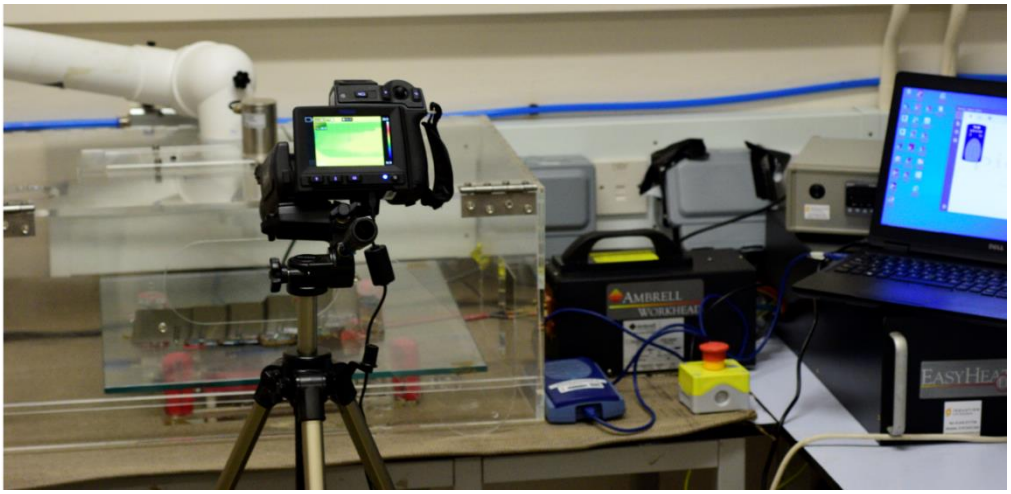

Figure 9-31 (Top) schematic and (bottom) photo of induction apparatus.

9.11.2 Testing procedure

The integrated laser in the induction equipment monitored the heat at a specific location on the panel and used that information to control the input from the coil; however, it did not offer a comprehensive thermal state of the workpiece. Further thermal assessment was carried out using a FLIR T650sc high resolution IR thermal camera. This IR camera offered visual imaging, thermal readings, and video recording of continuous testing on the sample surface. It allowed the hottest point on the sample surface to be identified, and the thermal laser could then be directed to this area, preventing overheating.

The TT thermal profile was assessed using embedded thermocouples positioned within the lay-ups. The RS PRO Type K thermocouples comprising of two wires were used for temperature measurement up to 250°C. A Pico Technology USB TC-08 Temperature Data Logger with a capacity for eight channels was used to record the input and was set to a sampling rate of one measurement per second; the output was exported using PicoLog6 software. The positions of the thermocouples varied depending on the fabric, ply lay-up and tufting pattern but were positioned to achieve maximum information on the TT thermal profile and the effects of the magnetic field generated by the coil. The thermocouples were positioned to take measurements of three areas of interest: centrally, at the area exposed to the maximum field, and an outer edge as shown in Figure 9-32.

Figure 9-32 Schematic of coil position under test specimen with emf range and shape indicated.

9.12 Preform and lay-up preparation

9.12.1 Materials

Three fabric types were used during this study: two carbon fibre fabrics, and a glass fibre fabric. The first was a Sigmatex 5011X carbon fibre PC414X UD fabric made of 12k HTS 5631 carbon fibre yarn with an epoxy sizing, with a 37 tex E-glass weft at 300-500 picks per metre. The second carbon fibre fabric was a Formax FCIM357PB 24k, 750 -45/0/+45 triaxial fabric. The glass fabric was supplied by East Coast Fibreglass Supplies and was an ECM Triaxial Clot 600g -45/0/+45 triaxial fabric. The layups were constructed so each preform comprised a total of 24 plies, i.e., 24 UD plies and eight plies of triaxial fabric. The lay-ups of triaxial fabric preforms were assembled to be as balanced as possible. Simulated triaxial preforms were also constructed with UD fabric to establish the effect of preform structure on induction capability (Figure 9-33).

Ply	Triax preform	UD preform	Simulated Triax preform
1	0	90	0
2	45	90	45
3	90	90	90
4	45	90	45
5	0	90	0
6	-45	90	-45
7	90	90	90
8	45	90	45
9	0	90	0
10	-45	90	-45
11	90	90	90
12	45	90	45
13	-45	90	-45
14	90	90	90
15	45	90	45
16	90	90	90
17	45	90	45
18	0	90	0
19	45	90	45
20	0	90	0
21	-45	90	-45
22	0	90	0
23	-45	90	-45
24	90	90	90

Figure 9-33 Preform layup. (Left) triaxial preform, (centre) unidirectional fabric and (right) simulated triaxial preform.

Infusion of the preforms was undertaken using a double bag vacuum assisted resin infusion system with Prime™27 resin and slow hardener. The mixed ratio of the resin to hardener was 100:28 parts by mass and was degassed for 30 minutes before infusion. The intended cure procedure was to gradually increase the temperature at a rate of 2°C/min to 80°C and then maintain this temperature

for 2 hours. Where deviations occurred, this is stated in the relevant experimental sections. Table 9-3 provides a test matrix of the parameters examined in this study.

Copper or nickel-chrome hybrid braided threads comprised of four wires and four carbon fibre tows were used as the tufting threads. The yarn interlacement was 1:1 with a lay-length of 8 mm as detailed in Section 3.4.3. Tufting was carried out using the adapted 3D printed chassis as detailed in Chapter 5. It was sometimes necessary to adjust tuft spacings depending on the preform type and avoid damaging the incorporated thermocouple wires. Consequently, some variability in the areal densities occurred. This variability in tuft areal density had limited influence in this study as the parameter of interest was the effect of tuft pattern and orientation relative to the preform fabric. Induction heating profiles were undertaken with dry, and resin infused preforms, and cured composites. Section9.13 provides more specific details on the type and condition of the preform, as well as whether or not a cured composite was used.

Table 9-3 Test matrix of examined panels

Section	Details	Layup	Studied parameters	Figure
9.13.1	Oven cured carbon fibre composite	Triaxial	Thermal profile of untufted cured specimen	Figure 9-34
9.13.2	Resin infused untufted carbon fibre preform	Triaxial	Effect of resin cure cycle on heating profile	Figure 9-36
9.13.3	Tufted resin infused carbon fibre preform	Triaxial	Effect of tufts on induction heating	Figure 9-40
9.13.4	Cross-hatched and parallel tufted carbon fibre preform	Triaxial	Effect of tufting pattern and cross linking on induction	Figure 9-45 Figure 9-46
9.13.5	Single ply and double ply [0/90]	UD	Effect of ply layup	Figure 9-49 Figure 9-51
9.13.6	Untufted and tufted carbon fibre preform	UD	Effect of ply direction on induction heating and influence of tufts	Figure 9-53 Figure 9-54
9.13.7	Tuft areal density 0.3% and 0.6%	UD	Effect of areal density on induction	Figure 9-55 Figure 9-56
9.13.8	Tufted parallel and perpendicular to top ply direction	UD – simulated triaxial panel	Effect of tuft direction on induction	Figure 9-58
	Tufted parallel and perpendicular to top ply direction	Triaxial	Effect of ply layup	Figure 9-59
9.13.9	Fibreglass tufted specimen	Triaxial	Effect of tufts in non-conductive material	Figure 9-60 Figure 9-61
9.13.10.	Copper – carbon fibre hybrid thread Nickle – chrome – carbon fibre hybrid thread	UD	Effect of braid materials	Figure 9-63

9.13 Observations and Discussion

9.13.1 Coil emf and heating profile of untufted composite

A conventionally oven cured untufted triaxial carbon fibre composite was used to initially examine the pattern of heat generated in a composite using the induction heater. Figure 9-34 provides a schematic of the coil position under the composite and corresponding IR images of the unheated and heated composite. The thermograph shows an inhomogeneous heating profile, which was ring or torus in shape. This torus shape resulted from the pancake coil shape of the induction heater used in these experiments. The thermal profile shows cooler areas in the centre and at the corners of the composite when inductively heated.

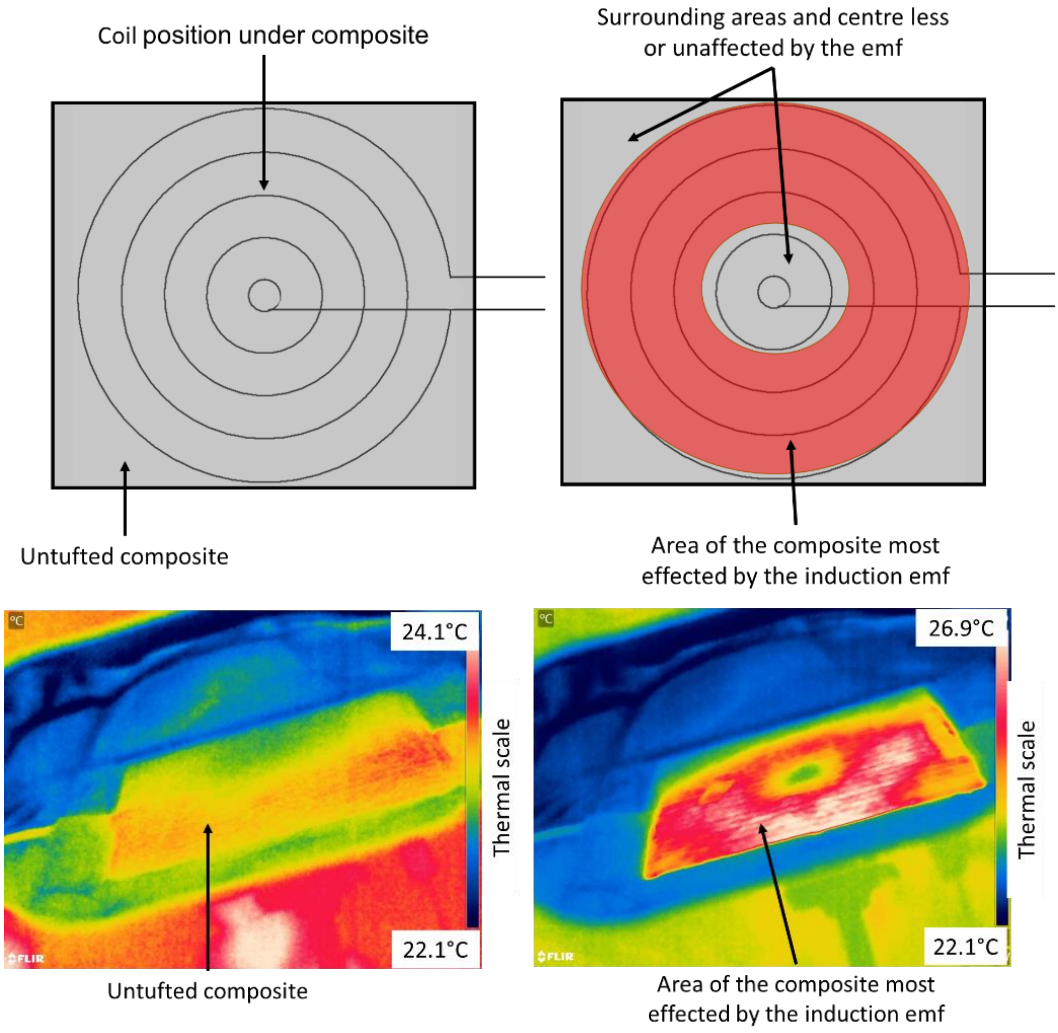

Figure 9-34 (Top) Specimen and coil schematic and (bottom) IR image of surface temperature of an untufted triaxial composite. (Left) At room temperature with induction heater off and (right) inductively heated.

The through-thickness (TT) thermal profile on this composite was monitored using a set of thermocouples placed between plies 2, 4, and 6 (Figure 9-35), which were positioned within the area most influenced by the emf (the area shaded in red in the schematic). The composite was inductively heated to 65°C at a rate of 5°C per minute. This assessment showed that within the areas heated through induction, there was no variability in the heating profiles in the TT. Each heated as rapidly as the other and the difference of 5˚C after 600 seconds was due to proximity to emf. It was assumed that temperature variations were more likely to occur due to limitations of emf shape, rather than by the skin effect or the thickness of the composite exceeding the effective range of the emf.

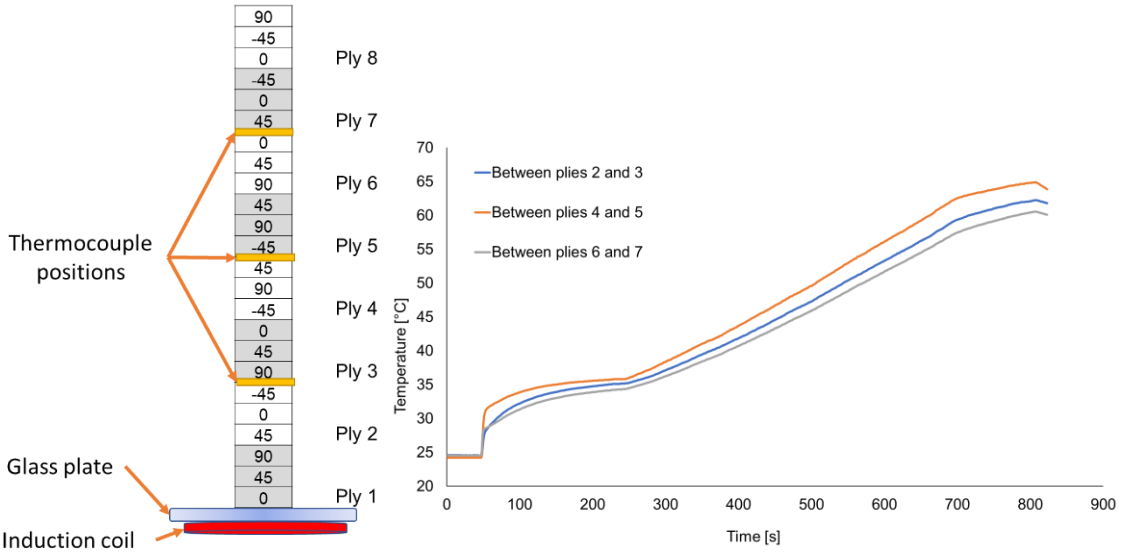

Figure 9-35 TT thermal assessment. (Left) Thermocouple positioning in triaxial composite and (right) plot of temperature vs time.

9.13.2 Induction cure of an untufted resin infused triaxial preform

Expanding on the initial assessment in Section 9.13.1, a procedure to enable the infusion and inductive curing in-situ was established. Infusion was undertaken with the bagged preform positioned on the Perspex® plate over the induction coil. Once the resin reached the outlet tubing and the preform was considered fully infused, induction commenced using a ramped heating rate of five degrees per minute up to 80°C and held at 80°C for 2 hours. Again, the dominant heating profile was torus in shape with the centre and corners cooler. No measurable changes in the heating ability of the induction heater were

observed despite the changes in the resin state from liquid to solid during cure. The thermograph also revealed uneven heating across the panel. (Figure 9-36). This suggested that the glass plate had shifted during infusion and was no longer positioned centrally over the coil. An edge effect where the emf deviated around the edge of the workpiece resulted in an uneven heat distribution over

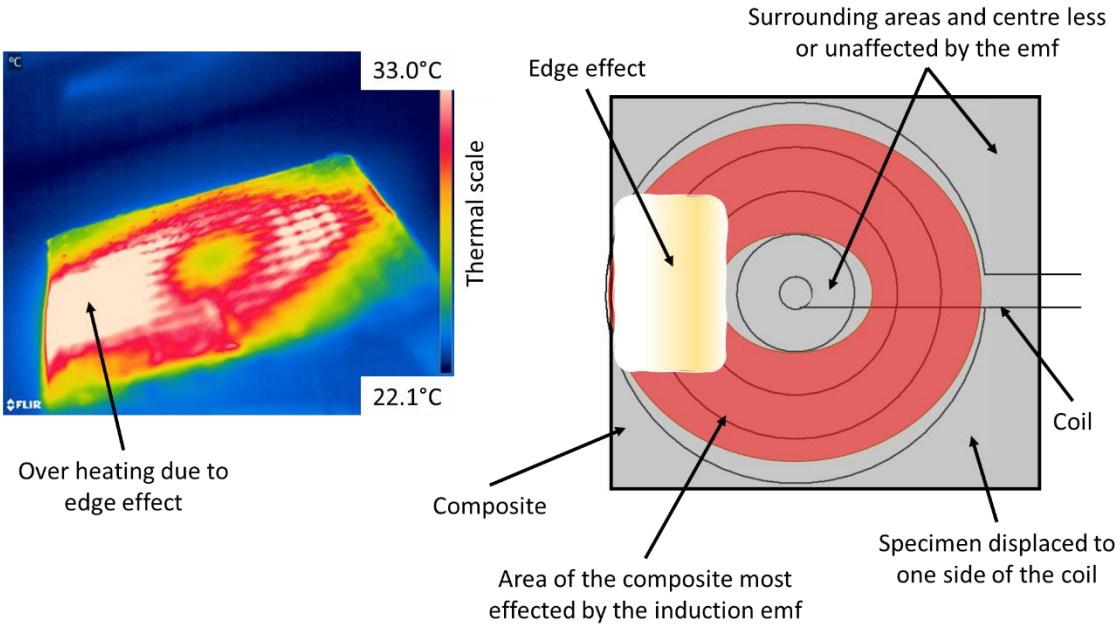

Figure 9-36 IR image of resin infused and cure of untufted triaxial carbon fibre preform and (right) schematic.

the part and the left-hand side experienced increased heating intensity compared to the right.

An assessment of thermal distribution during cure was undertaken using eight thermocouples placed TT of the preform (Figure 9-37). Their positions were chosen to assess the emf effect across the preform geometry and TT.

- C2, C4 and C6 – Centre of the preform between plies 2 and 3, plies 4 and 5, and plies 6 and 7, labelled C2, C4, and C6, respectively.
- RHC4 and RHC6 - Right-hand corner of the preform, one between plies 4 and 5 and the other between 6 and 7. These two were chosen to monitor areas assessed to be outside of the emf range from previous experiments. They were therefore thought to be the least likely to heat either by induction or conduction.
- L4 and L6 where placed on the left-hand side of the preform between plies 4 and 5, and plies 6 and 7.

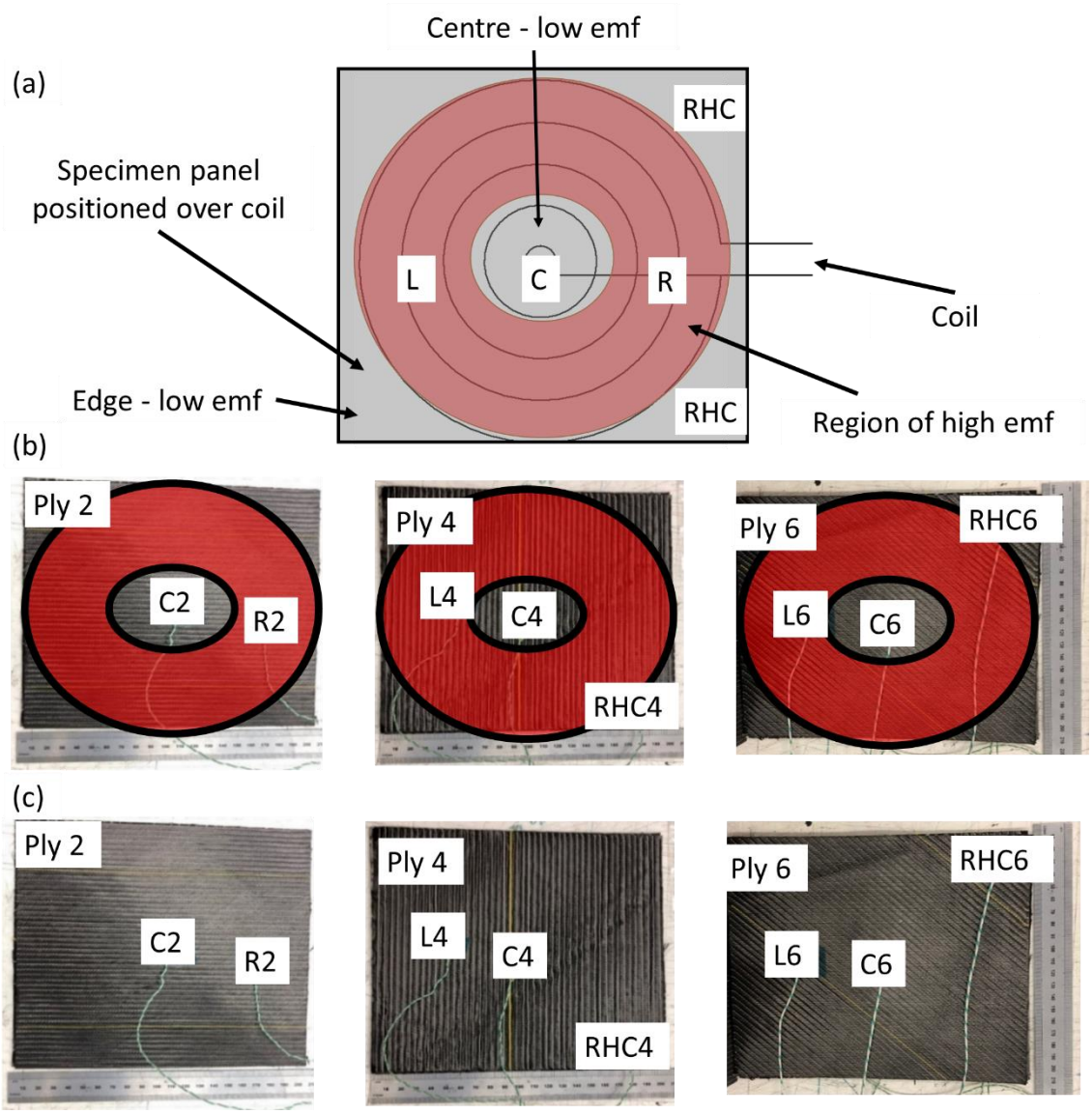

Figure 9-37 Thermocouple placements. (a) Schematic of positions relative to coil and effective emf, (b) placement on plies 2, 4 and 6 relative to effective emf and (c) photos of thermocouples positioned on plies.

- R2 was placed on the right-hand side between plies 2 and 3. The final three were placed within the torus region to be most affected by the emf.

Figure 9-38 shows a plot of temperature over time of the full curing process including the heating, 2-hour fixed temperature (target temperature 80°C), and cooling stages of the untufted resin infused preform. The plot in Figure 9-39 shows the first 125 seconds of the test and the temperature increase from the initial point the induction heater was turned on (indicated by the box in Figure 9-38

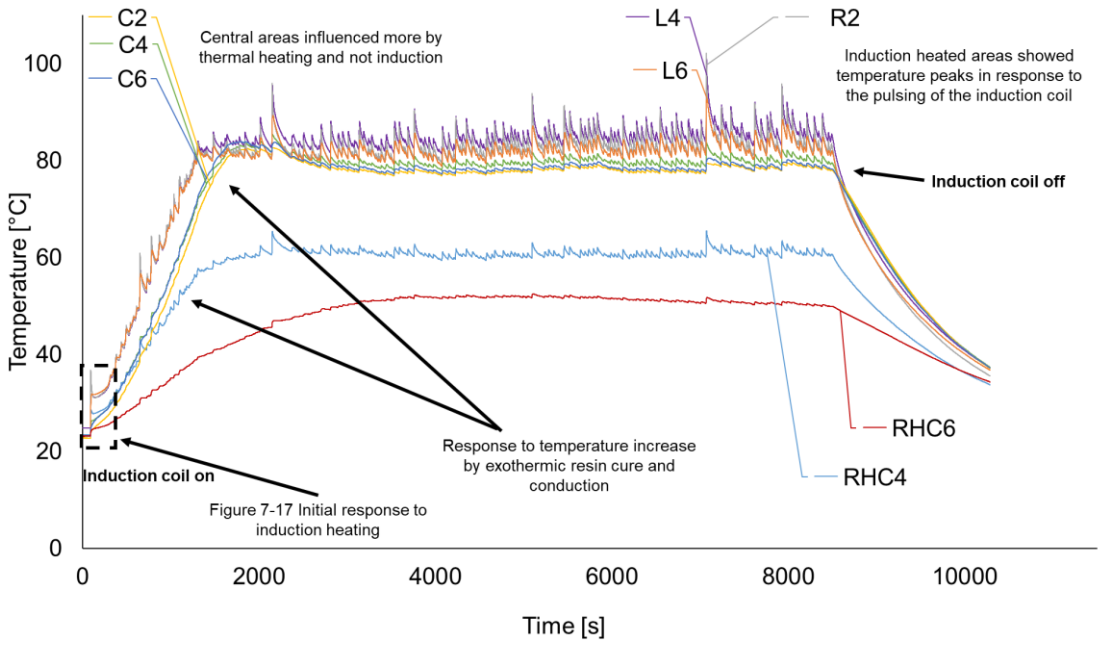

Figure 9-38 Temperature over time profile of cure cycle of resin infused untufted triaxial carbon fibre preform.

A number of key observations are notable from the graphs. The first is that heating intensity was influenced by the emf and coil geometry and greatest within the ring profile as predicted. The spiking in temperature profile was due to the induction heater switching on and off to maintain the target temperature and was most evident in the response from the thermocouples directly influenced by

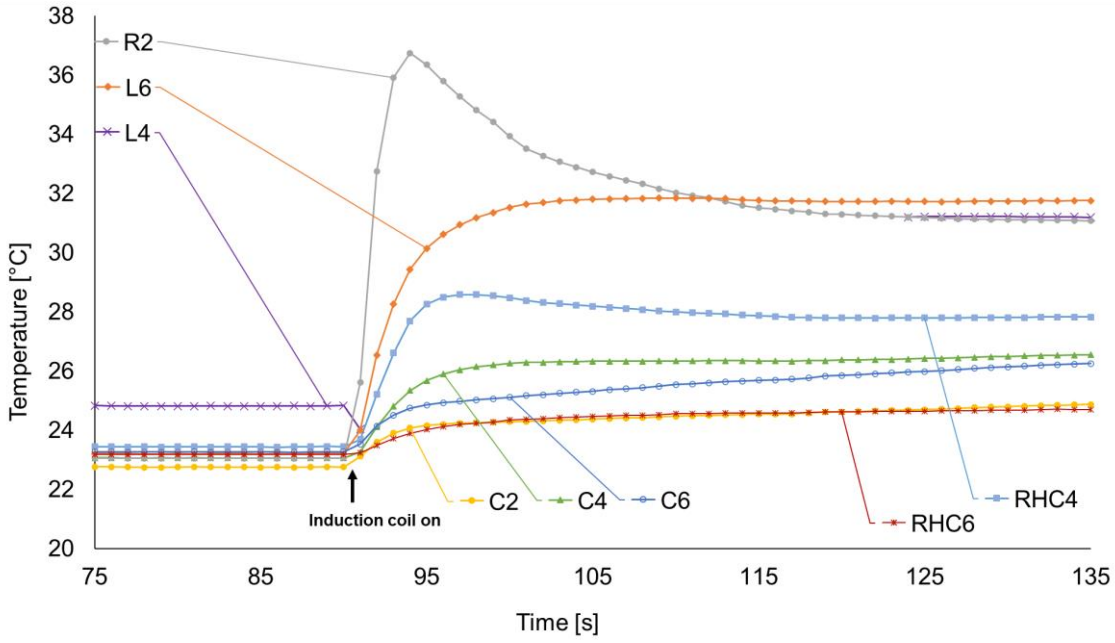

Figure 9-39 Temperature over time profile of first 30 seconds of induction heating of infused untufted triaxial carbon fibre preform.

the emf.

A disadvantage of the closed-loop PID was, when switched back on the induction coil introduced too high a current. This resulted in an instantaneous high intensity heating that overshot the target temperature. Another issue was that, despite the long cure time, conduction from inductively heated portions was insufficient to achieve a homogeneous temperature distribution throughout the composite.

Whilst the central areas (C2, C4 and C6) eventually reached the target temperature, this was predominantly through conduction and the residual heat from the inductively heated areas in the torus. Neither of the two monitored corners reached the target temperature, although their different responses to induction supported the theory that the infused preform was not placed centrally over the coil. The response of RHC4 mimics the spiking of those influenced by the emf (L2, L4 and L6), which suggested that RHC4 was also within the emf but to a lesser degree than L2, L4, and L6 due to the lower temperature reached.

The curing resin also introduces another temperature variable, caused by the exothermic reaction. This increase in temperature had to be regulated to avoid undesirable excess heating or uncontrolled exotherm, and possible composite degradation. A potential advantage of induction was the ability to quickly adjust temperature by simply turning the current off. Whilst there was an opportunity to optimise this temperature increase, the pulse control in this induction system was not accurate enough to avoid exceeding the target temperature.

9.13.3 Induction cure of tufted resin infused triaxial preform

A tufted triaxial preform was prepared using the copper-carbon fibre hybrid thread and tufted with 13 horizonal rows, each with 14 tufts. The preform was prepared with thermocouples positioned in the same manner as described in Section 9.13.2 and bagged, infused, and cured under the same conditions as the untufted specimen. The thermal profile at the onset of induction appeared similar to the untufted specimen with a dominant torus shaped heating profile, though a slight variation of the heating profile was observed in the tufted composite (Figure 9-40). In the tufted profile the heat propagated into the corners, suggesting a potential advantage from the use of tufts.

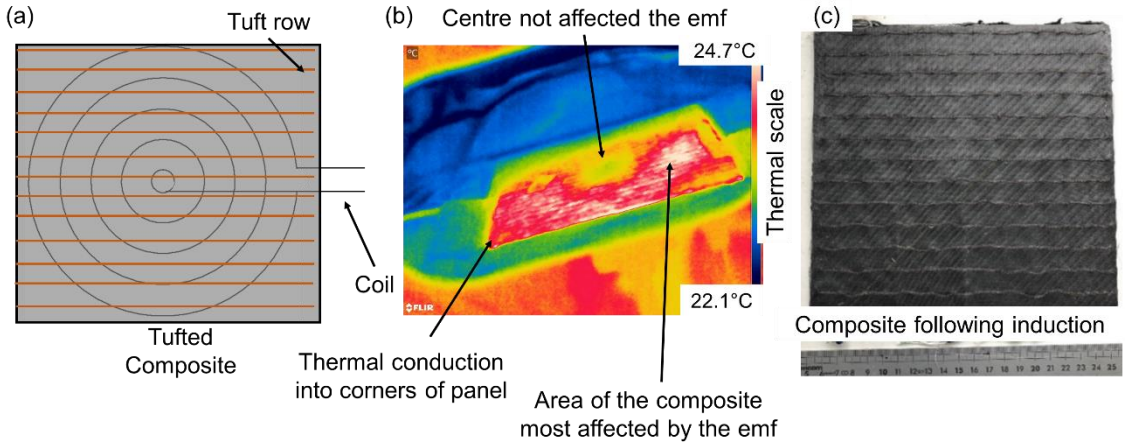

Figure 9-40 Induction cure of tufted triaxial preform, (a) schematic of preform positioned over coil (b) IR image of induction cure of tufted infused triaxial preform and (c) resulting composite.

The TT heating profile (Figure 9-41) showed that monitored areas had one of three distinct responses, similar to the untufted infused preform. R2, L6 and L4 instantly responded to the emf, heated to the target temperature, and pulsed due to the PID accordingly. The centre of the infused preform reached the target temperature through conduction and had little or no response to the emf. The temperature distribution to the corners showed some difference compared to the untufted composite.

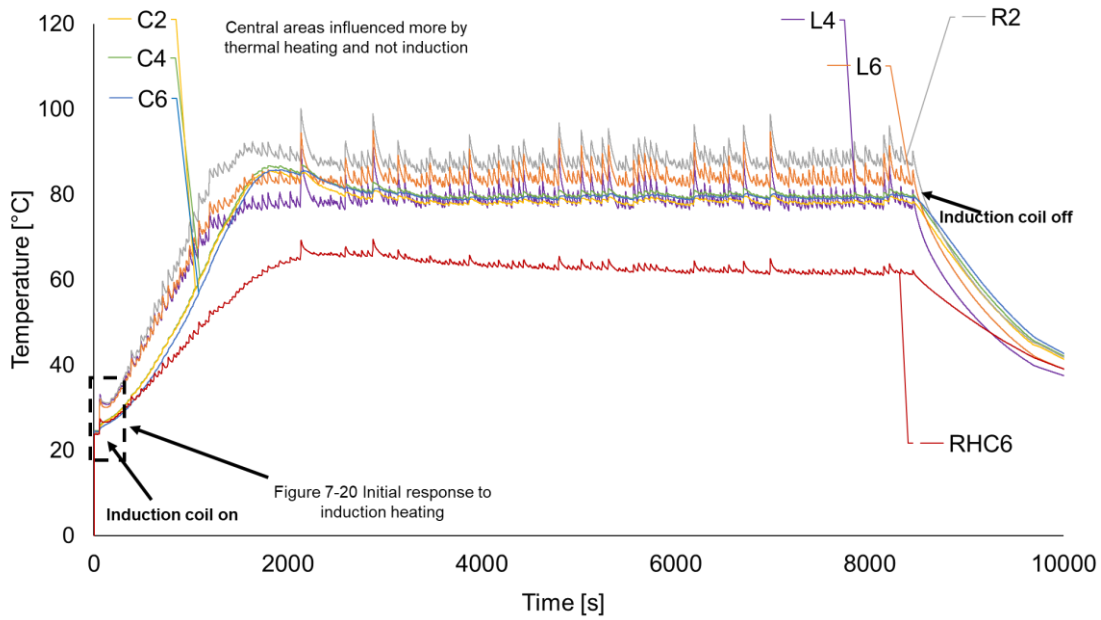

Figure 9-41 Temperature over time profile of cure cycle of resin infused tufted triaxial carbon fibre preform.

Unfortunately, only the RHC6 thermocouple provided a thermal response, due to technical failure of the RHC4 thermocouple. The RHC6 output along with the IR visual assessment, suggested that the heat distribution of the tufted composite extended further than the untufted composite. Although RHC6 never reached the target temperature throughout the cure cycle, it demonstrates that the inclusion of the hybrid thread could be used to manipulate the thermal distribution. The response of RHC6 was different from the onset.

Figure 9-42 shows the initial point of induction heating and that the heating of RHC6 increased from 23.9°C to 27.4°C in 10 seconds. In comparison, the untufted RHC6 went from 23.2 °C to 24.4 °C. RHC6 appeared to be influenced by the emf, indicated by the thermal spiking in response to the induction pulsing. However, unlike the untufted resin infused preform, there was no evidence from the IR image of edge effect. Overall, the presence of the hybrid thread appeared to reduce the thermal range within the infused preform, though, not sufficiently enough to achieve complete thermal homogeneity. The untufted resin infused preform had a range between 50°C and 84°C, whereas the temperatures of the tufted resin infused preform ranged from 64°C to 88°C, representing a reduction of 10°C in the thermal variability. The temperature measurements for each measured area over an hour of the hold time are provided in Table 9-4.

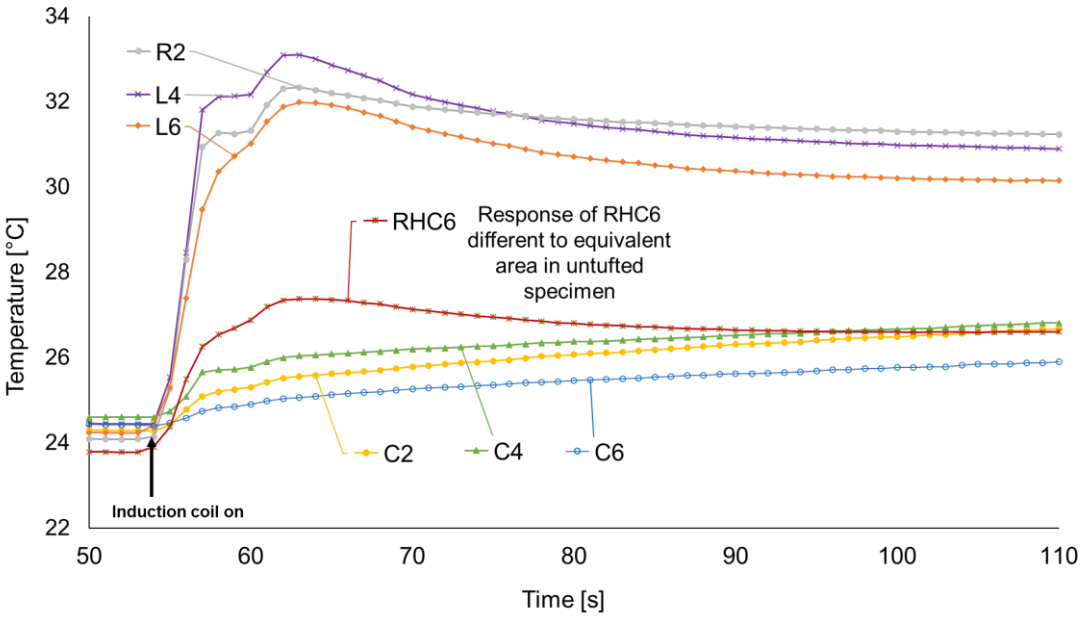

Figure 9-42 Temperature over time profile of first 50 seconds of cure cycle of resin infused tufted triaxial carbon fibre preform.

Table 9-4 Temperature ranges for monitored areas during cure of triaxial composites

	Untufted resin infused preform	**Tufted resin infused preform**
	[°C]	[°C]
L4	83.8 ± 1.3	79.6 ± 2.1
C4	79.7 ± 0.8	80.1 ±0.8
RHC4	61.2 ± 0.5	[-]
C2	78.4 ± 0.9	78.5 ± 0.7
R2	82.0 ±1.4	88.1± 2.0
L6	81.4 ± 1.0	84.4 ± 1.9
C6	78.8 ± 0.9	79.5 ± 0.7
RHC6	49.9 ± 1.2	63.8 ± 1.4

During testing it was difficult to determine whether induction was occurring directly within the hybrid thread or just within the carbon fibre composite during the cure. The thermal profiles were obscured by the bagging materials and the temperature increase caused by the resin. Following cure, the composite was unbagged, allowed to cool, placed upside down to view the external loops on the underside, and inductively heated using the thermal PID set to 40 °C. Figure 9-43 shows the incremental IR images of the panel for one second of induction heating. Using the FLIR software, seven surface areas were monitored to assess the response of the hybrid thread to the emf. The positions chosen were:

- Position 1 – The centre of the composite and not on the hybrid thread.
- Positions 2 and 3 – Within the range of the emf and not on the hybrid thread.
- Positions 4 and 5 – Similar to positions 2 and 3 but placed on tuft loops.
- Position 6 and 7 –Areas on the edge of the composite.

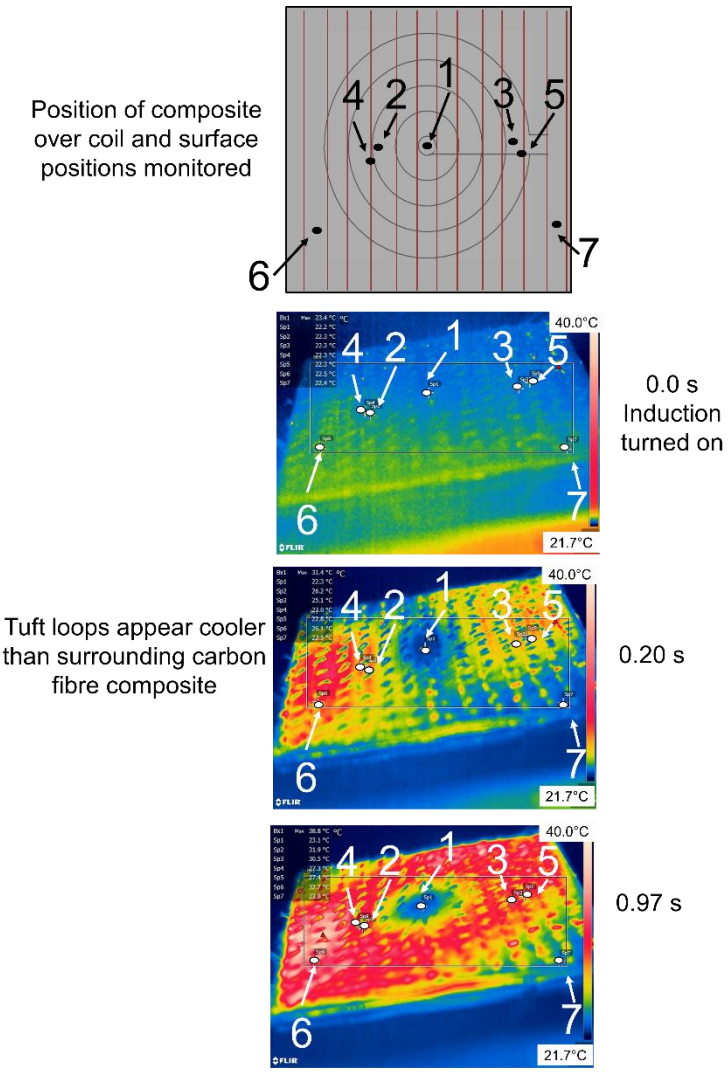

Figure 9-43 Schematic and IR images of underside of tufted composite during induction heating.

Figure 9-44 shows a plot of the monitored areas from the onset of heating. The heating response of the composite, at the onset of induction, suggested that the hybrid thread was not inductively heating. The threads appeared cooler than the surrounding carbon fibre–matrix composite. The response of positions 1, 2 and 3 corresponded to the expected characteristics of the emf. Position 1 was not heated, whilst positions 2 and 3 were rapidly heated. Positions 4 and 5 were in close proximity to positions 2 and 3, and responded with a similar heating profile, but at lower temperatures. Positions 4 and 5 were placed on hybrid thread loops and it was possible that the hybrid thread was heating due to conduction from the residual heat of the surrounding areas. Position 6 and 7 provided two very different profiles. Position 6 was similar to 2 and 3 suggesting that it was positioned within the emf range. While the response of position 7 was similar to position 1, suggesting it was outside of the emf. The thermograph

does indicate that the specimen was not centrally placed over the coil, therefore, position 6 may also have been influenced by the edge effect.

It appeared from this assessment, that the hybrid braid did not inductively heat or that the extent that it had inductively heated was less than the carbon fibre in the preform or composite. However, despite the lack of clarity in the induction response of the thread, inclusion of the hybrid thread as a tuft appeared to have some advantages. It did manipulate the heating profile, and extended heating into the composite corners beyond the limitations of the coil shape. The presence of the thread also seemed to reduce over-heating and reduced the range of temperatures across the composite. The change in heating profile was likely due to the high conductivity of the copper within the thread that enabled the dispersion of excess heat along the tuft rows from well heated to cooler areas.

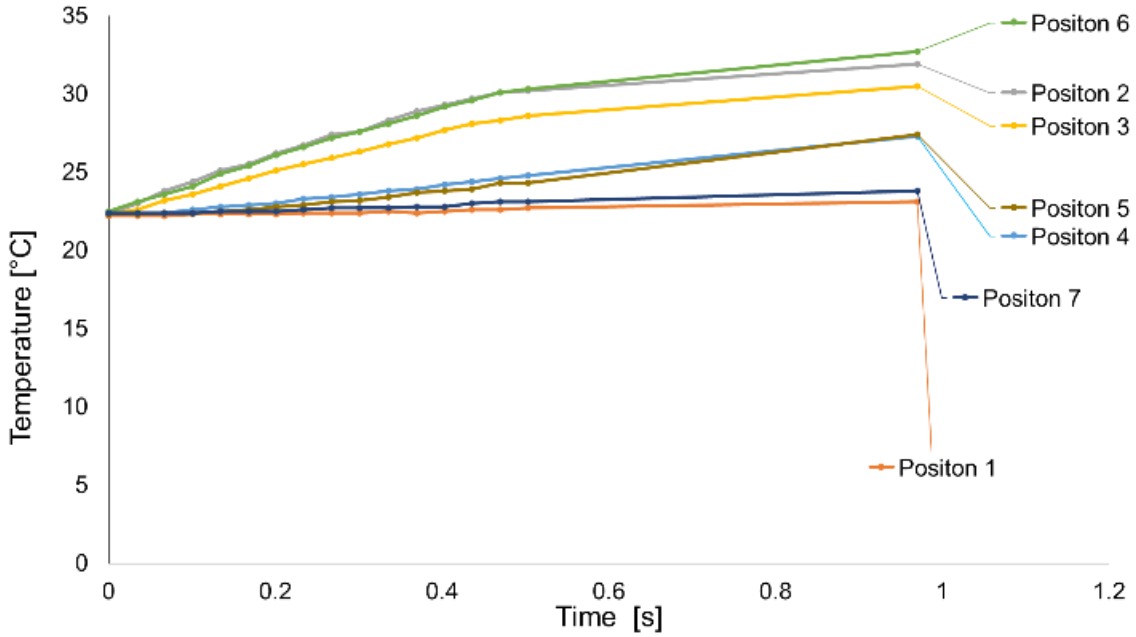

Figure 9-44 Plot of surface temperature vs time of tufted specimen.

9.13.4 Effect of tuft pattern on thermal profile

The effect of altering the tufting pattern was investigated using the triaxial preform as described in Section 9.12.1. Two different patterns were tufted into the panel using the copper–carbon fibre hybrid thread. One half was tufted with 13 horizontal parallel rows, each with 6 tufts spaced 14.7 mm part. The other was tufted with a cross-hatched pattern comprised of 13 horizontal parallel rows of 6 tufts, intersected perpendicularly with 6 rows of 12 tufts. The tufted rows

were positioned to avoid double tufts in one position. The horizontal rows in each section were unconnected to avoid conductive heating along the rows from one side of the panel to the other. This disconnection resulted in loose thread ends in the centre of the preform (Figure 9-45). The resulting areal densities of the parallel and the cross-hatched regions were 0.6% and 1.2% respectively.

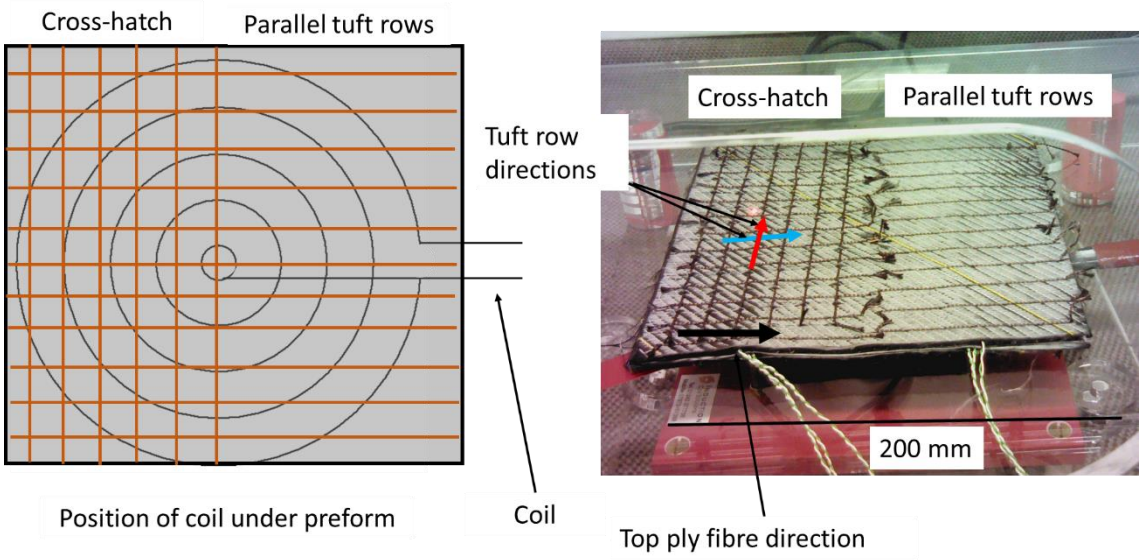

Figure 9-45 Carbon fibre triaxial preform tufted with cross-hatched and parallel patterns. (Left) Schematic of preform positioned over coil and (right) photo.

The tufted preform was heated using the induction heater operating in a closed loop function set to a target temperature of 50°C. The surface thermal profile was monitored using the IR camera with 8 areas of interest (Figure 9-46):

- Position 1 monitored the centre of the preform and as in previous experiments, was expected to be unaffected by the emf due to the coil shape (although the likely effect of the loose thread was unknown).
- Positions 2 and 3 monitored the carbon fibre preform outside the emf field (not on a tuft).
- Positions 4 and 5 monitored the carbon fibre preform inside the emf field (not on a tuft).
- Position 6 monitored cross-hatched overlapping threads and the left of the preform within the emf.
- Positions 7 and 8 were positioned on opposite sides of the preform on horizontal tufts.

The IR images indicated that heating through induction was more evident in the cross-hatched (left side) of the preform where local hot spots at the overlapping threads were observed at the instant the induction coil was turned on (Figure 9-46.

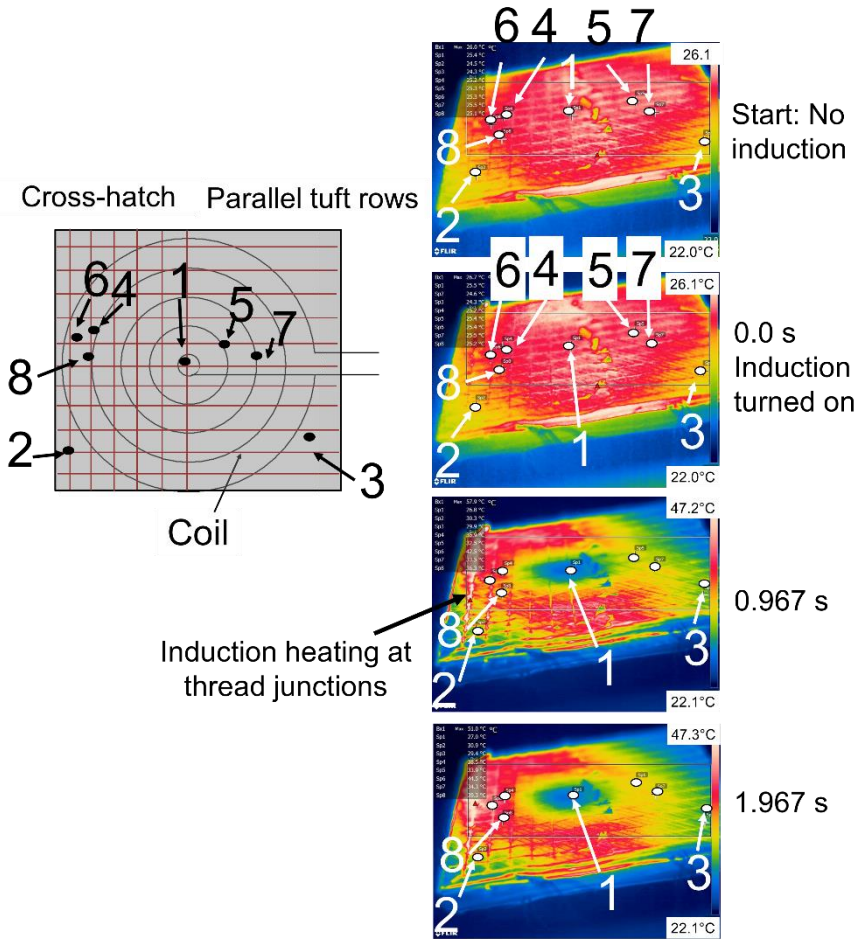

Figure 9-46 IR images of heated dry panel with (left) cross-hatched and (right) horizontal parallel tufting patterns.

Figure 9-47 provides a plot of surface temperatures of the monitored positions. As expected, the central position (position 1) showed no significant change in temperature while the other areas outside of the emf range (positions 2 and 3) gradually heated but did not achieve the target temperature. An area of overlapping threads within the emf (position 6), showed the greatest increase in temperature. The IR images also indicated that induction heating intensity was greatest at these overlapping thread positions, followed by the areas carbon fibre fabric within the emf range. The other tufted areas monitored, (positions 7 and 8), did not show as fast a heating rate, and conduction was possibly responsible for the majority of heating observed. Overall, whilst the effect of the

coil geometry emf remained dominant, the temperatures were highest and more uniform within the cross-hatched tufted area rather than to the horizontally tufted area.

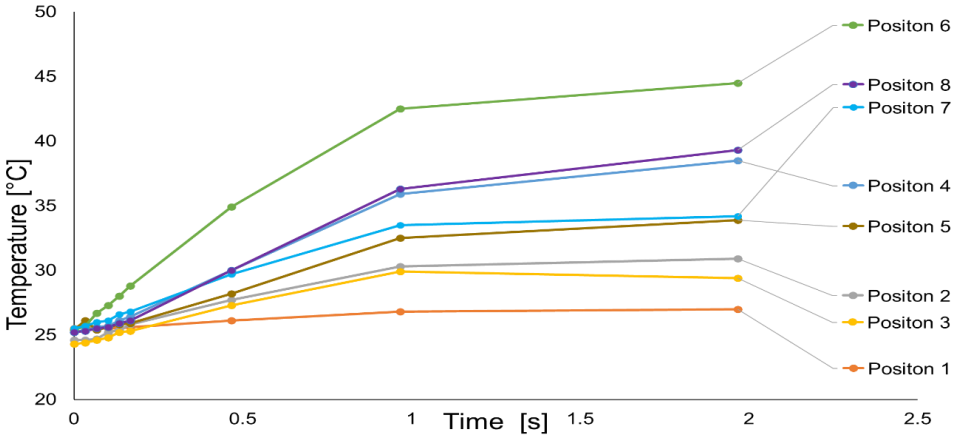

Figure 9-47 Plot of surface temperature vs time on a cross hatched and horizontally tufted preform.

To observe the effect of the liquid resin on the performance of the two different tufting patterns, this tufted preform was infused using Prime™27 resin under vacuum using the double bagging system. To enable a clearer IR assessment the breather in the outer bag of the bagging system was not placed towards the end of the panel (Figure 9-48). This enabled the IR camera to record the resin front as it moved through the prefrom. The images show that the resin temperature exceeded that of the inductivly heated threads (due to exothermic reaction). It was therefore not clear the extent to which the resin affected the induction of the hybrid threads.

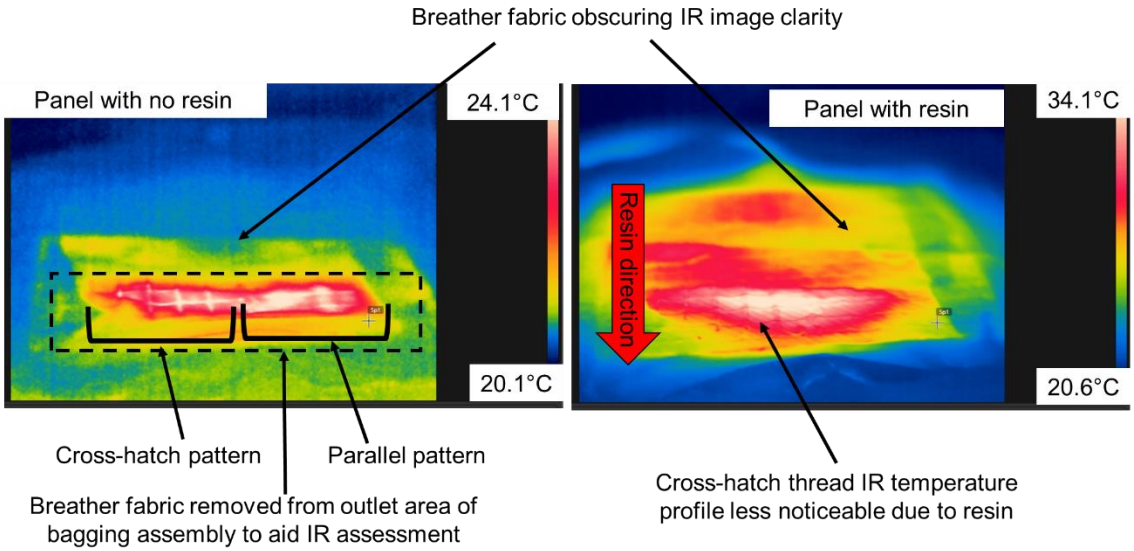

Figure 9-48 IR images of resin infusion of carbon fibre preform tufted with cross-hatched and horizontal parallel rows.

9.13.5 Induction heating of UD fabric

Figure 9-49 shows a schematic of monitored surface temperatures and the thermal response of a single ply of UD non-crimped fabric. A plot of temperature over time is provided in Figure 9-50. A constant current of 100 amps was set and held for 30 seconds. Nine surface spot temperatures were monitored using the IR camera, which indicated only a limited thermal response with temperatures ranging from 17°C to 18°C. This limited response to the induction heater was consistent with previous studies of UD fabrics [276].

Progressing from a single UD ply; the effect of ply lay-up was also examined by stacking a second UD carbon fibre ply perpendicular to the first, creating a two-ply stack of [0/90] carbon fibre plies. The current was again set to 100 amps but was turned off after approximately 3 seconds due to the rapid heating observed. Figure 9-51 shows the IR images from this test. In contrast to the single ply, the [0/90] lay-up reached temperatures up to 152°C in under 3 seconds. A plot is provided in Figure 9-52. Testing had to be stopped as the polymer stitching in the non-crimped fabric (NCF) started to melt and burn. These simple tests demonstrated the significant role ply orientation in creating conductive loops to facilitate induction heating within a panel.

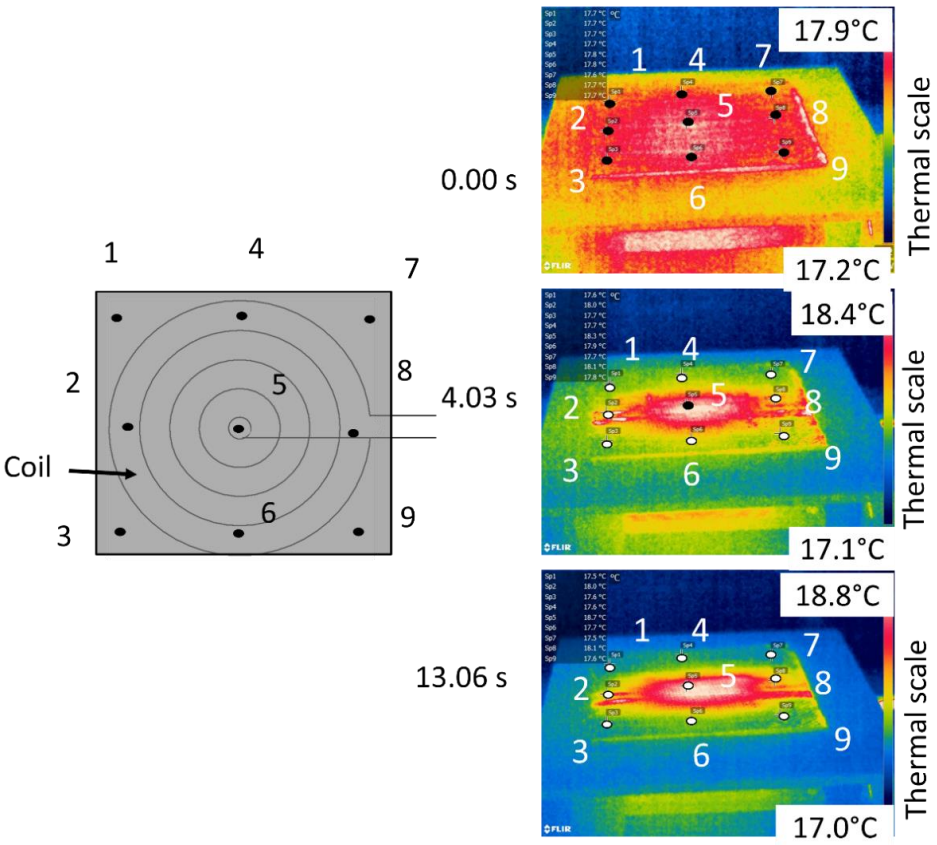

Figure 9-49 Response of a single ply of UD NCF fabric to induction heating.

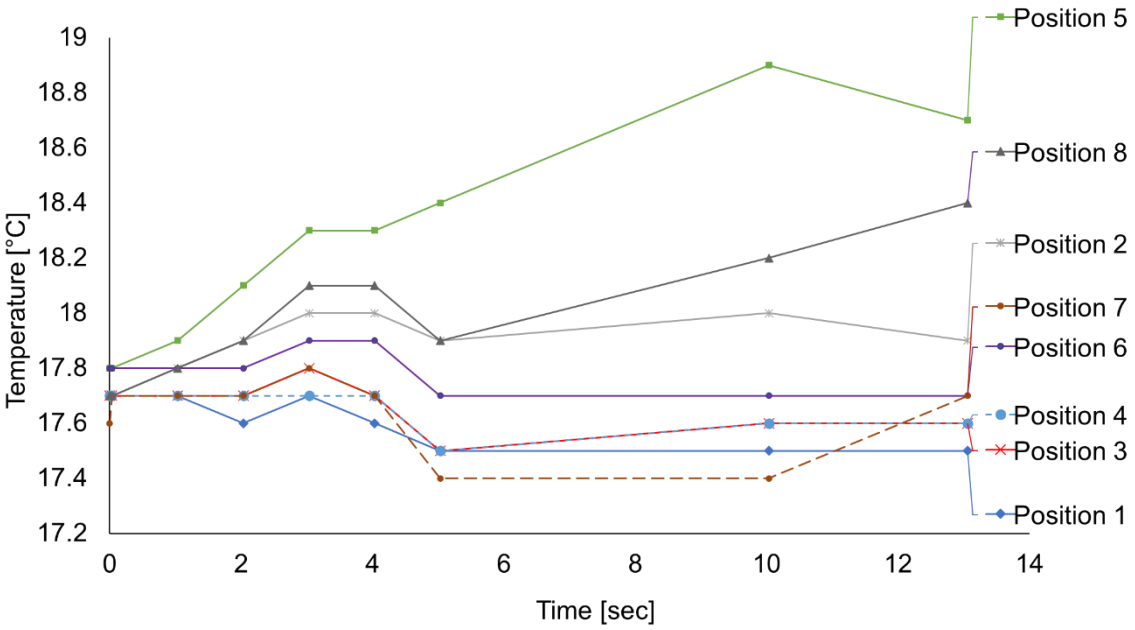

Figure 9-50 Plot of surface temperature vs time of a single UD ply.

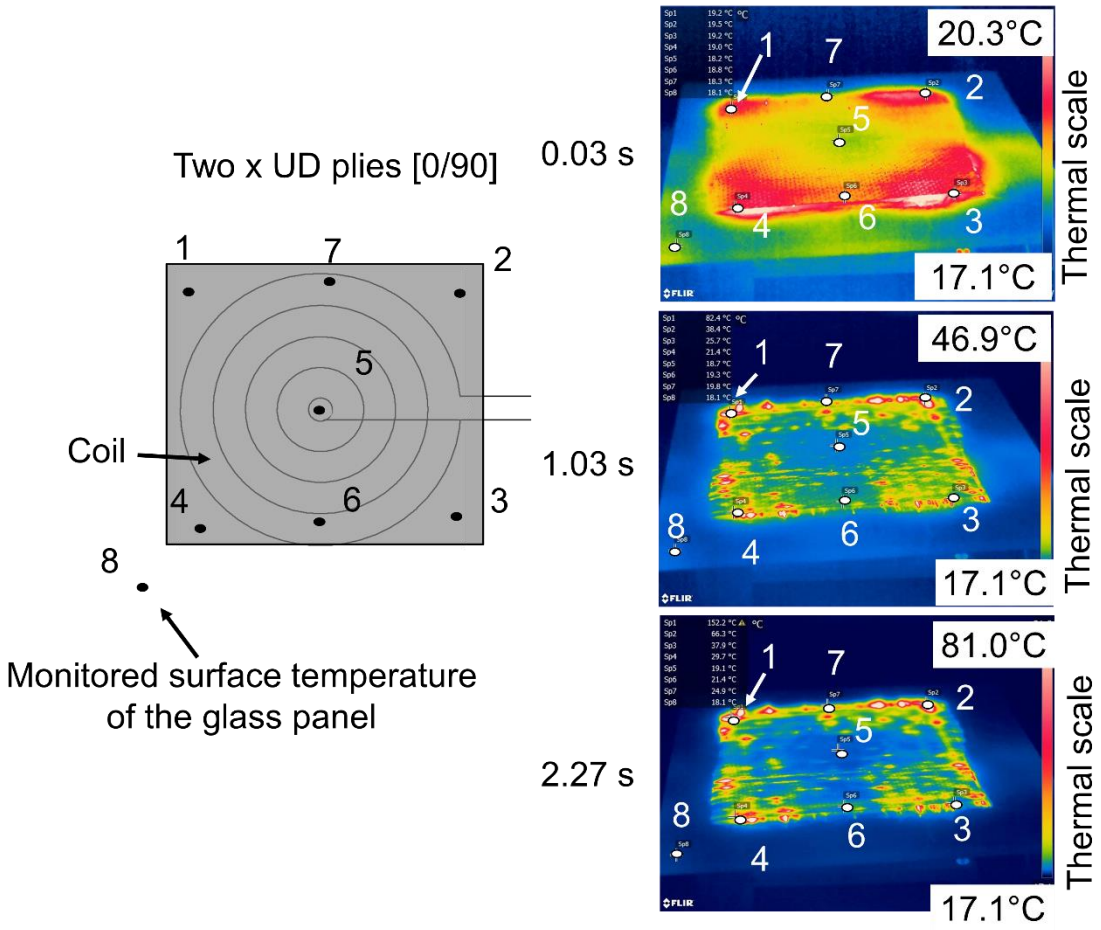

Figure 9-51 Induction response of 2 UD plies with a [0/90] lay-up.

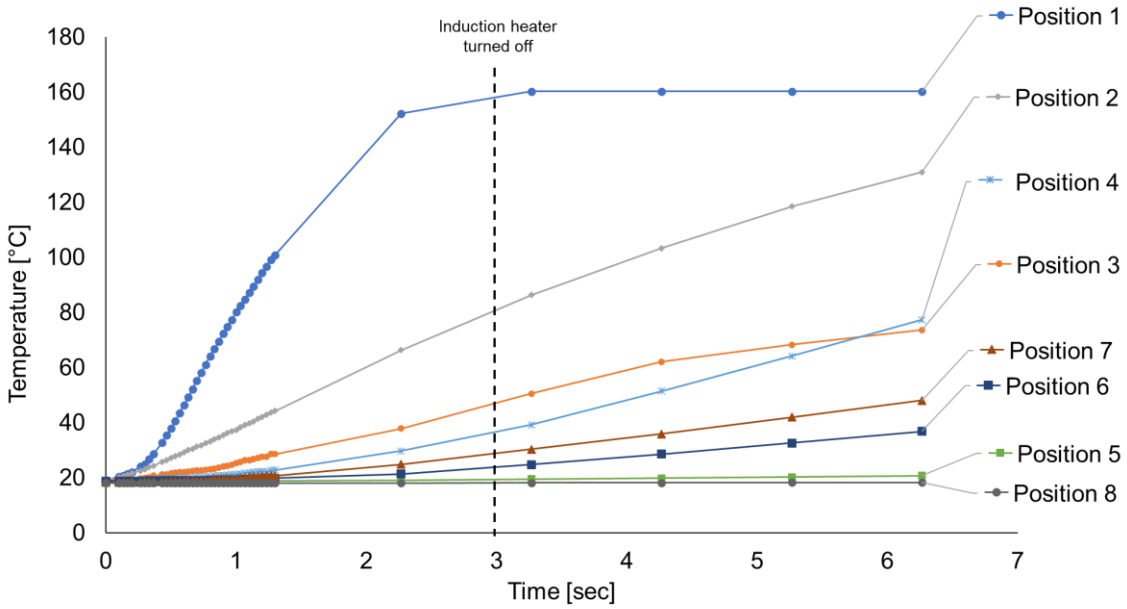

Figure 9-52 Plot of surface temperature vs time of 2UD plies with a [0/90] layup a single UD ply.

9.13.6 UD preform and cured composite

A UD preform comprised of 24 plies, tufted with the hybrid thread was examined within the emf (Figure 9-53). Half of the preform was untufted and the other half tufted with 7 parallel rows of 12 tufts laid perpendicular to the UD fabric. The rows were 10 mm apart and each tuft also 10 mm apart. The responses of the hybrid thread in the UD preform and composite was distinctly different to that of the triaxial preform and composite, with the hybrid thread heating in the UD specimens. However, heating only occurred in 3 of the 7 tuft rows. These were row 1 in the centre of the preform, and rows 3 and 4 as indicated in the IR image (Figure 9-53(c)). The tuft alignment relative to the to the emf was potentially the cause for the lack of response. However, further investigation showed that the heating of rows 1,3 and 4 was consistent, and they heated irrespective of the specimen orientation over the coil.

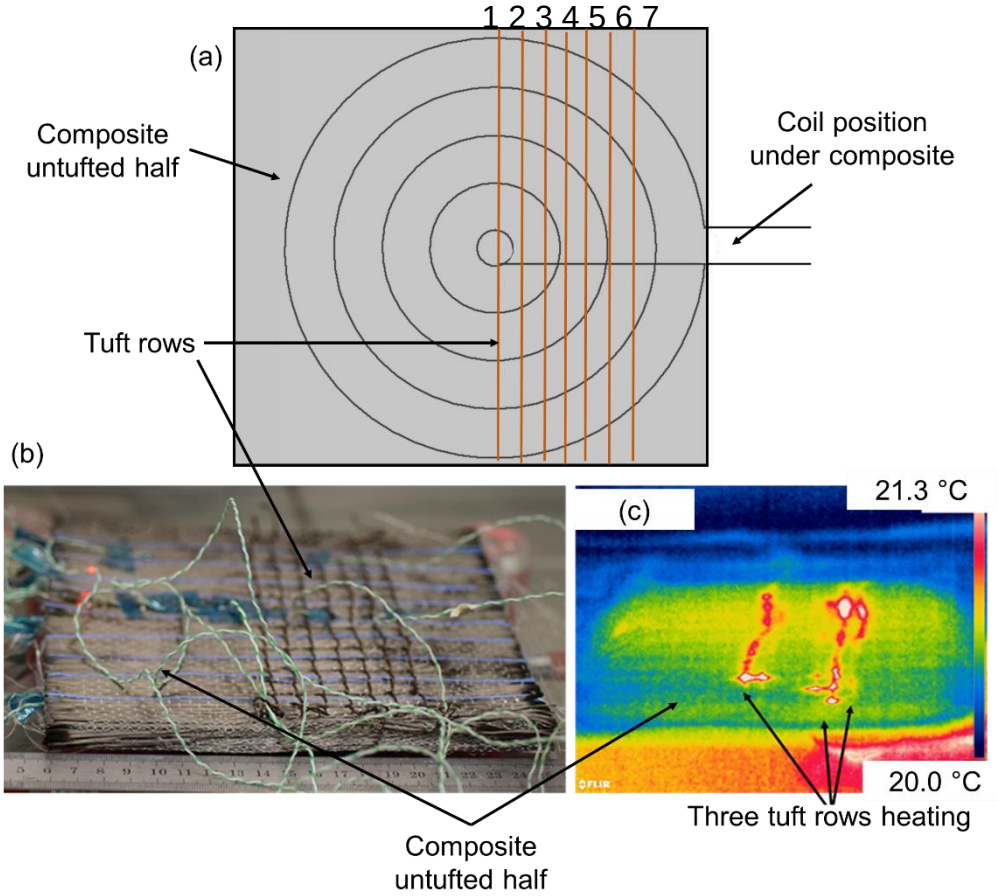

Figure 9-53 UD preform comprising 24 plies with the left-hand side untufted and the right side tufted with 7 horizontal rows 10 mm apart. (a) Schematic, (b) photograph of preform and (c) IR image of preform response to emf.

Another possible explanation, for the lack of response of the remaining rows, was that interference between the tuft rows occurred resulting in short circuiting of the currents preventing heating. The introduction of the resin during infusion did not alter the induction heating response and the cured panel also possessed the same heating profile.

To determine if interference between rows was occurring, an assessment of an identically manufactured cured UD carbon fibre composite with 7 rows of copper–carbon fibre tufts but 15 mm apart was examined within the emf (Figure 9-54). In this composite, rows 1, 4, 5, 6 and 7 were heated. Rows 2 and 3 did not heat by induction but after several minutes they too heated, most likely due to conduction. The change from 10 mm to 15 mm spaced rows indicated that the emf shape was affecting the induction of the rows. Varying the position of tufts suggested that localised induction heating occurred on the tuft rows and subsequently the remaining length of the hybrid thread heated through conduction. The absence of a central cool area, as experienced in the triaxial preforms, could be due to conduction along the tuft rows or because the UD preform enabled more uniform induction within the fabric compared with the overlapping triaxial junctions. Another noteworthy observation was the high intensity heating of the poorly infused area at the untufted end of the composite. This comparatively intense heating of a poorly infused area could be utilised as a quality control method during processing to signal variability in infusion quality.

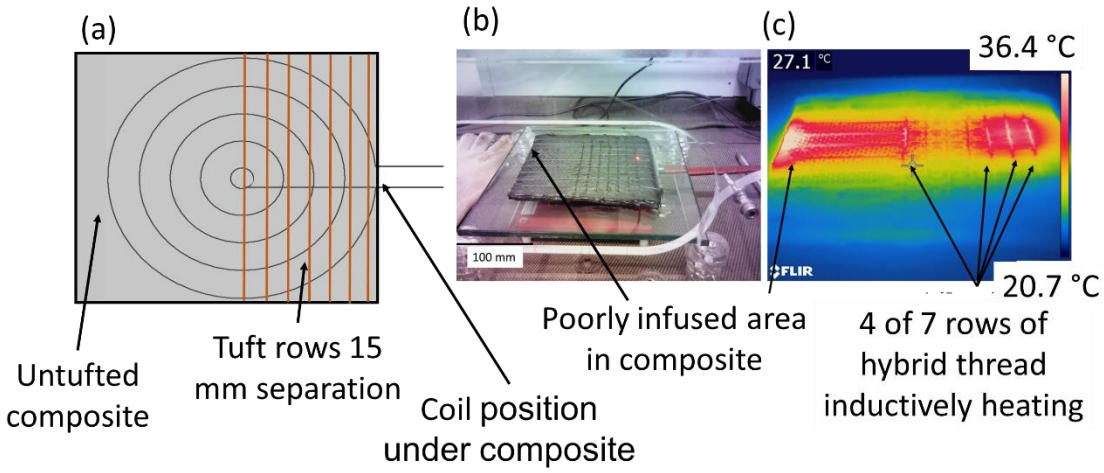

Figure 9-54 UD cured composite comprising 24 plies with the left-hand side untufted and the right side tufted with 7 rows 15 mm apart (a) Schematic (b) photograph of composite and (c) IR image of composite response to emf.

9.13.7 Effect of tuft areal density on the induction heating of cured UD carbon fibre composite tufted with hybrid thread

A UD preform comprised of 24 plies was tufted with two different areal densities using the hybrid thread. One half was tufted with seven rows of tufts spaced 14.7 mm apart in rows 14.7 mm apart. The other half with tufts 25 mm apart and rows 14.7 mm apart (Figure 9-55).

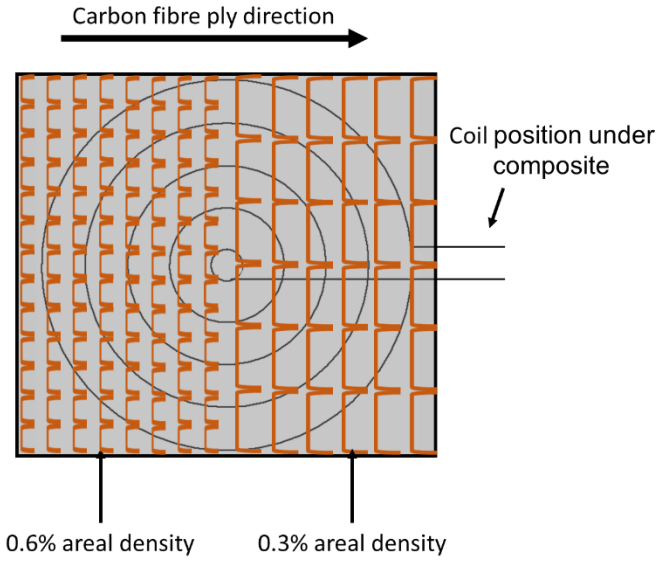

Figure 9-55 Schematic of tufted composite: areal densities 0.6% and 0.3%.

This created a tufting profile with areal densities of 0.6% and 0.3%. The lower areal density side possessed a longer length of hybrid thread between the inserted tuft points. This thread length was less taut than on the more densely tufted side. Figure 9-56 details the examination of varying tuft areal densities on a composites surface temperature profile. Nine areas or spot temperatures were monitored using the IR camera.

- Position 1 - The centre of the carbon fibre composite, not on a tuft and central relative to the coil. Based on previous experimental results, position 1 was likely to be the least affected by the emf of the induction coil.
- Position 2 and 3 - Positioned on tufts at the edge of the composite.
- Positions 4 and 5 - Positioned near the centre but within the vicinity of the tufted rows but not directly on a tuft row.
- Positions 6 and 7 - Positioned within the highest emf influenced area and on tufted rows.

- Positions 8 and 9 - Positioned in the highest emf influenced area not on tufts.

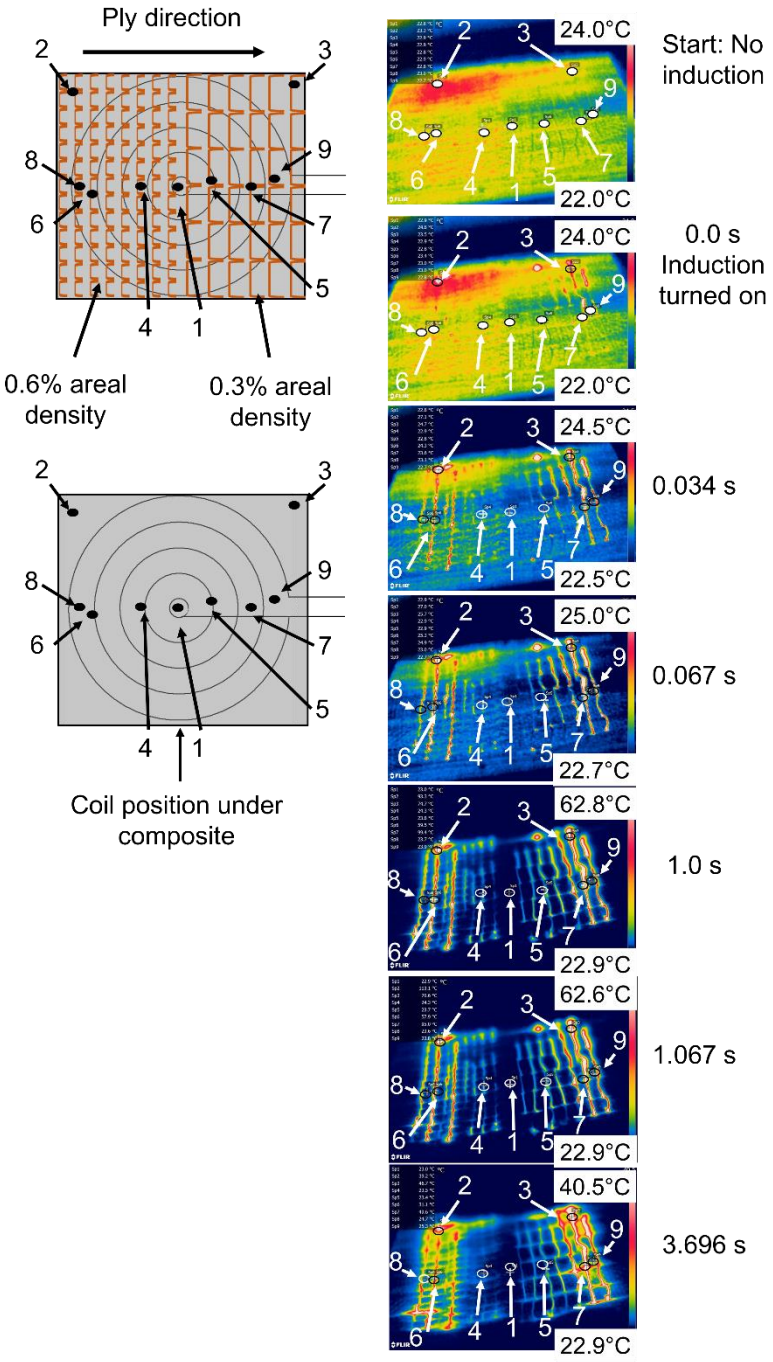

Figure 9-56 Effect of areal density on induction heating. (a) Schematic of monitored areas and (b) induction heating response of unidirectional carbon fibre infused panel.

This examination demonstrated the influence of coil geometry on the heating profile of a composite irrespective of the tuft densities. As expected, position 1 was unaffected by the emf, and no significant heating of the area was observed. Within the two tufted regions some variation of the surface thermal profile was observed but overall, the coil emf dominating factor of the heating profile.

Despite the limited effect of either of the two tufted regions in manipulating the coil emf, there were other notable observations (Figure 9-57). First, the influence of edge effect was evident around positions 2 and 3, this increased heat intensity in these regions. Highest temperatures (shown in white on the IR images) were observed within and along the side of the composite due to the edge effect. Positions 4 and 5 showed minimal increases in temperatures, with maximums of only 24.3°C and 23.7°C respectively.

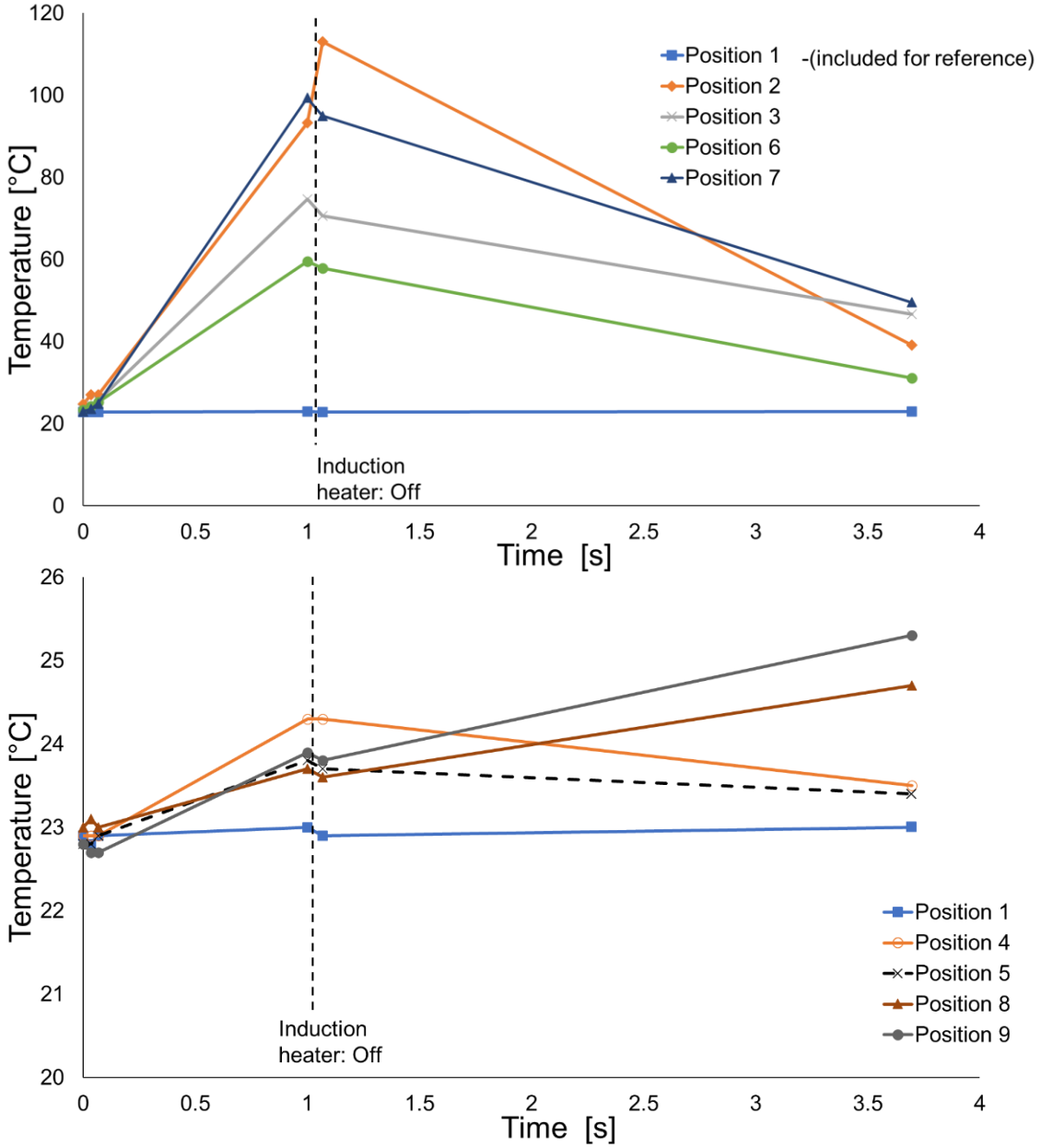

Figure 9-57 Plots of monitored surface temperatures over time. (Top) Positions on tufts and (bottom) off tuft positions.

Overall, no sizable difference in the temperature profile between the two tufted regions was observed, although, it was noted that position 4 responded slightly

quicker than position 5. This might have been a result of thread deviation near position 5 indicating that heating and heat dispersion was influenced by the condition of the tufts. Less tension in the hybrid thread was evident on the more sparsely tufted rows on the right hand-side of the preform. On the surface, the linking thread was less secure compared to the more densely tufted side. This resulted in the linking surface thread displaying increased waviness and vertically lifted from the preform. The lack of tension also caused reduced compaction on that side of the preform and was noticeably less robust compared to the more densely tufted side. The heating profile reflected the tuft waviness on the less densely tufted side and resulted in a less predictable surface thermal profile.

In comparison, the more densely tufted region showed greater uniformity. The maximum temperatures achieved by the tufted positions 6 and 7 were 59.5°C and 99.4°C respectively. Both areas quickly heated in response to the induction heater and decreased in temperature once the induction coil was turned off. In contrast, positions 8 and 9, which were both near but not on a tuft, slowly increased in temperature when the induction coil was turned on and continued to heat despite the induction coil being turned off. This suggested that the areas around the inductively heated tufts heated through conduction due to residual heat.

It was observed that the more densely and uniform tufted half of this specimen typically had lower maximum temperatures, with the exception of position 2, which was more influenced by edge effect than other monitored positions. It was possible that due to the greater amount of conductive copper within this half, the heat was dispersed more evenly by conduction along the copper in comparison to the less densely tufted half. This was indicated by the presences of less heat spots (white regions) on the IR images on the left-hand side of the composite compared to the right.

9.13.8 Influence of lay-up on induction heating in tufted composite

This experiment investigated the effect of the induction heating response of the hybrid thread when tufted into the triaxial and UD specimens. In the triaxial preform and composite, the hybrid thread appeared not to inductively heat or heated to a lesser extent than the surrounding carbon fibre fabric (Section

9.13.3). In contrast, within the UD preform and composite, the hybrid thread inductively heated, although inconsistently, with some rows heating and others failing to do so (Section 9.13.5). The variability of the response of the hybrid thread was investigated by manufacturing a specimen mimicking the layup of the triaxial preform using UD plies. This simulated triaxial preform was then tufted using the hybrid thread. Half of the preform was tufted with rows parallel to the top ply tow orientation while the other was tufted perpendicular to the ply fabric direction (Figure 9-58). A preform comprising triaxial fabric was also tufted with an identical tufting arrangement. Each region of both preforms contained identical tuft areal density of 0.6%.

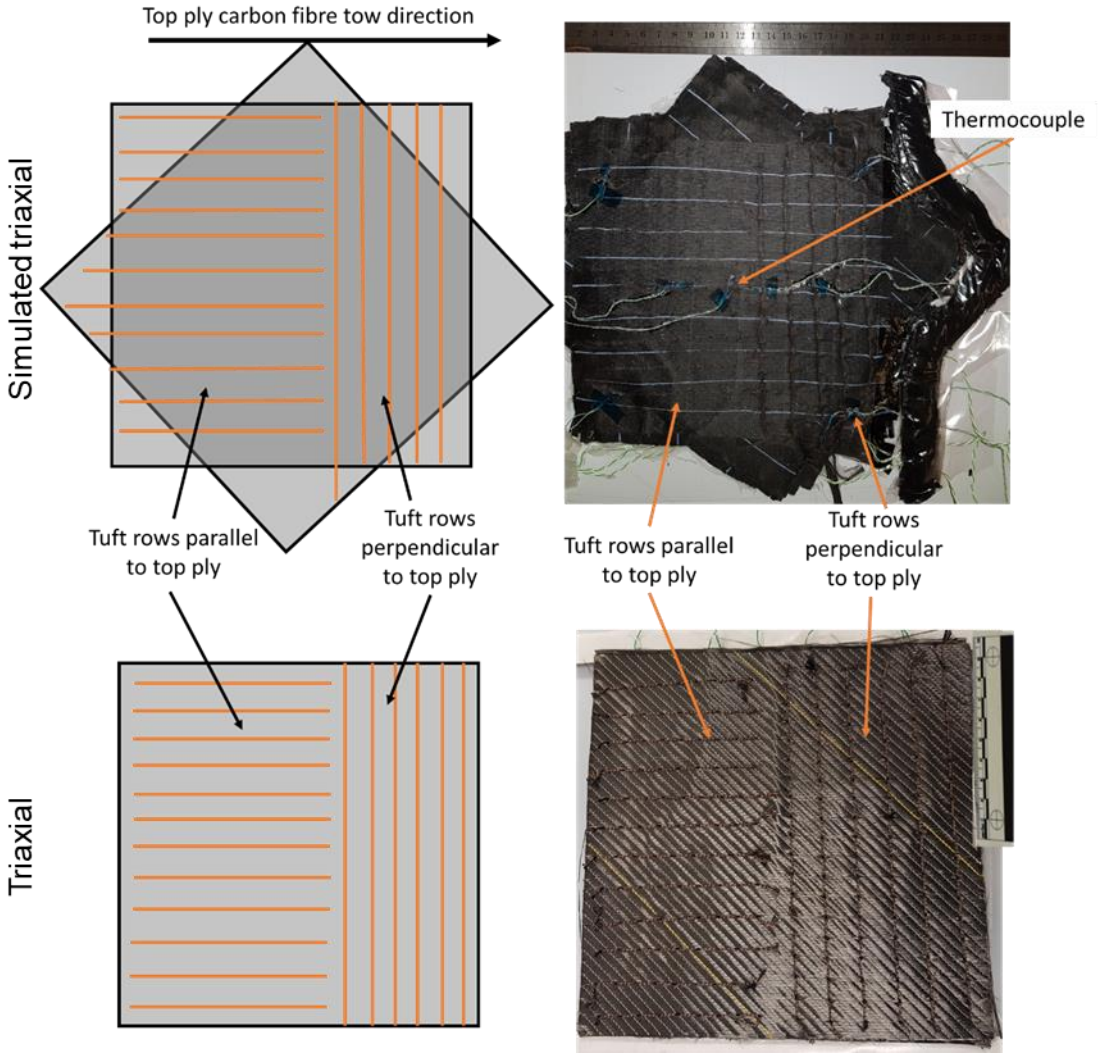

Figure 9-58 Schematics and pictures of specimens tufted with parallel and perpendicular tuft patterns. (Top) Simulated triaxial specimen and (bottom) triaxial specimen.

An investigation of tuft orientation relative to ply fibre direction was also undertaken. This was to determine if the alignment of interconnecting lengths of thread between each tuft influenced heating potential. In theory, tufts inserted

perpendicularly to the top ply should create closed loops between the carbon fibre and the hybrid braid similar to that in woven fibres. Previously, it has been shown that in woven fabric, closed loops are created by the crimped fibres and heating occurred between layers [276, 281, 293]. In contrast, those tufted in parallel should heat to a lesser extent.

The dry preforms, the resin infused uncured preform and the inductively cured composite were examined using the IR camera, with thermocouples placed throughout the surface and through-the-thickness. The TT thermal data from the thermocouples did not provide insight into the thermal response of the thread but confirmed the dominant effect of the emf shape observed in previous studies in this chapter. The IR images, however, indicated contrasting responses between the panels irrespective of whether they were dry, infused or cured. In each specimen, the parallel rows heated along the length (Figure 9-59). These parallel regions also appeared to be relatively uniform in temperature. In comparison, the perpendicularly tufted rows differed in their response. In the simulated triaxial specimen the temperatures were similar to that of the parallel side, although, each tuft insertion point was distinctly warmer than the surrounding untufted regions. In the triaxial specimen, maximum temperatures were achieved along the perpendicularly tufted rows and were distinctly different from the parallel tufted side.

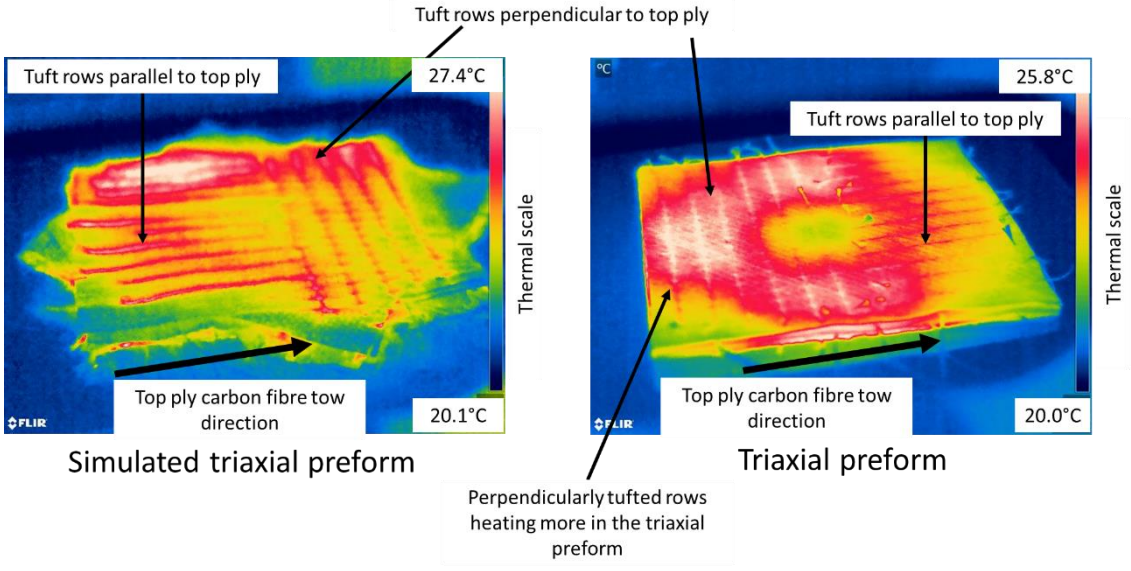

Figure 9-59 IR images of cross-hatched and parallel tufted hybrid thread. (left) Simulated triaxial preform after induction activation and (right) triaxial preform.

For both panels, the thermographs indicated that the hybrid thread tufted perpendicularly inductively heated rapidly on turning on the induction heater. Whereas the hybrid thread tufted in parallel, heated more slowly. This suggested that on the parallel side, the hybrid threads were likely to be heated through conduction, possibly from heat generated within the specimen. Some edge effect was also evident in the simulated triaxial specimen due to its star shaped constitution. To ensure that this was not affecting the thermal profile, the panel was rotated and retested. However, no alteration in thermal profiles of the tufted rows was observed.

9.13.9 Response of the hybrid tufted braid in a nonconductive glass panel

The previous experiments established that the inclusion of the hybrid braid influenced the induction profile of a composite specimen, although, it appeared that the orientation of the ply layups and the hybrid thread tuft direction played a greater part in enabling induction than the presence of the hybrid braid itself. From these experiments it was not possible to fully determine the extent to which the braid was inductively heating. This was because the induction of the hybrid thread was often obscured by induction of carbon fibre plies, the exothermic reaction of the resin cure and any subsequent conduction from residual heat. Due to the slow heating response, it was hypothesised that the parallel tufts were predominantly heated by conduction. To investigate this, a non-conductive fibre glass composite comprising 24 plies of East Coast Fibreglass triaxial cloth was used to determine the inductive response of the hybrid braid within a non-conductive specimen (Figure 9-60). The specimen was tufted with parallel and cross-hatched patterns as previously described in Section 9.13.4. The tuft areal density was 0.6% and 1.2% for the parallel and perpendicular areas respectively.

Figure 9-61 shows the thermal response of the composite to the induction heater set at 50 amps for 30 seconds. From the onset the cross-hatched tufted hybrid thread inductively heated with the intersections of the tufting hybrid thread heating the quickest. Nine surface spot temperatures were monitored during the induction as shown in Figure 9-61.

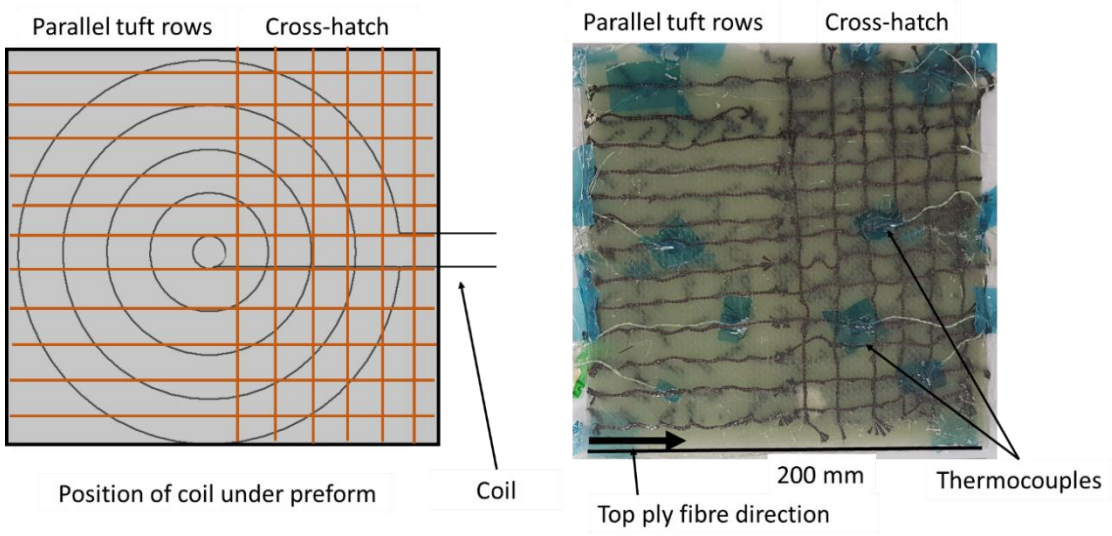

Figure 9-60 Fibreglass triaxial preform tufted with cross-hatched and parallel patterns. (left) schematic of preform positioned over coil and (right) photo.

Each spot point monitored the following areas.

- Position 1 - Outside the emf range and not on the hybrid thread.
- Positions 2 and 4 – Within the range of the emf and on the hybrid thread.
- Position 3 – Not on the hybrid braid and inside the emf range.
- Position 5 - Two intersecting tuft rows inside the emf.
- Position 6 - Two intersecting tuft rows outside the emf.
- Position 7- The central line along the perpendicular tuft row.
- Positions 8 and 9 –Near but not on the hybrid thread.

This experiment demonstrated the lack of heating of the parallel tufted thread within a nonconductive fibreglass specimen (Figure 9-62). This lack of response indicated that closed loops were not created by the hybrid braid in this configuration. Conversely, the cross-hatched side showed instantaneous heating with temperatures reaching over 90°C in some localised areas. This demonstrated that closed loops were created by overlapping surface threads intersecting, in this instance, at right angles.

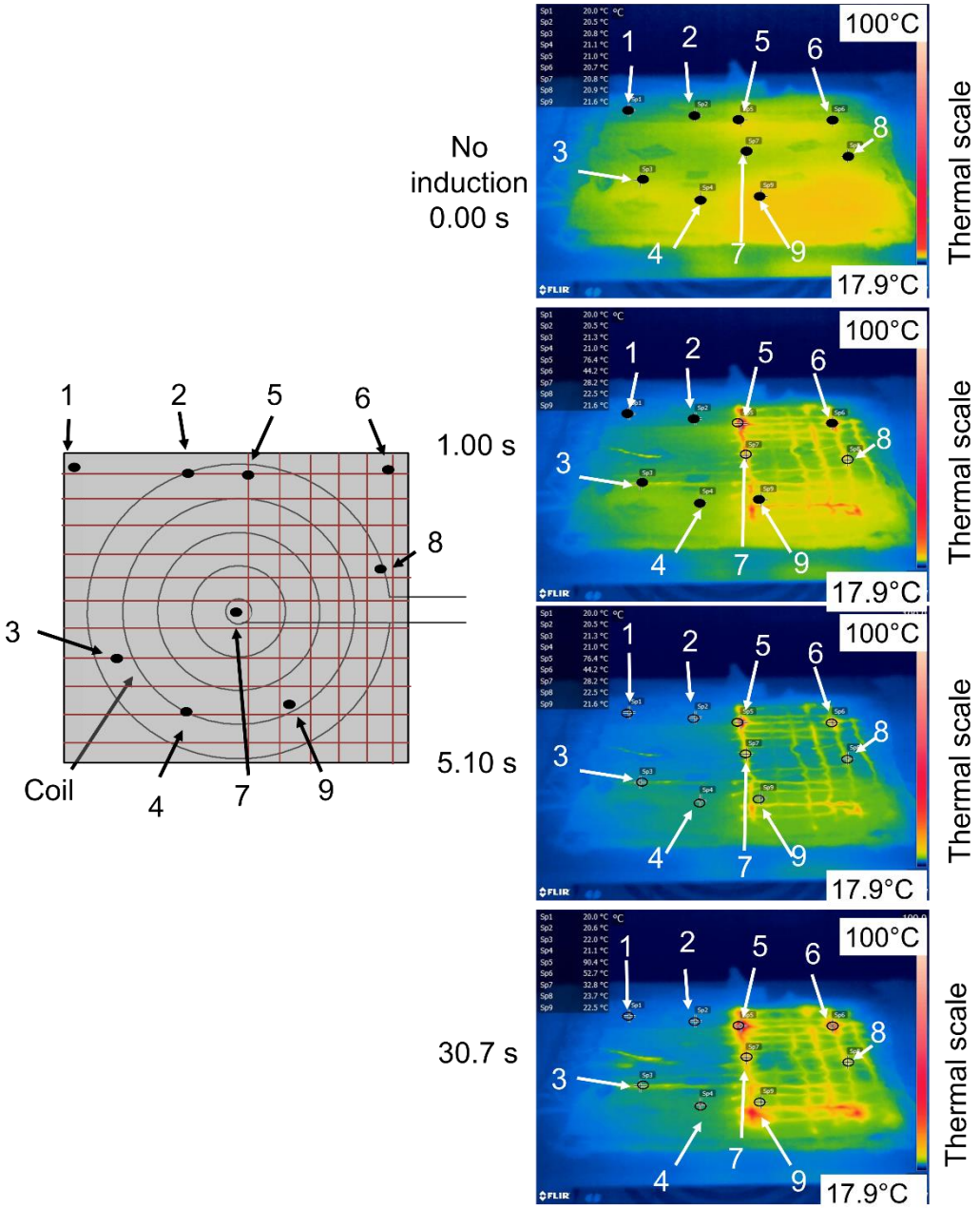

Figure 9-61 Response of the hybrid thread tufted into non-conductive fibreglass specimen. Schematic and thermograph images of monitored surface areas.

However, there was a considerable temperature gradient across the surface profile (Figure 9-62). Positions 5 and 6 monitored areas of overlapping tufting threads. The associated heating profiles of the areas are similar with an initial rapid increase from the onset of induction. The maximum temperatures were approximately 90°C and 50 °C for position 5 and 6 respectively. This variability was due to the extent that each was influenced by the emf. position 6 was less influenced and subsequently did not reach the temperature of position 5.

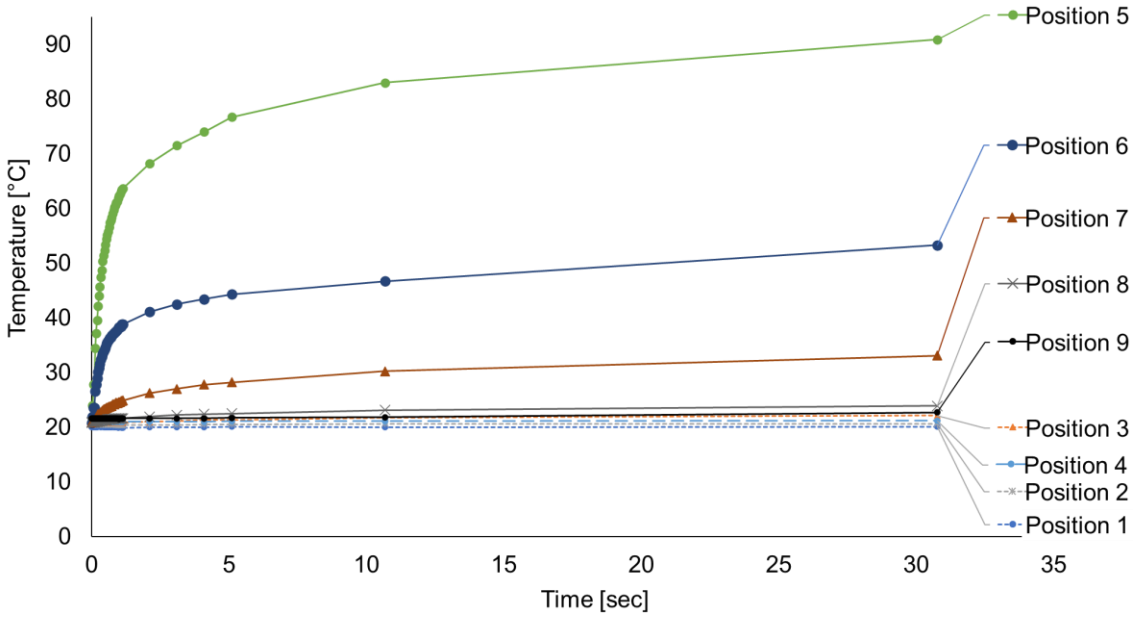

Figure 9-62 Plot of surface temperature over time. Response of the hybrid thread tufted in non-conductive fibreglass specimen. Positions 1 to 4 monitored parallel tufted pattern and positions 5 to 9 monitored the cross-hatched tufted pattern.

Positions 8 and 9 did not heat, despite the proximity to much warmer areas. The non-conductive properties of fibreglass prevented heat dispersal leading to contrasting thermal profiles. These areas had thermal profiles similar to the parallel tufted side of the composite and remained under 25°C. Position 7, on a hybrid thread but between tufts, displayed a more gradual heating profile than positions 5 and 6 and did not exceed 30°C. This gradual heating suggests that it heated conductivity by residual heat generated at thread intersection points.

9.13.10 Material effects: hybrid braid composition comparison

To determine the effect of different braid materials on induction, a split unidirectional panel with one side tufted with nickel-chrome hybrid thread and the other with copper hybrid braided thread was manufactured in both triaxial and UD specimens. Identical tufting patterns were used, resulting in an areal density of 0.6%. Assessments were undertaken in both dry preforms and infused and cured composites. The induction heater was manually operated with increasing current input.

Figure 9-63 shows the thermal response of the dry preform. Nickel-chrome braid heated at a greater rate and to a higher temperature. This difference in heating between the copper–carbon fibre thread and the nickel-chrome-carbon fibre thread was consistent in both the triaxial, and UD preforms as well as in

the composites. The difference could be attributed to the profiles of each thread. The construction of each braid was identical, as described in Chapter 3, however, filamentation of the carbon fibre was more evident in the nickel-chrome-carbon fibre braid. This braid was also less flexible. This was evident in the tufting stages of manufacture as the thread passed through the needle eye and began retracting back. Also, the nickel-chrome braid did not contract or expand as much as the copper–carbon fibre braid. The greater heating within the nickel – chrome carbon fibre could also be caused by an increase in Joule heating generated by the greater cross–sectional area of the filamented carbon fibre or the higher resistance of nickel-chrome compared to copper [294].

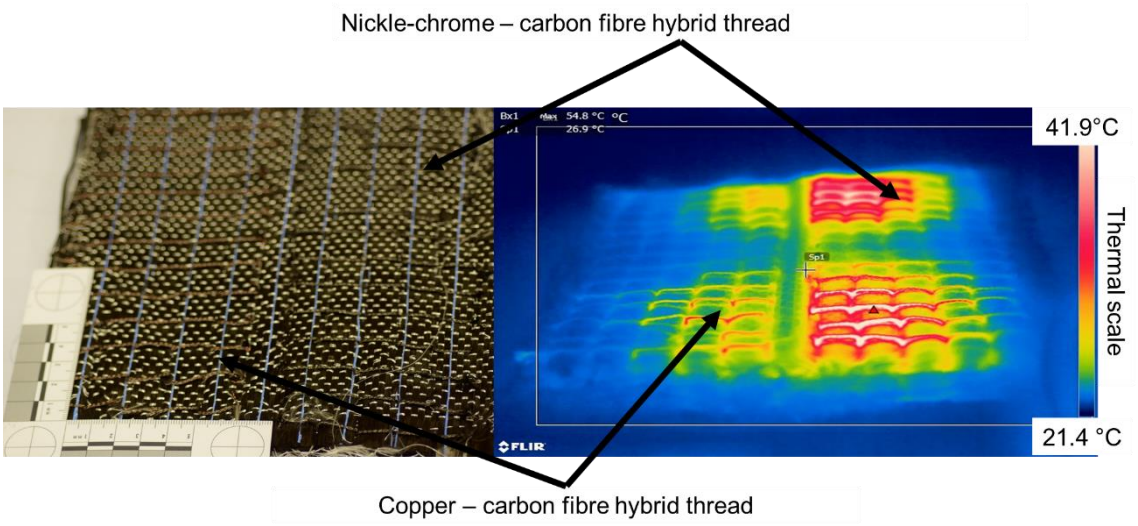

Figure 9-63 Preform tufted with copper-carbon fibre thread and nickel chrome- carbon fibre thread. (Left) Photo and (right) thermograph.

9.14 Conclusion and further work

This chapter described a preliminary investigation to establish an inductive curing method for thermoset carbon fibre reinforced composites. The aim was to utilise the conductive hybrid micro-braided tufting thread to increase TTC and increase interply fibre connections within a preform to improve the inductive response of a composite. This study demonstrated that fast, energy efficient heating was possible utilising the hybrid tufting thread. The main advantage of its use was the reduction in temperature variability throughout the specimens. The conductive properties of the hybrid thread distributed heat along its length and subsequently through the thickness of the specimen. The study provided an initial insight into the number of variables and contrasting mechanisms that need to be addressed in order to establish induction heating as an efficient

alternative to heat mats for composite repair. The next sections discuss the further work required to achieve a working induction method for composite repair.

9.14.1 Induction system

The dominant parameter affecting the induction heating profile of the specimens was the coil geometry and the subsequently generated emf shape. Irrespective of the other variables, such as ply lay-up, resin, or the inclusion of tufts; the coil geometry and torus shaped emf consistently affected the thermal output in all specimens. In this pilot study, it was not possible to change the coil shape due to cost, but different shaped coils are readily available off-the-shelf and should be chosen to match the workpiece shape or required heating profile.

Parameters such as closed loop operation of the induction heater and the surface temperature measurements by the thermal laser monitor also require optimisation to avoid hot spots and material degradation. For example, in order to avoid the initial output exceeding the target temperature, frequency and current control could be addressed by altering the operating setup. An alternative method to the pulse control used in this study would being desirable to avoid the excessive thermal fluctuations experienced during curing.

The induction of composites, especially carbon fibre composites, was complex due to the variability of material conductivity within a specimen. The insulating properties of the resin matrix and the anisotropic nature of carbon fibre plies increased the likelihood for localised hotspots and non-uniform heating. This could be addressed by the use of an adjustable heat sink such as that described by KVE INDUCT® to address surface material degradation [274]. A induction heating system that incorporated adjustable cooling and a tufted hybrid thread would enable an operator to adapt to any undesirable temperature spikes instantaneously. It would also enable heat dispersion into areas under-heated due to lack of conductivity or inductive response.

9.14.2 Braided hybrid microbraid thread effects.

From this pilot study, it was difficult to determine the extent of induction within the hybrid braid, as the braid did not inductively heat independently. Within a preform or composite, induction depended on the tuft pattern and the ply layup.

Despite not effectively inducting within the triaxial carbon fibre composite, the tufted hybrid thread did assist in dispersing high intensity heat spots and heating the corners of the composite. More substantial induction heating of the thread was achieved in the UD and nonconductive composites.

The study described in Section 7.5.9, did not fully examine the effect of tuft profile within the specimen or identify methods to potential induction in non-intersecting threads. Therefore, studies addressing braid manufacture and composition such as the inclusion of a core or over-braiding structure should be undertaken to increase self-induction of the tufting thread. This would be dependent on the hybridisation of the braid yarn materials.

Within the current braid thread structure, it was possible that the metal copper component was not inductively heating, and that any induction was due to the carbon fibre tow. As discussed in Mattheß et al. 2017, the wire shaped susceptors to inductively heat limited the extent to which the hybrid thread heated. However, the inclusion of the wire was essential for braid manufacture and to enable the tufting process as a more fibrous braid profile would fail to tuft as experienced in Chapter 3. Therefore, future work should undertake a full parameter assessment of fibrous metal combinations tuftabilty and induction potential.

Tufting using a hybrid thread increased the complexity of a composite structure. Localised variations such as fibre volume content, material properties, and ply fibre displacement all require further assessment. The tuft created variability in conductivity in TT and in-plane directions. The advantage of the braided structure was the interlacement consistency. This consistency ensures repetitive placement of the braided yarn materials within the composite. However, braid contraction when under tension can cause deviation. The microscopic images and CT scans (Section 6.5.2) also showed deviation of the tuft profile due to consolidation after infusion. The increased complexity made structural conduction measurements difficult and assessing mesoscale differentials depended on examination placement.

Overall, this pilot study demonstrated a curing approach with a number of competing mechanisms that need to be balanced. The inclusion of the hybrid thread can be tailored in braid material composition, areal density, profile, and location. Tuft insertion can be increased to enable both heat supply and heat

dispersion depending on materials. The use of heat sinks could address the lack of conductive uniformity within the tufted structure and prevent thermal gradients, hotspots, and specimen degradation.

Acknowledgement

The author would like to acknowledge the work of Mr. M. Jerome and Mr. J Uzzell co-supervised by C O'Keeffe and Dr. L.R. Pickard (University of Bristol) who conducted some of the experimentation during their undergraduate research projects.

REFERENCES

1. “wire” Collins English Dictionary. (2021). Retrieved January 7, 2021, from https://www.collinsdictionary.com/dictionary/english/wire
2. TEXTILE TERMS AND DEFINITIONS. (1956). *Journal of the Textile Institute Proceedings*, *47*(9), P817–P831. doi.org/10.1080/19447015608665337
3. Wilson, C. L., Lonkar, K., Roy, S., Kopsaftopoulos, F., & Chang, F.-K. K. (2018). Structural Health Monitoring of Composites. In P. W. R. Beaumont & C. H. Zweben (Eds.), *Comprehensive Composite Materials II, Volume 7* (2nd ed., pp. 382–407). Elsevier Ltd.
4. Giurgiutiu, V. (2014). Introduction. In *Structural Health Monitoring with Piezoelectric Wafer Active Sensors* (pp. 1–19). Elsevier.
5. Gibson, R. F. (2010). A review of recent research on mechanics of multifunctional composite materials and structures. *Composite Structures*, *92*(12), 2793–2810.
6. Collins, R. (2020). *Multifunctional Composites 2019-2029: Technology, Players, Market Forecasts: IDTechEx*. *IDTechEx Report*. Retrieved from https://www.idtechex.com/en/research-report/multifunctional-composites-2019-2029-technology-players-market-forecasts/630
7. Christodoulou, L., & Venables, J. D. (2003). Multifunctional material systems: The first generation. *The Journal of The Minerals, Metals & Materials Society (TMS)*, *55*(12), 39–45. doi.org/10.1007/s11837-003-0008-z
8. Breuer, U. P. (2016). *Commercial Aircraft Composite Technology*. Cham: Springer International Publishing. Retrieved from http://link.springer.com/10.1007/978-3-319-31918-6
9. Martins, A. (2018). *Analysis of damage mechanisms in composite structures reinforced by tufting (PhD Thesis)*. Université de Technologie de Compiègne.
10. Roh, H. D., Lee, H., & Park, Y. Bin. (2016). Structural health monitoring of carbon-material-reinforced polymers using electrical resistance

measurement. *International Journal of Precision Engineering and Manufacturing - Green Technology*, *3*(3), 311–321. doi.org/10.1007/s40684-016-0040-4

11. Diamanti, K., & Soutis, C. (2010). Structural health monitoring techniques for aircraft composite structures. *Progress in Aerospace Sciences*. Elsevier Ltd. doi.org/10.1016/j.paerosci.2010.05.001

12. Todoroki, A. (2008). Delamination monitoring analysis of CFRP structures using multi-probe electrical method. *Journal of Intelligent Material Systems and Structures*, *19*(3), 291–298. doi.org/10.1177/1045389X07084154

13. Li, H. C. H., Herszberg, I., Davis, C. E., Mouritz, A. P., & Galea, S. C. (2006). Health monitoring of marine composite structural joints using fibre optic sensors. *Composite Structures*, *75*(1–4), 321–327. doi.org/10.1016/j.compstruct.2006.04.054

14. Balaji, R., & Sasikumar, M. (2016). Structural health monitoring (SHM) system for polymer composites: A review. *Indian Journal of Science and Technology*. doi.org/10.17485/ijst/2016/v9i41/85832

15. Güemes, A., Fernández-López, A., Díaz-Maroto, P. F., Lozano, A., & Sierra-Perez, J. (2018). Structural health monitoring in composite structures by fiber-optic sensors. *Sensors (Switzerland)*, *18*(4), 1–11. doi.org/10.3390/s18041094

16. Zhou, G., & Sim, L. M. (2002). Damage detection and assessment in fibre-reinforced composite structures with embedded fibre optic sensors-review. *Smart Materials and Structures*, *11*(6), 925–939. doi.org/10.1088/0964-1726/11/6/314

17. Merzbacher, C. I., Kersey, A. D., & Friebele, E. J. (1996). Fiber optic sensors in concrete structures: a review. *Smart Materials and Structures*, *5*(2), 196–208. doi.org/10.1088/0964-1726/5/2/008

18. Sause, M. G. R., & Jasiūnienė, E. (2022). *Correction to: Structural Health Monitoring Damage Detection Systems for Aerospace*.

19. Gardiner, G. (2015). Structural health monitoring: Decades of demos build confidence. *Composites World*. Retrieved from https://www.compositesworld.com/articles/structural-health-monitoring-decades-of-demonstrations-build-confidence-in-local-shm

20. Gardiner, G. (2015). Structural health monitoring: NDT-integrated aerostructures. *Composites World*. Retrieved August 29, 2019, from https://www.compositesworld.com/articles/structural-health-monitoring-ndt-integrated-aerostructures-enter-service

21. Mouritz, A. P., Bannister, M. K., Falzon, P. J., & Leong, K. H. (1999). Review of applications for advanced three-dimensional fibre textile composites. *Composites Part A: Applied Science and Manufacturing*, *30*(12), 1445–1461.

22. Johnson, A., Tenney, D., Davis Jr, J., Pipes, R., & Johnston, N. (2001). NASA Composite Materials Development: Lessons Learned and Future Challenges. *Air & Space Europe*, *3*(3–4), 1–58. doi.org/10.1016/S1290-0958(01)90057-7

23. Clegg, H. (2020). *Towards the industrialisation and application of three-dimensional composite (PhD Thesis)*. University of Bristol.

24. Del Saz-Orozco, B., Ray, D., Kervennic, A., McGrail, P. T., & Stanley, W. F. (2016). Toughening of carbon fibre/polybenzoxazine composites by incorporating polyethersulfone into the interlaminar region. *Materials and Design*, *93*, 297–303. doi.org/10.1016/j.matdes.2015.12.138

25. Rana, S., P, S., Fangueiro, R., & Gomes Correia, A. (2016). A review on smart self-sensing composite materials for civil engineering applications. *AIMS Materials Science*, *3*(2), 357–379. doi.org/10.3934/matersci.2016.2.357

26. Boon, Y. Di, & Joshi, S. C. (2020). A review of methods for improving interlaminar interfaces and fracture toughness of laminated composites. *Materials Today Communications*, *22*, 100830. doi.org/10.1016/j.mtcomm.2019.100830

27. Bannister, M., & Herszberg, I. (1998). Advanced reinforcements. In T. Kruckenberg & R. Paton (Eds.), *Resin Transfer Moulding for Aerospace Structures* (pp. 83–111). Dordrecht: Springer Netherlands. Retrieved from http://link.springer.com/10.1007/978-94-011-4437-7_4

28. Dransfield, K., Baillie, C., & Mai, Y. W. (1994). Improving the delamination resistance of CFRP by stitching-a review. *Composites Science and Technology*, *50*(3), 305–317. doi.org/10.1016/0266-3538(94)90019-1

29. Bannister, M. (2001). Challenges for composites into the next millennium - A reinforcement perspective. *Composites - Part A: Applied Science and Manufacturing*, *32*(7), 901–910. doi.org/10.1016/S1359-835X(01)00008-2

30. Mouritz, A. P., Leong, K. H., & Herszberg, I. (1997). A review of the effect of stitching on the in-plane mechanical properties of fibre-reinforced polymer composites. *Composites Part A: Applied Science and Manufacturing*, *28*(12), 979–991. doi.org/10.1016/S1359-835X(97)00057-2

31. Aktas, A., Potluri, P., & Porat, I. (2013). Development of through-thickness reinforcement in advanced composites incorporating rigid cellular foams. *Applied Composite Materials*, *20*(4), 553–568.

32. Pappas, G., Joncas, S., Michaud, V., & Botsis, J. (2018). The influence of through-thickness reinforcement geometry and pattern on delamination of fiber-reinforced composites: Part I – Experimental results. *Composite Structures*, *184*, 924–934. doi.org/10.1016/j.compstruct.2017.09.091

33. Gnaba, I., Legrand, X., Wang, P., & Soulat, D. (2017). Literature review of tufted reinforcement for composite structures. *IOP Conference Series: Materials Science and Engineering*, *254*(4), 042011.

34. Gnaba, I., Legrand, X., Wang, P., & Soulat, D. (2018). Through-the-thickness reinforcement for composite structures: A review. *Journal of Industrial Textiles*, *0*(0), 1–26.

35. Mouritz, A. P., & Cox, B. N. (2010). A mechanistic interpretation of the comparative in-plane mechanical properties of 3D woven, stitched and pinned composites. *Composites Part A: Applied Science and Manufacturing*, *41*(6), 709–728. doi.org/10.1016/j.compositesa.2010.02.001

36. Dell'Anno, G., Treiber, J. W. G., & Partridge, I. K. (2016). Manufacturing of composite parts reinforced through-thickness by tufting. *Robotics and Computer-Integrated Manufacturing*, *37*, 262–272. doi.org/10.1016/j.rcim.2015.04.004

37. Tenney, D. R., Davis, John G., J., Pipes, R. B., & Johnston, N. (2009). NASA Composite Materials Development: Lessons Learned and Future Challenges. *NATO Research and Technology Agency AVT 164 - Support of Composite Systems*.

38. Dell'Anno, G. (2007). *Effect of tufting on the mechanical behaviour of carbon fabric/epoxy composites (PhD Thesis)*. Cranfield University.

39. Mitschang, P. (2011). Structural stitching of non-crimp fabric preforms for composites. In *Non-Crimp Fabric Composites* (pp. 67–83). Elsevier. Retrieved from https://linkinghub.elsevier.com/retrieve/pii/B9781845697624500035

40. Mirdehghan, A., Nosraty, H., Shokrieh, M. M., & Akhbari, M. (2018). The structural and tensile properties of glass/polyester co-wrapped hybrid yarns. *Journal of Industrial Textiles*, *47*(8), 1979–1997. doi.org/10.1177/1528083717716166

41. Alemour, B., Badran, O., & Hassan, M. R. (2019). A Review of Using Conductive Composite Materials in Solving Lightening Strike and Ice Accumulation Problems in Aviation. *Journal of Aerospace Technology and Management*, *11*, 1–23. doi.org/10.5028/jatm.v11.1022

42. Lombetti, D. M., & Skordos, A. A. (2019). Lightning strike and delamination performance of metal tufted carbon composites. *Composite Structures*, *209*(November 2018), 694–699. doi.org/10.1016/j.compstruct.2018.11.005

43. Salonitis, K., Pandremenos, J., Paralikas, J., & Chryssolouris, G. (2010). Multifunctional materials: Engineering applications and processing challenges. *International Journal of Advanced Manufacturing Technology*, *49*(5–8), 803–826. doi.org/10.1007/s00170-009-2428-6

44. Friedrich, K. (2015). Routes for achieving multifunctionality in reinforced polymers and composite structures. In K. Friedrich & U. Breuer (Eds.), *Multifunctionality of Polymer Composites: Challenges and New Solutions* (pp. 3–41). New York: Elsevier Inc.

45. Sairajan, K. K., Aglietti, G. S., & Mani, K. M. (2016). A review of multifunctional structure technology for aerospace applications. *Acta Astronautica*, *120*, 30–42.

46. Thompson, B. S., Gandhi, M. V., & Kasiviswanathan, S. (1992). An introduction to smart materials and structures. *Materials & Design*, *13*(1), 3–9. doi.org/10.1016/0261-3069(92)90045-J

47. Ferreira, A. D. B. L., Nóvoa, P. R. O., & Marques, A. T. (2016). Multifunctional Material Systems: A state-of-the-art review. *Composite Structures*, *151*, 3–35. doi.org/10.1016/j.compstruct.2016.01.028

48. Narayana, K. J., & Gupta Burela, R. (2018). A review of recent research on multifunctional composite materials and structures with their applications. *Materials Today: Proceedings*, *5*(2), 5580–5590.

49. Web of Science [v.5.35] - Citation Report. (n.d.). Retrieved May 27, 2021, from http://apps.webofknowledge.com/CitationReport.do?product=WOS&search_mode=CitationReport&SID=5EmXELx2ARGDHQ7uze3&page=1&cr_pqid=17&viewType=summary

50. Ghouti, H., Zegaoui, A., Derradji, M., Cai, W., Wang, J., Liu, W., & Dayo, A. (2018). Multifunctional Hybrid Composites with Enhanced Mechanical and Thermal Properties Based on Polybenzoxazine and Chopped Kevlar/Carbon Hybrid Fibers. *Polymers*, *10*(12), 1308.

51. González, C., Vilatela, J. J., Molina-Aldareguía, J. M., Lopes, C. S., & LLorca, J. (2017). Structural composites for multifunctional applications: current challenges and future trends. *Progress in Materials Science*, *89*, 194–251.

52. Breuer, U. P., & Schmeer, S. (2015). Carbon and metal-fiber-reinforced airframe structures. In K. Friedrich & U. Breuer (Eds.), *Multifunctionality of Polymer Composites: Challenges and New Solutions* (pp. 435–447). New York: Elsevier Inc.

53. Brown, S. C. C., Robert, C., Koutsos, V., & Ray, D. (2020). Methods of modifying through-thickness electrical conductivity of CFRP for use in structural health monitoring, and its effect on mechanical properties – A review. *Composites Part A: Applied Science and Manufacturing*, *133*, 105885. doi.org/10.1016/j.compositesa.2020.105885

54. Farrar, C. R., & Worden, K. (2007). An introduction to structural health monitoring. *Philosophical Transactions of the Royal Society A: Mathematical, Physical and Engineering Sciences*, *9*(7), 303–315. doi.org/10.1098/rsta.2006.1928

55. Jollivet, T., Peyrac, C., & Lefebvre, F. (2013). Damage of composite materials. *Procedia Engineering*, *66*, 746–758.

56. Belnoue, J. P. H., Nixon-Pearson, O. J., Ivanov, D., & Hallett, S. R. (2016). A novel hyper-viscoelastic model for consolidation of toughened prepregs under processing conditions. *Mechanics of Materials*, *97*, 118–134. doi.org/10.1016/j.mechmat.2016.02.019

57. Nixon-Pearson, O., Belnoue, J.-H., Ivanov, D., Potter, K., & Hallett, S. (2017). An experimental investigation of the consolidation behaviour of uncured prepregs under processing conditions. *Journal of Composite Materials*, *51*(13), 1911–1924. doi.org/10.1177/0021998316665681

58. Greenhalgh, E. S. (2009). Defects and damage and their role in the failure of polymer composites. In *Failure Analysis and Fractography of Polymer Composites* (pp. 356–440). Cambridge: Elsevier.

59. Boller, C., & Saarlandes, U. (2013). In-flight Aircraft Structure Health Monitoring Based on Smart Structures Technology. In *Conference: Smart Structures for Aircraft and Spacecraft* (pp. 17–19). Lindau, Germany.

60. Chung, D. (2007). Damage detection using self-sensing concepts. *Proceedings of the Institution of Mechanical Engineers, Part G: Journal of Aerospace Engineering*, *221*(4), 509–520. doi.org/10.1243/09544100JAERO203

61. Cantwell, W. J., & Morton, J. (1985). Detection of impact damage in

CFRP laminates. *Composite Structures*, *3*(3–4), 241–257. doi.org/10.1016/0263-8223(85)90056-X

62. AAIB. (2020). AAIB Bulletin 11/2020 ISSN 0309-4278. Aldershot: Air Accidents Investigation Branch.

63. Boller, C., & Buderath, M. (2007). Fatigue in aerostructures - Where structural health monitoring can contribute to a complex subject. *Philosophical Transactions of the Royal Society A: Mathematical, Physical and Engineering Sciences*, *365*(1851), 561–587. doi.org/10.1098/rsta.2006.1924

64. Kim, S. B., Park, J. H., Ahn, H., Liu, D., & Kim, D. J. (2011). Temperature effects on output power of piezoelectric vibration energy harvesters. *Microelectronics Journal*, *42*(8), 988–991. doi.org/10.1016/j.mejo.2011.05.005

65. Culshaw, B., & Kersey, A. (2008). Fiber-optic sensing: A historical perspective. *Journal of Lightwave Technology*, *26*(9), 1064–1078. doi.org/10.1109/JLT.0082.921915

66. Hofer, B. (1987). Fibre optic damage detection in composite structures. *Composites*, *18*(4), 309–316. doi.org/10.1016/0010-4361(87)90294-1

67. Di Sante, R. (2015). Fibre Optic Sensors for Structural Health Monitoring of Aircraft Composite Structures: Recent Advances and Applications. *Sensors*, *15*(8), 18666–18713. doi.org/10.3390/s150818666

68. Miguel Giraldo, C., Zúñiga Sagredo, J., Sánchez Gómez, J., & Corredera, P. (2017). Demonstration and Methodology of Structural Monitoring of Stringer Runs out Composite Areas by Embedded Optical Fiber Sensors and Connectors Integrated during Production in a Composite Plant. *Sensors*, *17*(7), 1683. doi.org/10.3390/s17071683

69. Waite, S. R., & Sage, G. N. (1988). The failure of optical fibres embedded in composite materials. *Composites*, *19*(4), 288–294. doi.org/10.1016/0010-4361(88)90005-5

70. Rocha, H., Semprimoschnig, C., & Nunes, J. P. (2021). Sensors for process and structural health monitoring of aerospace composites: A review. *Engineering Structures*, *237*(July 2020). doi.org/10.1016/j.engstruct.2021.112231

71. Schueler, R., Joshi, S. P., & Schulte, K. (2001). Damage detection in CFRP by electrical conductivity mapping. *Composites Science and Technology*, *61*(6), 921–930. doi.org/10.1016/S0266-3538(00)00178-0

72. Raihan, R., Adkins, J.-M., Baker, J., Rabbi, F., & Reifsnider, K. (2014). Relationship of dielectric property change to composite material state degradation. *Composites Science and Technology*, *105*, 160–165. doi.org/10.1016/j.compscitech.2014.09.017

73. Schulte, K., & Baron, C. (1989). Load and failure analyses of CFRP laminates by means of electrical resistivity measurements. *Composites Science and Technology*, *36*(1), 63–76. doi.org/10.1016/0266-3538(89)90016-X

74. Ceysson, O., Salvia, M., & Vincent, L. (1996). Damage mechanisms characterisation of carbon fibre/epoxy composite laminates by both

electrical resistance measurements and acoustic emission analysis. *Scripta Materialia*, *34*(8), 1273–1280. doi.org/10.1016/1359-6462(95)00638-9

75. Zappalorto, M., Panozzo, F., Carraro, P. A., & Quaresimin, M. (2017). Electrical response of a laminate with a delamination: modelling and experiments. *Composites Science and Technology*, *143*, 31–45. doi.org/10.1016/j.compscitech.2017.02.023

76. Cheng, X., Zhou, H., Wu, Z., & Hu, X. (2018). Detection of bending direction and amplitude by electrical resistance measurement of axial carbon fibers in braided composite tube. *Textile Research Journal*, *89*(12), 2500–2508.

77. Cartié, D. D. R., Troulis, M., & Partridge, I. K. (2006). Delamination of Z-pinned carbon fibre reinforced laminates. *Composites Science and Technology*, *66*(6), 855–861. doi.org/10.1016/j.compscitech.2004.12.018

78. Saboktakin, A., Vu-Khanh, T., Butun, V., & Pantyukhov, P. (2018). Characteristics of tufted preforms subjected to different mechanical loading for aerospace applications. *FME Transactions*, *46*(2), 224–229. doi.org/10.5937/fmet1802224S

79. Baker, A., Dutton, S., & Kelly, D. (2004). *Composite Materials for Aircraft Structures.* (J. A. Schetz, Ed.) (2nd ed.). Reston, Virginia: American Institute of Aeronautics and Astronautics, Inc.

80. Najafloo, B., Rezadoust, A. M., & Latifi, M. (2016). Effect of through-the-thickness areal density and yarn fineness on the mechanical performance of three-dimensional carbon-phenolic composites. *Journal of Reinforced Plastics and Composites*, *35*(20), 1447–1459. doi.org/10.1177/0731684416653839

81. Pingkarawat, K., & Mouritz, A. P. (2016). Comparative study of metal and composite z-pins for delamination fracture and fatigue strengthening of composites. *Engineering Fracture Mechanics*, *154*, 180–190. doi.org/10.1016/j.engfracmech.2016.01.003

82. Cantwell, W. J., & Morton, J. (1991). The impact resistance of composite materials - a review. *Composites*, *22*(5), 347–362. doi.org/10.1016/0010-4361(91)90549-V

83. Wilkinson, S. P., Ward, T. C., & McGrath, J. E. (1993). Effect of thermoplastic modifier variables on toughening a bismaleimide matrix resin for high-performance composite materials. *Polymer*, *34*(4), 870–884. doi.org/10.1016/0032-3861(93)90376-L

84. Cardwell, B. J., & Yee, A. F. (1998). Toughening of epoxies through thermoplastic crack bridging. *Journal of Materials Science*, *33*(22), 5473–5484. doi.org/10.1023/a:1004427123388

85. Mezzenga, R., Boogh, L., & Månson, J. A. E. (2001). A review of dendritic hyperbranched polymer as modifiers in epoxy composites. *Composites Science and Technology*, *61*(5), 787–795. doi.org/10.1016/S0266-3538(01)00022-7

86. Sprenger, S. (2015). Improving mechanical properties of fiber-reinforced composites based on epoxy resins containing industrial surface-modified silica nanoparticles: Review and outlook. *Journal of Composite Materials*,

49(1), 53–63. doi.org/10.1177/0021998313514260

87. Bucknall, C. B., & Gilbert, A. H. (1989). Toughening tetrafunctional epoxy resins using polyetherimide. *Polymer*, *30*(2), 213–217. doi.org/10.1016/0032-3861(89)90107-9

88. Takeichi, T., Kawauchi, T., & Agag, T. (2008). High Performance Polybenzoxazines as a Novel Type of Phenolic Resin. *Polymer Journal*, *40*(12), 1121–1131. doi.org/10.1295/polymj.PJ2008072

89. Tang, Y., Ye, L., Zhang, Z., & Friedrich, K. (2013). Interlaminar fracture toughness and CAI strength of fibre-reinforced composites with nanoparticles - A review. *Composites Science and Technology*, *86*, 26–37. doi.org/10.1016/j.compscitech.2013.06.021

90. Iredale, R. J., Ward, C., & Hamerton, I. (2017). Modern advances in bismaleimide resin technology: A 21st century perspective on the chemistry of addition polyimides. *Progress in Polymer Science*, *69*, 1–21. doi.org/10.1016/j.progpolymsci.2016.12.002

91. Akca, E., & Gursel, A. (2015). A Review on the Matrix Toughness of Thermoplastic Materials. *Periodicals of Engineering and Natural Sciences (PEN)*, *3*(2), 1–8. doi.org/10.21533/pen.v3i2.52

92. Farooq, U., Teuwen, J., & Dransfeld, C. (2020). Toughening of epoxy systems with interpenetrating polymer network (IPN): A review. *Polymers*, *12*(9). doi.org/10.3390/POLYM12091908

93. Wu, S., Ladani, R. B., Ravindran, A. R., Zhang, J., Mouritz, A. P., Kinloch, A. J., & Wang, C. H. (2017). Aligning carbon nanofibres in glass-fibre/epoxy composites to improve interlaminar toughness and crack-detection capability. *Composites Science and Technology*, *152*, 46–56. doi.org/10.1016/j.compscitech.2017.09.007

94. Yee, A. F., & Pearson, R. A. (1983). Toughening Mechanism in Elastomer-Modified Epoxy Resins - Part 1. *NASA Contractor Reports*, (August 1983).

95. Mouritz, A. P. (2020). Review of z-pinned laminates and sandwich composites. *Composites Part A: Applied Science and Manufacturing*, *139*(July), 106128. doi.org/10.1016/j.compositesa.2020.106128

96. Mouritz, A. P., Gallagher, J., & Goodwin, A. A. (1997). Flexural strength and interlaminar shear strength of stitched GRP laminates following repeated impacts. *Composites Science and Technology*, *57*(5), 509–522. doi.org/10.1016/S0266-3538(96)00164-9

97. Bianchi, F., & Zhang, X. (2012). Predicting mode-II delamination suppression in z-pinned laminates. *Composites Science and Technology*, *72*(8), 924–932. doi.org/10.1016/j.compscitech.2012.03.003

98. Ogale, A., & Mitschang, P. (2004). Tailoring of textile preforms for fibre-reinforced polymer composites. *Journal of Industrial Textiles*, *34*(2), 77–96. doi.org/10.1177/1528083704046949

99. Mouritz, A. P. (2007). Compression properties of z-pinned composite laminates. *Composites Science and Technology*, *67*(15–16), 3110–3120. doi.org/10.1016/j.compscitech.2007.04.017

100. Cartié, D. D. R., Cox, B. N., & Fleck, N. A. (2004). Mechanisms of crack

bridging by composite and metallic rods. *Composites Part A: Applied Science and Manufacturing*, *35*(11), 1325–1336. doi.org/10.1016/j.compositesa.2004.03.006

101. Chang, P., Mouritz, A. P., & Cox, B. N. (2006). Properties and failure mechanisms of z-pinned laminates in monotonic and cyclic tension. *Composites Part A: Applied Science and Manufacturing*, *37*(10), 1501–1513. doi.org/10.1016/j.compositesa.2005.11.013

102. Treiber, J. W. G. (2011). *Performance of tufted carbon fibre/epoxy composites (PhD Thesis)*. Cranfield University.

103. Beier, U., Sandler, J. K. W., Altstädt, V., Spanner, H., & Weimer, C. (2009). Mechanical performance of carbon fibre-reinforced composites based on stitched and bindered preforms. *Composites Part A: Applied Science and Manufacturing*, *40*(11), 1756–1763.

104. Göktaş, D., Kennon, W. R., & Potluri, P. (2017). Improvement of Mode I Interlaminar Fracture Toughness of Stitched Glass/Epoxy Composites. *Applied Composite Materials*, *24*(2), 351–375.

105. Kostopoulos, V., Sarantinos, N., & Tsantzalis, S. (2020). Review of Through-the-Thickness Reinforced z-Pinned Composites. *Journal of Composites Science*, *4*(1), 31. doi.org/10.3390/jcs4010031

106. Mills, A. R., & Jones, J. (2010). Investigation, manufacture, and testing of damage-resistant airframe structures using low-cost carbon fibre composite materials and manufacturing technology. *Proceedings of the Institution of Mechanical Engineers, Part G: Journal of Aerospace Engineering*, *224*(4), 489–497. doi.org/10.1243/09544100JAERO573

107. Alagirusamy, R., Fangueiro, R., Ogale, V., & Padaki, N. (2006). Hybrid Yarns and Textile Preforming for Thermoplastic Composites. *Textile Progress*, *38*(4), 1–71.

108. Yudhanto, A., Lubineau, G., Ventura, I. A., Watanabe, N., Iwahori, Y., & Hoshi, H. (2015). Damage characteristics in 3D stitched composites with various stitch parameters under in-plane tension. *Composites Part A: Applied Science and Manufacturing*, *71*, 17–31. doi.org/10.1016/j.compositesa.2014.12.012

109. British Standards Institution. (1991). BS 3870-1:1991 ISO 4915:1991. Stitches and seams - Part 1: Classification and terminology of stitch types. Retrieved December 1, 2017, from http://www.standardsuk.com/

110. Dow, M. B., & Dexter, H. B. (1997). *Development of Stitched, Braided and Woven Composite Structures in the ACT Program and at Langley Research Center (1985-1997)*. Hampton, VA.

111. Jain, L. K., Dransfield, K. A., & Mai, Y. W. (1998). On the effects of stitching in CFRPs - II. Mode II delamination toughness. *Composites Science and Technology*, *58*(6), 829–837. doi.org/10.1016/S0266-3538(97)00186-3

112. Ogale, A. (2007). *Investigations of sewn preform characteristics and quality aspects for the manufacturing of fiber reinforced polymer composites (PhD Thesis)*. University of Kaiserslautern.

113. Plain, K. P., & Tong, L. (2011). An experimental study on mode i and II

fracture toughness of laminates stitched with a one-sided stitching technique. *Composites Part A: Applied Science and Manufacturing*, *42*(2), 203–210. doi.org/10.1016/j.compositesa.2010.11.006

114. Tan, K. T., Watanabe, N., Iwahori, Y., & Ishikawa, T. (2012). Effect of stitch density and stitch thread thickness on compression after impact strength and response of stitched composites. *Composites Science and Technology*, *72*(5), 587–598. doi.org/10.1016/J.COMPSCITECH.2012.01.003

115. Tan, K. T., Watanabe, N., Iwahori, Y., & Ishikawa, T. (2012). Understanding effectiveness of stitching in suppression of impact damage: An empirical delamination reduction trend for stitched composites. *Composites Part A: Applied Science and Manufacturing*, *43*(6), 823–832. doi.org/10.1016/j.compositesa.2011.12.022

116. Scarponi, C., Perillo, A. M., Cutillo, L., & Foglio, C. (2007). Advanced TTT composite materials for aeronautical purposes: Compression after impact (CAI) behaviour. *Composites Part B: Engineering*, *38*(2), 258–264. doi.org/10.1016/j.compositesb.2006.03.014

117. Koziol, M. (2013). Effect of thread tension on mechanical performance of stitched glass fibre-reinforced polymer laminates -experimental study. *Journal of Composite Materials*, *47*(16), 1919–1930. doi.org/10.1177/0021998312452179

118. Dexter, H. B., & Funk, J. G. (1986). *Impact resistance and interlaminar fracture toughness of through-the-thickness reinforced graphite/epoxy*. *27th AIAA paper 86-CP*. Hampton, VA.

119. Tan, K. T., Yoshimura, A., Watanabe, N., Iwahori, Y., & Ishikawa, T. (2015). Further investigation of Delamination Reduction Trend for stitched composites. *Composites Science and Technology*, *118*, 141–153. doi.org/10.1016/j.compscitech.2015.08.019

120. Mignery, L. A., Tan, T. M., & Sun, C. T. (1985). The Use of Stitching to Suppress Delamination in Laminated Composites. *Delamination and Debonding*, *876*, 371–385. doi.org/http://dx.doi.org/10.1520/STP36315S

121. Mouritz, A. P., & Cox, B. N. (2000). A mechanistic approach to the properties of stitched laminates. *Composites Part A: Applied Science and Manufacturing*, *31*(1), 1–27.

122. Velmurugan, R., & Solaimurugan, S. (2007). Improvements in Mode I interlaminar fracture toughness and in-plane mechanical properties of stitched glass/polyester composites. *Composites Science and Technology*, *67*(1), 61–69. doi.org/10.1016/j.compscitech.2006.03.032

123. Chen, L., Ifju, P. G., & Sankar, B. V. (2001). A novel double cantilever beam test for stitched composite laminates. *Journal of Composite Materials*, *35*(13), 1137–1149. doi.org/10.1106/3FT5-102A-XQT0-UTRW

124. Partridge, I. K., Yasaee, M., Allegri, G., & Lander, J. K. K. (2015). Damage-tolerant composite structures by Z-pinning. In Q. Qin & J. Ye (Eds.), *Toughening Mechanisms in Composite Materials* (pp. 161–189). Cambridge, UK: Elsevier Inc.

125. Mouritz, A. P. (2007). Review of z-pinned composite laminates. *Composites Part A: Applied Science and Manufacturing*, *38*(12), 2383–

2397. doi.org/10.1016/j.compositesa.2007.08.016

126. Johnson, W., Masters, J., Wilson, D., Dickinson, L., Farley, G., & Hinders, M. (1999). Translaminar Reinforced Composites: A Review. *Journal of Composites Technology and Research*, *21*(1), 3. doi.org/10.1520/CTR10607J

127. Rugg, K. L., Cox, B. N., Ward, K. E., & Sherrick, G. O. (1998). Damage mechanisms for angled through-thickness rod reinforcement in carbon-epoxy laminates. *Composites Part A: Applied Science and Manufacturing*, *29*(12), 1603–1613. doi.org/10.1016/S1359-835X(98)00087-6

128. Yasaee, M., Lander, J. K., Allegri, G., & Hallett, S. R. (2014). Experimental characterisation of mixed mode traction-displacement relationships for a single carbon composite Z-pin. *Composites Science and Technology*, *94*, 123–131. doi.org/10.1016/j.compscitech.2014.02.001

129. Cui, H., Yasaee, M., Hallett, S. R., Partridge, I. K., Allegri, G., & Petrinic, N. (2018). Dynamic bridging mechanisms of through-thickness reinforced composite laminates in mixed mode delamination. *Composites Part A: Applied Science and Manufacturing*, *106*, 24–33. doi.org/10.1016/j.compositesa.2017.11.017

130. Lenzi, F., Riccio, A., Clarke, A., & Creemers, R. (2007). Coupon tests on z-pinned and unpinned composite samples for damage resistant applications. In *Macromolecular Symposia* (Vol. 247, pp. 230–237).

131. Martins, A. T., Aboura, Z., Harizi, W., Laksimi, A., & Khellil, K. (2018). Analysis of the impact and compression after impact behavior of tufted laminated composites. *Composite Structures*, *184*, 352–361. doi.org/10.1016/j.compstruct.2017.09.096

132. Liu, L., Wang, P., Legrand, X., & Soulat, D. (2017). Investigation of mechanical properties of tufted composites: Influence of tuft length through the thickness reinforcement. *Composite Structures*, *172*, 221–228. doi.org/10.1016/j.compstruct.2017.03.099

133. Lombetti, D. M. (2015). *Tufting of complex composite structures (PhD Thesis)*. Cranfield University.

134. Chehura, E., Dell'Anno, G., Huet, T., Staines, S., James, S. W., Partridge, I. K., & Tatam, R. P. (2014). On-line monitoring of multi-component strain development in a tufting needle using optical fibre Bragg grating sensors. *Smart Materials and Structures*, *23*(7), 075001. doi.org/10.1088/0964-1726/23/7/075001

135. Scott, M., Dell'Anno, G., & Clegg, H. (2018). Effect of Process Parameters on the Geometry of Composite Parts Reinforced by Through-the-Thickness Tufting. *Applied Composite Materials*, *25*(4), 785–796. doi.org/10.1007/s10443-018-9710-4

136. Partridge, I. K., Treiber, J. W. G., & Préau, M. (2011). Deformation and failure in a tufted carbon fabric / epoxy Ω – stiffener. In *Deformation and Fracture of Composites (DFC-11)*. Cambridge, UK.

137. Mankodi, H. R. (2011). Development in hybrid Yarns. In R. H. Gong (Ed.), *Specialist yarn and fabric structures: developments and applications* (pp. 21–55). Cambridge, UK: Woodhead Publishing Limited.

138. Verma, K. K., Viswamurthy, S. R. R., Gaddikeri, K. M., Ramesh, S., Kumar, S., & Bose, S. (2020). Tufting thread and density controls the mode-I fracture toughness in carbon/epoxy composite. *Composite Structures*, 113272. doi.org/10.1016/j.compstruct.2020.113272

139. Verma, K. K., Padmakara, G., Gaddikeri, K. M., Ramesh, S., Kumar, S., & Bose, S. (2019). The key role of thread and needle selection towards 'through-thickness reinforcement' in tufted carbon fiber-epoxy laminates. *Composites Part B: Engineering*, *174*, 106970. doi.org/10.1016/j.compositesb.2019.106970

140. Colin de Verdiere, M., Pickett, A. K., Skordos, A. A., & Witzel, V. (2009). Evaluation of the mechanical and damage behaviour of tufted non crimped fabric composites using full field measurements. *Composites Science and Technology*, *69*(2), 131–138. doi.org/10.1016/j.compscitech.2008.08.025

141. Hui, C., Wang, P., & Legrand, X. (2019). Improvement of tufting mechanism during the advanced 3-dimensional tufted composites manufacturing: To the optimisation of tufting threads degradation. *Composite Structures*, *220*, 423–430. doi.org/10.1016/j.compstruct.2019.04.019

142. Koissin, V., Kustermans, J., Lomov, S. V., Verpoest, I., Van Den Broucke, B., & Witzel, V. (2009). Structurally stitched NCF preforms: Quasi-static response. *Composites Science and Technology*, *69*(15–16), 2701–2710. doi.org/10.1016/j.compscitech.2009.08.015

143. Gnaba, I., Wang, P., Legrand, X., & Soulat, D. (2018). Evaluation of the mechanical behaviour of tufted preforms. *IOP Conference Series: Materials Science and Engineering*, *406*(1), 012019.

144. Hartley, J. W., & Ward, C. (2017). Improving the Understanding of Tufted Energy Absorbing Sandwich Structures. In *32nd Technical Conference of the American Society of Composites* (pp. 2260–2273). West Lafayette, IA.

145. Eguibar, D. F. (2019). *Selective stithing on composite skin-stiffener bonding for improved damage tolerant structures (PhD Thesis)*. Univeristy of Stuttgart.

146. Liu, L., Zhang, T., Wang, P., Legrand, X., & Soulat, D. (2015). Influence of the tufting yarns on formability of tufted 3-Dimensional composite reinforcement. *Composites Part A: Applied Science and Manufacturing*, *78*, 403–411. doi.org/10.1016/j.compositesa.2015.07.014

147. Liu, L. (2017). *Development and optimization of the tufting process for textile composite reinforcement (PhD Thesis)*. Université de Lille.

148. Dell'Anno, G., Cartié, D. D. R., Partridge, I. K., & Rezai, A. (2007). Exploring mechanical property balance in tufted carbon fabric/epoxy composites. *Composites Part A: Applied Science and Manufacturing*, *38*(11), 2366–2373. doi.org/10.1016/j.compositesa.2007.06.004

149. Gnaba, I., Wang, P., Legrand, X., & Soulat, D. (2019). Manufacturing and characterization of tufted preform with complex shape. *Advances in Aircraft and Spacecraft Science*, *6*(2), 105–116. doi.org/10.12989/aas.2019.6.2.105

150. Bigaud, J., Aboura, Z., Martins, A. T., & Verger, S. (2018). Analysis of the

mechanical behavior of composite T-joints reinforced by one side stitching. *Composite Structures*, *184*, 249–255. doi.org/10.1016/j.compstruct.2017.06.041

151. Treiber, J. W. G., Cartié, D. D. R., & Partridge, I. K. (2009). Determination of crack bridging laws in tufted composites. In *ICCM International Conferences on Composite Materials*.

152. Martins, A. T., Aboura, Z., Harizi, W., Laksimi, A., & Hamdi, K. (2019). Structural health monitoring by the piezoresistive response of tufted reinforcements in sandwich composite panels. *Composite Structures*, *210*, 109–117. doi.org/10.1016/j.compstruct.2018.11.032

153. Mouritz, A. P., Baini, C., & Herszberg, I. (1999). Mode I interlaminar fracture toughness properties of advanced textile fibreglass composites. *Composites Part A: Applied Science and Manufacturing*, *30*(7), 859–870. doi.org/10.1016/S1359-835X(98)00197-3

154. Cartié, D. D. R., Dell'Anno, G., Poulin, E., & Partridge, I. K. (2006). 3D reinforcement of stiffener-to-skin T-joints by Z-pinning and tufting. *Engineering Fracture Mechanics*, *73*(16), 2532–2540. doi.org/10.1016/j.engfracmech.2006.06.012

155. Kratz, J., Clegg, H., Dell'Anno, G., & Partridge, I. K. (2015). Improving the damage tolerance of composite joints with tufting. In *ICCM20 - 20th International Conference on Composite Materials*. Copenhagen, Denmark.

156. Bader, M. G. (2002). Selection of composite materials and manufacturing routes for cost-effective performance. *Composites - Part A: Applied Science and Manufacturing*, *33*(7), 913–934. doi.org/10.1016/S1359-835X(02)00044-1

157. Harman D, Grove S, Summerscales J., Harman, D., Grove, S., & Summerscales, J. (2014). The economics of through-thickness fibre reinforcement using single sided robotic tufting. *16th European Conference on Composite Materials, ECCM 2014*, (June), 22–26.

158. Harman, D. E. (2013). *An economic evaluation of the robotic tufting process considering the application of a novel composite wing rib post (PhD Thesis)*. University of Plymouth. Retrieved from https://pearl.plymouth.ac.uk/handle/10026.1/10847

159. Liu, W., Hoa, S. V., & Pugh, M. (2005). Fracture toughness and water uptake of high-performance epoxy/nanoclay nanocomposites. *Composites Science and Technology*, *65*(15-16 SPEC. ISS.), 2364–2373. doi.org/10.1016/j.compscitech.2005.06.007

160. Kinloch, A. J., Masania, K., Taylor, A. C., Sprenger, S., Egan, D., Egan, S. S. Æ. D., … Egan, D. (2008). The fracture of glass-fibre-reinforced epoxy composites using nanoparticle-modified matrices. *Journal of Materials Science*, *43*(3), 1151–1154. doi.org/10.1007/s10853-007-2390-3

161. Aymerich, F., Pani, C., & Priolo, P. (2007). Effect of stitching on the low-velocity impact response of [03/903]s graphite/epoxy laminates. *Composites Part A: Applied Science and Manufacturing*, *38*(4), 1174–1182.

162. Mouritz, A. P. (1996). Flexural properties of stitched GRP laminates. *Composites Part A: Applied Science and Manufacturing*, *27*(7 PART A), 525–530. doi.org/10.1016/1359-835X(96)00010-3

163. Abot, J. L., Song, Y., Vatsavaya, M. S., Medikonda, S., Kier, Z., Jayasinghe, C., … Schulz, M. J. (2010). Delamination detection with carbon nanotube thread in self-sensing composite materials. *Composites Science and Technology*, *70*(7), 1113–1119.

164. Kandare, E., Khatibi, A. A., Yoo, S., Wang, R., Ma, J., Olivier, P., … Wang, C. H. (2015). Improving the through-thickness thermal and electrical conductivity of carbon fibre/epoxy laminates by exploiting synergy between graphene and silver nano-inclusions. *Composites Part A: Applied Science and Manufacturing*, *69*, 72–82. doi.org/10.1016/j.compositesa.2014.10.024

165. Böger, L., Wichmann, M. H. G., Meyer, L. O., & Schulte, K. (2008). Load and health monitoring in glass fibre reinforced composites with an electrically conductive nanocomposite epoxy matrix. *Composites Science and Technology*, *68*(7–8), 1886–1894. doi.org/10.1016/j.compscitech.2008.01.001

166. Hirano, Y., Yamane, T., & Todoroki, A. (2016). Through-thickness electric conductivity of toughened carbon-fibre-reinforced polymer laminates with resin-rich layers. *Composites Science and Technology*, *122*, 67–72. doi.org/10.1016/j.compscitech.2015.11.018

167. Gu, B., Liu, H. Y., & Mai, Y. W. (2006). A theoretical model on piezoelectric fibre pullout with electric input. *Engineering Fracture Mechanics*, *73*(14), 2053–2066. doi.org/10.1016/j.engfracmech.2006.03.009

168. Gu, B., Liu, H. Y., & Mai, Y. W. (2007). Effect of Input Electric Field on Fatigue Degradation of Piezoelectric Fibre Bridging Force. *Key Engineering Materials*, *334–335*, 593–596. doi.org/10.4028/www.scientific.net/KEM.334-335.593

169. Liu, H.-Y., Qin, Q. H., & Mai, Y. W. (2003). Theoretical model of piezoelectric fibre pull-out. *International Journal of Solids and Structures*, *40*(20), 5511–5519. doi.org/10.1016/S0020-7683(03)00277-4

170. Gu, B., Zhang, H., Wang, B., Zhang, S., & Feng, X. (2015). Fracture toughness of laminates reinforced by piezoelectric z-pins. *Theoretical and Applied Fracture Mechanics*, *77*, 35–40. doi.org/10.1016/j.tafmec.2015.01.007

171. Zhang, B., Allegri, G., Yasaee, M., Hallett, S. R., & Partridge, I. K. (2016). On the delamination self-sensing function of Z-pinned composite laminates. *Composites Science and Technology*, *128*, 138–146. doi.org/10.1016/j.compscitech.2016.03.019

172. Zhang, B., Allegri, G., & Hallett, S. R. (2016). An experimental investigation into multi-functional Z-pinned composite laminates. *Materials and Design*, *108*, 679–688. doi.org/10.1016/j.matdes.2016.07.035

173. Pegorin, F., Pingkarawat, K., & Mouritz, A. P. (2017). Controlling the electrical conductivity of fibre-polymer composites using z-pins. *Composites Science and Technology*, *150*, 167–173.

doi.org/10.1016/j.compscitech.2017.07.018

174. Pegorin, F., Pingkarawat, K., & Mouritz, A. P. (2018). Electrical-based delamination crack monitoring in composites using z-pins. *Composites Part A: Applied Science and Manufacturing*, *104*, 120–128. doi.org/10.1016/j.compositesa.2017.10.025

175. Martins, A. T., Aboura, Z., Harizi, W., Laksimi, A., & Khellil, K. (2019). Structural health monitoring for GFRP composite by the piezoresistive response in the tufted reinforcements. *Composite Structures*, *209*, 103–111. doi.org/10.1016/j.compstruct.2018.10.091

176. Grigoriou, K., Ladani, R. B., & Mouritz, A. P. (2019). Electrical properties of multifunctional Z-pinned sandwich composites. *Composites Science and Technology*, *170*(September 2018), 60–69. doi.org/10.1016/j.compscitech.2018.11.030

177. Kalashnyk, N., Faulques, E., Schjødt-Thomsen, J., Jensen, L. R., Rauhe, J. C. M., & Pyrz, R. (2017). Monitoring self-sensing damage of multiple carbon fiber composites using piezoresistivity. *Synthetic Metals*, *224*, 56–62.

178. Ko, F. K., Pastore, C. M., & Head, A. A. (1989). *Atkins & Pearce Handbook of Industrial Braiding*. (A. & Pearce, Ed.). Covington: Atkins & Pearce.

179. Rana, S., & Fangueiro, R. (2016). *Braided structures and composites Production, Properties, Mechanics, and Technical Applications*. Florida: CRC Press.

180. Carey, J. P. (2017). Introduction to braided composites. In J. P. Carey (Ed.), *Handbook of Advances in Braided Composite Materials* (pp. 1–21). Duxford, UK: Woodhead Publishing Limited.

181. Omeroglu, S. (2006). The effect of braiding parameters on the mechanical properties of braided ropes. *Fibres and Textiles in Eastern Europe*, *14*(4), 53–57.

182. Brunnschweiler, D. (1953). BRAIDS AND BRAIDING. *Journal of the Textile Institute Proceedings*, *44*(9), P666–P686. doi.org/10.1080/19447015308687874

183. Dickinson, H. W. (1942). A Condensed History of Rope-making. *Transactions of the Newcomen Society*, *23*(1), 71–91. doi.org/10.1179/tns.1942.007

184. Zhang, Q., Beale, D., & Broughton, R. M. (1999). Analysis of Circular Braiding Process , Part 1 : Theoretical Investigation of Kinematics of the Circular Braiding Process. *Journal of Manufacturing Science and Engineering*, *121*(3), 345–350.

185. Roy, S. S., & Potluri, P. (2016). Braiding: From Cordage to Composites. In *Textile Research Conference,* (pp. 3–6). Dhaka, Bangladesh Braiding:

186. Branscomb, D., Beale, D., & Broughton, R. (2013). New Directions in Braiding. *Journal of Engineered Fibres and Fabrics*, *8*(2), 11–24.

187. Brunnschweiler, D. (1954). The structure and tensile properties of braids. *Journal of the Textile Institute Transactions*, *45*(1), T55–T77. doi.org/10.1080/19447025408662631

188. Bicking, A., & Oxenham, W. (2012). Variables and Methods for Aesthetic Braid Design. *Journal of Textile and Apparel, Technology and Management*, *7*(4), 1–17.

189. Carey, J. P. (2016). *Handbook of Advances in Braided Composite Materials: Theory, Production, Testing and Applications.* (J. P. Carey, Ed.). Duxford, UK: Woodhead Publishing Limited.

190. Melenka, G. W., Hunt, A. J., van Ravenhorst, J. H., Akkerman, R., Pastore, C. M., Ko, F. K., … Carey, J. P. (2017). Manufacturing processes for braided composite materials. In J. P. Carey (Ed.), *Handbook of Advances in Braided Composite Materials* (pp. 47–153). Cambridge, UK: Woodhead Publishing Limited.

191. Ayranci, C., & Carey, J. P. (2008). 2D braided composites: A review for stiffness critical applications. *Composite Structures*, *85*(1), 43–58.

192. Kyosev, Y. (2015). Patterning of braided products. In Y. Kyosev (Ed.), *Braiding Technology for Textiles* (pp. 29–46). Cambridge, UK: Woodhead Publishing Limited.

193. Melenka, G. W., & Ayranci, C. (2020). Advanced measurement techniques for braided composite structures: A review of current and upcoming trends. *Journal of Composite Materials*, *0*(0), 1–23.

194. Kyosev, Y., & Cordes, A. (2016). Geometrical Modelling of Tubular and Flat Braids Within the Jamming Limits—Verification and Limitations. In Y. Kyosev (Ed.), *Recent Developments in Braiding and Narrow Weaving* (pp. 23–31). Mönchengladbach Germany: Springer International Publishing Switzerland.

195. Potluri, P., & Nawaz, S. (2011). Developments in braided fabrics. In R. H. Gong (Ed.), *Specialist Yarn and Fabric Structures* (pp. 333–353). Cambridge, UK: Woodhead Publishing Limited.

196. Zhang, Q., Beale, D., Adanur, S., Broughton, R. M., & Walker, R. P. (1997). Structural analysis of a two-dimensional braided fabric. *Journal of the Textile Institute*, *88*(1), 41–52. doi.org/10.1080/00405009708658528

197. Arold, B., Gessler, A., Metzner, C., & Birkefeld, K. (2015). Braiding processes for composite manufacture. In P. Boisse (Ed.), *Advances in Composites Manufacturing and Process Design* (pp. 1–25). Cambridge, UK: Woodhead Publishing Ltd.

198. Heieck, F., Hermann, F., Middendorf, P., & Schladitz, K. (2017). Influence of the cover factor of 2D biaxial and triaxial braided carbon composites on their in-plane mechanical properties. *Composite Structures*, *163*, 114–122. doi.org/10.1016/j.compstruct.2016.12.025

199. Noughabi, H., Vadood, M., Johari, M. S., & Safar Johari, M. (2018). Investigating the effect of pattern and core yarn on the mechanical properties of braids and braided composites. *Materials Research Express*, *5*(6), 065324. doi.org/10.1088/2053-1591/aacc0b

200. Carr, D. J., Heward, A. G., Laing, R. M., & Niven, B. E. (2009). Measuring the strength of knotted suture materials. *Journal of the Textile Institute*, *100*(1), 51–56. doi.org/10.1080/00405000701608177

201. Naniz, M. A., Bodaghi, M., Johari, M. S., & Zolfagharian, A. (2020).

Influence of hybridization on tensile behaviors of non-absorbable braided polymeric sutures. *Polymers*, *12*(3). doi.org/10.3390/polym12030682

202. Potluri, P. (2012). Braiding. In L. Nicolais & A. Borzacchiello (Eds.), *Wiley Encyclopedia of Composites* (2nd ed.). New York: Wiley.

203. Ivey, M., Ayranci, C., & Carey, J. P. (2016). Braidtrusion. In J. P. Carey (Ed.), *Handbook of Advances in Braided Composite Materials. Theory, Production, Testing and Applications* (pp. 433–450). Duxford, UK: Woodhead Publishing Limited.

204. Bradford, P. D., & Bogdanovich, A. E. (2010). Carbon nanotube yarn and 3-D braid composites. Part II: Dynamic mechanical analysis. *Composites Part A: Applied Science and Manufacturing*, *41*(2), 238–246. doi.org/10.1016/j.compositesa.2009.10.003

205. Rana, S., Zdraveva, E., Pereira, C., Fangueiro, R., & Correia, A. G. (2014). Development of hybrid braided composite rods for reinforcement and health monitoring of structures. *The Scientific World Journal*, (170187), 1–9. doi.org/10.1155/2014/170187

206. Legrand, X., Cochrane, C., & Koncar, V. (2016). A complex shaped-reinforced thermoplastic composite part made of commingled yarns with an integrated sensor. In *Smart Textiles and Their Applications* (pp. 353–374). Elsevier Inc.

207. Sakaguchi, M., Nakai, A., Hamada, H., & Takeda, N. (2000). The mechanical properties of unidirectional thermoplastic composites manufactured by a micro-braiding technique. *Composites Science and Technology*, *60*(5), 717–722. doi.org/10.1016/S0266-3538(99)00175-X

208. Hristov, K., Armstrong-carroll, E., Dunn, M., Pastore, C., & Gowayed, Y. (2004). Mechanical Behavior of Circular Hybrid Braids Under Tensile Loads. *Texcomp-12 Conference*, *74*(1), 20–26. doi.org/10.1177/004051750407400104

209. Chiu, C. H., Tsai, K. H., & Huang, W. J. (1999). Crush-failure modes of 2D triaxially braided hybrid composite tubes. *Composites Science and Technology*, *59*(11), 1713–1723. doi.org/10.1016/S0266-3538(99)00036-6

210. Han, H., Taheri, F., Pegg, N., & Lu, Y. (2007). A numerical study on the axial crushing response of hybrid pultruded and ±45° braided tubes. *Composite Structures*, *80*(2), 253–264. doi.org/10.1016/j.compstruct.2006.05.012

211. Karbhari, V. M., Falzon, P. J., & Herzberg, I. (1997). Energy Absorption Characteristics of Hybrid Braided Composite Tubes. *Journal of Composite Materials*, *31*(12), 1164–1186. doi.org/10.1177/002199839703101201

212. Amirkhizi, A. V, Plaisted, T., & Nemat-Nasser, S. C. (2003). Metallic Coil-Polymer Braid Composites : I . The Numerical Modeling and Chirality. In *14th Ann. Int. Conf. on Composite Materials*. San Diego, CA.

213. Plaisted, T. A., Amirkhizi, A. V., Arbelaez, D., Nemat-nasser, S. S. C. S., & Nemat-nasser, S. S. C. S. (2003). Metallic Coil-Polymer Braid Composites : II . Material Processing and Characterization. In *Material processing and characterization ICCM: 14th Ann. Int. Conf. on Composite Materials*. San Diego, CA.

214. Nemat-Nasser, S., Nemat-Nasser, S., Plaisted, T., Starr, A., & Vakil Amirkhizi, A. (2005). Multifunctional Materials. In Y. Bar-Cohen (Ed.), *BIOMIMETICS: Biologically Inspired Technologies* (pp. 309–340). Pasadena, California: CRC Press. Retrieved from http://www.crcnetbase.com/doi/abs/10.1201/9781420037715.ch12

215. Zhao, C., Farajikhah, S., Wang, C., Foroughi, J., Jia, X., & Wallace, G. G. (2015). 3D braided yarns to create electrochemical cells. *Electrochemistry Communications*, *61*, 27–31. doi.org/10.1016/j.elecom.2015.09.021

216. Heward, A. G., Laing, R. M., Carr, D. J., & Niven, B. E. (2004). Tensile Performance of Nonsterile Suture Monofilaments Affected by Test Conditions. *Textile Research Journal*, *74*(1), 83–90. doi.org/10.1177/004051750407400115

217. Ben Abdessalem, S., Debbabi, F., Jedda, H., Elmarzougui, S., & Mokhtar, S. (2009). Tensile and Knot Performance of Polyester Braided Sutures. *Textile Research Journal*, *79*(3), 247–252. doi.org/10.1177/0040517508094090

218. Zhai, W., Wang, P., Legrand, X., Soulat, D., & Ferreira, M. (2020). Effects of micro-braiding and co-wrapping techniques on characteristics of flax/polypropylene-based hybrid yarn: A comparative study. *Polymers*, *12*(11), 1–14. doi.org/10.3390/polym12112559

219. Hamouda, T., Aly, N. M., & Elshakankery, M. (2020). An experimental study on the interaction between braiding structural parameters and their effects on ropes mechanical properties. *Journal of Industrial Textiles*, 152808372096073. doi.org/10.1177/1528083720960732

220. Rawal, A., Kumar, R., Saraswat, H., Rana, R. S., Purohit, R., & Das, S. (2012). Tensile mechanics of braided sutures. *Textile Research Journal*, *82*(16), 1703–1710. doi.org/10.1177/0040517512445340

221. Rufai, O., Gautam, M., Potluri, P., & Gresil, M. (2019). Optimisation of optical fibre using micro-braiding for structural health monitoring. *Journal of Intelligent Material Systems and Structures*, *30*(2), 171–185. doi.org/10.1177/1045389X18810805

222. Gautam, M., Katnam, K. B., Potluri, P., Jha, V., Latto, J., & Dodds, N. (2017). Hybrid composite tensile armour wires in flexible risers: A multi-scale model. *Composite Structures*, *162*, 13–27. doi.org/10.1016/j.compstruct.2016.11.090

223. Memon, A., & Nakai, A. (2013). The processing design of jute spun yarn/PLA braided composite by pultrusion molding. *Advances in Mechanical Engineering*, (2013), 1–8. doi.org/10.1155/2013/816513

224. Ghaedsharaf, M., Brunel, J. E., & Laberge Lebel, L. (2020). Thermoplastic composite rod manufacturing using biaxial braid-trusion. In *ECCM 2018 - 18th European Conference on Composite Materials* (pp. 1–8). Athens.

225. Wang, Y., & Sun, X. (2001). Digital-element simulation of textile processes. *Composites Science and Technology*, *61*(2), 311–319. doi.org/10.1016/S0266-3538(00)00223-2

226. Zhou, G., Sun, X., & Wang, Y. (2004). Multi-chain digital element analysis in textile mechanics. *Composites Science and Technology*, *64*(2), 239–244. doi.org/10.1016/S0266-3538(03)00258-6

227. Thompson, A. J., El Said, B., Ivanov, D., Belnoue, J. P. H., & Hallett, S. R. (2018). High fidelity modelling of the compression behaviour of 2D woven fabrics. *International Journal of Solids and Structures*, *154*, 104–113. doi.org/10.1016/J.IJSOLSTR.2017.06.027

228. El Said, B., Green, S., & Hallett, S. R. (2014). Kinematic modelling of 3D woven fabric deformation for structural scale features. *Composites Part A: Applied Science and Manufacturing*, *57*, 95–107. doi.org/10.1016/j.compositesa.2013.11.006

229. Green, S. D., Long, A. C., El Said, B. S. F., & Hallett, S. R. (2014). Numerical modelling of 3D woven preform deformations. *Composite Structures*, *108*(1), 747–756. doi.org/10.1016/j.compstruct.2013.10.015

230. Sun, X., Kawashita, L. F., Wollmann, T., Spitzer, S., Langkamp, A., & Gude, M. (2018). Experimental and numerical studies on the braiding of carbon fibres over structured end-fittings for the design and manufacture of high performance hybrid shafts. *Production Engineering*, *12*(2), 215–228. doi.org/10.1007/s11740-018-0824-1

231. Del Rosso, S., Curtis, P. T., Iannucci, L., & Curtis, P. T. (2019). Finite Element Simulation of the braiding process. *Mechanics of Advanced Materials and Modern Processes*, *5*(1), 1–11. doi.org/10.1115/IMECE2008-67017

232. Ghosh, A., Ishtiaque, S. M., Rengasamy, R. S., Mal, P., & Patnaik, A. (2004). Spun yarn strength as a function of gauge length and extension rate: A critical review. *Journal of Textile and Apparel, Technology and Management*, *4*(2).

233. Gspann, T. S., Ngern, N. H. H., Kiley, P. J., McKeown, P. A., Bulmer, J. S., Windle, A. H., … Elliott, J. A. (2020). A comparative study of the tensile failure of carbon nanotube, Dyneema and carbon fibre tows over six orders of strain rate. *Carbon*, *164*, 407–421. doi.org/10.1016/j.carbon.2020.03.051

234. Balasubramanian, P., & Salhotra, K. R. (1985). Effect of Strain Rate on Yarn Tenacity. *Textile Research Journal*, *55*(1), 74–75. doi.org/10.1177/004051758505500114

235. Ebel, C., Mierzwa, A., & Kind, K. (2016). *Yarn damage during braiding of reinforcement fibers for composites*. *Advances in Braiding Technology*. Elsevier Ltd. Retrieved from http://dx.doi.org/10.1016/B978-0-08-100407-4.00013-2

236. Ou, Y., Zhu, D., Huang, M., & Li, H. (2017). The effects of gage length and strain rate on tensile behavior of Kevlar® 29 single filament and yarn. *Journal of Composite Materials*, *51*(1), 109–123. doi.org/10.1177/0021998316639121

237. Chattopadhyay, R. (1999). The Influence of the Strain Rate on the Characteristics of the Load—Elongation Curves of Ring-spun and Air-jet-spun Yarns. *Journal of the Textile Institute*, *90*(2), 268–271. doi.org/10.1080/00405009908690629

238. Ghosh, A., Ishtiaque, S. M., & Rengasamy, R. S. (2005). Analysis of Spun Yarn Failure. Part I: Tensile Failure of Yarns as a Function of Structure and Testing Parameters. *Textile Research Journal*, *75*(10), 731–740.

doi.org/10.1177/0040517505053956

239. British Standards Institution. (2009). BS EN ISO 2062:2009. Textiles — Yarns from packages — Determination of single-end breaking force and elongation at break using constant rate of extension. Retrieved February 1, 2018, from http://www.standardsuk.com/.

240. British Standards Institution. (2000). BS ISO 3341:2000. Textile glass— Yarns—Determination of breaking force and breaking elongation.

241. Gondo, S., Suzuki, S., Asakawa, M., Takemoto, K., Tashima, K., & Kajino, S. (2018). Establishing a simple and reliable method of measuring ductility of fine metal wire. *International Journal of Mechanical and Materials Engineering*, *13*(1). doi.org/10.1186/s40712-018-0091-0

242. British Standards Institution. (1993). BS 7658-2: 1993, ISO 10120:1991. Carbon fibre — Part 2: Method for determination of linear density. Retrieved February 1, 2018, from http://www.standardsuk.com/

243. Harizi, W., Azzouz, R., Martins, A., Hamdi, K., Aboura, Z., & Khellil, K. (2019). Electrical resistance variation during tensile and self-heating tests conducted on thermoplastic polymer-matrix composites. *Composite Structures*, *224*. doi.org/10.1016/j.compstruct.2019.111001

244. Osmiani, C. (2017). *Multi-scale characterisation and modelling of tufted composites (PhD Thesis)*. Univeristy of Bristol.

245. Osmiani, C., Mohamed, G., Treiber, J. W. G., Allegri, G., & Partridge, I. K. (2016). Exploring the influence of micro-structure on the mechanical properties and crack bridging mechanisms of fibrous tufts. *Composites Part A: Applied Science and Manufacturing*, *91*, 409–419. doi.org/10.1016/j.compositesa.2016.08.008

246. Zhang, B. (2015). *Mechanical performance and self-sensing of through-thickness reinforced composites (PhD Thesis)*. Univerisity of Bristol.

247. ASTM International. (2007). ASTM Standard D5528 – 01 (Reapproved 2007). Standard Test Method for Mode I Interlaminar Fracture Toughness of Unidirectional Fiber-Reinforced Polymer Matrix Composites. West Conshohocken,Pennsylvania, USA.

248. 3M Electrical Products Division. (1998). 245 Tape Embossed Copper Foil Data Sheet Product Description. Retrieved October 8, 2020, from http://www.3m.com/elpd

249. Technical Fibre Products Ltd. (2014). Optiveil® Technical data Sheet. Copper & nickel coated carbon mat 20444B. Retrieved October 29, 2019, from www.tfpglobal.com

250. Technical Fibre Products Ltd. (2015). Optimat® Technical Data Sheet 20444A Copper & Nickel Coated Carbon Mat. Retrieved October 29, 2019, from www.tfpglobal.com

251. Halliwell, S. (2012). Repair of fibre reinforced polymer (FRP) structures. National Composites Network Best Practice Guide. *NetComposites*. Retrieved May 5, 2020, from http://www.netcomposites.com

252. Landers, R. G., Barton, K., Devasia, S., Kurfess, T., Pagilla, P., & Tomizuka, M. (2020). A Review of Manufacturing Process Control. *Journal of Manufacturing Science and Engineering*, *142*(11), 110814.

doi.org/10.1115/1.4048111

253. Marsh, G. (2012). The challenge of composite fuselage repair. *Reinforced Plastics*, *56*(3), 30–35. doi.org/10.1016/S0034-3617(14)70085-2

254. Katnam, K. B., Da Silva, L. F. M., & Young, T. M. (2013). Bonded repair of composite aircraft structures: A review of scientific challenges and opportunities. *Progress in Aerospace Sciences*, *61*, 26–42. doi.org/10.1016/j.paerosci.2013.03.003

255. Santhanakrishnan Balakrishnan, V., & Seidlitz, H. (2018). Potential repair techniques for automotive composites: A review. *Composites Part B: Engineering*, *145*, 28–38. doi.org/10.1016/j.compositesb.2018.03.016

256. Budhe, S., Banea, M. D., & de Barros, S. (2018). Bonded repair of composite structures in aerospace application: a review on environmental issues. *Applied Adhesion Science*, *6*(1), 1–27. doi.org/10.1186/s40563-018-0104-5

257. Katnam, K. B., Comer, A. J., Roy, D., Da Silva, L. F. M., & Young, T. M. (2015). Composite repair in wind turbine blades: An overview. *Journal of Adhesion*, *91*(1–2), 113–139. doi.org/10.1080/00218464.2014.900449

258. Matsen, M. (2020). Final Technical Report. Energy Efficient Thermoplastic Composite Manufacturing. Seattle, WA: Boeing Research and Technology USDOE Office of Energy Efficiency and Renewable Energy (EERE). Retrieved August 21, 2021, from 10.2172/1609100

259. Lucia, O., Maussion, P., Dede, E. J., & Burdio, J. M. (2014). Induction heating technology and its applications: Past developments, current technology, and future challenges. *IEEE Transactions on Industrial Electronics*, *61*(5), 2509–2520. doi.org/10.1109/TIE.2013.2281162

260. Manral, A., Ahmad, F., & Sharma, B. (2020). Advances in Curing Methods of Reinforced Polymer Composites. In P. K. Bajpai & I. Singh (Eds.), *Reinforced Polymer Composites: Processing, Characterization and Post Life Cycle Assessment* (pp. 77–104). Weinheim, Germany: Wiley-VCHVerlag GmbH& Co. KGaA.

261. Rider, A. N., Wang, C. H., & Cao, J. (2011). Internal resistance heating for homogeneous curing of adhesively bonded repairs. *International Journal of Adhesion and Adhesives*, *31*(3), 168–176. doi.org/10.1016/j.ijadhadh.2011.01.001

262. Ashrafi, M., Smith, B. P., Devasia, S., & Tuttle, M. E. (2017). Embedded resistive heating in composite scarf repairs. *Journal of Composite Materials*, *51*(18), 2575–2583.

263. Smith, B. P. (2017). *Bondline temperature control using carbon fiber embedded resistive heaters (PhD thesis)*. University of Washington.

264. Forintos, N., & Czigany, T. (2019). Multifunctional application of carbon fiber reinforced polymer composites: Electrical properties of the reinforcing carbon fibers – A short review. *Composites Part B: Engineering*, *162*, 331–343. doi.org/10.1016/j.compositesb.2018.10.098

265. Wang, T., & Liu, J. (2000). A review of microwave curing of polymeric materials. *Journal of Electronics Manufacturing*, *10*(3), 181–189. doi.org/10.1142/S0960313100000162

266. Kwak, M., Robinson, P., Bismarck, A., & Wise, R. (2015). Microwave curing of carbon-epoxy composites: Penetration depth and material characterisation. *Composites Part A: Applied Science and Manufacturing*, *75*, 18–27. doi.org/10.1016/j.compositesa.2015.04.007

267. Rudnev, V., Loveless, D., & Cook, R. L. (2017). *Handbook of Induction Heating (Second edition)*. *Taylor & Francis Group*. Boca Raton: CRC Press.

268. Papargyris, D. A., Day, R. J., Nesbitt, A., & Bakavos, D. (2008). Comparison of the mechanical and physical properties of a carbon fibre epoxy composite manufactured by resin transfer moulding using conventional and microwave heating. *Composites Science and Technology*, *68*(7–8), 1854–1861. doi.org/10.1016/j.compscitech.2008.01.010

269. Mgbemena, C. O., Li, D., Lin, M.-F., Liddel, P. D., Katnam, K. B., Kumar, V. T., & Nezhad, H. Y. (2018). Accelerated microwave curing of fibre-reinforced thermoset polymer composites for structural applications: A review of scientific challenges. *Composites Part A: Applied Science and Manufacturing*, *115*, 88–103. doi.org/10.1016/j.compositesa.2018.09.012

270. Li, N., Li, Y., Jelonnek, J., Link, G., & Gao, J. (2017). A new process control method for microwave curing of carbon fibre reinforced composites in aerospace applications. *Composites Part B: Engineering*, *122*, 61–70. doi.org/10.1016/j.compositesb.2017.04.009

271. Hayes, S. A., Lafferty, A. D., Altinkurt, G., Wilson, P. R., Collinson, M., & Duchene, P. (2015). Direct electrical cure of carbon fiber composites. *Advanced Manufacturing: Polymer and Composites Science*, *1*(2), 112–119. doi.org/10.1179/2055035915Y.0000000001

272. Nguyen, N., Hao, A., Park, J. G., & Liang, R. (2016). In Situ Curing and Out-of-Autoclave of Interply Carbon Fiber/Carbon Nanotube Buckypaper Hybrid Composites Using Electrical Current. *Advanced Engineering Materials*, *18*(11), 1906–1912. doi.org/10.1002/adem.201600307

273. Flanagan, M., Doyle, A., Doyle, K., Ward, M., Bizeul, M., Canavan, R., … Goggins, J. (2019). Comparative manufacture and testing of induction-welded and adhesively bonded carbon fibre PEEK stiffened panels. *Journal of Thermoplastic Composite Materials*, *32*(12), 1622–1649. doi.org/10.1177/0892705718792362

274. Labordus, M., & Bach, M. (2020). Qualification Approach for Induction Welding of Thermoplastic Composites Using UD-Based Materials. *GBM Webinars*. Retrieved November 12, 2020, from https://register.gotowebinar.com/register/8693806964942357004?source=

275. Van Ingen, J., Buitenhuis, A., Van Wijngaarden, M., Simmons, F., Van Wijngaarden, M Simmons III, F., & Van Wijngaarden, M Simmons, F. (2010). Development of the Gulfstream G650 induction welded thermoplastic elevators and rudder. In *International SAMPE Symposium and Exhibition*. Seattle, WA: SAMPE, California.

276. Grouve, W., Vruggink, E., Sacchetti, F., & Akkerman, R. (2020). Induction heating of UD C / PEKK cross-ply laminates. *Procedia Manufacturing*, *47*(2019), 29–35. doi.org/10.1016/j.promfg.2020.04.112

277. Mizukami, K., Mizutani, Y., Todoroki, A., & Suzuki, Y. (2015). Detection of delamination in thermoplastic CFRP welded zones using induction heating assisted eddy current testing. *NDT and E International*, *74*, 106–111.

278. Nele, L., & Palmieri, B. (2020). Electromagnetic heating for adhesive melting in CFRTP joining: study, analysis, and testing. *International Journal of Advanced Manufacturing Technology*, *106*(11–12), 5317–5331. doi.org/10.1007/s00170-019-04910-9

279. Becker, S., & Mitschang, P. (2019). Influence of thread count of carbon twill textile-reinforced polyamide 66 laminates on the inductive heating behavior. *Journal of Thermoplastic Composite Materials*, 1–27. doi.org/10.1177/0892705719854493

280. Baek, I., & Lee, S. (2020). A study of films incorporating magnetite nanoparticles as susceptors for induction welding of carbon fiber reinforced thermoplastic. *Materials*, *13*(2), 1–10. doi.org/10.3390/ma13020318

281. Ahmed, T. J., Stavrov, D., Bersee, H. E. N., & Beukers, A. (2006). Induction welding of thermoplastic composites-an overview. *Composites Part A: Applied Science and Manufacturing*, *37*(10), 1638–1651.

282. Bayerl, T., Duhovic, M., Mitschang, P., & Bhattacharyya, D. (2014). The heating of polymer composites by electromagnetic induction - A review. *Composites Part A: Applied Science and Manufacturing*, *57*(2014), 27–40. doi.org/10.1016/j.compositesa.2013.10.024

283. Miller, A. K., Chang, C., Payne, A., Gur, M., Menzel, E., & Peled, A. (1990). The nature of induction heating in graphite-fiber polymer-matrix composite materials. *SAMPE Journal*, *26*(4), 37–54.

284. Fink, B. K., McCullough, R. L., & Gillespie, J. W. (1995). A model to predict the through-thickness distribution of heat generation in cross-ply carbon-fiber composites subjected to alternating magnetic fields. *Composites Science and Technology*, *55*(2), 119–130. doi.org/10.1016/0266-3538(95)80024-7

285. Yarlagadda, S., Kim, H. J., Gillespie, J. W., Shevchenko, N. B., & Fink, B. K. (2002). A study on the induction heating of carbon fiber reinforced thermoplastic composites. *Advanced Composite Materials*, *11*(1), 71–80. doi.org/10.1163/156855102753613309

286. O'Shaughnessey, P. G., Dubé, M., & Fernandez Villegas, I. (2016). Modeling and experimental investigation of induction welding of thermoplastic composites and comparison with other welding processes. *Journal of Composite Materials*, *50*(21), 2895–2910. doi.org/10.1177/0021998315614991

287. Rudolf, R., Mitschang, P., & Neitzel, M. (2000). Induction heating of continuous carbon-fibre-reinforced thermoplastics. *Composites Part A: Applied Science and Manufacturing*, *31*(11), 1191–1202. doi.org/10.1016/S1359-835X(00)00094-4

288. Xu, X., Zhang, Y., Jiang, J., Wang, H., Zhao, X., Li, Q., & Lu, W. (2017). In-situ curing of glass fiber reinforced polymer composites via resistive heating of carbon nanotube films. *Composites Science and Technology*,

149, 20–27. doi.org/10.1016/j.compscitech.2017.06.001

289. Farahani, R. D., Janier, M., & Dubé, M. (2018). Conductive films of silver nanoparticles as novel susceptors for induction welding of thermoplastic composites. *Nanotechnology*, *29*(12), 125701. doi.org/10.1088/1361-6528/aaa93c

290. Rhodes Jr, B. L., & Van Tooren, M. (2020). Welding and consolidation of thermoplastic composites using vacuum bagging, air cooling and induction. Patent No. US 20200086583 A1. Columbia, US. Retrieved from https://www.freepatentsonline.com/y2020/0086583.html

291. Moser, L. (2012). *Experimental analysis and modeling of susceptorless induction welding of high performance thermoplastic polymer composites (PhD Thesis)*. University of Kaiserslautern.

292. Fink, B. K., McCullough, R. L., & Gillespie, J. W. (1992). A local theory of heating in cross-ply carbon fiber thermoplastic composites by magnetic induction. *Polymer Engineering & Science*, *32*(5), 357–369. doi.org/10.1002/pen.760320509

293. Guo, J., Gao, X., Toma, E., & Netzelmann, U. (2017). Anisotropy in carbon fiber reinforced polymer (CFRP) and its effect on induction thermography. *NDT and E International*, *91*, 1–8. doi.org/10.1016/j.ndteint.2017.05.004

294. Mattheß, D., Landgrebe, D., & Drossel, W. G. (2017). Inductive heating of glass fibre-reinforced thermoplastics using fibre- and wire-shaped stainless steel susceptors. *Journal of Thermoplastic Composite Materials*, *30*(1), 67–87. doi.org/10.1177/0892705715583179

295. Li, D., Lu, Z., & Fang, D. (2009). Longitudinal compressive behavior and failure mechanism of three-dimensional five-directional carbon/phenolic braided composites at high strain rates. *Materials Science and Engineering A*, *526*(1–2), 134–139. doi.org/10.1016/j.msea.2009.07.009

296. Ji, X., Khatri, A. M., Chia, E. S., Cha, R. K., Yeo, B. T., Joshi, S. C., & Chen, Z. (2014). Multi-scale simulation and finite-element-assisted computation of elastic properties of braided textile reinforced composites. *Journal of Composite Materials*, *48*(8), 931–949. doi.org/10.1177/0021998313480198

297. Buchamp, B., Legrand, X., & Soulat, D. (2018). The tensile behaviour of biaxial and triaxial braided fabrics. *Journal of Industrial Textiles*, *47*(8), 2184–2204.

298. Kyosev, Y. (2015). Carrier mechanics in braiding operations. In Y. Kyosev (Ed.), *Braiding Technology for Textiles* (pp. 211–229). Cambridge, UK: Woodhead Publishing Limited. Retrieved from http://linkinghub.elsevier.com/retrieve/pii/B978085709135250009X